UNIVERSIDADE DO ALGARVE

Faculdade de Ciências e Tecnologia

Digital Quadrature Demodulation of Doppler Signals

Manuel Mateus e Silva Rocha

Mestrado em Engenharia Electrónica e Telecomunicações

especialidade de Processamento de Sinal

2009

UNIVERSIDADE DO ALGARVE

Faculdade de Ciências e Tecnologia

Digital Quadrature Demodulation of Doppler Signals

Manuel Mateus e Silva Rocha

Dissertação orientada por:

Maria da Graça Cristo dos Santos Lopes Ruano

Mestrado em Engenharia Electrónica e Telecomunicações

especialidade de Processamento de Sinal

2009

Resumo

A descobertas dos ultrassons deu-se em 1880 [39]. A utilização de ultrassons como ferramenta de diagnóstico existe há pelo menos 4 décadas [28]. O uso de ultrassons tem abrangido diversas áreas deste a detecção e quantificação de obstruções no sistema cardiovascular [79], à detecção de gravidez e avaliação de vários aspectos na saúde do feto, bem como à localização e medição dos cálculos renais. A utilização dos ultrassons no diagnóstico tem sofrido uma evolução crescente permitindo actualmente a identificação de micro-êmbolos bem como a sua caracterização em termos da constituição e dimensão [79]. As técnicas de ultrassom têm igualmente evoluído de forma a possibilitar a apresentação dos resultados em imagens 2D coloridas [1], bem como imagens 3D [86] como as aplicadas para visualizar o feto num espaço tridimensional.

Se considerarmos o caso específico do diagnóstico aplicado à detecção e quantificação ao nível do sistema cardiovascular os ultrassons podem ser aplicados de diferentes formas, permitindo a obtenção qualitativa e quantitativa de várias informações. Actualmente e inserido no projecto Desarrollo de Sistemas Ultrasónicos y Computacionales para Diagnóstico Cardiovascular (SUCoDiC) [85] a informação recolhida com recurso aos ultrassons é proveniente de três técnicas: Avaliação do fluxo sanguíneo através do efeito de Doppler [40][41][42], medição do volume de fluxo sanguíneo através das técnicas de Transit-Time Flow Measurements (TTFM) [36] e o estudo das propriedades mecânicas das paredes dos vasos sanguíneos através da técnica de elastografia [37] [38].

No contexto do projecto mencionado, estas três técnicas são aplicadas para avaliar a qualidade de conjuntos de bypasses realizados durante cirurgias cardíacas. Com recurso a estas técnicas o cirurgião determina, durante a cirurgia, se cada bypass criado conduz uma quantidade de fluxo sanguíneo adequada e, recorrendo à tecnica de elastografia avalia se as propriedades mecânicas da veia a utilizar no bypass por forma a evitar que futuramente o paciente tenha de sujeitar-se a nova operação. A combinação das três técnicas durante a intervenção cirúrgica possibilitam a diminuição de problemas pós-operatórios, na medida em que auxiliam os cirurgiões através de imagens e da quantificação de parâmetros cruciais no momento de avaliar a qualidade de cada bypass aplicado.

Convém igualmente referir que os ultrassons são uma ferramenta muito eficaz em diversas áreas, não estando estas limitadas à medicina. Podemos encontrar exemplos de aplicações dos ultrassons noutras áreas como na indústria (para limpeza de materiais, processos químicos, desgaseificação de solventes, obtenção de informações sobre defeitos [39]) , em sistemas de localização em interiores (*indoor location*) (reportando-se serem mais precisos do que sistemas baseados em infravermelhos,

radio-frequência ou sensores no chão [84]), entre outras áreas.

O trabalho realizado nesta tese enquadra-se no processamento de sinais biomédicos obtidos por ultrassom de Doppler. No projecto SUCoDiC, um sistema analógico [40] é responsável pelo processamento dos sinais de ultrassom resultantes do retro-espalhamento das partículas contidas no fluxo sanguíneo. Neste sistema, os sinais de ultrassons recebidos são desmodulados analogicamente por forma a obterem-se as componentes em fase (I) e em quadratura (Q) do respectivo sinal. Estas duas componentes são posteriormente utilizadas para a obtenção de informação sobre a direcção do fluxo sanguíneo através do seu processamento digital. Foi, no entanto, verificado que a existência de um desiquilíbrio nos ganhos nos canais do desmodulador (um canal para a componente em fase e outro para a componente em quadratura) provoca problemas na separação do fluxo directo e reverso.

Através das pesquisas realizadas, verificou-se que os desmoduladores digitais em quadratura são sugeridos como alternativas ao desmodulador analógico actualmente utilizado no referido projecto. De facto, o recurso aos desmoduladores em fase e em quadratura digitais permite solucionar problemas associados a ganhos desiguais, diferenças de fase diferentes de 90^o e ainda variações do valor das componentes DC entre os canais relativos às componentes em fase e em quadratura.

O resurso a técnicas digitais para realizar o processamento dos sinais e consequente obtenção das componentes em fase e em quadratura, apresenta igualmente vantagens associadas à flexibilidade destas técnicas, no que respeita à alteração de parâmetros de uma determinada técnica, bem como à flexibilidade de substituição de uma técnica por outra. Associado a esta flexibilidade surge igualmente a rapidez com que as alterações podem ser feitas.

Devido às características inerentes ao ultrassom utilizado foram encontradas, na prática, limitações impostas pelo conversor analógico-para-digital em relação à frequência de amostragem possível de ser utilizada. Como forma de contornar este obstáculo duas estratégias foram implementadas. Numa, recorrendo à função heteródina, os sinais de ultrassons, no domínio da rádio-frequência, são deslocados para portadoras de frequência inferior, permitindo desta forma a amostragem dos sinais sem que ocorra aliase. Outra estratégia, recorre a uma amostragem passabanda uniforme, e realiza a amostragem directa dos sinais de ultrassons no domínio da rádio-frequência, onde a frequência de amostragem é seleccionada por forma a criar uma aliase deliberada nos sinais de rádio-frequência. Ao criarem-se aliases do sinal desejado faz-se a sua translação espectral para uma frequência conhecida sem, no entanto, causar aliase no conteúdo do sinal.

A pesquisa realizada sobre técnicas digitais de quadratura foi concentrada no estudo de cinco abordagens digitais para a obtenção das componentes em fase e em quadratura. Três técnicas digitais de quadratura são sugeridas como alternativas viáveis ao desmodulador analógico e consequentemente deverão ser implementadas e testadas em processamento em tempo real.

Associado ao trabalho de processamento digital de sinal, foram igualmente desenvolvidas nesta tese aplicações em software e firmware com vista ao controlo de dispositivos, quer comerciais, quer desenvolvidos no decorrer deste trabalho. Para além da componente de software, vários módulos de hardware foram criados, como sendo, um circuito controlador de uma bomba de fluxo, um módulo

regulador de tensão, um módulo contendo um sintetizador de frequências baseado numa *Phase Locked Loop (PLL)* e ainda um módulo contendo um multiplicador analógico, filtros e um amplificador sintonizado.

A avaliação das técnicas digitais de quadratura é realizada recorrendo a um sinal de teste, simulado, que permitiu uma boa caracterização de inúmeros aspectos relativos à performance de cada uma das técnicas. No campo experimental, sinais cujo conteúdo espectral é conhecido e bem caracterizado foram produzidos por geradores de funções e, amostrados recorrendo às duas estratégias referidas (utilização da função heteródina e amostragem passabanda uniforme).

Os resultados obtidos pelas diferentes metodologias propostas são apresentados, criticados e, apontam-se as soluções que se consideram mais relevantes para integração no projecto de investigação no qual este trabalho se insere.

Palavras-Chave: Amostragem Passabanda, Doppler, Fluxo Sanguíneo, Quadratura Digital, Função Heteródina

Abstract

Ultrasound has for many years been an important tool in the detection and quantification of various health problems. In vascular diseases, for example, the ultrasound can be applied with different techniques such as Transit-Time Flow Measurements (TTFM) [36], Doppler [28][40][41][42] and elastography [37] [38].

Research has been developed focusing the signal processing of Doppler ultrasound signals. In an ongoing project, named Desarrollo de Sistemas Ultrasónicos y Computacionales para Diagnóstico Cardiovascular (SUCoDiC), Doppler ultrasound signals are processed by an analog signal processing unit, in order to obtain the inphase (I) and quadrature (Q) components of the Doppler ultrasound signals, to allow directional blood flow separation.

Problems associated with unbalanced channels' gain of the employed analog system have been detected, resulting in an inapropriate directional blood flow separation.

This thesis reports the research performed to eliminate such problems by substituting the analog system's demodulator by digital signal processing approaches aiming at the achievement of the same goals, i.e., obtaining the Doppler ultrasound signal's inphase (I) and quadrature (Q) components, for efficient directional blood flow separation.

Five digital quadrature techniques have been studied to achieve such goal. Also, given technical constraints imposed by the nature of the Doppler ultrasound signals to be used, and limitations of the sampling rate of the Analog-to-Digital Converter (ADC) used, two strategies to acquire the Doppler ultrasound signals were studied. Such strategies involved the sampling of a downconversion version of the Doppler ultrasound signals (by application of the heterodyne function) and direct sampling of the Doppler ultrasound signals using uniform bandpass sampling.

From the results obtained, three approaches are selected and proposed for real time implementation. Comparison between both signal sampling strategies employed are also presented.

Keywords: Bandpass Sampling, Doppler, Blood Flow, Digital Quadrature, Heterodyne Function

Agradecimentos

Primeiramente quero agradecer à minha orientadora Professora Doutora Maria da Graça Cristo dos Santos Lopes Ruano, pelo convite inicial, pelo apoio e amizade ao longo deste mestrado e pelas condições de trabalho proporcionadas para que nada faltasse em termos materiais. Graças aos seus conselhos e orientação foi possível, nos momentos difíceis, reflectir e encontrar caminhos para seguir sempre em frente.

Quero igualmente agradecer aos restantes membros do Grupo de Processamento de Sinal Biomédico, nomeadamente à Professora Doutora Maria Margarida Madeira e Moura e à Professora Doutora Ana Isabel Leiria pelas sugestões apresentadas por elas no início do trabalho, ao Engenheiro Sérgio Silva pela sua ajuda nalgumas aplicações criadas em linguagem Python, e um agradecimento especial ao Doutor César Teixeira pelas suas sugestões e pela troca de ideias ao longo de todo o trabalho realizado.

Quero agradecer à Letícia Costa, minha namorada, pelo carinho, pela imensa paciência e pelo apoio demonstrado ao longo deste mestrado.

Um agradecimento muito especial aos meus pais que sempre me apoiaram, ajudaram e pela muita paciência que têm tido.

Por fim quero fazer um agradecimento aos meus amigos e colegas de curso que me ajudaram durante o curso, em especial ao Eduardo Domingues Gonçalves, grande amigo e colega de curso, que ao longo de vários anos neste curso, sempre apresentou o seu apoio e ajuda.

Contents

List of Figures

List of Tables

Chapter 1

Introduction

1.1 Motivation

Arterial disease is one of the major causes of mortality in the developed world. It is known that there are many health risk factors associated with the development of arterial disease. Arterial obstruction or embolization is a consequence of atherosclerotic plaque development over time [1].

Ultrasound has presented itself as an important tool on the investigation and diagnosis of venous disorders, some of which can be fatal such as deep vein thrombosis [1].

With the use of ultrasound equipment early diagnosis of cardiovascular diseases can be made [46]. Several works have been published aiming at the development of equipment and signal processing strategies that allow better diagnosis of cardiovascular diseases as refered in [46], [49], [28], [40], [41] just to mention some examples.

Blood flow in the arteries, as the result of the contraction of the heart which forces the blood to circulate in the body, depends on two factors: (1) the energy available to drive the blood flow and (2) the resistance to flow presented by the vascular system [1]. It is known from physics that for an ideal fluid flowing through a pipe of nonuniform size, the product of the area and the fluid speed at all points along a pipe is constant if the fluid is considered incompressible [3] . This means that if a fluid encounters narrower sections in a tube, the fluid velocity will increase as it passes through the narrowed section [1], in order for the volume flux to be constant [3].

The presence of arterial disease in the arteries, such as stenoses or occlusions, can cause the vessel reduction. As the vessel diameter is reduced, the blood velocity will increase. Measurements of velocity can be made using Doppler ultrasound and it is often the change in velocity of blood within a diseased artery that is used to quantify the degree of narrowing [1].

When cardiovascular disease cause the obstruction of the blood vessels connected to the heart, one of the more efficient medical solutions is a heart surgery, where bypasses are made. The presence of the bypasses will increase the life time of the persons with high risc of suffering a stroke [36].

One of the major difficulties related to this type of surgery is the measurement of the volumetric blood flow that passes through the bypass, while the patient still have the chest open. By knowing

the volumetric blood flow, the doctor can better evaluate the success of the surgery. Also, the probabilities of post surgery complications tend to decrease [36].

Today, there are two fundamental techniques based in the ultrasound application used to evaluate the quality of the bypass. In one of these techniques Doppler frequency shift is used and the other one is the Transit-Time Flow Measurements (TTFM) technique. The application of Doppler technique allow the identification of unreachable blood vessels, identification of the blood flow direction, to determine if it is arterial or venous blood and finally to detect the position and the dimension of the stenosys. The TTFM technique allow a more precise quantification of the volume of flow that passes through the blood vessel [36].

In the case of vascular ultrasound, the Doppler effect is used since an emitted ultrasound beam is backscattered by the moving blood cells and the returning echo is received. The observed Doppler shift depends on the frequency of the ultrasound originally transmitted by the transducer, the velocity of the blood cells from which the ultrasound is backscattered and on the angle from which the movement of the blood is observed (i.e., the angle between the ultrasound beam and the direction of the blood flow) [1].

The TTFM principle is based on the difference between the propagation times of the ultrasonic signals that travel in the direction of the blood flow and against it. With this time difference, one can obtain an electric signal in real-time, whose amplitude is proportional to the volumetric blood flow that crosses a given vein or artery, and its sign reflects the direction of movement [36].

Because of the transducer characteristics, theoretically the measurements of the volumetric blood flow do not depend on the blood flow profile, the blood vessels geometry nor regarding the alignment of the transducer in relation to the blood vessels [36].

The TTFM is a technique that is currently used as an important complement to the verification of the coronary implants during the surgery [36].

Another technique increasingly being used in cardiovascular surgery is the elastrography. It is employed to characterize mechanical properties of tissues. Elastography involves the visual display of tissue mechanical properties' data, allow the detection of pathological tissue alterations in real-time [37].

Elastography evaluates the elasticity by extrapolating tissue characteristics from ultrasound wave reflections [37].

Noninvasive measurements of the mechanical properties of a blood vessel, such as elasticity, is useful for the diagnose of atherosclerosis, since there are significant differences between the elasticity of a normal blood vessel and those that are affected [38].

There is a project being developed with the intend of developing and manufacturing low-cost ultrasound-based instruments (Doppler, Transit-Time and Elastography) to measure vessel elastic properties and blood flow in coronary implants and bypasses. This project is denominated SUCoDiC [1] [85].

[1] Development of ultrasonic and computer systems to cardiovascular diagnosis

In this project, the electronic component devoted to the development of the Doppler system consists in a device that generates and transmits a pulsed ultrasound beam. After receiving the backscattered echoes from the moving blood cells, it demodulates the RF received signal in order to obtain this signal's inphase and quadrature baseband components. These components are then acquired through the computer's line-in port (which will digitize the analog signal) to be processed in the computer [40] [41]. The generation of the I and Q components of the RF signal are made with analog circuitry. Later experiments allowed the detection that an imbalance between the gains of the demodulaters was responsible for inapropriate blood flow separation.

The aim of the work developed in this thesis is to provide better and more flexible solutions to the analog system used in the SUCoDiC project. Consequently, by using digital quadrature techniques which process the RF signal (or a downconversion of it) the referred problems (frequently found in analog systems) are easier to avoid.

It is known [68] that it can be difficult to create two circuits chains in which the produced I and Q components have matched gains, phases and frequency responses. As stated in [67], digital approaches for obtaining quadrature demodulation on digitized signals eliminate problems associated with matching of analog components. So, to overcome the problems generated by signal processing circuits chains which introduce I and Q amplitude and phase mismatch, some digital I/Q demodulation techniques have been developed over the years [63]-[72].

1.2 Proposed goals

The main goal of this thesis is to select one or more digital I/Q demodulation techniques to be applied (in the frame of the SUCoDiC project) to blood flow signals. The following tasks were envisaged:

- the identification of the hardware sections in an analog I/Q demodulation system that could be implemented in software;
- the implementation and testing of some digital I/Q demodulation techniques;
- the comparison between the obtained I and Q components, for each technique, based on the blood flow separation;
- the acquisition of experimental signals using BPS theory and heterodyning technique, and compare the performance with the one produced by the studied techniques;
- and finally, if possible, the real-time implementation of the selected approaches.

1.3 Thesis outline

This chapter describes the motivation of the work based on main background readings and the proposed goals.

In Chapter 2 general concepts on Doppler ultrasound systems are made, presenting some description on the Doppler frequency shift, the usage of ultrasound in the detection and quantification of vascular disease and simple Doppler Continuous Wave (CW) and Pulsed Wave (PW) systems. Since the demodulator is responsible for extracting the Doppler spectrum from all the signals received from the transducer, it will be further explored in Chapter 3, by presenting digital quadrature approaches capable of replacing the usually employed analog quadrature demodulators, avoiding consequently tipical problems verified on analog quadrature demodulators.

Section 3.1, from Chapter 3 reports the fundamental aspects associated to the heterodyne function used to downconvert the RF signal to an Intermediate Frequency (IF) signal. It is also characterized in this section a PLL system which will be the central block to create a frequency synthesizer (see Chapter 4). With the synthesized frequency, this mixture with the RF signal will provide the downconvertion of such signal, for further acquisition, digitalization and digital signal processing by the studied digital quadrature approaches.

In section 3.2, from Chapter 3, another strategy for acquiring the RF signal is presented. The theory behind it is called Bandpass Sampling (BPS), and this section presents some theory related to BPS, contextualizing its principles.

Having the acquired signal, after using one of the techniques presented in section 3.1 or presented in section 3.2, in section 3.3 the description of the studied digital quadrature techniques is made. A total of five approaches are described on section 3.3.3.

The experimental setup developed is mentioned in Chapter 4, where the software applications and hardware circuits developed in this thesis are described. In this Chapter, a flow pump controller (circuitry and associated applications) is presented. Also shown are the circuits associated with the heterodyning technique (frequency synthesizer, the mixer, and filters). The circuitry used for BPS techniques is also presented. There was also the need to create an application responsible for controlling the used NI DAQ USB 6251 , for acquiring signals to be processed.

Important considerations associated with the parametrization of the digital quadrature techniques are made in section 4.3. In this Chapter, results related to the setup of the external components of the PLL-based frequency synthesizer are shown. It is presented and characterized the testing signal which, after being processed by the studied digital quadrature techniques, will produce the results shown in section 5.1. The spectrum characterization of the experimental signals to be acquired, and then after being processed by such techniques is also presented, results being presented in sections 5.2 and 5.3.

The sampling frequency to be used in BPS is determinated in section 4.3. Since the evaluation of the efficiency of each digital quadrature technique is made through the observation of the directional components separation, the strategy used for such separation is indicated. Consideration about the types of filters used, *Matlab* routines used for filter design and other related aspects are presented.

Chapter 5 presents both testing signal results (section 5.1) and experimental signals results (sections 5.2 and 5.3). On section 5.2 are presented experimental signals results from to the processing

of the acquired signal using the BPS technique and on section 5.3 are presented experimental signals results after the RF signal downconversion by heterodyning. Also, at the end of each of the sections 5.1, 5.2 and 5.3 comments are made on the presented results.

In Chapter 6 general considerations are presented and concluding remarks are presented in order to stand out the selected digital quadrature approaches, proposed for real-time implementation. Finally, future research lines are established.

Complementary information required during the development of this thesis to achieve the proposed goals is shown in the various appendixes.

Chapter 2

General Concepts on Doppler Ultrasound Systems

2.1 Introduction

Ultrasonic waves are sound waves which present frequencies above the audible range. Sound is a mechanical energy transmitted by pressure waves through a medium [2]. Sound waves travel through any material medium with a speed that depends on the compressibility, density and temperature of that medium. During the sound traveling through air, elements of the air vibrate producing changes in density and pressure along the direction of the motion of the wave [3]. The propagation of sound from one position to another is made by alternations of compressions, continuously compressing the region just in front of itself, and rarefactions which are low pressure regions, following the compressions [2] [3].

2.2 Doppler Shift

The Doppler effect is the change in the observed frequency of a wave due to the relative motion of the source and the observer [1]. Lets consider a stationary observer (where stationary means at rest with respect to the medium). The observer is receiving an ultrasonic wave from an ultrasonic source. If we consider that the source is also stationary and sending a wave with frequency f, the observer will receive an ultrasonic wave with the same frequency f [1] [3]. Assuming now that the observer remains stationary but the source moves towards the observer, with a velocity $\vec{v}$, continuously sending a wave with frequency f, the observer will "see" the wavefronts of the emitted wave more quickly then when the source was stationary. This way the observer will detect a higher frequency wave than that emitted by the source. However, if the source is moving away from the observer, with a velocity $\vec{v}$, continuously sending a wave with frequency f the observer will "see" the wavefronts of the emitted wave less often and consequently the observer will detect a lower frequency wave than that emitted by the source. The resulting change in the observed frequency is known as the Doppler

shift. The magnitude of the Doppler shift frequency if proportional to the relative velocities of the source and the observer. The magnitude of the Doppler shift frequency is also affected by the angle between the direction of the propagation of the wave and the direction of the velocity between the source and the observer[1] [3].

Combining the motion of the source toward and away from the observer, taking into consideration the angle between the direction of propagation of the wave and the observer, the resultant observed Doppler shift frequency [28] (difference between the transmitted and the received wave) is given by

$$f_D = 2f\cos(\theta)\frac{v}{c} \tag{2.1}$$

where f is the transmitted frequency, θ is the angle between the direction of the propagation of the wave and the direction of the velocity between the source and the observer, v is the magnitude of velocity of the source (in m/s), and c is the magnitude of the speed of the ultrasonic wave in the medium (in m/s). In equation (2.1) it is assumed that $c >> v$. The factor of 2 shown in the equation indicates that the Doppler shift has occurred on both directions (emission and reception) [1], as explained next.

2.3 Ultrasound backscattered from blood

Blood is composed of platelets, erythrocytes (red blood cells, with biconcave disc shape and a diameter of $7\mu m$ [1].) and the leukocytes (white blood cells) suspended in a liquid called plasma. In the plasma there are a large number of proteins, metabolic wastes, nutrients, and other molecules being transported. Erythrocytes account for more than 99 percent of blood cells. The constant motion of the blood, in the cardiovascular system, keeps the cells well dispersed [34].

In medical ultrasonic applications applied to the detection and quantification of vascular disease, an ultrasonic beam is mainly backscattered from moving blood cells [28].

Recent studies [76] mention that backscattering properties of blood are dependent on factors such as hematocrit (proportion of blood volume that is occupied by red blood cells [34]), plasma protein concentrations, the nature of blood flow and shear rate (rate of change of velocity at which one layer of fluid passes over an adjacent layer [35]).

Scattering happens when an ultrasonic wave travels through a medium and strikes a discontinuity (which can be changes in density and/or compressibility) similar or less than a wavelength, resulting on some energy of the wave being scattered in many directions.

The increase of scatterer size greatly increases the ultrasonic scattering. Studies based on the evaluation of ultrasonic backscattering of blood showed that the backscattering tends to increase with factors that favor the formation of red cell aggregation [76].

Also, as stated in [78], red cells may form a larger structure called rouleau, as the result of the aggregation of several individual red cells, if some conditions are encountered. These conditions are

mainly related with the shear rate and the hematocrit. The higher the shear rate the less red cells aggregation will be found (such as in normal flow conditions), and higher hematocrit tends for favor the formation of such aggregation.

Measurements of the backscattering coeficient from red cell suspensions under steady laminar and turbulent flow suggested that the backscatter is higher with the increase of turbulent intensity. Consequently, based on theoretical models, scattering from a dense distribution of small scatterers is affected by the variance of the scatterer concentration or its fluctuation [76].

Doppler ultrasound has had an important role in the noninvasive evaluation of arterial occlusive diseases. Today, CW techniques allow the detection of stenoses ranging from 50 percent occlusion (moderate stenoses) to 100 percent occlusion (severe occlusion) [77]. To this autors, the detection of minor stenoses can be made evaluating with detail the spectral content of the Doppler signals from blood flow disturbances created by such (minor) stenoses.

Based on what has been stated and from experimental work, the backscatter from blood (although mainly because of the red cells quantity) is also affected by the presence of the arteries and veins (because the tissue boundary causes different acoustic impedance between the outside and the inside of the walls). Also, [79] ultrassound is backscattered by microembolus (embolus small enough so as not to block flow in major arteries in a given organ, but large enough to obstruct flow in the terminal branches of arteries and/or the microcirculation). As a consequence, Doppler ultrasound can be used in the detection of microembolus. In [79] the theory presented summarizes pulse Doppler detection of ultrasound backscattering from emboli in blood, based on the ratio of the acoustic power backscattered from the embolus to that of the moving blood surrounding the embolus. Also, [79] presents strategies for discriminating between gas and formed-element emboli, determining detection limits, and estimating the size of formed-element emboli in blood.

In vascular ultrasound the Doppler effect occurs on both directions (emission and reception). First the transducer is a stationary source while the blood cells are moving receivers of the ultrasound waves. The ultrasound is backscattered from the blood cells, that now acts like a moving ultrasound source, being the transducer a stationary observer. As characterized in (2.1) the Doppler shift depends on the frequency of the ultrasound wave created by the transducer, the velocity of the blood cells which will backscatter the ultrasound and on the angle between the ultrasound beam and the direction of the blood [1].

The speed of ultrasound in blood is reported to be in the range 1540 m/s to 1600 m/s. In the frequency range of 1 MHz - 20 MHz the speed of ultrasound is independent of the frequency, meaning that dispersion effects need not be taken into account [28]. Also the effect of small temperature changes can also be ignored. Usually the value of the speed of sound in blood is considered to be 1570 m/s or 1580 m/s [28]. For some other materials, such as soft tissue (average), Table 3.1 of [28] presents the speed values of ultrasound.

The relationship between a wave wavelength, frequency and velocity of propagation in a given medium is

$$\lambda f = v \tag{2.2}$$

where λ is the wave wavelength, f its frequency and v the velocity magnitude of propagation in that medium [3]. Considering a velocity value of ultrasound propagation in blood of 1570 m/s and an ultrasound wave of frequency 8 MHz, the wavelength has a value close to $196\mu m$.

Since scattering happens when an ultrasonic wave travels through a medium and strikes a discontinuity similar or less than a wavelength, this means that groups of red cells act as scatterers of ultrasound [1].

2.4 Basic Doppler Systems

An ultrasonic transducer, when excited with a voltage signal during transmission, converts it into a mechanical wave. During the reception, the acoustic energy of the received ultrasound wave is converted to an electric signal. This energy transformation is possible through the use of an active element that depends on the piezoelectric effect for their operation [28]. The ultrasound signal that returns to the transducer causes the piezoelectric element to vibrate, and an electrical signal is generated. This electrical pulse is called a radiofrequency (RF) signal [2].

The detailed electronic circuits of Continuous Wave (CW) or Pulsed Wave (PW) systems used to measure blood flow will not be described in this thesis. Such information has already been published, for example in [28], [42] - [44]. What is important is to understand the general diagram of such systems.

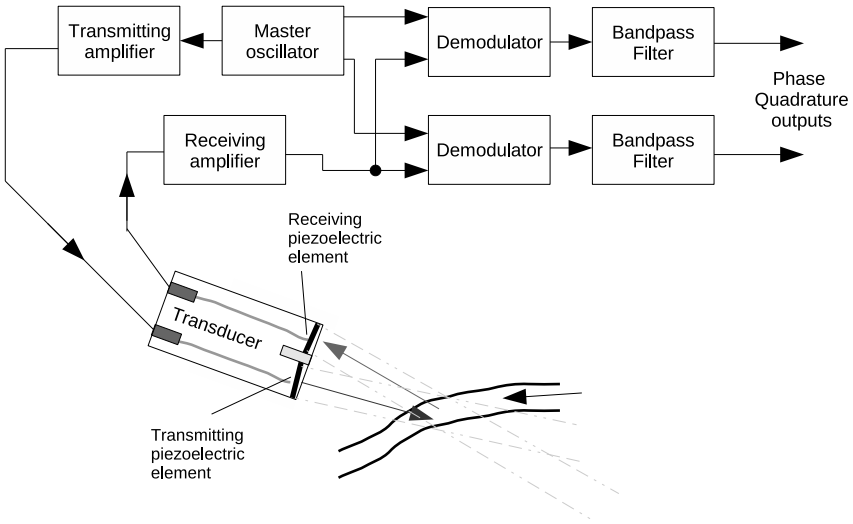

Figure 2.1: Block diagram of a continuous wave Doppler system (Adapted from figure 6.1 in [28] and from figure 1 in [45]

Figure 2.1 presents the block diagram of a CW Doppler system. The master oscillator, operating with a constant frequency, is an essential component of the Doppler system providing both a

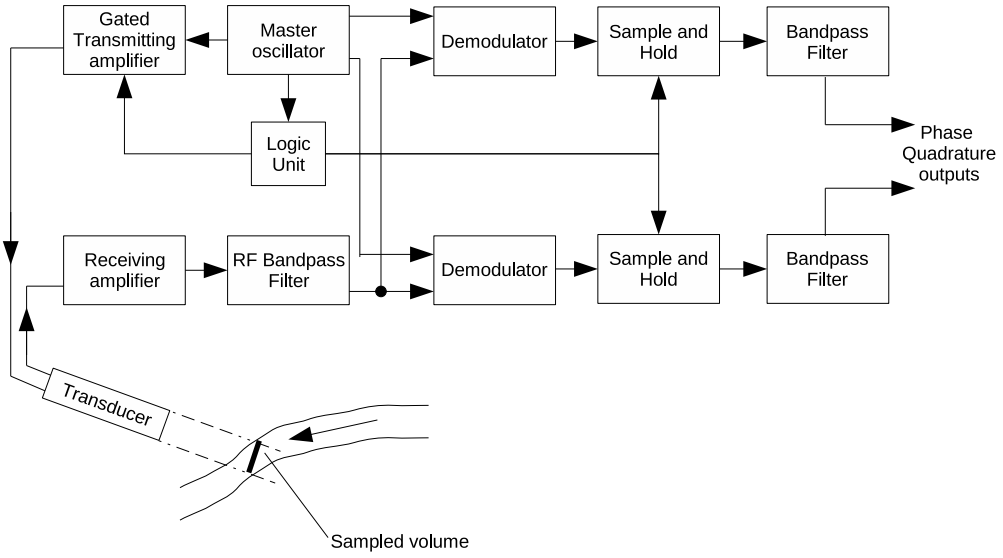

Figure 2.2: Block diagram of a pulsed wave Doppler system (Adapted from figure 6.11 in [28])

reference frequency for the circuit operation and the reference signals used by the demodulator. The master oscillator's signal, after being amplified by the transmitting amplifier, excites the transmitting piezoelectric material of the probe. The transmitter excites the piezoelectric material with a square wave rather than a sine wave. The higher harmonics are filtered by the narrow bandwidth of the piezoelectric crystal. As a consequence of the crystal excitation by the electric signal, an ultrasound wave is emitted [28].

The returning ultrasound signal, carrying echoes as a consequence of the moving objects backscatter, hits the receiving piezoelectric element of the probe. The produced electric signal is fed to the RF receiving amplifier. The receiving amplifier has to amplify the small voltages generated by the receiving piezoelectric crystal. The amplified signal is demodulated and filtered to produce audio frequency signals, usually in phase quadrature, whose spectral content (frequencies and amplitudes) make possible to retrieve information about motion in the blood vesels [28].

Figure 2.2 shows the block diagram of a PW Doppler system. A PW Doppler system is usually used to gather information at a specific range from the face of the transducer. The main difference of the PW Doppler system to the CW Doppler system is that the transducer is excited by bursts of pulses instead of being continuously excited. As with CW Doppler system, the ultrasound wave travels into the body were the moving particles and structures will produce Doppler shifts to its frequency. However, against what happens with a CW Doppler system, here the returning ultrasound signal, is received by the same transducer and by the same piezoelectric crystal. The process repeats itself with the next burst. Like in CW Doppler system, the receiving amplifier has to amplify the small voltages generated by the piezoelectric crystal. The amplified signal is demodulated and filtered to produce audio frequency signals [28].

In terms of the received information, the demodulated signal (received after each burst) contains the Doppler shifts associated to a given sampled volume obtained at a specific range from the face

of the transducer [28].

The output of the demodulator is sampled at a specific time, in order to capture the information at the depth of interest. This amount of time corresponds to the time taken by the sound to travel from the transducer to the defined distance from the face of the transducer and back again. The sample and hold amplifier is updated after every transmission burst [28].

2.4.1 The Demodulator

The demodulator is used to extract the Doppler spectrum from all the signals received by the transducer. The backscattered ultrasound echoes contain the components of the Doppler shift centered at the carrier's frequency. The shift of components from the carrier frequency have a frequency proportional to the scattering blood cells velocity value. Depending on the direction of the movement of the blood flow, with respect to the transducer, the backscattered components will be above or below the carrier frequency. Both demodulators must be identical in order to obtain an exact output of the two channels so that correct flow separation can be properly made [43].

In order to obtain directional information of the blood flow, three analog solutions can be applied: single sideband detection, heterodyne detection and quadrature phase detection.

Single Sideband Detection (SSB)

The basic principle behind SSB is to apply a Lowpass Filter (LPF) and a Highpass Filter (HPF) directly to the RF signal. The LPF will remove the upper sideband and the HPF will remove the lower sideband of the RF signal. The output of each filter is then coherently demodulated in order to get the signal's components associated to the forward flow and the reverse flow. The information of the forward flow results from the coherent demodulation of the output of the HPF and the reverse flow is obtained from the coherent demodulation of the output of the LPF. The problem with this technique is that these lowpass and highpass filters need to have a very high Q-factor, in order to get proper information separation [28]. Figure 2.3 shows the block diagram of SSB technique.

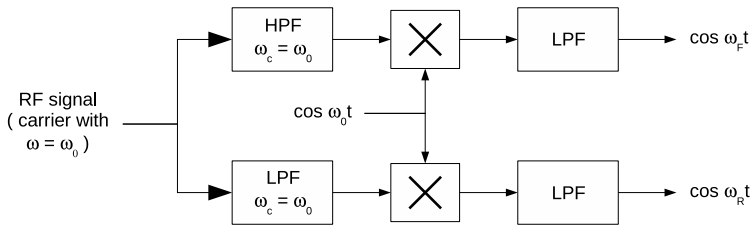

Figure 2.3: Block diagram of a SSB demodulator (Adapted from figure 6.6 in [28]), where ω_c stands for the filter cutoff frequency, ω_0 stands for the carrier frequency of the RF signal, and ω_F and ω_R are, respectively, the frequencies associated with the forward and reverse flow

Heterodyne Demodulation

The principle used in this technique is to coherently demodulate the ultrasound echo signal with an oscillator whose frequency is lower than the frequency used in the ultrasound carrier (produced by the master oscillator). Although the heterodyne frequency is lower than the carrier frequency, it must be higher than the highest Doppler frequency shift received as a consequence of the ultrasound backscatter. After mixing the carrier wave with the heterodyne oscillator's wave, the resulting signal passes through a LPF and is mixed with the backscattered ultrasound echo signal [28]. Figure 2.4 shows the block diagram of heterodyne demodulation technique.

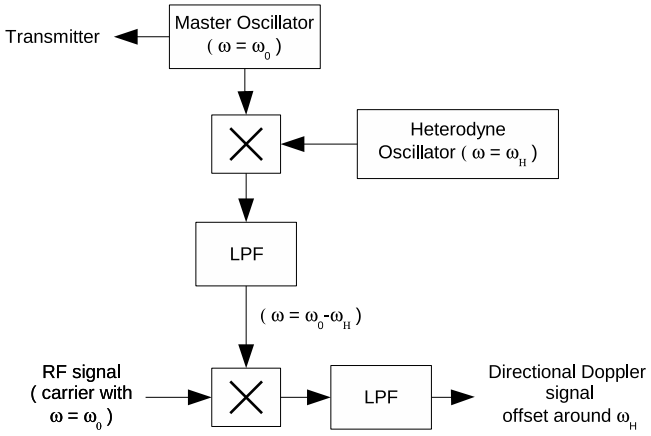

Figure 2.4: Block diagram of a heterodyne demodulator (Adapted from figure 6.7 in [28]), where ω_H stands for the heterodyne frequency and ω_0 stands for the carrier frequency of the RF signal.

Quadrature Phase Detection

In this technique the returned backscattered ultrasound echo is coherently demodulated by the signal generated by the master oscillator and by a signal equal to the one of the master oscillator but shifted $\frac{\pi}{2}$ radians (i.e., in quadrature). This way, the imaginary and real components of the Doppler signal are preserved [28].

Figure 2.5 shows the block diagram of quadrature phase detection technique.

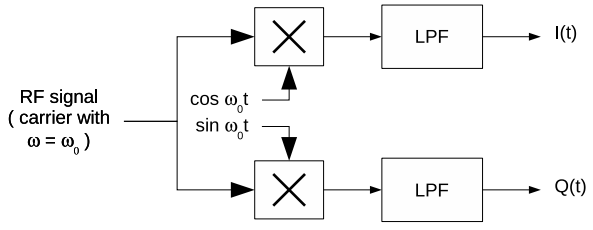

Figure 2.5: Block diagram of a quadrature phase detection demodulator(figure 6.8 in [28]), where ω_0 stands for the carrier frequency of the RF signal

Chapter 3

Doppler Ultrasound System's Demodulators

3.1 Heterodyning Function

3.1.1 Introduction

In section 2.4.1 it was presented in a superficial way, some of the demodulators employed to extract the Doppler spectrum from all the signals received by the transducer.

Since this thesis focus in applying digital quadrature techniques to obtain the I and Q components of a signal, for being processed it must be sampled and digitized. Consequently, if one wants to digitally obtain the I and Q components of the signal, it must be captured before entering the analog demodulator.

Observing figures 2.1 and 2.2 the signal to be sampled and digitized is the one that exits the *Receiving amplifier* in the case of the CW Doppler system (figure 2.1) and the signal in the output of the *RF bandpass filter* in the PW Doppler system (figure 2.2).

However, in some applications the ADC device can impose a limit in the maximum frequency component that a signal can have. If one considers the Nyquist theorem, a sampled bandlimited continuous signal is uniquely determined by its samples if $f_s \geq 2f_U$, where f_U is the maximum frequency value of the signal [8]. As will be explained later (see subsection 4.2.3) in the work developed the ADC imposes such limitation.

One strategy to overcome the ADC sampling rate limitation is to translate the signal centered at a given frequency to a lower frequency, and then one can obtain the desired continuous time signal, whose frequency components allow a sampling without causing aliasing.

Such strategy is implemented in what is called superheterodyne receiver [12]. As a part of such receiver we encounter a RF section, a mixer, a local oscillator and an Intermediate Frequency (IF) section.

The mixer and the local oscillator constitute the heterodyne technique, were a RF signal is

converted into an IF signal of known frequency, usually of lower frequency than the input signal's carrier frequency, without modifying the relation of the sidebands of the input signal [12].

Adding the block diagram responsible for the heterodyne technique in figures 2.1 and 2.2, and also indicating the presence of the ADC responsible for the sampling and digitalization of the signal, both figures will be altered. Doing this adaptations, the block diagrams of the CW and PW Doppler systems will be as shown in figures 3.1 and 3.2, respectively.

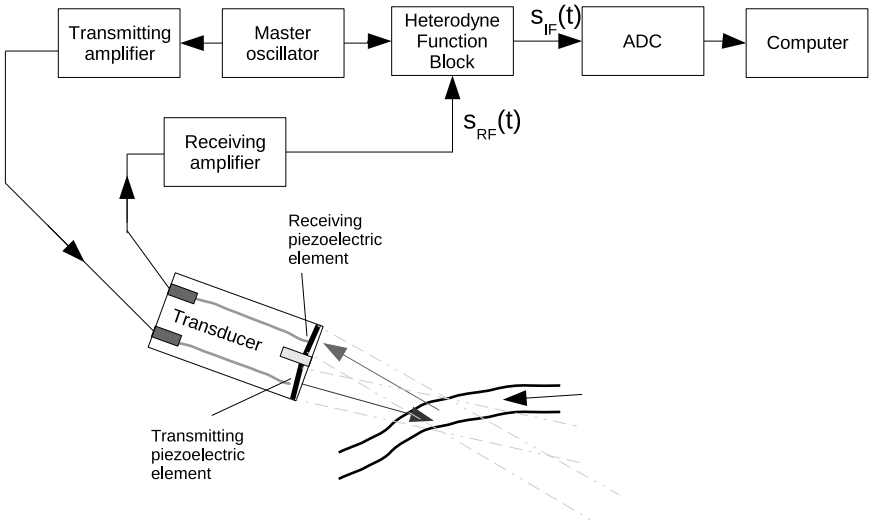

Figure 3.1: Block diagram of a continuous wave Doppler system, where the RF signal containing the Doppler frequency shift information is downconverted to an IF signal and sampled

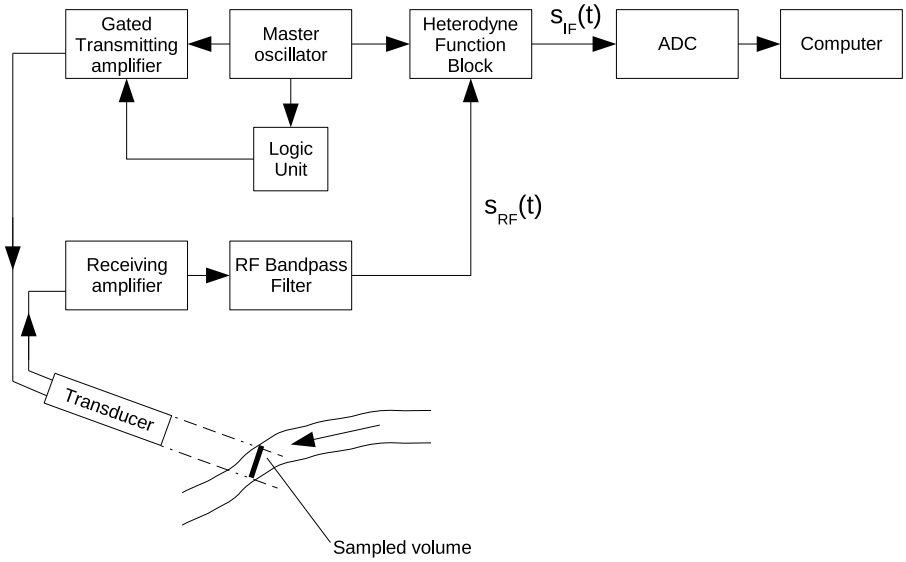

Figure 3.2: Block diagram of a pulsed wave Doppler system, where the RF signal containing the Doppler frequency shift information is downconverted to an IF signal and sampled

The application of the heterodyning can produce an IF carrier defined by

$$f_{IF} = f_0 - f_{LO} \tag{3.1}$$

where f_{IF} is the IF frequency to which the RF signal is translated to, f_0 is the RF signal's carrier frequency and f_{LO} is the frequency generated by the local oscillator.

As a consequence of the mixing process, a replica of the RF signal is translated to the desired IF frequency, and another image signal is translated to a frequency equal to $f_0 + f_{LO}$.

In order to obtain the desired IF signal, the mixer's output signal is filtered, so that only the desired frequencies centered at the IF frequency will be used in the following stages of signal processing.

One way to implement the heterodyne technique is according to the following block diagram where the local oscillator is a Phase Locked Loop (PLL) based system organized as a frequency synthesizer.

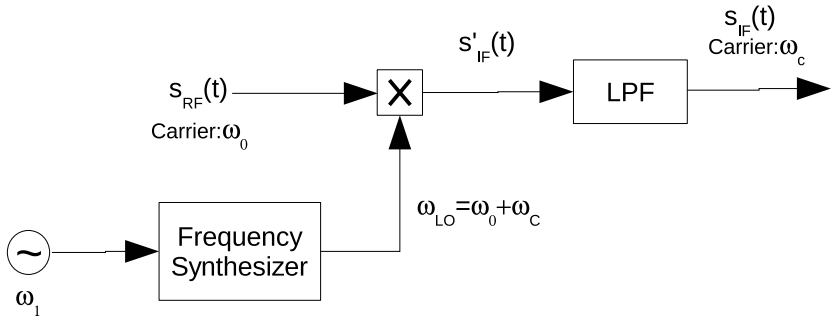

Figure 3.3: Block diagram of the heterodyne technique used to obtain the IF signal. The local oscillator is a frequency synthesizer block, implemented using a PLL, where ω_0 stands for the master oscillator frequency (which is also the carrier frequency of the ultrasound wave) and ω_{LO} stands for the local oscillator frequency. The frequency $\omega_c = 2\pi f_{IF}$ is the value of the carrier frequency that the IF signal will have

With this strategy a RF signal whose spectrum is centered at a frequency ω_0 (figure 3.4 (A)) can be translated to a lower or higher frequency (figure 3.4 (B)). The undesired frequencies of the translated spectrum are removed with a filter (figure 3.4 (C)).

The essential blocks that need attention are the frequency synthesizer and the LPF used. In the case of the frequency synthesizer we are dealing with a feedback system where the relative stability, settling time and other requirements must be fulfilled. In the next section this theoretical requirements will be addressed.

In the case of the LPF, its details will be specified later in the Heterodyne Technique subsection (page 43). However, care must be taken when choosing the type of filter do use since it is important to keep the distortion of the signal's frequency components of interest to a minimum.

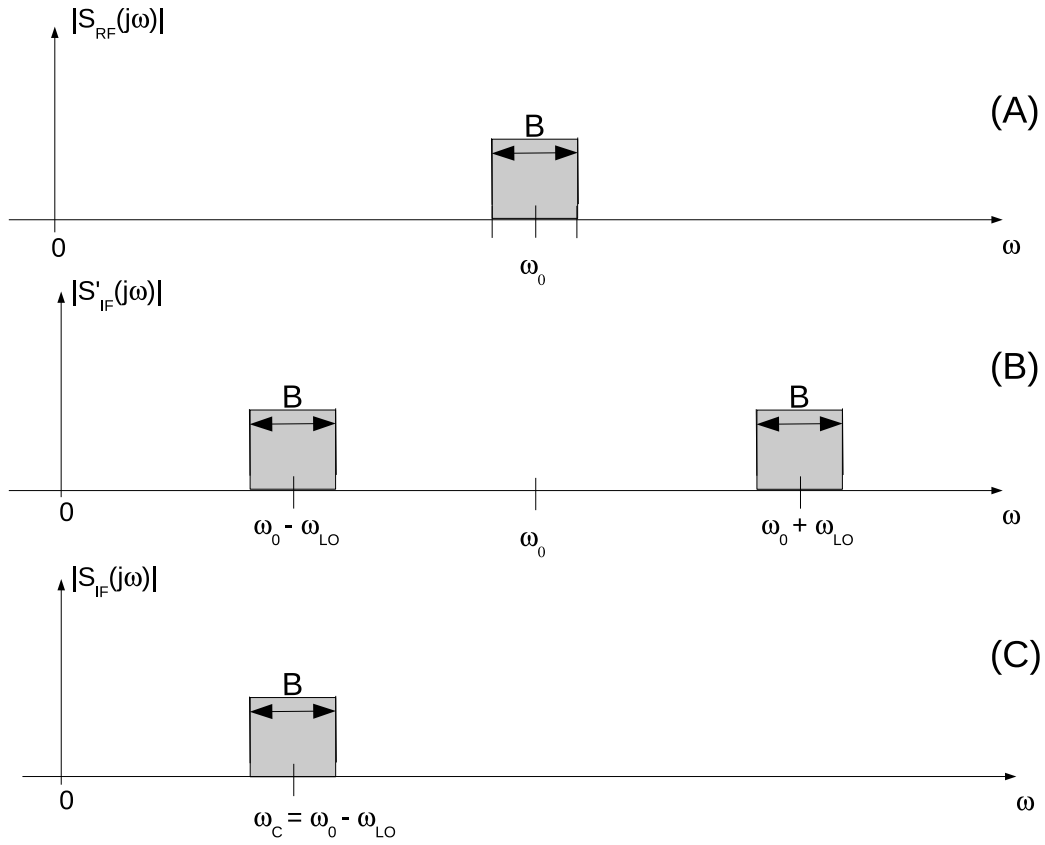

Figure 3.4: Spectral representation of the signals indicated in figure 3.3, where ω_0, ω_{LO} and ω_c have the same meaning as the ones presented in figure 3.3

3.1.2 Phase Locked Loop

Lets consider the mathematical model for a PLL in the locked state (figure 3.5). The Phase Detector (PD) can be further expanded as shown in figure 3.6.

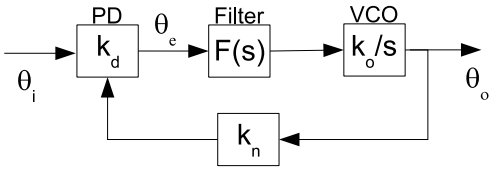

Figure 3.5: Mathematical model of a PLL in the locked state [17], where k_d stands for the phase comparator conversion gain, k_o stands for the Voltage Controlled Oscillator (VCO) conversion gain, $F(s)$ is the loop filter transfer function, $k_n = \frac{1}{N}$ with N being the value by which the VCO output frequency is divided, θ_o and θ_i are, respectively, the phase of the input (reference) signal of the PLL and the phase of the output signal (generated by the VCO) and θ_e if the phase error

Given the feedforward transfer function $G_1(s) = k_d \cdot F(s) \cdot \frac{k_o}{s}$, where k_d stands for the phase comparator conversion gain, k_o stands for the Voltage Controlled Oscillator (VCO) conversion gain, and $F(s)$ is the loop filter transfer function, and the feedback transfer function $G_2(s) = k_n$, where $k_n = \frac{1}{N}$ is the feedback loop divider ratio, with N being the value by which the VCO output frequency is divided, it can be demonstrated that the transfer function of a feedback system like this is given by [24]

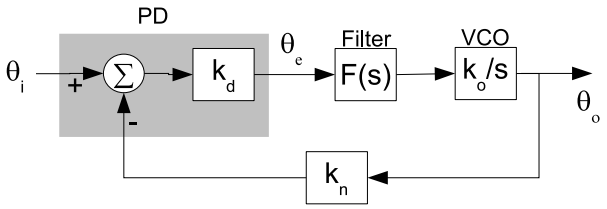

Figure 3.6: PLL locked state mathematical model with the PD block expanded [22], where k_d stands for the phase comparator conversion gain, k_o stands for the Voltage Controlled Oscillator (VCO) conversion gain, $F(s)$ is the loop filter transfer function, $k_n = \frac{1}{N}$ is the feedback loop divider ratio, with N being the value by which the VCO output frequency is divided, θ_o and θ_i are, respectively, the phase of the input (reference) signal of the PLL and the phase of the output signal (generated by the VCO) and θ_e if the phase error

$$\frac{\Theta_o(s)}{\Theta_i(s)} = \frac{G_1(s)}{1 + G_1(s) \cdot G_2(s)} \tag{3.2}$$

where $\Theta_o(s)$ and $\Theta_i(s)$ are, respectively, the phase of the input (reference) signal of the PLL and the phase of the output signal (generated by the Voltage Controlled Oscillator (VCO)).

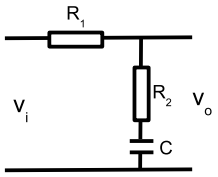

Figure 3.7: Typical passive filter used in a PLL [17], where v_i stands for the input signal and v_o stands for the output signal of the filter

Knowing that the transfer function of the passive filter shown in figure 3.7 is given by

$$\frac{V_o(s)}{V_i(s)} = F(s) = \frac{1 + s\tau_2}{1 + s(\tau_1 + \tau_2)} \tag{3.3}$$

where $V_o(s)$ is the filter's output signal, $V_i(s)$ is the filter's input signal, $\tau_1 = R_1 \cdot C$ and $\tau_2 = R_2 \cdot C$ [17]; R_1, R_2 and C represent the values of the resistors and capacitor of the filter of figure 3.7.

The transfer function of the system in figure 3.6 is given by

$$\frac{\Theta_o(s)}{\Theta_i(s)} = \frac{k_d \cdot k_o \cdot F(s)}{s + k_d \cdot k_o \cdot k_n \cdot F(s)} \tag{3.4}$$

$$= \frac{\frac{\omega_n^2}{k_n} \cdot (1 + s\tau_2)}{s^2 + 2 \cdot \xi\omega_n s + \omega_n^2} \tag{3.5}$$

where ξ is the damping ratio and ω_n is the undamped natural frequency which, for the considered filter, are defined by

$$\xi = \frac{\omega_n}{2}\left(\tau_2 + \frac{1}{k_n \cdot k_o \cdot k_n}\right) \tag{3.6}$$

$$\omega_n = \sqrt{\frac{k_o \cdot k_n \cdot k_d}{\tau_1 + \tau_2}} \tag{3.7}$$

It can be considered the error-transfer function [25] defined by $H_e(s) = \dfrac{\Theta_e(s)}{\Theta_i(s)}$, where $\Theta_e(s)$ stands for the phase error, and it can be demonstrated that for the system in figure 3.6, $H_e(s)$ assumes the expression

$$H_e(s) = 1 - k_n \cdot \frac{\Theta_o(s)}{\Theta_i(s)} \tag{3.8}$$

The stability of a system, such as the one in focus in this section (figure 3.6) can be studied by drawing its root locus [24] [25].

The phase margin and the gain margin of the system can be obtained by the Bode plot of the feedforward transfer function [18] [26]. For the system in figure 3.6, the feedforward transfer function is given by

$$\begin{aligned} G(s) &= G_1(s) \cdot G_2(s) \\ &= \frac{k_o \cdot k_d \cdot k_n \cdot F(s)}{s} \end{aligned} \tag{3.9}$$

The phase margin is defined by $PM = \pi - \Phi(\omega_{GC})$, where $\Phi(\omega_{GC})$ is the phase of $G(s)$ at the gain crossover frequency (frequency where $G(s)$ has a gain of 0 dB).

The gain margin is defined by $GM = \dfrac{1}{A(\omega_{PC})}$, where $A(\omega_{PC})$ is the gain of $G(s)$ at the phase crossover frequency (frequency where $G(s)$ has a phase of $-\pi$ rad) [26].

In practical terms the phase margin is the amount of phase shift at the frequency ω_{GC} that the system can sustain before making the system marginally stable [25]. The gain margin is the variation of the magnitude that the system can support before making the system marginally stable [26].

The desired range of phase margins are between 30^o and 60^o [17], and the gain margin should be greater than 6 dB [24]. Other authors consider that the phase margin should be of at least 45^o , being 60^o preferable [19]. For second order systems the phase margin and the damping ratio are directly related [24], and this relation can be approximated to $\xi = \dfrac{PM}{100}$ for $0 \leq \xi \leq 0.6$. Consequently, if the phase margin is small (just a few degrees) the system will be heavily underdamped, and the transient response presents a larger settling time (for a given value of ω_n). If the phase margin is very large the system will tend to a critically dumped system ($\xi = 1$) with a lower settling time (for a given value of ω_n) with a transient response of the type $1 - e^{-\omega_n t}(1 + \omega_n t)$ $t \geq 0$ [24].

If a PLL is designed to be a second order system, a desired damped ratio is $\xi = \frac{1}{\sqrt{2}}$ [17], to originate an underdamped system in which the transfer function have the shape of a second order Butterworth LPF (optimally flat transfer function).

The choice of the PLL filter's bandwidth is a critical parameter [27], since its choice involves a trade-off between the spur levels and the lock time of the system. Spur levels are a consequence of the ripple in the input of the VCO, that modulates the VCO output, leading to spurious sidebands in the VCO spectrum, affecting its purity. A small bandwidth will avoid these spurious levels but will increase the system's lock time. On the opposite, a large bandwidth will produce a small lock time but larger spur levels. Because of this trade-off it is important to find a filter whose bandwidth gives a good equilibrium between the spur levels and the lock time.

In control theory the settling time (tipically called lock time in PLL related literature) can usually be defined with a 2% or 5% criterion [24],[25],[26]. Considering the 2% criterion, the settling time t_s is given by

$$t_s = \frac{4}{\xi\omega_n} \tag{3.10}$$

It can be demonstrated that for the type of filter used (see figure 3.7) the following relations [107]

$$\tau_1 + \tau_2 = \frac{k_o \cdot k_d \cdot k_n}{\omega_n^2} \tag{3.11}$$

$$\tau_2 = \frac{2\xi}{\omega_n} - \frac{1}{k_o \cdot k_d \cdot k_n} \tag{3.12}$$

$$\tau_1 = \frac{k_o \cdot k_d \cdot k_n}{\omega_n^2} - \tau_2 \tag{3.13}$$

where k_o is the VCO conversion gain, k_d is the phase comparator conversion gain and $k_n = \frac{1}{N}$ is the feedback loop divider ratio.

Also important is the system's steady state error, this is, the way the system behaves when time approaches infinity.

For a PLL system, the steady state error is evaluated considering that the system is initially in the locked stated, and that the input signal suffers a variation of phase.

Since it is being considered a passive LPF like the one presented in figure 3.7, the PLL will be a type I, second order system [18][24]. Using equations (3.3), (3.4) and (3.8), it is shown that

$$\begin{aligned} \frac{\Theta_e(s)}{\Theta_i(s)} &= \frac{s}{s + k_o \cdot k_d \cdot k_n \cdot F(s)} \\ &= \frac{s^2(\tau_1 + \tau_2) + s}{s^2(\tau_1 + \tau_2) + s\left(1 + k_o \cdot k_d \cdot k_n \cdot \tau_2\right) + k_o \cdot k_d \cdot k_n} \end{aligned}$$

Consequently, the phase error $\Theta_e(s)$ relates to the input signal's phase $\Theta_i(s)$ by the expression (3.14)

$$\Theta_e(s) = \frac{s^2(\tau_1+\tau_2)+s}{s^2(\tau_1+\tau_2)+s\left(1+k_o\cdot k_d\cdot k_n\cdot\tau_2\right)+k_o\cdot k_d\cdot k_n}\cdot\Theta_i(s) \tag{3.14}$$

Using the Laplace transform initial value theorem [24] [25] one can determine the phase error value in the time domain, from its Laplace expression

$$\lim_{s\to 0} s\cdot\Theta_e(s) = \lim_{t\to\infty}\theta_e(t) \tag{3.15}$$

If one considers a variation of the input signal's phase $\Theta_i(s)$, the steady state error will be evaluated by

$$\lim_{s\to 0} s\cdot\Theta_e(s) = \lim_{s\to 0}\frac{s\cdot\left[s^2(\tau_1+\tau_2)+s\right]}{s^2(\tau_1+\tau_2)+s\left(1+k_o\cdot k_d\cdot k_n\cdot\tau_2\right)+k_o\cdot k_d\cdot k_n}\cdot\Theta_i(s) \tag{3.16}$$

Assuming an initial locked state in the PLL, if the input signal's phase suffers a step variation $\Theta_i(s)=\dfrac{\Delta\Phi}{s}$ [17] from (3.16) emerges that

$$\begin{aligned}\lim_{s\to 0} s\cdot\Theta_e(s) &= \frac{s\cdot\left[s^2(\tau_1+\tau_2)+s\right]}{s^2(\tau_1+\tau_2)+s\left(1+k_o\cdot k_d\cdot k_n\cdot\tau_2\right)+k_o\cdot k_d\cdot k_n}\cdot\frac{\Delta\Phi}{s} \\ &= 0\end{aligned} \tag{3.17}$$

If the instant frequency of the input signal experiences a step variation which induces a ramp variation in its phase [17], the steady state error is given by

$$\begin{aligned}\lim_{s\to 0} s\cdot\Theta_e(s) &= \frac{s\cdot\left[s^2(\tau_1+\tau_2)+s\right]}{s^2(\tau_1+\tau_2)+s\left(1+k_o\cdot k_d\cdot k_n\cdot\tau_2\right)+k_o\cdot k_d\cdot k_n}\cdot\frac{\Delta\omega}{s^2} \\ &= \frac{\Delta\omega}{k_o\cdot k_d\cdot k_n}\end{aligned} \tag{3.18}$$

where $\Delta\omega$ stands for the magnitude of the frequency step.

Finally assuming that the instant frequency of the input signal experiences a ramp variation, which has the consequence that its phase will evolve in a quadratic way [17], the steady state error is given by

$$\lim_{s\to 0} s\cdot\Theta_e(s) = \frac{s\cdot[s^2(\tau_1+\tau_2)+s]}{s^2(\tau_1+\tau_2)+s\,(1+k_o\cdot k_d\cdot k_n\cdot\tau_2)+k_o\cdot k_d\cdot k_n}\cdot\frac{\dot{\Delta\omega}}{s^3} \qquad (3.19)$$
$$= \infty$$

where $\dot{\Delta\omega}$ stands for the rate of change of the reference frequency.

Based on the previous results a second order PLL, being a type I system, only presents null phase steady state error if the input signal's phase variation is in a step fashion [17], [18],[24],[25].

3.2 Bandpass Sampling

3.2.1 Introduction

Section 3.1 presented a strategy to acquire the RF signal when the ADC imposes a lower sampling rate than necessary. In that strategy an additional electronic block was placed between the block responsible for outputing the RF signal (that we desire do acquire) and the ADC.

According to [58] a superheterodyne receiver architecture, is usually used in receivers for wireless communications because of its better performance. In these receivers' systems, the sampling operation is performed on a baseband or on an IF signal. However, aiming at reduced size communication systems with multiple capabilities, the superheterodyne architecture presents the disadvantage of requiring many analog components. As a consequence digital receivers have become more attractive and hence more widespread, for example in cellular mobile phones. This way direct sampling is advantageous over a superheterodyne receiver, since the RF signal can be frequency shifted directly to baseband [58]. Also, the image suppression problem is eliminated [58].

When direct sampling of high frequency signals is aimed, the available ADC is frequently too expensive (because its difficult to fabricate high resolution high speed ADCs [55]) or there isn't an ADC capable of achieving such sampling frequencies. If such ADC exists there is also the need to consider if the following stage of software is capable of processing such amount of data with a reasonable time delay.

Using direct digitalization by applying Bandpass Sampling (BPS) there is a reduction of the amount of components associated with frequency downconversion. The BPS is known in literature by other designations such as IF sampling, harmonic sampling, sub-Nyquist sampling and undersampling [6]. With BPS intentional aliasing of the signal's bandwidth is used [55] [56], providing frequency-shifting [52] [54]. As further will be described, the choice of the sampling frequency depends on the signal's carrier frequency, the bandwidth of the signal, the IF of the aliased replica [55] and on the relationship between the sampling frequency and the signal's bandwidth [50].

Selecting a sampling frequency based on the bandwidth of the continuous time bandpass signal, the digital signal processing rate can be reduced [56].

The usage of BPS has been successfully applied in many applications such as GPS receiver [55], with multiple distinct RF signals [56], radio software receivers [58], biomedical signal processing [49], radar [50], sonar [50], and instrumentation [50].

If one now considers BPS as a strategy to acquire the RF signal, figures 2.1 and 2.2 can be adapted to express this situation. Such adaptation in presented in figures 3.8 and 3.9, respectively, for CW and PW Doppler systems.

By observing figures 3.8 and 3.9 it can be seen that the only the ADC is present between the block responsible for outputing the RF signal and the computer.

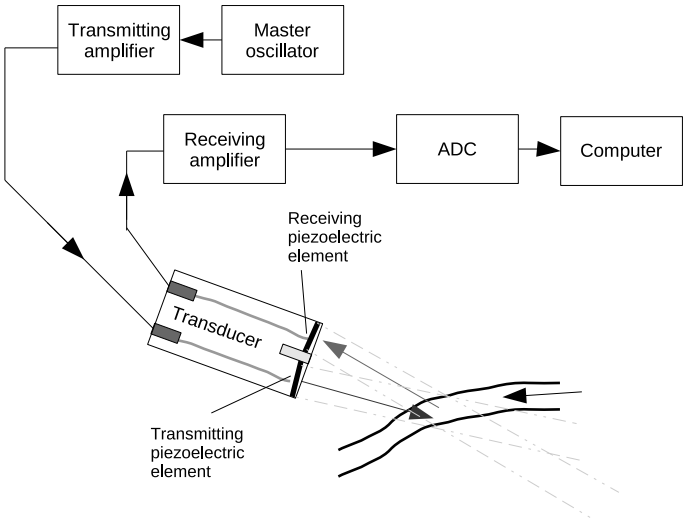

Figure 3.8: Block diagram of a continuous wave Doppler system, where the RF signal containing the Doppler frequency shift information is sampled by and ADC with a proper sampling rate

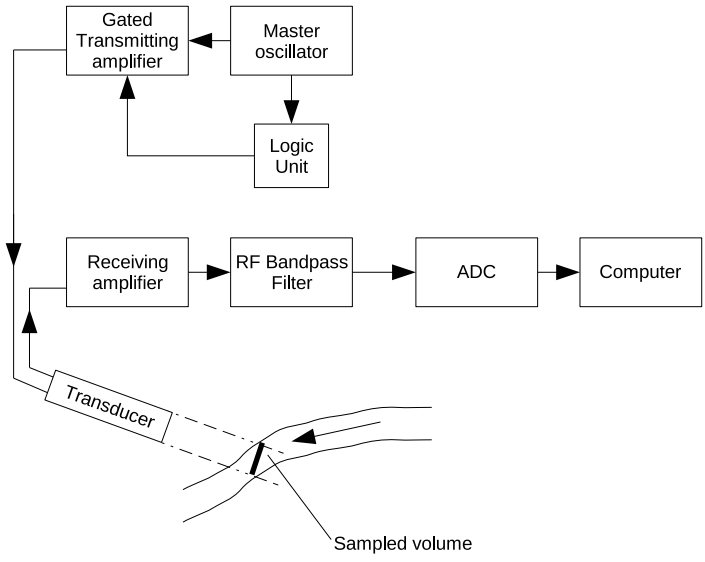

Figure 3.9: Block diagram of a pulsed wave Doppler system, where the RF signal containing the Doppler frequency shift information is sampled by and ADC with a proper sampling rate

3.2.2 BPS Frequency Selection

Lets consider a continuous bandpass signal centered at a frequency f_0, with total bandwidth B as presented in figure 3.10. The signal has a maximum frequency component with value f_U and it's lowest frequency component has the value f_L.

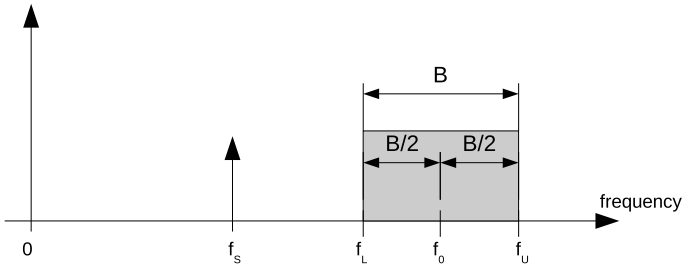

Figure 3.10: Spectrum of a bandpass continuous signal centered at a frequency f_0 and total bandwidth of B. The sampling frequency value is denoted by f_s. Only positive frequencies are presented (obtained from figure 1 in [50])

According to the classical bandpass theorem for uniform sampling [50] (Shannon's theorem [50][54]), a signal can be recovered if it is sampled at a minimum frequency value given by [50]

$$f_s^{min} = 2 \cdot \frac{f_U}{n} \tag{3.20}$$

where n is the largest integer within $\frac{f_U}{B}$. The theoretical relation for minimum sampling rate $f_s = 2 \cdot B$ can only be applied if we are sampling a signal with integer positioned band [50]. An *integer band positioning* occurs if $f_L = n \cdot (f_U - f_L)$ with $n = 0, +1, +2, \ldots$ and a *half-integer band positioning* occurs if $f_L = \frac{2n+1}{2} \cdot (f_U - f_L)$ with $n = 0, +1, +2, \ldots$.

However, the relation $f_s = 2 \cdot B$ is only applied to signals with no frequency components at the frequencies values f_U and f_L. The same approach is applied to the Nyquist sampling theorem, stating that a sampled bandlimited continuous signal is uniquely determined by its samples if $f_s \geq 2f_U$ [8]. In this case, $f_s \geq 2f_U$ is only true if there is no signal component at the frequency value f_U [50].

When applying minimum sampling frequencies values, any device imperfections will cause aliasing (this is why minimum sampling frequencies are said to be pathological [50]). To avoid this problem, sampling frequency's values should be above the minimum values. This is, a strategy considering guard-bands (see figure 3.11). However, arbitrarily increasing the sampling frequency can create unforeseen results, because there are bands of rates where aliasing will occur [50].

3.2.3 Uniform Sampling

When applying BPS with uniform sampling, only some rates are acceptable [50]. This rates are in the range given by

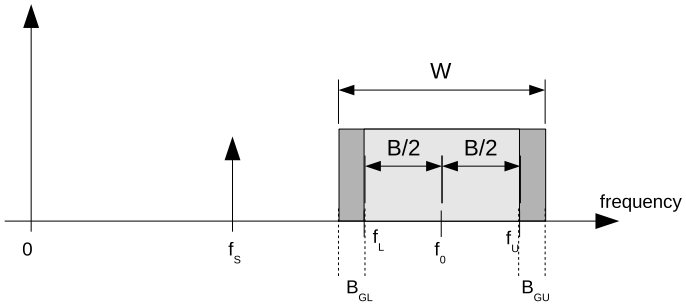

Figure 3.11: Spectrum of a bandpass continuous signal centered at a frequency f_0 and bandwidth of B. To prevent aliasing an upper guard-band (B_{GU}) and a lower guard-band (B_{GL}) are considered. The sampling frequency value is denoted by f_s. Only positive frequencies are presented (obtained from figure 5 in [50])

$$\frac{2f_U}{n} \leq f_s \leq \frac{2f_L}{n-1} \tag{3.21}$$

where n is an integer in the range

$$1 \leq n \leq I_g\left[\frac{f_U}{B}\right] \tag{3.22}$$

with $I_g\left[\frac{f_U}{B}\right]$ representing the largest integer within $\frac{f_U}{B}$.

The signal to be sampled must be known well enough in order to use (3.21), because a frequency component at $f = f_L$ or $f = f_U$ will be aliased.

Considering the relations (3.21) and (3.22), the allowed and disallowed uniform sampling frequencies can be determined. Figure 3.12 demonstrates such results. The allowed zones for uniform sampling without aliasing are presented in white and the shaded areas represent the uniform sampling rates that will result in aliasing.

If the sampling rate is increased above the minimum allowed rate, it can be thought as increasing the bandwidth of the signal with the inclusion of guard-bands (figure 3.11). The total bandwidth of the signal is considered $W = B + B_{GT}$, starting at the frequency $f_{Lg} = f_L - B_{GL}$ and ending at the frequency $f_{Ug} = f_U + B_{GU}$, were B_{GU} and B_{GL} are, respectively, the upper and lower guard-bands [50].

Now the allowed sampling frequencies are located in the range

$$\frac{2f_{Ug}}{n_g} \leq f_s \leq \frac{2f_{Lg}}{n_g - 1} \tag{3.23}$$

where n_g is an integer given by

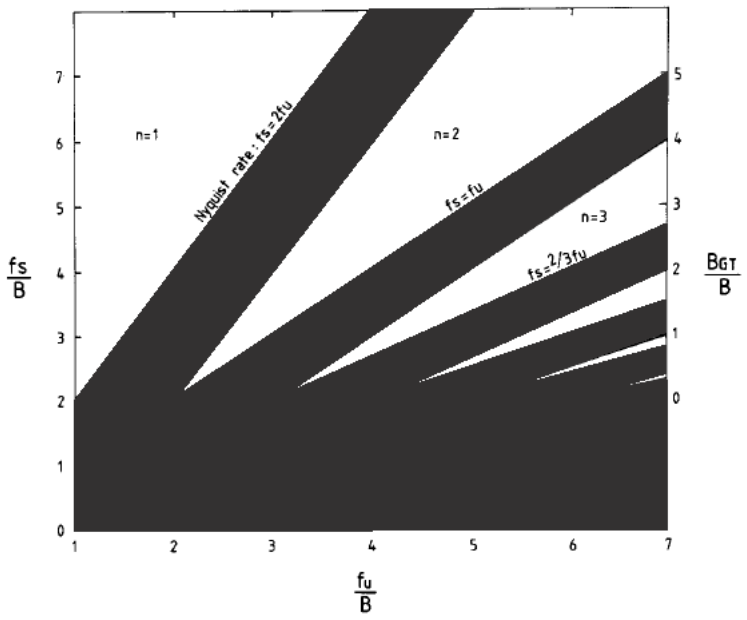

Figure 3.12: The allowed (white areas) and disallowed (shaded areas) for uniform sampling frequencies versus band position. $B_{GT} = f_s - 2B$ represents the total guard-band, f_s the sampling frequency and B is the bandwidth. (obtained from figure 4 in [50])

$$1 \leq n_g \leq I_g \left[\frac{f_{Ug}}{W} \right] \tag{3.24}$$

with $I_g \left[\frac{f_{Ug}}{W} \right]$ representing the largest integer within $\frac{f_{Ug}}{W}$.

Using the variability of equation (3.23) the allowed sampling frequencies can then vary [50] according to

$$\Delta f_s = \frac{2f_{Lg}}{n_g - 1} - \frac{2f_{Ug}}{n_g} \tag{3.25}$$

Other authors have used a different criteria for selecting the value of the sampling frequency. Tortoli [49] have used the relation expressed in equation (3.26) between the carrier frequency and the sampling frequency. The relation depends on an integer value k chosen to make the value of f_s nearest to twice the signal's bandwidth B. Apparently given the signal's bandwidth value, k can assume any value as long as f_s is the nearest to $2B$ as possible.

$$f_s = \frac{4f_0}{2k + 1} \tag{3.26}$$

Akos [57] have chosen the minimum sampling frequency based on the signal's information bandwidth presenting the relation

$$f_s > 2B_I \tag{3.27}$$

where B_I is the information bandwidth. However it seems [57] that any sampling frequency fulfilling the relation (3.27) is acceptable.

Akos [55] presents a way to predict the location of the IF shifted signal (which will have a carrier of frequency f_{IF}) subjected to BPS

$$if\ fix\left(\frac{f_0}{\frac{f_s}{2}}\right)\ is\ \begin{cases} even, & f_{IF} = rem(f_0, f_s) \\ odd, & f_{IF} = f_s - rem(f_0, f_s) \end{cases} \tag{3.28}$$

where $fix(n)$ is the truncated integer portion of the argument n, and $rem(\alpha, \beta)$ is the remainder after the division of α by β.

3.2.4 Spectral Inversion

Although the allowed values of sampling frequencies determined from (3.21), if no guard-band is assumed, or from (3.23) assuming a given guard-band, will avoid aliasing problems. Some will generate a baseband spectrum that is an inversion of the positive and negative shapes of the original continuous bandpass signal's spectrum [6]. In other words, the negative baseband will have the inverted shape of the half positive from the original spectrum. Based on the example presented in [6] and the relations (3.21) or (3.23), it is shown in appendix B that spectral inversion will happen if n is even.

If the spectrum of the signal in hand is symmetrical, spectral inversion will not cause any problems. However, if spectral inversion is unacceptable it should be avoided or corrected [54].

If the spectrum of the sampled signal is an inverted shape of the original spectrum and needs to be corrected, the spectrum of any digital signal can be inverted through the product of the signal's time samples by the sequence $(-1)^k$ with $k = 0, +1, +2, \ldots$, which is the same as multiplying the samples of the signal by a cosine with frequency equal to $\frac{f_s}{2}$ [6].

3.2.5 BPS Disadvantages

Although BPS presents, as already mentioned, some advantages there are also disadvantages such as problems with DC offsets, even order distortion and I/Q mismatch. [58]. Also, when frequency shifting a RF signal to a lower IF, the Signal-to-Noise Ratio (SNR) is not preserved [50] [58]. One solution is to use a bandpass filter (very high Q-factor), with high stopband attenuation, before applying BPS. Aperture jitter [58] must also be considered when applying BPS.

3.3 Digital Quadrature Techniques

3.3.1 Introduction

This section describes the fundamental theory of digital quadrature techniques and the different approaches applied in this thesis.

Frequently the continuous signal that needs to be processed is a bandpass signal. To be processed digitally it needs to be sampled. In order to have a digitally bandpass signal, sampling can be made to an IF signal (see section 3.1) or directly sampled using bandpass sampling methods (see section 3.2) but with careful selection of the sampling frequency (to avoid aliasing of the signal's frequency content). For the type of biomedical signals that are supposed to be processed with the following quadrature techniques, when applying BPS the signal must not be shifted to baseband, but instead to an IF frequency. This way it is possible to retrieve the I and Q components of such signal.

Once having the sampled bandpass signal, it can be represented by what is called its quadrature components [5]. It can also be demonstrated that any bandpass signal can be written by an equivalent lowpass signal, where (in general) this lowpass signal is a complex signal, whereas the bandpass signal is real [5].

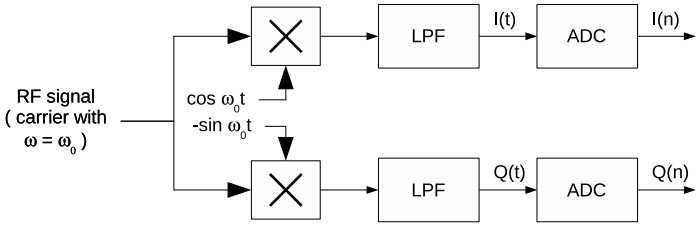

Figure 3.13: Typical complex sampling strategy using two analog channels and two ADC (Adapted from [63]), where ω_0 stands for the carrier frequency of the RF signal

In the classical approach, to obtain $I(n)$ and $Q(n)$, the input RF signal is mixed with two baseband analog mixers which yield the analog versions of the I and Q signal's components, $I(t)$ and $Q(t)$ respectively. The digitalization of the analog I and Q components was made by two ADC [64]. In this case two equal circuit chains, one to obtain and process the I component, and another to obtain and process the Q component, as well as two equal ADC devices was needed.

However, the gains, phases and frequency responses of the two circuit channels are often difficult to match. Also, a problem comes from error results on DC offsets introduced during the ADC operation on the analog I and Q components [67].

In fact, another team developing work related to the SUCoDiC project faced this problem. The generation of the baseband I and Q components of the RF signal are made with analog circuitry. Later experiments detected that an imbalance between the gains of the demodulaters was responsible for inapropriate blood flow separation. The importance of the work developed in this thesis is to provide better and more flexible solutions to the analog system used in the SUCoDiC project. Consequently, by using digital quadrature techniques which process the RF signal (or a downconversion of it) will

avoid such problems, frequently found in analog systems. In [60] the effects of imbalances and DC offsets in I/Q demodulation are extensively studied.

Consequently an usual solution consists in downconverting the RF signal to an IF signal and digitize it using only one ADC [68]. By digitalization of the IF signal, problems related to the matching of the analog circuitry of the two channels used in the classical approach, such as in figure 3.13, are eliminated [67].

The problem now is to find the balance between the order of the digital filters used and the consequent processing time, if the application is to be in real-time [67].

The usage of the digital filters must take into account their phase and group delay. It is known [4]-[9] that a FIR filter can be designed to have linear phase response and constant group delay. In contrast, a causal IIR filter cannot achieve exactly linear phase nor constant group delay; however, an IIR filter has a much smaller transition band than a FIR filter of the same order.

The choice on whether to use an IIR or a FIR filter depends on the specific process requirements (such as avoiding phase distortion during the filtering process) and the available hardware. Once the selection is performed, one have to select the digital structure to be implementd. However, if constant group delay filter is needed, the linear phase response of a FIR filter is worth the cost.

The usage of IIR filters presents the challenge of frequency dependent group delays, while FIR filters, with their constant group delay, can be a good choice at the expense of the computational cost (which can be a disadvantage given the number of coefficients that might be needed to achieve the wanted frequency response behaviour).

In this thesis the structure to implement the chosen filters will not be addressed till the effects of the quantization coefficient and the roundoff noise are studied. The best way to implement an IIR or FIR filter considering the minimization of the coefficient quantization or the roundoff noise, can be found in literature such as [5] - [10].

However, considering that FIR filters up to 100 coefficients can be used in practice with a good impact in the results [81], the length of such filters will not extend beyond this value, in this thesis. If the FIR filter requires more coefficients than 100 then an IIR will be used.

3.3.2 Bandpass Signal Representation

Let us consider a complex lowpass signal

$$x(n) = x_R(n) + jx_I(n) \tag{3.29}$$

where $x_I(n)$ is the Hilbert transform of $x_R(n)$, and $X\left(e^{j\omega T}\right) = 0$ for $-\pi \leq \omega T < 0$ [8]. Since the negative frequencies spectrum is zero this signal is called an analytic signal.

If the complex signal (3.29) is multiplied by $e^{j\omega_c n}$, where ω_c is a generic frequency, we will get

$$s(n) = x(n) \cdot e^{j\omega_c n} = s_R(n) + j s_I(n) \tag{3.30}$$

where both $s_R(n)$ and $s_I(n)$ are real sequences [8].

The relation between the spectrum of the signal (3.30) and the spectrum of the signal (3.29) is

$$S(e^{j\omega T}) = X\left(e^{j(\omega-\omega_c)T}\right) \tag{3.31}$$

From equation (3.31) it can be seen that the spectrum $S(e^{j\omega T})$ is a shifted version of the spectrum $X(e^{j\omega T})$ by a quantity $\omega_c T$. It can also be demonstrated that $s_I(n)$ is the Hilbert transform of $s_R(n)$

From the equations (3.29) and (3.30) it can be shown that [5] [8]

$$s_R(n) = x_R(n)\cos(\omega_c \cdot n) - x_I(n)\sin(\omega_c \cdot n) \tag{3.32}$$

$$s_I(n) = x_R(n)\sin(\omega_c \cdot n) + x_I(n)\cos(\omega_c \cdot n) \tag{3.33}$$

Equations (3.32) and (3.33) are the time domain representation of a general complex bandpass signal $s(n)$ expressed in terms of the real and imaginary components of a complex lowpass signal $x(n)$ [8]. Specifically equation (3.32) is the representation (in the time domain) of the real bandpass signal with respect to the I component $x_R(n)$ and a $\frac{\pi}{2}$ rad shifted component $x_I(n)$. The $\frac{\pi}{2}$ rad shifted $x_I(n)$ component is also called quadrature component [8]. Because of these properties $x_R(n)$ and $x_I(n)$ are denominated quadrature components of the bandpass signal $s(n)$ [5].

Another possible representation of a signal like $s(n)$, (equation (3.34)) exposes its magnitude and phase [8]

$$s(n) = A(n)e^{j(\omega_c n + \phi(n))} \tag{3.34}$$

where $A(n) = \sqrt{(x_R(n))^2 + (x_I(n))^2}$ is the magnitude and $\phi(n) = arctan\left(\frac{x_I(n)}{x_R(n)}\right)$ is the phase.

3.3.3 Complex Sampling

Typically digital signal processing applications data are written in what is called complex format, with its real (inphase) and imaginary (quadrature) components [6].

To obtain the time domain digital signal with complex notation it is used a technique called complex sampling, which in the literature is also known as quadrature sampling, complex demodulation, complex down-conversion, quadrature heterodyning and I/Q sampling [6]

Over the years techniques for digital quadrature demodulation have been proposed. A few examples are presented in [64] where an LPF realization and a HPF are proposed to obtain I/Q demodulation; [66] where third-band FIR filters are proposed to digital quadrature demodulation; [67] where FIR filters having as few as eleven nonzero coefficients are proposed for digital quadrature demodulation; [65] where a pair of FIR filters having six and five nonzero coefficients are used to obtain digital quadrature demodulation; [63] [6] where with the use of only one ADC and sampling the bandpass signal with a frequency four times the carrier frequency, the I/Q demodulation is obtained by multiplying the sampled data by sequences $+1, 0, -1, 0$ and $0, 1, 0, -1$ [6] to yield, respectively, the inphase and quadrature components; [71] where undersampling is used in conjunction with Hilbert transform to obtain the I/Q signal's components; [68] where a pair of 90^o phase splitting networks are used.

Published works have also used adaptive techniques to obtain I/Q demodulation, such as [31] and [72].

In the following sections it will be presented the approaches used to generate the input signal's I and Q baseband components.

However, before presenting the applied strategies, a few comments must be made:

- In all these strategies the input signal is not the received RF signal from the transducer, but a frequency translated version of it that will be denominated $s_{IF}(t)$. How and why it is used an IF signal is out of the scope of this section.

- The magnitude spectrum of the IF signal, $S_{IF}(j\omega)$, considers that it is a bandpass signal, with a total bandwidth B, centered at a known carrier frequency ω_c.

- The magnitude spectrum of the sampled IF signal $\hat{s}_{IF}(n)$ is assumed to be as shown in figure 3.15. It is assumed that $\hat{s}_{IF}(n)$ results from ideal sampling process (impulse modulated signal [9]).

- $S_{IF}(e^{j\omega T})$, the spectrum of the digital signal $s_{IF}(n)$, relates [9] to $S_{IF}(j\omega)$ the spectrum of the continuous analog signal $s_{IF}(t)$, by
  $S_{IF}(e^{j\omega T}) = \frac{1}{T}\sum_{k=-\infty}^{\infty} S_{IF}(j\omega + jk\omega_s)$, with $T = \frac{2\pi}{\omega_s}$.

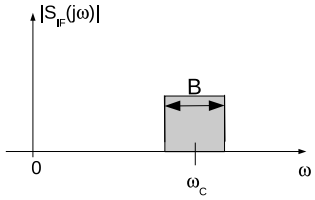

Figure 3.14: Magnitude spectrum of the IF signal $s_{IF}(t)$. $S_{IF}(j\omega)$ has a total bandwidth B, centered at a known carrier frequency ω_c.

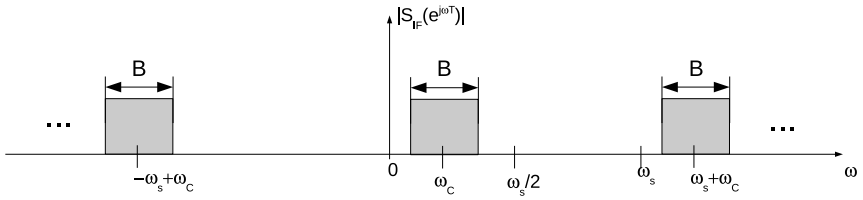

Figure 3.15: Magnitude spectrum of the digitized IF signal $s_{IF}(n)$, $S_{IF}(e^{j\omega T})$, where ω_s stands for the used sampling frequency and ω_c stands for the center frequency of the signal.

Approach 1

Observing the block diagram presented in figure 2.5, on page 12, an analog RF signal's I and Q baseband components are obtained by mixing the signal with a cossine wave (to obtain the I component) and with a sine wave (to obtain the Q component), both with frequency equal to the RF signal's carrier frequency. The signals obtained through mixing are then both filtered by two equal LPF with the same bandwidth.

Based on figure 2.5 the first digital approach considered is presented in figure 3.16.

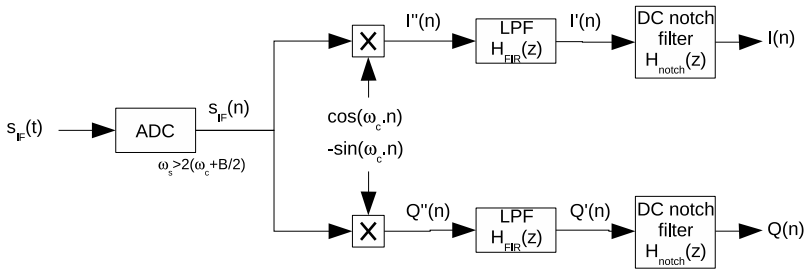

Figure 3.16: Digital quadrature phase selection strategy used in approach 1, where ω_s stands for the used sampling frequency, ω_c stands for the center frequency of the signal and B is the signal's total bandwidth.

The IF signal, $s_{IF}(t)$, is sampled at a rate bigger than twice the maximum frequency component of the bandpass signal according to the Nyquist sampling theorem, as previously presented in section 3.2. After having the digitized version of the analog IF signal $s_{IF}(t)$, the digitized signal $s_{IF}(n)$ is mixed with a digital cossine wave and with a digital sine wave to yield, respectively, the signals $I''(n)$ and $Q''(n)$

$$\begin{aligned} I''(n) &= s_{IF}(n) \cdot \cos(\omega_c \cdot n) \\ Q''(n) &= s_{IF}(n) \cdot [-\sin(\omega_c \cdot n)] \end{aligned}$$

Both signals $I''(n)$ and $Q''(n)$ are then filtered by the same lowpass FIR filter, in order to obtain the baseband signals $I'(n)$ and $Q'(n)$, respectively. The following equations describe this process, were $*$ denotes convolution.

$$
\begin{aligned}
I'(n) &= I''(n) * h_{FIR}(n) \\
Q'(n) &= Q''(n) * h_{FIR}(n)
\end{aligned}
$$

However, it can be proved that both signals $I'(n)$ and $Q'(n)$ can contain a DC component (see appendix D). In order to remove this DC component without significantly affecting the amplitude of the signal's low frequencies, a DC notch filter is used. After removing the DC frequency from $I'(n)$ and $Q'(n)$ it is obtained the desired baseband quadrature signals $I(n)$ and $Q(n)$, according to

$$
\begin{aligned}
I(n) &= I'(n) * h_{notch}(n) \\
Q(n) &= Q'(n) * h_{notch}(n)
\end{aligned}
$$

Approach 2

The block diagram associated with this approach is shown is figure 3.17

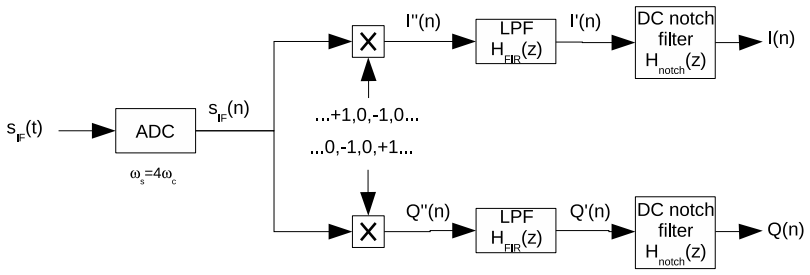

Figure 3.17: Digital quadrature phase selection strategy used in approach 2 (Adapted from [6]), where ω_s stands for the used sampling frequency and ω_c stands for the center frequency of the signal.

In this case the analog signal is sampled at a rate equal to four times the signal's carrier frequency. The digital signal $s_{IF}(n)$ is then multiplied by two repetitive four-element sequences. Through the multiplication of $s_{IF}(n)$ with $+1, 0, -1, 0, \ldots$, the signal's I component, $I''(n)$, is obtained. With the multiplication of $s_{IF}(n)$ by $0, +1, 0, -1, \ldots$, the signal's Q component, $Q''(n)$, is obtained [6].

A similar strategy, but with different two repetitive four-element sequences, was studied by Considine [63].

The two repetitive four-element sequences are orthogonal to each other and translate the input signal by exactly $\frac{f_s}{4}$. Since the sampling frequency is four times the signal's carrier frequency, the sampled signal is shifted to baseband. The advantage of this technique is that the I and Q signal's components and their shift to baseband is done without multiplications, because mixing is implemented by sign changes on $s_{IF}(n)$ [6].

$$
\begin{aligned}
I''(n) &= s_{IF}(n) \cdot \cos\left(\frac{\pi}{2} \cdot n\right) \\
Q''(n) &= s_{IF}(n) \cdot \sin\left(\frac{\pi}{2} \cdot n\right)
\end{aligned}
$$

Both signals $I''(n)$ and $Q''(n)$ are then filtered by the same lowpass FIR filter, in order to obtain the baseband signals $I'(n)$ and $Q'(n)$, respectively, according to the following equations, were $*$ denotes convolution.

$$
\begin{aligned}
I'(n) &= I''(n) * h_{FIR}(n) \\
Q'(n) &= Q''(n) * h_{FIR}(n)
\end{aligned}
$$

To remove the DC component, without significantly affecting the amplitude of the signal's low frequencies, a DC notch filter is again used. After removing the DC frequency from $I'(n)$ and $Q'(n)$ it is obtained the desired baseband quadrature signals $I(n)$ and $Q(n)$, according to

$$
\begin{aligned}
I(n) &= I'(n) * h_{notch}(n) \\
Q(n) &= Q'(n) * h_{notch}(n)
\end{aligned}
$$

Approach 3

The block diagram associated with this approach is shown is figure 3.18.

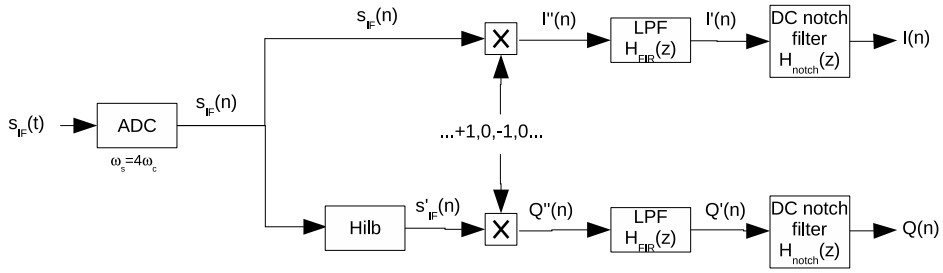

Figure 3.18: Digital quadrature phase selection strategy used in approach 3 (Adapted from [8]), where ω_s stands for the used sampling frequency and ω_c stands for the center frequency of the signal.

In this approach a quadrature version of the sampled signal $s_{IF}(n)$ is created with the use of the Hilbert transform, denoted by *Hilb* block, originating $s'_{IF}(n)$. Both $s_{IF}(n)$ and $s'_{IF}(n)$ are bandpass signals which are converted to baseband using the four-element repetitive sequence $+1, 0, -1, 0, \ldots$. The usage of this four-element repetitive sequence is possible, because in this case the analog signal is also sampled at a rate four times its carrier frequency.

$$
\begin{aligned}
I''(n) &= s_{IF}(n) \cdot \cos\left(\frac{\pi}{2} \cdot n\right) \\
Q''(n) &= s'_{IF}(n) \cdot \cos\left(\frac{\pi}{2} \cdot n\right)
\end{aligned}
$$

Both signals $I''(n)$ and $Q''(n)$ are then filtered by the same lowpass FIR filter, in order to obtain the baseband signals $I'(n)$ and $Q'(n)$, respectively, according to the following equations, were $*$ denotes convolution.

$$
\begin{aligned}
I'(n) &= I''(n) * h_{FIR}(n) \\
Q'(n) &= Q''(n) * h_{FIR}(n)
\end{aligned}
$$

Removal of the DC component is again performed by usage of a DC notch filter. After removing the DC frequency from $I'(n)$ and $Q'(n)$ it is obtained the desired baseband quadrature signals $I(n)$ and $Q(n)$, according to

$$
\begin{aligned}
I(n) &= I'(n) * h_{notch}(n) \\
Q(n) &= Q'(n) * h_{notch}(n)
\end{aligned}
$$

Approach 4

The block diagram associated with this approach is shown is figure 3.19

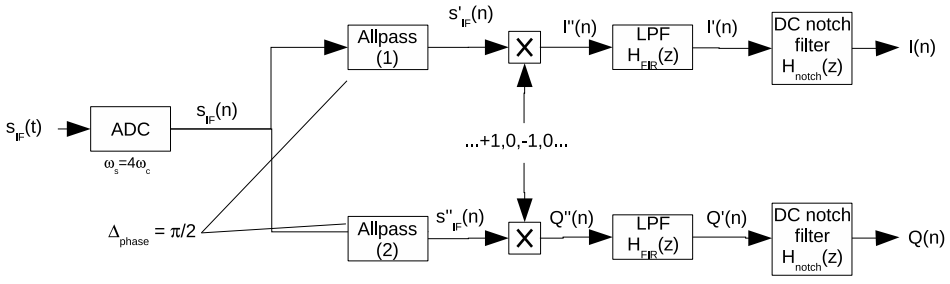

Figure 3.19: Digital quadrature phase selection strategy used in approach 4 (Adapted from [68]), where ω_s stands for the used sampling frequency and ω_c stands for the center frequency of the signal.

This strategy uses what is called in the literature [69] phase-splitting network, where the phase splitter is implemented using two allpass filters presenting a phase difference of $\frac{\pi}{2}$ rad between each other.

An allpass filter [73] presents a frequency response $A(e^{j\omega T})$ with unit magnitude for all frequencies. As the signal passes through the filter, the signal's amplitude is not affected but the phase is. Because

of this characteristic, allpass filters are used to shape the phase (and hence the group delay) response, compensating any phase distortion [8].

$$|A(e^{j\omega T})|^2 = 1, \ for\ all\ \omega \tag{3.35}$$

In an IIR allpass filter the frequency response can be written [74] as

$$A(z) \ = \ z^{-N}\frac{D(z^{-1})}{D(z)} \tag{3.36}$$

where $D(z) = \sum_{k=0}^{N} a_k \cdot z^{-k}$ with a_k being real coefficients.

The sampled signal $s_{IF}(n)$ is filtered by two allpass filters that present a phase difference between each other of $\frac{\pi}{2}$ rad, generating the signals $s'_{IF}(n)$ and $s''_{IF}(n)$. From equation (3.35) the amplitude of $s'_{IF}(n)$ and $s''_{IF}(n)$ should be equal to the amplitudes of $s_{IF}(n)$, and the phase difference between $s'_{IF}(n)$ and $s''_{IF}(n)$ should be of $\frac{\pi}{2}$ rad.

Both $s'_{IF}(n)$ and $s''_{IF}(n)$ are bandpass signals which are converted to baseband using the four-element repetitive sequence $+1, 0, -1, 0, \ldots$. The usage of this four-element repetitive sequence is possible, because in this case the analog signal is also sampled at a rate four times its carrier frequency.

$$\begin{aligned} I''(n) &= s'_{IF}(n) \cdot \cos\left(\frac{\pi}{2} \cdot n\right) \\ Q''(n) &= s''_{IF}(n) \cdot \cos\left(\frac{\pi}{2} \cdot n\right) \end{aligned}$$

Both signals $I''(n)$ and $Q''(n)$ are then filtered by the same lowpass FIR filter, in order to obtain the baseband signals $I'(n)$ and $Q'(n)$, respectively, according to the following equations, were $*$ denotes convolution.

$$\begin{aligned} I'(n) &= I''(n) * h_{FIR}(n) \\ Q'(n) &= Q''(n) * h_{FIR}(n) \end{aligned}$$

As previously, the DC component removal is performed by means of a DC notch filter. The desired baseband quadrature signals $I(n)$ and $Q(n)$, are obtained according to

$$\begin{aligned} I(n) &= I'(n) * h_{notch}(n) \\ Q(n) &= Q'(n) * h_{notch}(n) \end{aligned}$$

Approach 5

The block diagram associated with this approach is shown is figure 3.20

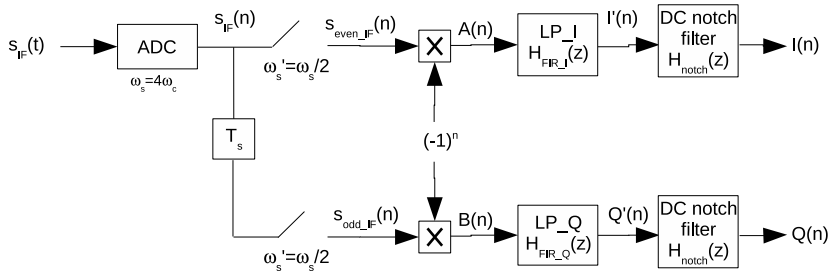

Figure 3.20: Digital quadrature phase selection strategy used in approach 5 (Adapted from [64]), where ω_s stands for the used sampling frequency and ω_c stands for the center frequency of the signal.

In this technique the input IF signal is sampled at a rate four times higher than the signal's carrier frequency. The sampled signal $s_{IF}(n)$ is then separated in its odd and even samples, referred as $s_{odd\_IF}(n)$ and $s_{even\_IF}(n)$, respectively. Inkol *et al* [64] show that instead of using two HPF to obtain the quadrature between the two signals $s_{odd\_IF}(n)$ and $s_{even\_IF}(n)$, two LPF can be used if the signals $s_{odd\_IF}(n)$ and $s_{even\_IF}(n)$ are multiplied by $(-1)^n$ before filtering.

Also important [66] is that these two FIR LPFs, LP_I and LP_Q, are obtained by subsampling the impulse response of a FIR filter defined by $M = 2K + 1$ coefficients. That is, being $h_{FIR}(n)$ the impulse response of the $M = 2K + 1$ coefficients initial FIR filter, then

$$\begin{aligned} h_{FIR\_I}(n) &= 2 \cdot h_{FIR}(2n) \\ h_{FIR\_Q}(n) &= 2 \cdot h_{FIR}(2n+1) \\ n &= 0, 1, \ldots, M-1 \end{aligned}$$

According to [66], the block diagram presented in figure 3.20 assumes an odd value of M (K is even).

With this in mind,

$$\begin{aligned} s_{even\_IF}(n) &= s_{IF}(2n) \\ s_{odd\_IF}(n) &= s_{IF}(2n+1) \\ n &= 0, 1, \ldots \end{aligned}$$

With signals $I'(n)$ and $Q'(n)$ given by

$$\begin{aligned} I'(n) &= A(n) * h_{FIR\_I}(n) \\ Q'(n) &= B(n) * h_{FIR\_Q}(n) \end{aligned}$$

The removal of the DC component is made with a notch DC filter

$$\begin{aligned} I(n) &= I'(n) * h_{notch}(n) \\ Q(n) &= Q'(n) * h_{notch}(n) \end{aligned}$$

Chapter 4

Experimental Setup Developed

4.1 Introduction

The Doppler ultrasound demodulator techniques to be developed and compared on this thesis are to be included in an experimental apparatus (figure 4.1). A blood phantom is activated by a flow pump bomb to simulate blood flow in natural arteries. An ultrasound transducer will produce signals to test the different demodulator techniques. It is envisaged that at a final stage of the project, the blood flow simulator components will be computer controlled through the flow pump driver circuit, as shown in figure 4.1.

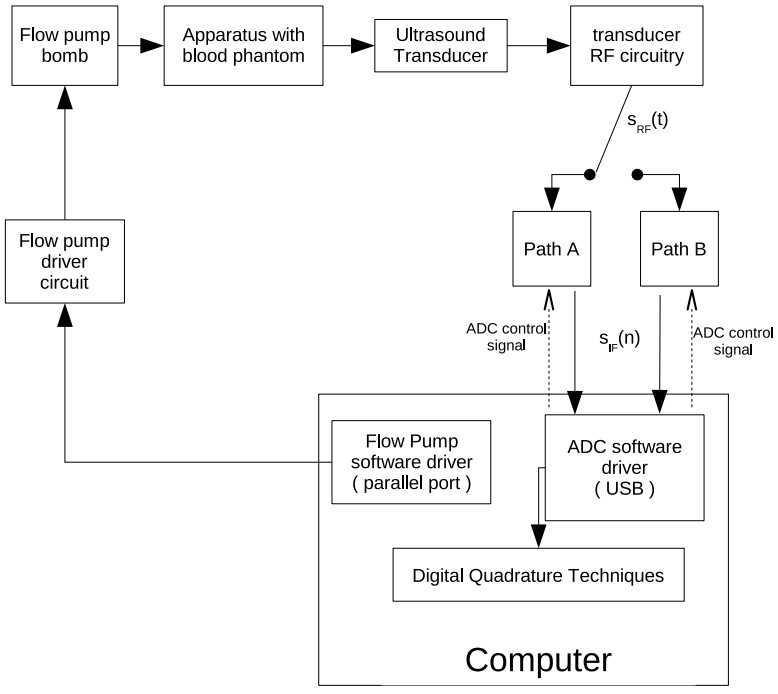

Figure 4.1: Block diagram of the experimental apparatus main blocks

With the use of an ultrasound transducer, the backscatter ultrasound will be received by the RF circuitry (previous developed as part of the SUCoDiC project). The received signal, $s_{RF}(t)$, can be

acquired by the computer by two separated paths. One path (see figure 4.2) will acquire the signal using the BPS methodology (section 3.2) . The other path (see figure 4.3) translates the RF signal to a lower frequency, allowing it to be lowpass sampled, after applying the heterodyne technique on the signal (section 3.1) . Then the received signal (by either paths) is processed by the digital quadrature techniques mentioned in section 3.3 and the results presented to the user.

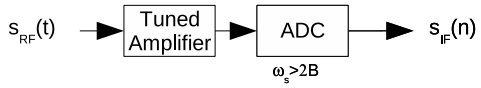

Figure 4.2: Block diagram of path A shown in figure 4.1, where ω_s stands for the sampling frequency and B the total bandwith of the signal. In this path the BPS principles are used.

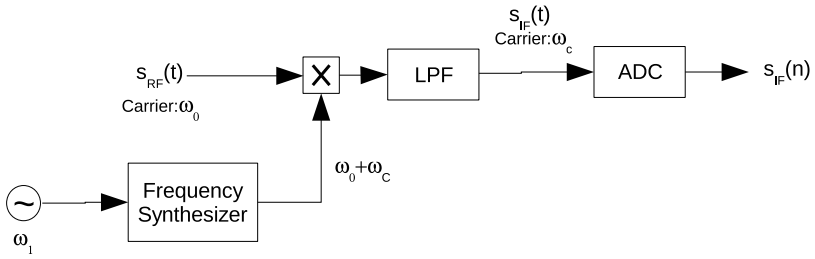

Figure 4.3: Block diagram of path B shown in figure 4.1, where ω_1 stands for the local oscillator frequency, ω_0 is the RF signal carrier frequency and ω_c is the IF signal carrier frequency. In this path the RF signal is down converted after applying the heterodyne technique.

In practice, at the moment, although both paths A and B are implemented, the connection between the *transducer RF circuitry* and any of the paths has not been created. The reason is the following. Since in this thesis it is expected to implement some digital I/Q demodulation techniques and study them, the RF signals to be used must be well characterized in terms of their spectral content (complete information of the frequency components location relative to the carrier and their relative amplitudes). If the signal that comes from the *transducer RF circuitry* is used, correct evaluation of the efficiency of the studied digital quadrature techniques is difficult, because the spectral content of the received signal is not exactly known. For this reason, this study uses RF signals created by a function generator, namely Frequency Modulated (FM) signals whose spectral content is well known (see [12] and [62]).

By doing so, this does not invalidate the need to develop the rest of the software and hardware to control the flow pump, given the fact that it will be used in the future.

In the next sections each of the developed components (hardware or software) will be described.

4.2 Experimental Setup Implemented

4.2.1 Equipment used

For the creation of the FM signal an Agilent 33220A 20 MHz Function/Arbitrary Waveform Generator was used. Such FM modulated signal results from modulating a 1 Volt amplitude 8 MHz sine

wave, with a 1 Volt 13 kHz sine wave ($f_m = 13\ kHz$). The maximum frequency deviation (Δf) was 26 kHz, resulting in a FM signal with $\beta = \dfrac{\Delta f}{f_m} = 2$ [12]. To measure the signals frequency and to visualize the signals, a Tektronix TDS2024 200 MHz (2 GS/s) was used. The voltages, currents and resistor values were measured with a Keithley 2700 Multimeter/Data acquisition system. The power supply used was an ISO TECH Programmable Power Supply IPS 3202. To sample and digitize the signals, a National Instruments (NI) Data Acquisition system NI DAQ USB 6251 16-Bit, 1.25 MS/s M Series was employed [91]. To create the reference signal for the PLL based frequency synthesizer a GW Function Generator Model GFG-8015G was used.

The computer used to collect the digitized data was a Packard Bell EasyNote MT85-T-001, equipped with 4096 MB of RAM, an Intel Core 2 Duo Model T9600 (2.53 GHz, 6 MB of L2 cache, FSB = 1066 MHz) processor. The operating system installed in the computer is Windows Vista. The NI DAQ USB 6251 Application Programming Interface (API) version is NI-DAQmx 8.6.1.

4.2.2 Flow Pump Control

Flow Pump Driver Circuit

The flow pump driver circuit (see figure 4.4 for the diagramatic scheme) was conceived considering two possibilities. One is a direct control of the flow pump through the computer's parallel port. The other is that a binary sequence is sent to a PIC 16F684 microcontroller, which mission is to interpret the binary data sequence and start or stop the pulse generation with desired period and duty cycle.

These two alternatives were implemented to avoid circuitry to stop in case the PIC 16F684 gets damaged. The latter has the advantage of including an internal ADC which can be used to acquire signals produced by sensors such as pressure, flow or others and to monitor the blood flow.

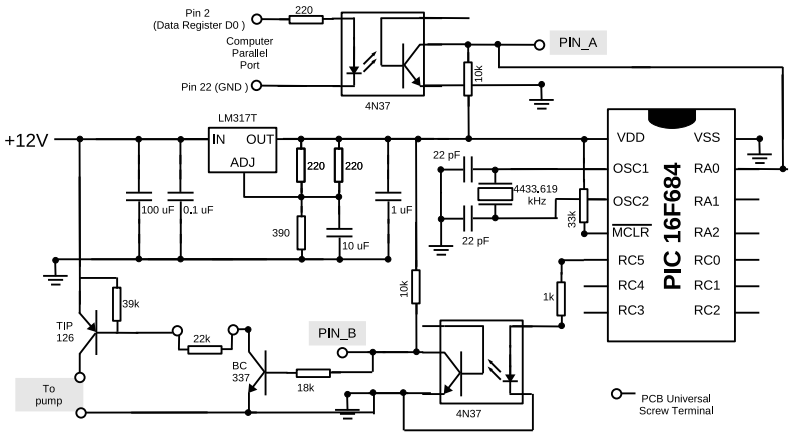

Figure 4.4: Schematic diagram of the circuit built to control the flow pump motion through the computer's parallel port

In figure 4.4 , in case the PIC 16F684 is damaged, it can be removed from the circuit, and PIN_A will be directly connected to PIN_B, allowing the signal coming from the parallel port to control the motion of the flow pump.

Flow Pump Software Driver

In order to communicate the desired duty cycle and period of the pulses generated by the flow pump, two computer software applications and one firmware application were developed. Like stated in subsection 4.2.2, the flow pump can be operated directly through the computer parallel port, or, the computer instructs the PIC 16F684 microcontroller about the desired duty cycle and period of the pulses and controls also the flow pump on its own.

Both software applications were created in Python programming language [90], while the firmware code was developed in Assembly language [87] for PIC 16F684 .

The software applications flow_pump_control_threads.py receives the desired duty cycle and period through a GUI (see figure 4.5). A thread will be created generating the pulses through the parallel port. These pulses will control the flow pump through the power amplification stage of the flow pump circuitry.

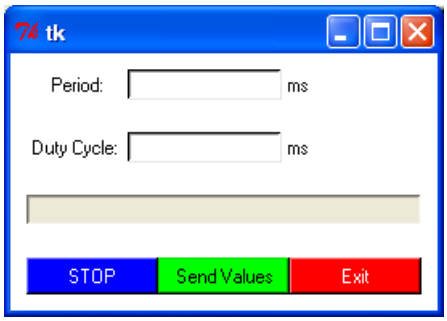

Figure 4.5: GUI interface for user input of the desired duty cycle and period of the pulses to be generated.

Another software application, the flow_pump_control_PIC.py presents the same GUI interface window as the previous application, but instead of creating the desired duty cycle and period of the pulses, converts these values to a binary sequence and send it through the parallel port (bit D0 of Data register - see figure 4.6). The firmware programmed in the PIC 16F684 , designated as pump_control.asm, interprets the binary sequence and will control the flow pump through the power amplification stage in the flow pump circuitry.

Both computer software applications need a Python module named *winioport* [88].

Once the user fills the text fields associated to the duty cycle and to the period presented in the GUI interfaces and presses *Send Values*, the software will generate the desired pulses or, as previous mentioned, depending on the application, will communicate with the PIC 16F684 microcontroller to create those pulses. In case the user wants to stop the current pulses from being generated, it is just enough the user to press *STOP*. In this case, the thread running to accomplish that routine will be ordered to stop. If the pulses were being generated by the PIC 16F684 microcontroller, then the software will send a binary code sequence to the microcontroller, stopping its action.

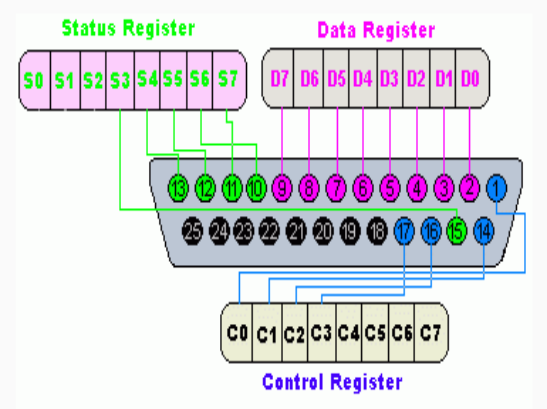

Figure 4.6: Parallel port pins and associated memory registers [89]

4.2.3 Signal Acquisition

The RF signal to be acquired and digitized by the ADC can come from two paths (see figures 4.2 and 4.3). In one strategy one wishes to apply the theory related to BPS and sample the RF signal directly. In another strategy the RF signal is first downconverted to a lower carrier frequency applying the heterodyne technique, filtered to remove the higher frequency components (which result from the heterodyne technique) and then the signal is sampled.

Since the study of blood flow information from the analysis of the RF signals is not in the scope of this thesis, and, due to the fact that the spectral content of blood flow signals is not completely known (for instances, the exact amplitude of each spectral content), and also the spectral content of such signals is very complex, usage of blood flow signal simulator makes difficult assessing the performance of the particular system to be developed in this thesis.

To be mentioned that, testing the circuitry to be developed would require repeating signals under similar conditions. With the signal's simulator one has no garantee that a series of pump pulses will produce exactly the same blood flow signals, because the phantom scatters are not guaranted to be homogeneously distributed through out the phantom nor that casual agglomeration of these scatterers is avoided. For such reasons the RF signal containing the information to be processed must be a signal whose spectral content is known with precision in terms of spectral locations of the frequency components and their relative amplitudes.

BPS strategy

In order to sample the RF signal (FM modulated sine wave) directly, a tuned amplifier (circuit shown in figure 4.7) was used between the function generator and the ADC. The tuned amplifier allowed the amplitude of the RF signal to be amplified by a factor of 5.14. It is intended to tune the frequency around the carrier (8 MHz) and to attenuate the frequencies outside its bandwidth. Ideally this tuned amplifier should have a bandwidth of only 78 kHz, which would demand a Q factor of 102.6**.** However, in practice, with the circuit employed, a 2.3 MHz bandwidth was obtained. However,

since a FM modulated sine wave in a sine carrier was used, one knows that the sidebands spectral components amplitudes tend to be quite small after the 3rd sideband spectral component (see table 5-2, page 318 of [14]). The tuned amplifier, although not satisfying the project's required bandwidth, does attenuate the noise outside the tuned amplifier bandwidth. The presence of this tuned amplifier not only amplifies the desired signal but also attenuates the noise outside the amplifier bandwidth, since the SNR is not preserved when using BPS [50] [58]. Although not ideal (in terms of the Q factor value) the tuned amplifier employed was enough (for the RF signal studied) to enhance the important signal's spectral content, as can be seen from the results presented in section 5.2.

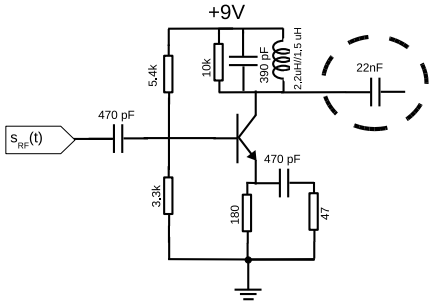

Figure 4.7: Tuned amplifier with central frequency of 8 MHz and an expected bandwidth of $BW = \frac{1}{2\pi(10\ k\Omega)(390\ pF)} = 40.8\ kHz$ [93]. The practical $-3\ dB$ bandwidth ranges from 6.6 MHz to 8.9 MHz. The capacitor in the BC337-16 transistor's collector was later added (not soldered on the perfboard) to remove the signal's DC component

Heterodyne Technique

Analysing the RF signal and the available devices' constraints some problems were detected.

The RF signal (from the already existent blood flow acquisition device [40]) presents a carrier of 8 MHz, imposing a sampling frequency greater than 16 MHz.

However, the available ADC has a maximum sampling rate of 1.25 MS/s, per each single channel data acquisiton.

Since it is forseen the need for multiple channel acquisitions on future developments of the whole Doppler ultrasound signal analyser system, and, due to the NI DAQ USB 6251 multiplexed strategy for multichannel sampling, and also, the fact that the computer used to receive the digitized data cannot put the data in memory faster than the rate at which the ADC produces it, a strategy had to be developed to sort the above mentioned problems.

For these reasons, the RF signal needs to be downconverted so that the maximum signal's frequency component is at a frequency capable of being sampled by the device. Down converting the 8 MHz carrier signal to a 50 kHz carrier, with a total bandwidth of 78 kHz, provides a situation capable of allowing the signal to be sampled at rates that the ADC and the computer supports. To implement such strategy the block diagram shown in figure 4.3 was implemented as described in the following paragraphs.

As presented in figure 4.3, in order to obtain a signal centered at a frequency ω_c the RF signal with a carrier's frequency ω_0 must be mixed with a wave whose frequency is $\omega_0 + \omega_c$. To produce such

frequency a PLL-based frequency synthesizer was developed. The circuit of this frequency sinthesizer is presented in figure 4.8.

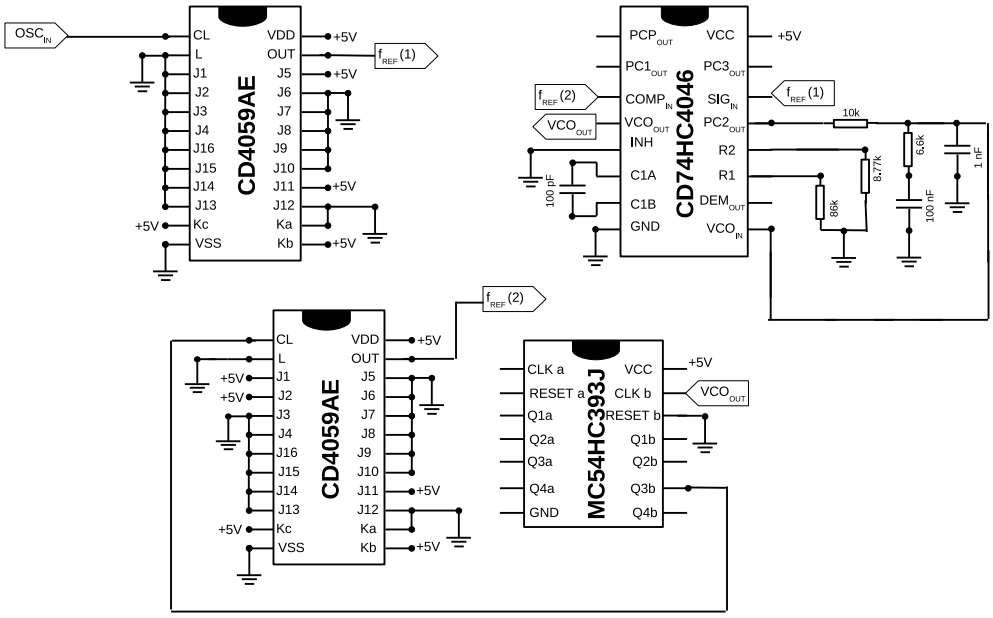

Figure 4.8: Schematic circuit of the PLL based frequency sinthesizer

Decision was made to sinthesize a frequency of 8050 kHz to be mixed with the 8 MHz carrier FM signal. To obtain a PLL output frequency (VCO OUT) with that value, the frequency dividers were configured with the values presented in figure 4.9.

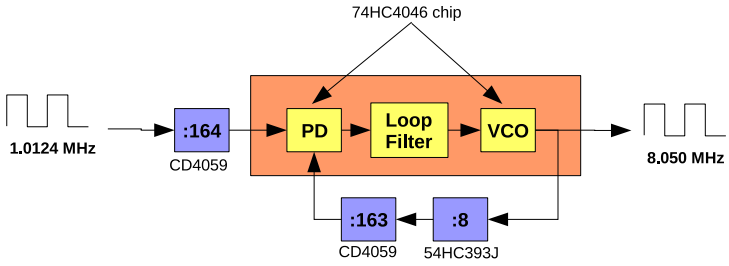

Figure 4.9: Block diagram of the PLL-based frequency synthesizer, indicating the values on each frequency divider, the PLL reference oscillator and the output frequency synthesized by the circuit

The mixing was made by the circuit presented in figure 4.10 [42].

Since the output of the mixer has the desired signal centered at a frequency of 50 kHz and an image at 16.05 MHz the high frequency signal needs to be removed.

To remove this high frequency components it was used a Linear Phase filter with Equiripple Error of 0.05 ^{o} which besides removing the high frequency components also presents a linear phase with equiripple behaviour frequency response. As a consequence of the linear phase (with an equiripple error) the group delay tends to be linear (with equiripple behaviour) extending even after the cutoff frequency [32] [103]. Such filter is a 6th order, implemented using Sallen-Key topology [33], with a

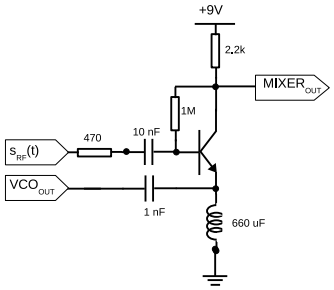

Figure 4.10: Schematic circuit of the RF signal mixer with the signal output (VCO_{OUT}) of the frequency sinthesizer (figure 4.8)

$-3dB$ cutoff frequency of 95 kHz. To remove the DC component and some lower frequencies a RC highpass filter was used. This filter presents a $-3dB$ cutoff frequency of 159 Hz and was implemented before the 6th linear phase with equiripple error filter, as presented in figure 4.11.

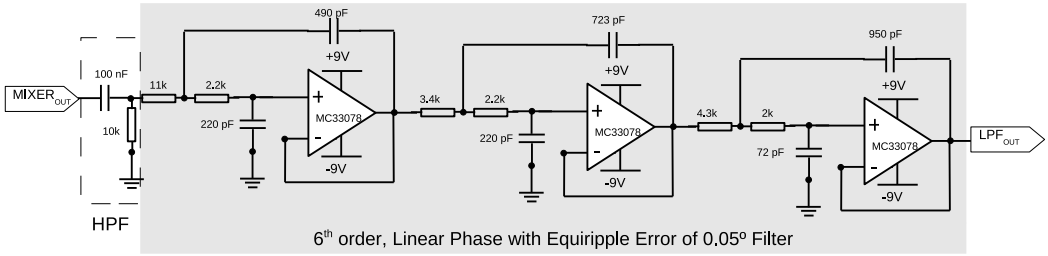

Figure 4.11: Sallen-Key 6th order Lowpass Linear Phase with Equiripple Error of 0.05 ^{o} filter, used to filter the output of the mixer (in figure 4.10)

Frequency Synthesizer Characterization

The external PLL chip's (CD74HC4046) capacitor and resistors were chosen with the following values:

- C = 100 pF
- R_1 = 86 kΩ
- R_2 = 8.77 kΩ

With these values, the minimum VCO output frequency is equal to 7.69 MHz (VCO input voltage of 0 Volts) and the VCO output frequency has the value of 8.25 MHz when the VCO input voltage is equal to 4 Volts. From the presented values it can be seen that the desired frequency to be synthesized (8.050 MHz) is in the VCO supported frequency range.

From several acquired values for the VCO input voltage and consequent VCO output frequency the average value for the VCO conversion gain k_o is equal to 9.8039×10^4 rad/s/V.

As a phase detector it was used a positive-edge-triggered phase and frequency detector. The phase comparator conversion gain (k_d) is equal to 0.3979 V/rad. The settling time, considering a 2% error criteria, was of 10 ms.

From the previous considerations, the value of the damping ratio ξ assumed the following values $\xi = \{0.3, 0.4, 0.45, 0.5, 0.55, 0.6, 0.65, 0.707, 0.8, 0.9\}$. From these values, only the values $\xi = \{0.65, 0.707, 0.8, 0.9\}$ made possible the desired loop filter, i.e., only these values of ξ generated positive time constants τ_1 and τ_2.

After identifying the above values of ξ, the natural undamped frequency (ω_n) of the PLL-based frequency synthesizer, the $-3\ dB$ cutoff frequency (w_{-3dB}) and the gain and phase margins were determined. The results are shown in table 4.1. In the last column of this table the transfer function of the loop filter (figure 4.12) is also written.

The $-3\ dB$ cutoff frequency was calculated by $\omega_{-3dB} = \omega_n\sqrt{1 + 2\xi^2 + \sqrt{2 + 4\xi^2 + 4\xi^4}}$ [17] [101] .

ξ/rad^{-1}	$\omega_n/(rad\ s^{-1})$	$w_{-3dB}/(k\ rad^{-1})$	Phase Margin/^{o}	Gain Margin/dB	$F(s)$
0.650	615.38	1.22	63.9 ($\omega = 460\ rad/s$)	∞	$\frac{0.0002859s+1}{0.001446s+1}$
0.707	565.77	1.16	69.2 ($\omega = 453\ rad/s$)	∞	$\frac{0.0006727s+1}{0.00171s+1}$
0.800	500.00	1.09	77.1 ($\omega = 457\ rad/s$)	∞	$\frac{0.001373s+1}{0.00219s+1}$
0.900	444.44	1.04	83.8 ($\omega = 481\ rad/s$)	∞	$\frac{0.002223s+1}{0.002772s+1}$

Table 4.1: Table showing for each of the considered values of ξ, for a settling time of 10 ms, the values of the natural undamped frequency of the PLL-based frequency synthesizer ω_n, the $-3\ dB$ cutoff frequency (w_{-3dB}) and the gain and phase margins, as well as the loop filter's transfer functions associated to each ξ value.

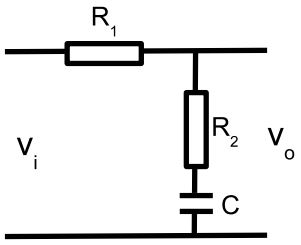

Figure 4.12: Passive filter used in a PLL [17], where v_i stands for the input signal and v_o stands for the output signal of the filter

For each of the values of ξ in table 4.1, the PLL-based frequency synthesizer was characterized by:

- the phase margin and the gain margin, obtained by the Bode plot of the feedforward transfer function (equation (3.9)) [18] [26];
- it's stability, using the root locus [24] [25];

- the error-transfer function [25] (equation (3.8));
- it's step response [24] [25];

The plots for each value of ξ are presented in appendix C.

Based on what is stated in subsection 3.1.2, the desired range of phase margins are between 30^o and 60^o [17], and the gain margin should be greater than 6 dB [24]. Other authors consider that the phase margin should be of at least 45^o , being 60^o preferable [19]. If a PLL is designed to be a second order system (as in this case), the desired damped ratio is $\xi = \frac{1}{\sqrt{2}}$ [17], in order to originate an underdamped system in which the transfer function have the shape of a second order Butterworth LPF (optimally flat transfer function).

Consequently it was decided to use a value of $\xi = \frac{1}{\sqrt{2}} \approx 0.707$ (see plots in subsection C.2, page 113). With the values ξ=0.707 and $\omega_n = 565.77\ rad/s$ the theoretical PLL-based frequency synthesizer parameter presented in table 4.2 are obtained. As a consequence of this choice, the values of the loop filter's resistors and capacitor the theoretical values are $R_1 = 10.4\ k\Omega$, $R_2 = 6.7\ k\Omega$ and $C = 100\ pF$. In practice, the resistors values were $R_1 = 10\ k\Omega$, $R_2 = 6.6\ k\Omega$.

Parameter [17]	Designation	Theoretical Value
$\Delta\omega_H$	*Hold range*	∞
$\Delta\omega_L = 4\pi\xi\omega_n$	*Lock Range*	5027.3 rad/s
$\Delta\omega_P$	*Pull-in Range*	∞
$T_P = 2(\tau_1 + \tau_2)\ln\left(\frac{1}{1 - \frac{2N\Delta\omega_0}{Vk_o}}\right)$	*Pull-in time*	14.35 μs

Table 4.2: Table with a few usual parameters and correspondent values characterizing the developed PLL system

To evaluate the PLL's output frequency variation, considering figure 4.9, the input signal had a frequency of 1.01243 MHz (obtained with the Agilent 33220A Function Generator). The obtained output frequency had a value of (8.05000 ± 0.00001) MHz, and a jitter value of 8 ns. This means that the measured variation in the PLL's output frequency has a maximum value of 10 Hz.

4.2.4 NI DAQ USB 6251 Control Software Application

The NI DAQ USB 6251 device comes with an Application Programming Interface (API) which was used to create a software application to setup the desired acquisition conditions. With the developed software application the data acquired from the ADC can also be retrieved for further processing.

The software created to control this device was implemented in Python programming language, and presents an user interface as shown in figure 4.13.

The application is formed by several sub applications.

One sub application (Control_NIDAQmx_USB6251.py) contains the routines to communicate with the NI DAQ USB 6251 device, in order to setup the desired sampling conditions and to retrieve the sampled data. This sub application is designated by *Server* application, because it acts like named

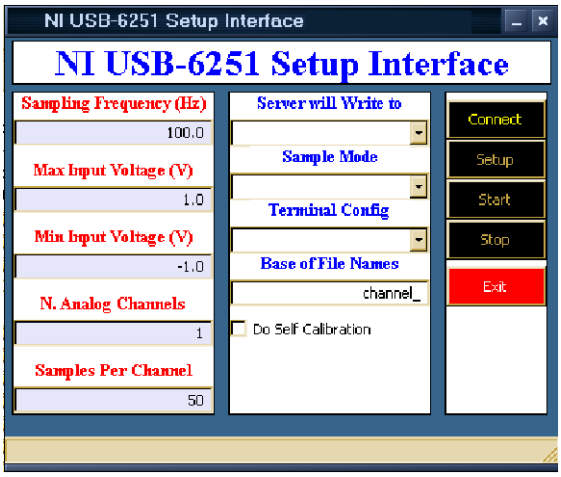

Figure 4.13: GUI of the software used to setup the acquisition conditions of the NI DAQ USB 6251 device

piped server. The *Server* application is initiated and waits in standby for the connection to the other sub application (Interface_Control.pyw), as may be seen on figure 4.13.

To operate the developed application the user must indicate the wanted sampling frequency, the expected maximum and minimum voltage associated with the signal to be acquired, the number of analog channels to be acquired and how many samples per channel to acquire. The user also needs to indicate in the field "Server will Write to" were the *Server* application will write the acquire data to (file or named pipe). The *Sample Mode* and *Terminal Config* are parameters which, respectively, configure the NI DAQ USB 6251 how the acquired data is organized and how to determine the reference voltage. The available options are specified in the NI DAQ USB 6251 manual and API. The parameter *Base of file Names* will be the base name of the file or named pipe to which is added a number relating the file or named pipe designation and the used analog channel(s). If wanted, self calibration can be ordered.

Once every fields are filled (with the exception of the *Do Self Calibration* which is not compulsory) the user presses *Connect* to connect to the *Server* application. The *Setup* button can then be pressed so that the data in the interface is passed to the *Server* application. Once the *Start* button is pressed, the NI DAQ USB 6251 device is setup and begins retrieving the sampled data whenever it becomes available. To stop the current acquisition its enough to press the *Stop* button.

The *Server* application is named as *Server* because once the sub application Interface_Control.pyw exits, it returns to the initial state and waits for another Interface_Control.pyw "client" to connect and demands a new sampling operation.

The *Server* application communicates with the NI DAQ USB 6251 device, receives the digitized data and can write it to a file or to a named pipe. The developed application can order that the sampling is made in multichannels, and for each channel a file or named pipe is created.

If the digitized data is written in named pipes, an example application named Client_Read_Pipes.py shows how to read from those named pipes.

The advantage of individual named pipes are: each pipe contains data from a specific analog

input channel; each channel may contain information from a particular signal; each named pipe can be processed by a different client, where each client may be executing different sets of routines to process the sampling signal associated with that named pipe.

Another advantage of using the named pipe strategy is that a client application that will process the sampled data, can be written in another programming language different from the *Server* application.

The collected data is written in the binary format to file or named pipe. Each element has 64 bit size (see NI DAQ USB 6251 manual for further explanation).

When multichannel acquisition is to be executed care must be taken in choosing the sampling frequency because the NI DAQ USB 6251 device samples multi channels in a multiplexed way.

For the experimental signals acquired either to be processed with BPS or after applying the heterodyne technique, only one channel was used, and the *Terminal Config* was set to *RSE* (see NI DAQ USB 6251 manual for details).

4.3 Digital Techniques Parametrization

4.3.1 Testing and Experimental Signal's Characterization

In this section the testing signal and the experimental signal generated in practice to be acquired with the BPS strategy and with the heterodyne technique will be presented.

A testing signal has been created to allow precise characterization of the parameters. This signal is from now on referred as test signal, and will be described in subsection 4.3.1.

Using the test signal, the efficiency of each approach presented in subsection 3.3.3 is evaluated. For precision sake, the evaluation of each approach was also studied under noisy signals, so random gaussian noise was added to the test signal. This noise had null mean and 30 mV variance.

Next, the same sequence of approaches (approaches 1 to 5 in subsection 3.3.3) were evaluated with what will be designated as experimental signals. These signals were acquired by application of the heterodyne technique (section 3.1) and by using the BPS theorem principles (section 3.2).

All digital signal processing is developed in *Matlab* . As disadvantage, the real-time efficiency of each approach will not be considered. Also worth mention is that all magnitude spectra presented are the result of a 1024 point Fast Fourier Transform (FFT). For approaches 1 to 4 the spectrogram images are created using a 1024 point signal and a 512 point Hanning window size. For approach 5, because decimation by two occurs, the spectrogram is created from a 512 point signal with a 256 size Hanning window. The spectrogram was calculated using the *Matlab* 's routine *spectram*. The application of the Hanning window was made by overlaping sections of samples with a lenght equal to half of the used Hanning window size.

For all the FFT magnitude spectra presented in this thesis the unit of the ordinate values is Volts.

Since the strategies studied in this thesis will be applied to digital processing of Doppler blood

Blood velocity value (mm/s)	$\theta/^o$								
	0	10	20	30	40	50	60	70	80
1	10.19	10.04	9.58	8.82	7.81	6.55	5.10	3.49	1.77
2	20.38	20.07	19.15	17.65	15.61	13.10	10.19	6.97	3.54
5	50.96	50.18	47.88	44.13	39.03	32.75	25.48	17.43	8.85
10	101.91	100.36	95.76	88.26	78.07	65.51	50.96	34.86	17.70
20	203.82	200.72	191.53	176.51	156.14	131.01	101.91	69.71	35.39
30	305.73	301.09	287.29	264.77	234.20	196.52	152.87	104.57	53.09
40	407.64	401.45	383.06	353.03	312.27	262.03	203.82	139.42	70.79
50	509.55	501.81	478.82	441.29	390.34	327.54	254.78	174.28	88.48
100	1019.11	1003.62	957.65	882.57	780.68	655.07	509.55	348.56	176.97
150	1528.66	1505.44	1436.47	1323.86	1171.02	982.60	764.33	522.83	265.45
250	2547.77	2509.06	2394.12	2206.43	1951.70	1637.68	1273.89	871.39	442.42
350	3566.88	3512.69	3351.77	3089.01	2732.39	2292.74	1783.44	1219.94	619.38
450	4585.99	4516.32	4309.42	3971.56	3513.07	2947.82	2292.99	1568.50	796.35
750	7643.31	7527.19	7182.36	6619.30	5855.12	4913.03	3821.66	2614.17	1327.25
1000	10191.08	10036.26	9576.48	8825.74	7806.82	6550.70	5095.54	3485.56	1769.66
1500	15286.62	15054.39	14364.73	13238.60	11710.23	9826.05	7643.31	5228.33	2654.49
2000	20382.16	20072.51	19152.97	17651.47	15613.64	13101.40	10191.08	6971.11	3539.32
3000	30573.25	30108.77	28729.46	26477.21	23420.47	19652.10	15286.62	10456.67	5308.99
4000	40764.33	40145.03	38305.94	35302.95	31227.29	26202.81	20382.17	13942.22	7078.65

Table 4.3: Doppler frequency shifts for some selected values of blood flow velocity, and some angles between the direction of the ultrasound waves and the flow direction, computed using equation (2.1)

flow signals, it is important to relate the value of the velocity of the blood with the amount of Doppler frequency shift. Considering the speed value of ultrasound waves in blood to be 1570 m/s [28] the values of Doppler frequency shift can be obtained as a function of the angle between the direction of the blood motion and the direction of the ultrasonic wave. Table 4.3 presents such values.

Article [40], reports the development of a system in which the range of magnitudes of the blood flow velocity was considered to be from 20 mm/s to 750 mm/s. However since the digital lowpass FIR filters bandwidth can be easily changed, decision was made to maximize their bandwidth to about 36.5 kHz. This way even if the blood velocity value is much higher than normally considered, consequent Doppler frequency shift can be detected.

Testing Signal

As mentioned earlier, a test signal will be created for the sake of obtaining precise characterization of circuitry parameters when each of the demodulator approaches are to be tested.

This subsection reports how the test signal was developed.

The wave used to excite the transducer has 8 MHz frequency value consequently, if bandpass sampling is not considered, the Nyquist rate [83] would have to be at least 16 MHz. Such sampling rate cannot be attained by the NI DAQ USB 6251 device. For that matter, the signal needs to be translated in frequency to a lower frequency, such that the Nyquist rate used can be supported by the ADC device and the volume of data to be acquired can be supported by the computer on use. Considering a total bandwidth of 78 kHz, when such signal is translated from a carrier frequency value equal to 8 MHz to another carrier, with a frequency value equal (or near) to 50 kHz, both the supported sampling rate by the NI DAQ USB 6251 and the volume of data to be acquired and processed by the computer, are fulfilled.

Based on the simplified ultrasound signal from [28], the signal in equation (4.1) was considered

as the theoretical IF signal to be processed. It is assumed that the signal is already in its digitized form.

$$\begin{aligned} s_{IF}(n) &= A_C \cos(\omega_C \cdot n + \phi_C) \\ &+ A_F \sum_{k=1}^{4} \cos\left[(\omega_C + \omega_{F_k}) \cdot n + \phi_{F_k}\right] \\ &+ A_R \sum_{m=1}^{4} \cos\left[(\omega_C - \omega_{R_m}) \cdot n + \phi_{R_m}\right] \end{aligned} \tag{4.1}$$

where $\{C, F, R\}$ represents, respectively, the carrier, forward blood flow and reverse blood flow.

- A_i with $i = \{C, F, R\}$ are the amplitudes of the signal's components;
- ω_i with $i = \{C, F_k, R_m\}$ are the frequencies of the signal's components;
- ϕ_i with $i = \{C, F_k, R_m\}$ are the phases of the signal's components;

After performing several tests, the following values were selected:

- $A_C = 2$, $A_F = 1.5$, $A_R = 0.75$. The reason for these values is to allow better visual identification of the spectral peaks associated to each flow direction, and to evaluate, for each strategy, if the relative amplitudes are maintained.
- For the frequency values, the following values were chosen
  - For the forward flow: 500 Hz, 5 kHz, 20 kHz and 45 kHz
  - For the reverse flow: 500 Hz, 5 kHz, 10 kHz and 35 kHz
- The common frequency values $\{500\ Hz, 5\ kHz\}$ will evaluate if the forward flow and reverse flow having equal frequency components will be properly separated, preserving the relative amplitudes. The 500 Hz value will also serve as an indication of the influence of the DC notch filter.
- The distinct frequency values $\{20\ kHz, 45\ kHz\}$ for the forward flow and $\{10\ kHz, 35\ kHz\}$ for the reverse flow, will enable detection if proper flow separation is made and if this separation leaves any *residual* peaks, i.e, if peaks at frequencies $\{10\ kHz, 35\ kHz\}$ will be present in the forward flow or if peaks $\{20\ kHz, 45\ kHz\}$ will be present in the reverse flow.
- Since the lowpass FIR filter will have a -3 dB cutoff frequency of approximately 36.5 kHz, with stopbands attenuation of approximately 60 dB, 80 dB and 120 dB, the value of 45 kHz will evaluate the efficiency of the filter in removing this peak.

- all of the signal's component phases ϕ_i with $i = \{C, F_k, R_m\}$ are considered zero. As a consequence (see Appendix D) a DC component will be present in the I component.

The magnitude spectrum of signal used to test the various strategies presented in subsection 3.3.3, is shown in figure 4.14

Experimental Signal

For testing the different approaches in a practical basis it was considered a FM signal. The message signal was a 1 V amplitude 13 kHz sine wave, which was used to frequency modulate a 1 V amplitude 8 MHz sinusoidal carrier. The FM signal presented a modulation index [12] β of 2. According to [14], 98% of the total bandwidth can be evaluated by the Carson's rule.

$$B_T = 2(\beta + 1)B \tag{4.2}$$

where B_T is the bandwidth of the FM modulated signal and B is the bandwidth of the message signal, which in this case has the value of 13 kHz.

Given (4.2) the expected bandwidth of the FM modulated signal is of 78 kHz, with carrier and major sideband components distributed according to figure 4.15. The ordinate of this graph presents the value of the Bessel function $J_n(\beta)$ [14], instead of the magnitude of each component in the spectrum.

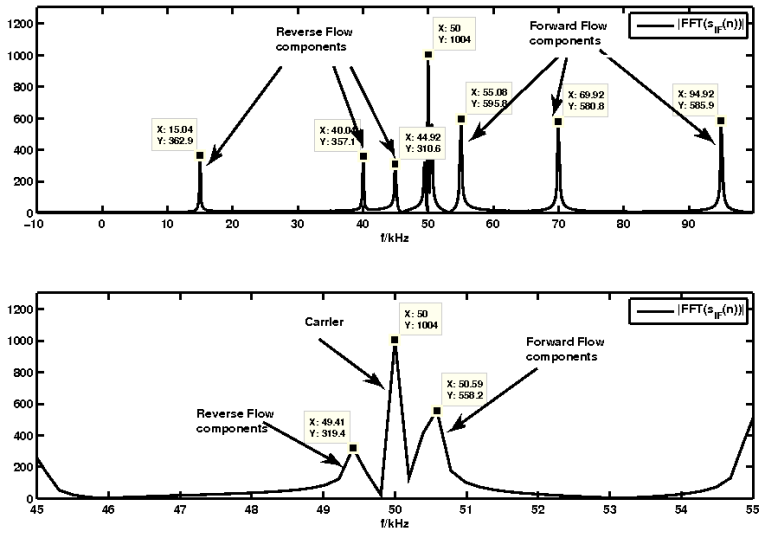

Figure 4.14: Magnitude spectrum of signal used to test the various strategies presented in subsection 3.3.3. The bottom figure is a zoom of the top figure, showing only frequency components from 45 kHz to 55 kHz.

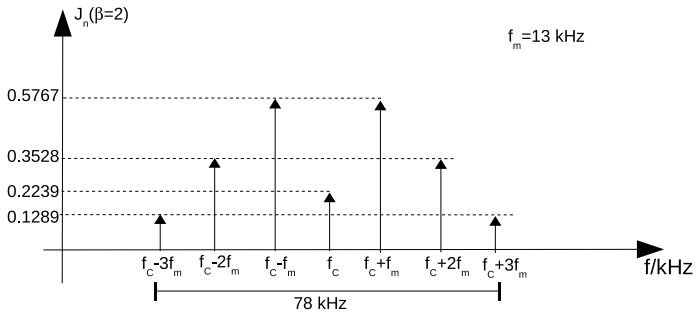

Figure 4.15: Expected carrier and sideband components distribution for a sinusoidal carrier modulated by a sinusoidal signal, with $\beta = 2$ [14]. In the figure f_c is the carrier frequency

4.3.2 BPS Frequency Determination

Before selecting the so called experimental signals (see subsection 4.3.1), it was considered a signal with 90 kHz bandwidth. With this value the signal cannot be classified as a half-integer positioning nor integer positioning signal. But by adding a guard-band of 10 kHz, the signal centered at 8 MHz will have a 100 kHz bandwidth with $f_L = 7950\ kHz$ and $f_U = 8050\ kHz$. From section 3.2.2 it can be shown that

$$\begin{aligned} f_L &= \frac{2n+1}{2} \cdot (f_U - f_L) \\ \Leftrightarrow n &= \frac{\left[\frac{2f_L}{(f_U - f_L)}\right] - 1}{2} \\ \Leftrightarrow n &= 79 \end{aligned}$$

since n is integer the considered signal is half-integer positioning and can be processed with uniform bandpass sampling.

Changing the value of n in order to obtain a sampling rate capable of being applied by the ADC available and which will translate the spectrum to a lower frequency near 50 kHz, the value of $n = 67$ serves that purpose. Also, as stated in subsection 3.2.4 since n is odd no spectral inversion will occur.

Using $n = 67$ it can be shown that $240.298\ kHz \leq f_s \leq 240.909 kHz$, consequently $\Delta f_s = 610.5 Hz$. If we consider the mean value of the allowed sampling frequencies, the value to be used is $f_s = 240.6038\ kHz$.

Knowing the sampling frequency, the maximum bandwidth that the signal can have is equal to $\frac{f_s}{2} = 120.3\ kHz$. However the signal's components of interest have a 78 kHz bandwidth. So, using this sampling frequency and considering the 78 kHz bandwidth signal, the sampling frequency to be used in practice imposes a total guard-band of 42.3 kHz to be added.

From figure 4.15, if we assume that $f_C = 8\ MHz$ represents the analog continuous FM modulated signal, it is expected that when sampling the analog signal (with an allowed bandpass sampling rate) the shape of the spectrum will be the same as the one of the analog signal, except for the value f_C, which will take a lower value, consequence of the frequency shifting carried out by the bandpass sampling [52] [54] [55]-[57].

By applying equation (3.28) the value of f_C after the bandpass sampling is expected to be 60.1 kHz, if the carrier wave is exactly 8 MHz and the sampling rate 240.604 kHz.

4.3.3 Separation between Forward and Reverse Flow

The digital quadrature strategies studied and to be tested envisage better separation of the forward and reverse flow than the one achieved with analog solutions. A poor quadrature technique will create poorly separated forward and reverse flow signals. The major concern will be enabling easier and faster methods of detecting changes on the signal's bandwidth.

As a consequence of this objective, the evaluation of the quality of the quadrature components of the IF signal will be made observing the magnitude spectrum and the spectrograms of the forward and reverse flows. Therefore evaluation of each digital quadrature technique will be an indirect one.

Like previously stated, the efficiency of the digital quadrature techniques is evaluated considering their directional flow separation. There are many strategies to obtain directional Doppler digital techniques [48]. From the available techniques it was selected to be used the phasing-filter technique, implemented according to figures 4.16 and 4.17, for approaches $\{1, 3, 4\}$ and $\{2, 5\}$, respectively. The Hilbert Tranform, denoted by *Hilb* block, was implemented as describe later in subsection 4.3.4.

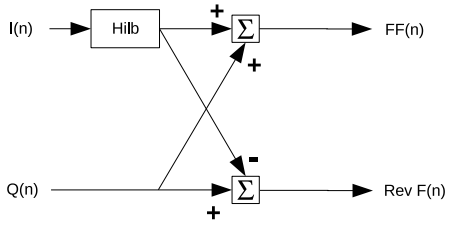

Figure 4.16: Quadrature to Directional format using digital approaches $\{1, 3, 4\}$ (Adapted from [48]), where $FF(n)$ denotes forward flow signal and *Rev* $F(n)$ denotes reverse flow signal

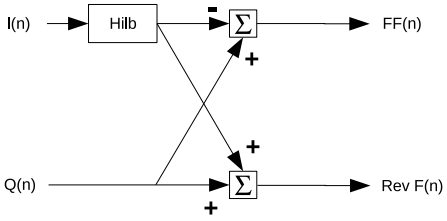

Figure 4.17: Quadrature to Directional format using digital approaches $\{2, 5\}$ (Adapted from [48]), where $FF(n)$ denotes forward flow signal and *Rev* $F(n)$ denotes reverse flow signal

4.3.4 Filters to be Used

Before presenting the results, a few comments about the filters to be used must be made.

With exception of the FIR filters used in Approach 5, for all other approaches, the lowpass FIR filters employed were designed using optimization algorithm known as the Remez exchange algorithm (using *Matlab* remez *Parks-McClellan optimal equiripple FIR filter design* routine). Details on the usage of such routine is well documented in [4].

Given the fact that the FIR filter's order to fulfil subject to the experimental constraints depend on the sampling frequency used. All detailed FIR filter characteristics charts (impulse response, absolute amplitude, relative absolute amplitude in dB, phase response, group delay and phase delay) and impulse response coefficients are presented in appendix F.

What is important to retain is that the filter design of all Parks-McClellan lowpass FIR filters aims the following particular specifications:

- Maximum passband ripple amplitude of 1 dB;
- Stopband attenuation of 60 dB, 80 dB or 120 dB;
- Passband edge frequency equal to 35 kHz, and
- Stopband edge frequency equal to 45 kHz;

With Approach 5, the window method for FIR was used in the *Matlab* routine *fir1*. To the test signal the Kaiser and Blackman windows were used. The cutoff frequency defined was the mean value between the passband edge frequency and stopband edge frequency defined for the Parks-McClellan lowpass FIR filters to be used. However for the so called experimental signals only the Kaiser window was used, based on the comments presented in the conclusion of [66], and on the comments found in [67]. According to [67], good results (low phase error) are obtained with Kaiser window if the window's parameter have a high value. A 9.5 Kaiser parameter presents good blood flow separation results.

In this case the sampling frequency is only used to determine the cutoff frequency from the passband and stopband edge frequencies.

DC notch filter

All the filters employed presented an attention coincident with the phase distortion that they would introduce. Consequently, whenever possible, FIR filters were used. However, with the DC notch filter the linear phase requirement could not be attended, as justified next.

The choice for DC notch filter must take into account, among other things, how narrower is the filter's band. For a notch FIR filter a comb FIR was used. According to [82]: << The narrowest possible notch bands are exhibited by comb FIR filters optimal in the Chebyshev sense with equiripple behaviour of the frequency response in the passbands.>>. The comb FIR filter's impulse response coefficients were obtained with the code presented in Table II of [82], considering the width of the notch bands to be 0.01 rad, and a maximal attenuation on the passbands of -3.397 dB. The order of this filter is 933. Making the attenuation of the passbands closer to zero drastically increases the filter order.

For an IIR filter DC notch, it was used the filter defined by (4.3) (see [7]), with $\alpha = 0.995$.

$$H(z) = \frac{1 - z^{-1}}{1 - \alpha z^{-1}} \tag{4.3}$$

Lets compare the two DC notch filters above mentioned.

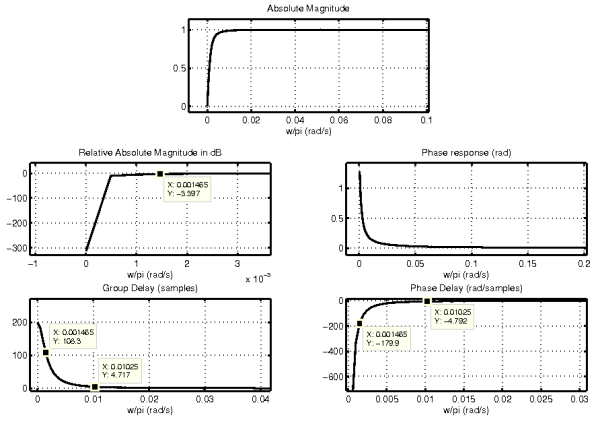

Figure 4.18: IIR allpass notch filter used, defined by (4.3) with $\alpha = 0.995$

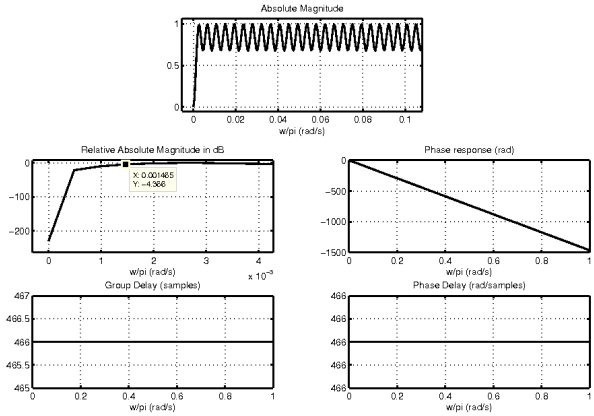

Figure 4.19: Comb FIR filter used for comparison with the allpass IIR filter

A given signal with DC component was filtered by both filters. The results are presented in figures 4.20, were the signal was filtered by the IIR allpass notch filter, and figure 4.21, were the signal was filtered by the Comb FIR filter.

As previously stated only FIR filter up to 100 coefficients would be used in this thesis. For that reason in all digital quadrature techniques used, the DC frequency components were removed with an IIR DC notch filter. Also, from figure 4.20 it can be seen that frequency components of the signal near DC are not significantly attenuated.

If the value of α in (4.3) was increased to 0.999, for example, the group and phase delay at the lower

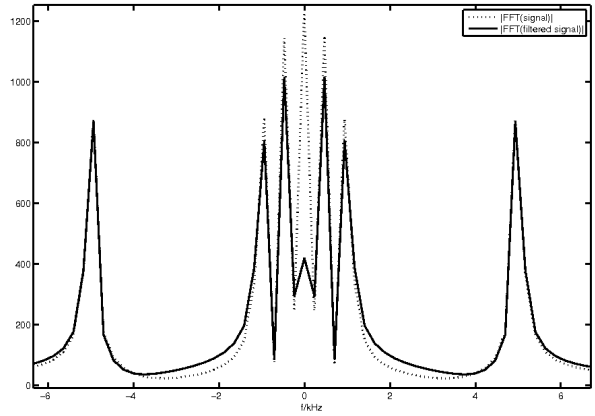

Figure 4.20: Magnitude spectra of an original signal with DC component and the filtered version by the IIR allpass notch filter

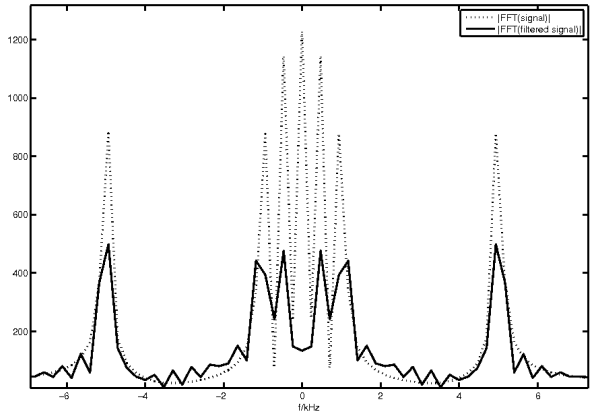

Figure 4.21: Magnitude spectra of an original signal with DC component and the filtered version by the Comb FIR filter

frequencies was significantly larger. By experiments it has been observed that a good equilibrium between DC attenuation and group and phase delay at the lower frequencies was obtained with $\alpha = 0.995$.

Allpass Filters

In the case of the approach 4 (subsection 3.3.3), the central block associated with the quadrature of the two signals are two allpass digital filters, presenting a phase difference of $\frac{\pi}{2}$ between them in the bandwidth of interest.

To obtain the zeros and poles of the impulse response of these filters, it was used the algorithm 1 presented in [74].

The allpass filters' orders employed were of $N = \{5, 15, 30\}$, using $100 \cdot N$ points to obtain the least square sense minimization. For all the filters the bandwidth varied from 0.03π to 0.94π.

The details of each of these used filters are presented in appendix F.

Hilbert Transform

In the specific case of approach 3 (subsection 3.3.3), the Hilbert Transform presented in the block diagram of figure 3.18, denoted by *Hilb* block, was implemented using *Matlab hilbert* function. Since this function returns the discrete-time analytic signal containing the original signal (real part) and the imaginary part (the Hilbert Transform of the original signal) the *Matlab* routine *imag* was used to retrieve only the imaginary component.

The same methodology was used in figures 4.16 and 4.17 of subsection 4.3.3

Chapter 5

Results Obtained with the 5 Approaches Implemented

5.1 Results of the Different Demodulator Circuitry Approaches Using the Developed Testing Signals

5.1.1 Introduction

In this section, the approaches presented in subsection 3.3.3 are applied to the signal called test signal, described in subsection 4.3.1. Using this signal, the evaluation of the efficiency of each technique is possible, since the used signal has frequency components at known frequencies and with different amplitudes associated with forward blood flow direction and reverse blood flow direction. From the chosen frequencies it is expected to evaluate the efficiency of each technique is terms of how good the blood flow separation is made, i.e, the relative amplitudes of the forward blood flow and reverse blood flow, as well as the correct frequency separation.

The evaluation of the behaviour of each approach when the signal has a noise component is also made adding random gaussian noise with a null mean and 30 mV variance.

This section is composed only by figures, whose legends contain some concluding aspects.

5.1.2 Approach 1: signal without noise

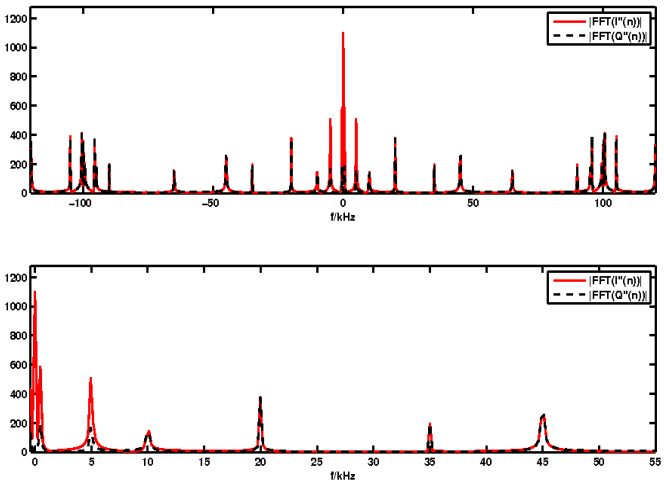

Figure 5.1: Magnitude spectra of the quadrature signals $I"(n)$ and $Q"(n)$ obtained when the IF signal is multiplied by a cosine and a sine wave with frequency equal to the IF signal's carrier frequency. The bottom figure is a zoom of the top figure, showing only frequency components from DC to 55 kHz.

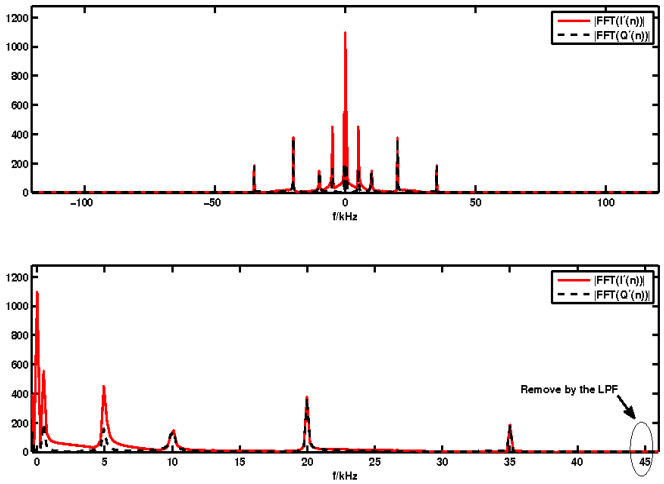

Figure 5.2: Magnitude spectra of the quadrature signals $I'(n)$ and $Q'(n)$, which result on the filtering of the signals whose spectrum is presented in figure 5.1 by the lowpass FIR filter in figure F.1. The bottom figure is a zoom of the top figure, showing only frequency components from DC to 45 kHz.

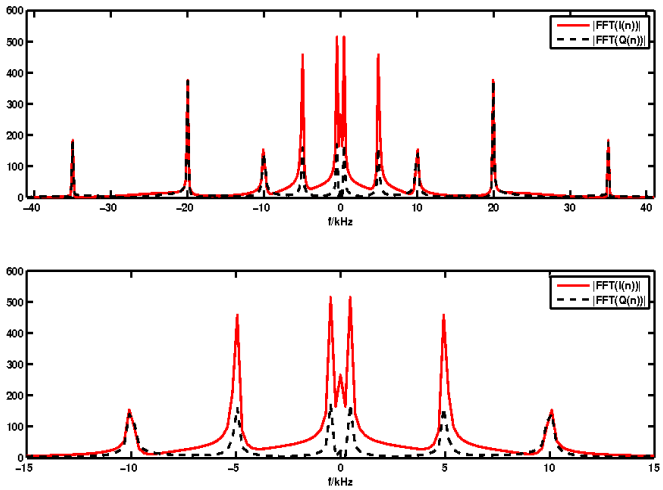

Figure 5.3: After the application of the DC notch filter of figure 4.18, the DC component is attenuated. The bottom figure is a zoom of the top figure, showing only frequency components from -15 kHz to 15 kHz.

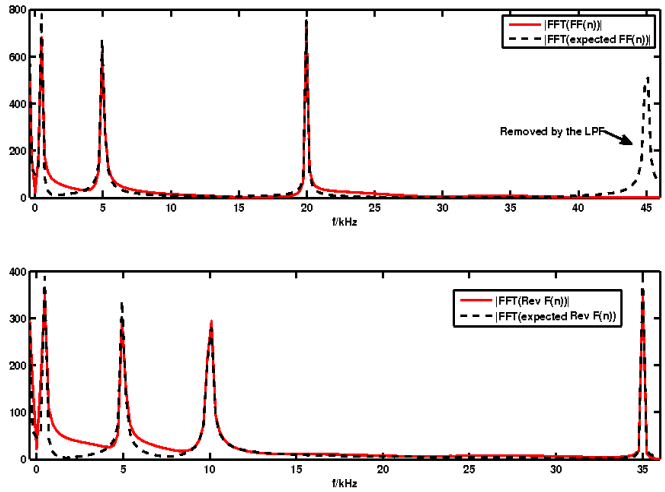

Figure 5.4: Comparison between the obtained and expected magnitude spectra for the forward (top figure) and reverse (bottom figure) flow signals. As desired the 45 kHz component has been removed by the filtering.

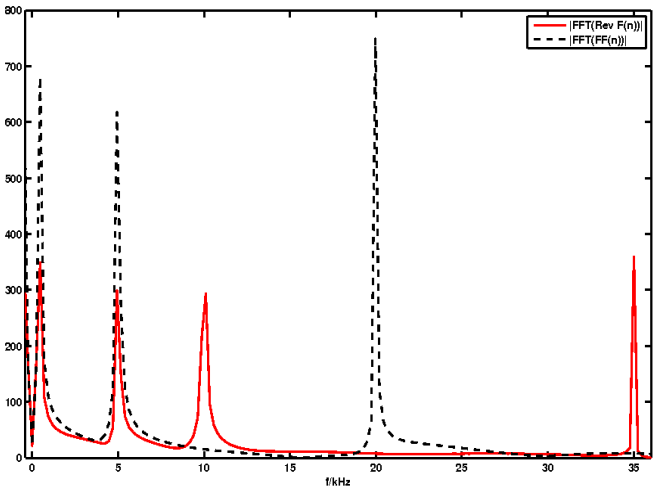

Figure 5.5: Comparison between the obtained forward and reverse flow signals magnitude spectra.

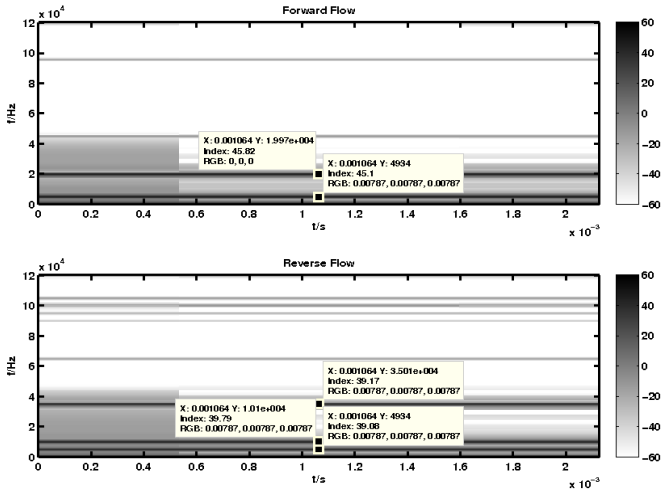

Figure 5.6: Spectrogram of the obtained forward and reverse flow signals

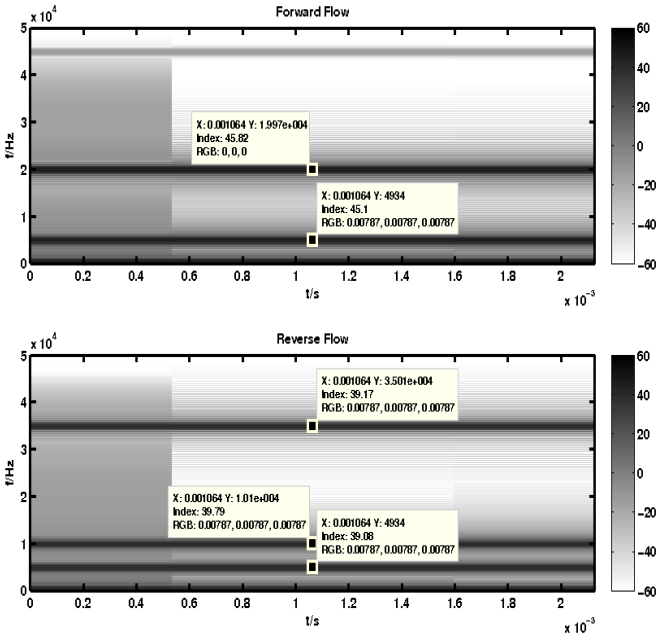

Figure 5.7: Zoom of figure 5.6 on the important frequency range

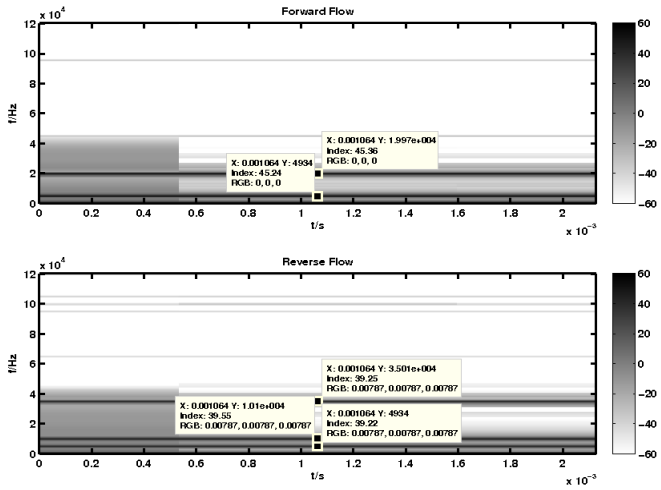

Figure 5.8: Spectrogram of the obtained forward and reverse flow signals, if the lowpass FIR filter used has 80 dB stopband attenuation (figure F.2)

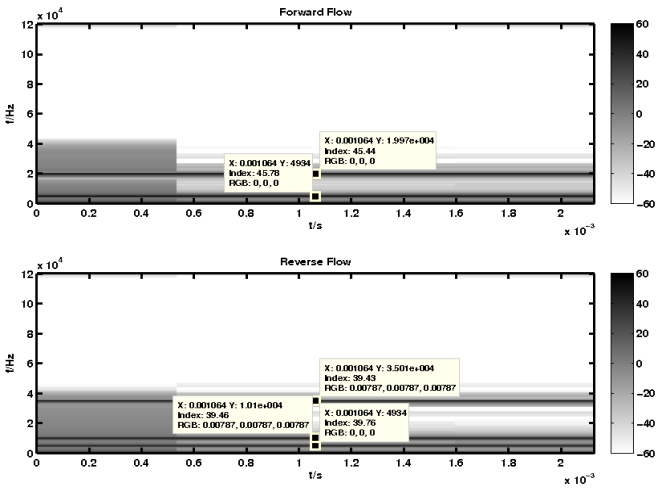

Figure 5.9: Spectrogram of the obtained forward and reverse flow signals, if the lowpass FIR filter used has 120 dB stopband attenuation (figure F.3)

5.1.3 Approach 1: signal with noise

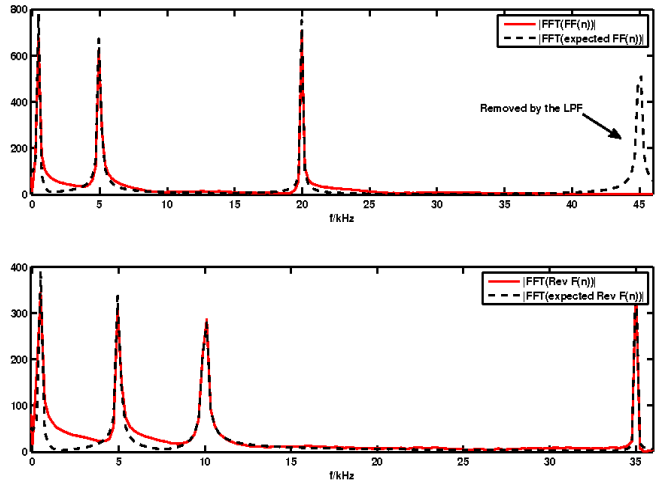

Figure 5.10: Comparison between expected (without noise) and the obtained (with noise) magnitude spectra for the forward (top figure) and reverse (bottom figure) flow signals.(Lowpass FIR filter of figure F.2 was used).

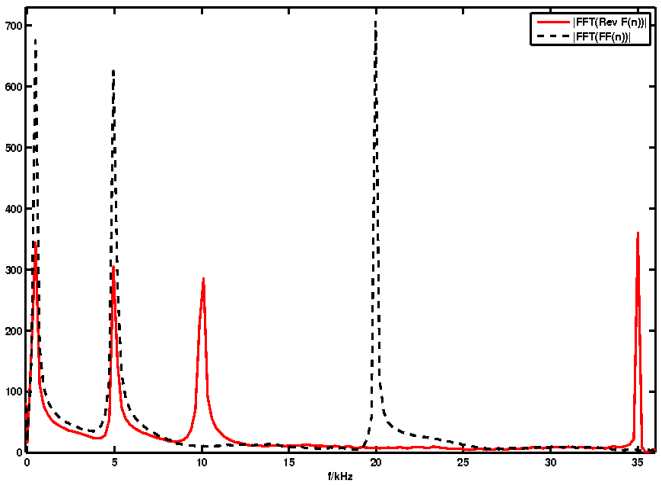

Figure 5.11: Comparison between the obtained forward $FF(n)$ and reverse $Rev\ F(n)$ flow signals magnitude

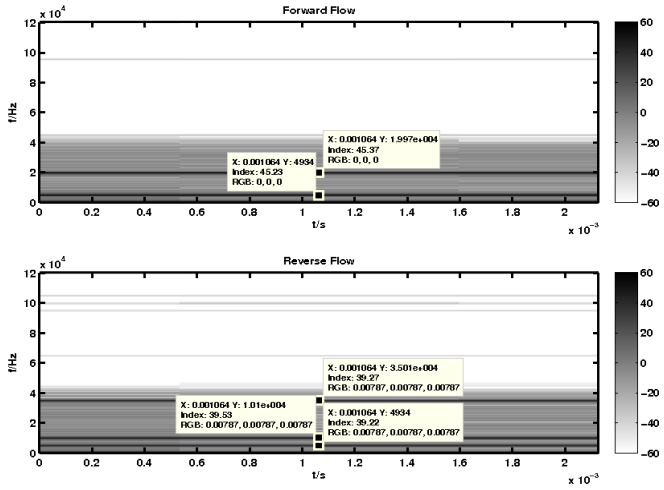

Figure 5.12: Spectrogram of the obtained forward and reverse flow signals

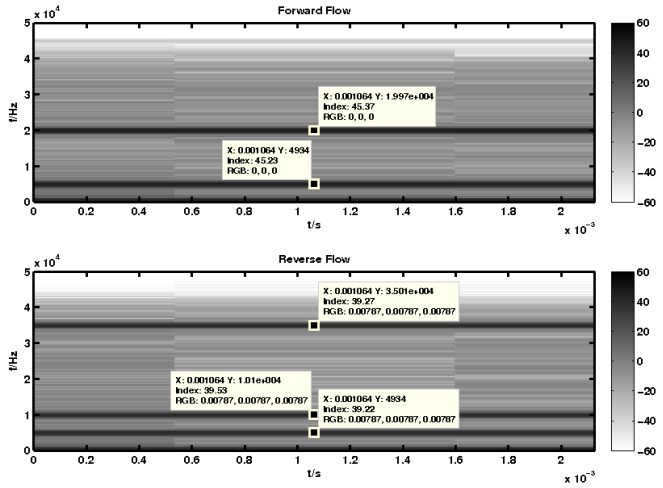

Figure 5.13: Zoom of figure 5.12 on the important frequency range

5.1.4 Approach 2: signal without noise

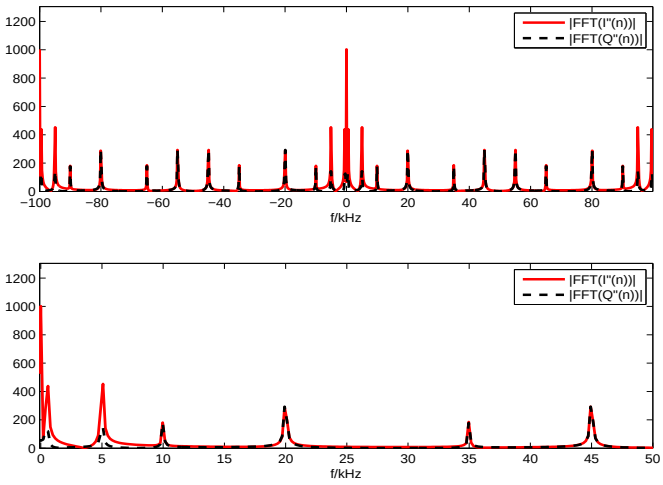

Figure 5.14: Magnitude spectra of the quadrature signals $I"(n)$ and $Q"(n)$ obtained when the IF signal is multiplied, respectively, by sequences $+1, 0, -1, 0$ and $0, 1, 0, -1$ [6]. The bottom figure is a zoom of the top figure, showing only frequency components from DC to 50 kHz.

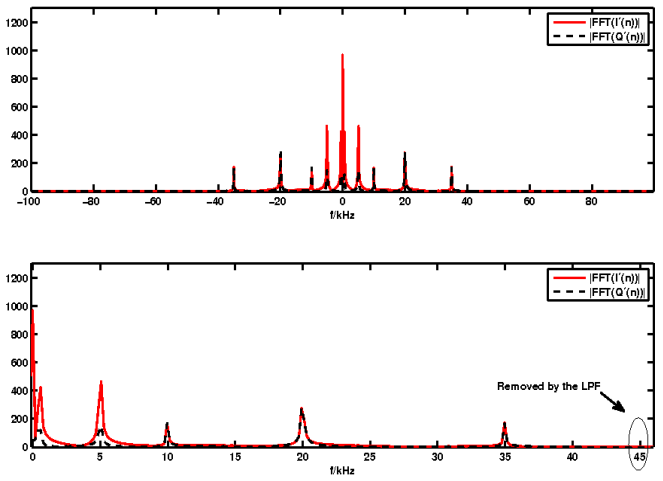

Figure 5.15: Magnitude spectra of the quadrature signals $I'(n)$ and $Q'(n)$, which result on the filtering of the signals whose spectra are presented in figure 5.14 by the lowpass FIR filter in figure F.5. The bottom figure is a zoom of the top figure, showing only frequency components from DC to 45 kHz.

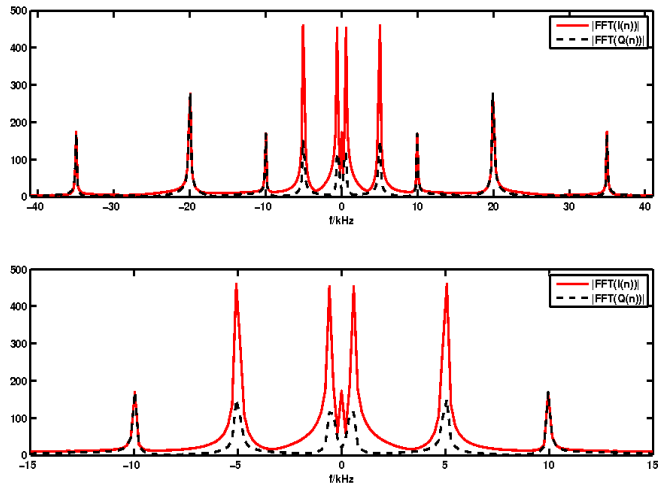

Figure 5.16: After the application of the DC notch filter of figure 4.18, the DC component is attenuated. The bottom figure is a zoom of the top figure, showing only frequency components from -15 kHz to 15 kHz.

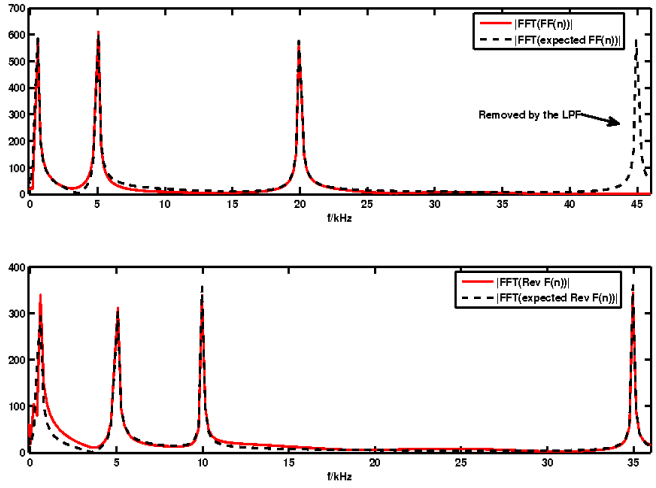

Figure 5.17: Comparison between the obtained and expected magnitude spectra for the forward (top figure) and reverse (bottom figure) flow signals. As desired the 45 kHz component has been removed by the filtering.

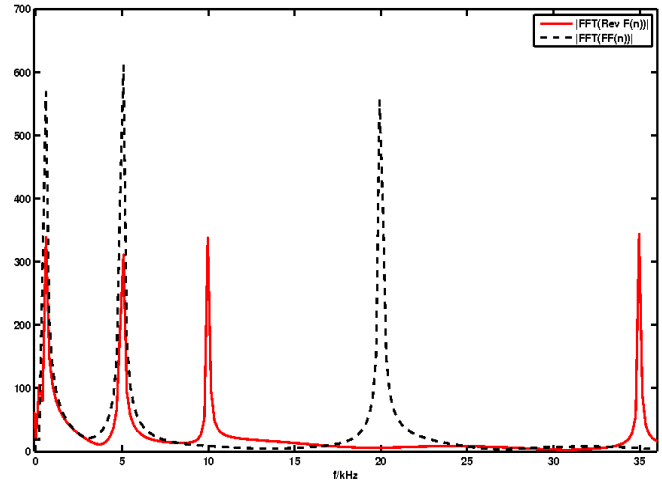

Figure 5.18: Comparison between the obtained forward $FF(n)$ and reverse $Rev\ F(n)$ flow signals magnitude spectra.

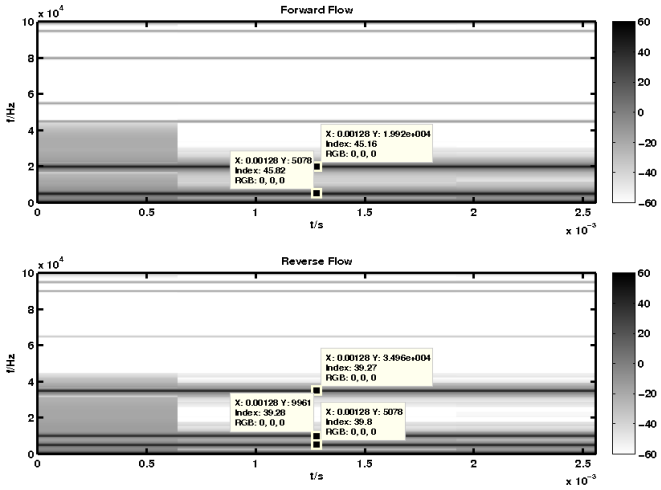

Figure 5.19: Spectrogram of the obtained forward and reverse flow signals.

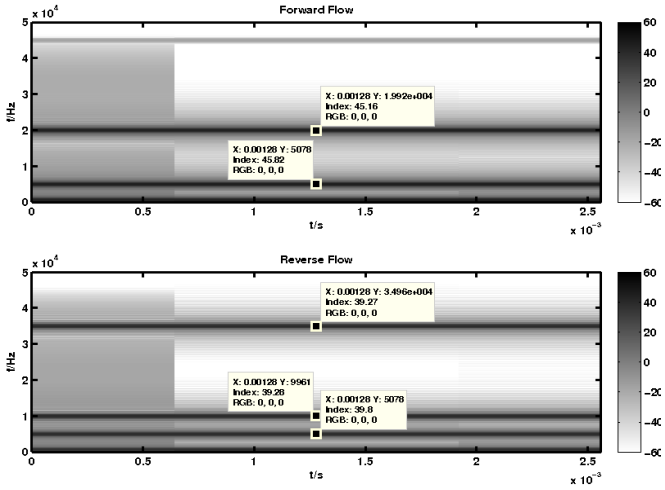

Figure 5.20: Zoom of figure 5.19 on the important frequency range

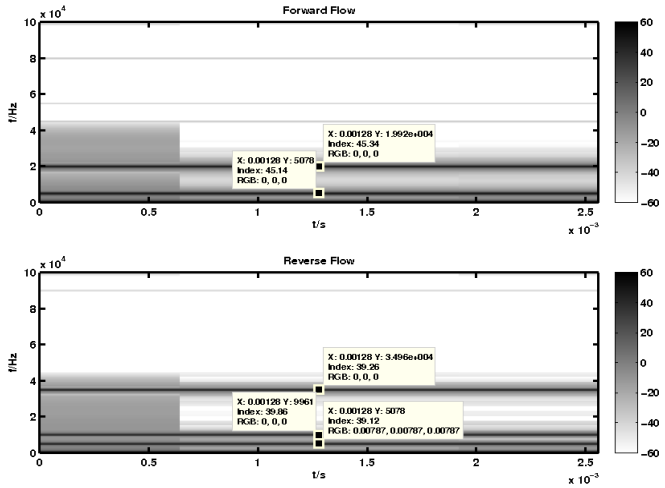

Figure 5.21: Spectrogram of the obtained forward and reverse flow signals, if the lowpass FIR filter used has 81 dB stopband attenuation (figure F.6)

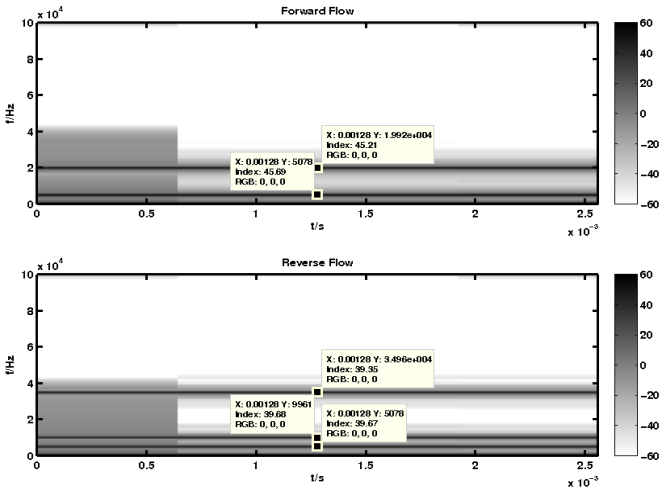

Figure 5.22: Spectrogram of the obtained forward and reverse flow signals, if the lowpass FIR filter used has 120 dB stopband attenuation (figure F.7)

5.1.5 Approach 2: signal with noise

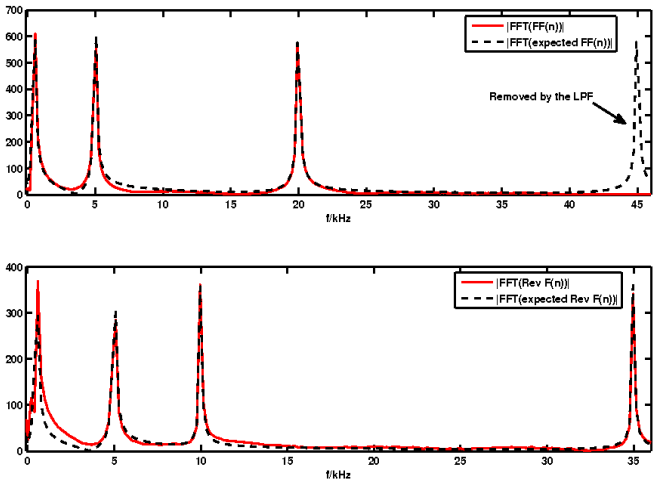

Figure 5.23: Comparison between expected (without noise) and the obtained (with noise) magnitude spectra for the forward (top figure) and reverse (bottom figure) flow signals. (Lowpass FIR filter of figure F.6 was used).

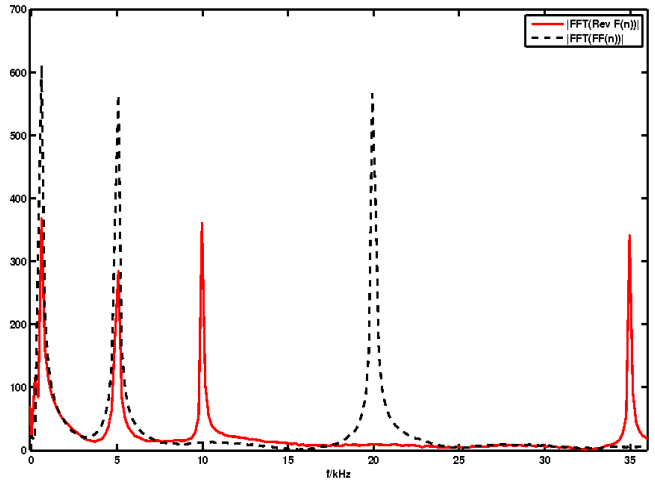

Figure 5.24: Comparison between the obtained forward $FF(n)$ and reverse $Rev\ F(n)$ flow signals magnitude spectra.

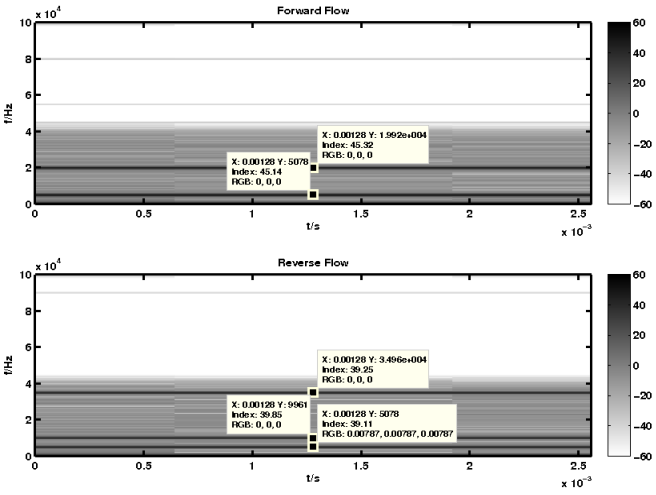

Figure 5.25: Spectrogram of the obtained forward and reverse flow signals

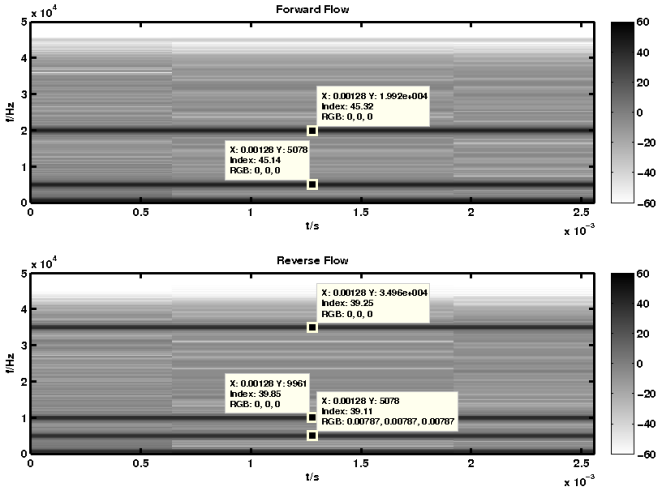

Figure 5.26: Zoom of figure 5.25 on the important frequency range

5.1.6 Approach 3: signal without noise

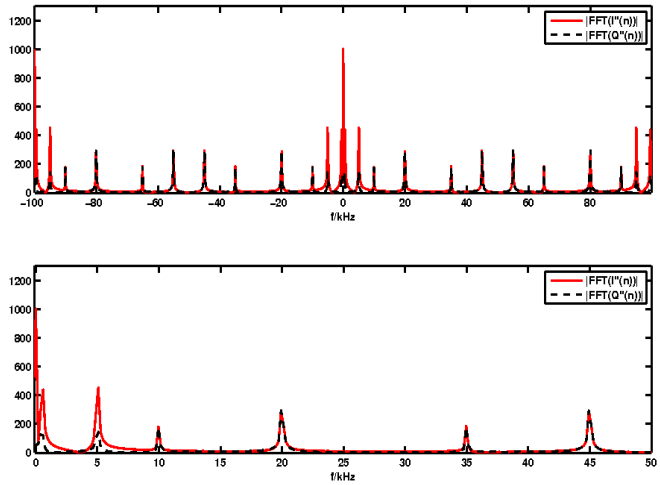

Figure 5.27: Magnitude spectra of the quadrature signals $I"(n)$ and $Q"(n)$. $Q"(n)$ is obtained by applying the Hilbert Transform to the IF signal.The bottom figure is a zoom of the top figure, showing only frequency components from DC to 50 kHz.

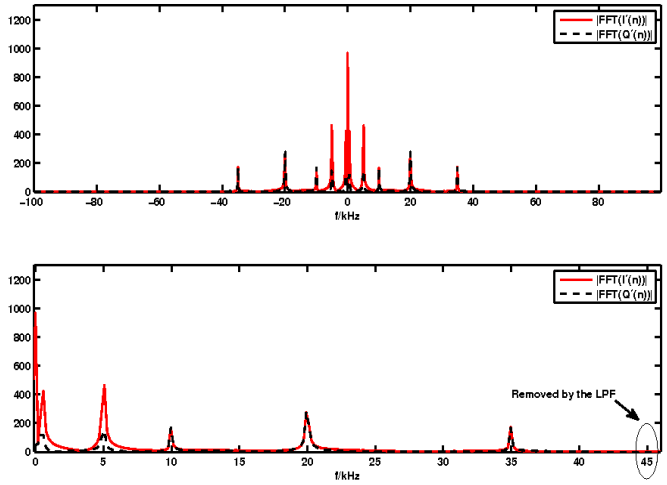

Figure 5.28: Magnitude spectra of the quadrature signals $I'(n)$ and $Q'(n)$, which result on the filtering of the signals whose spectra are presented in figure 5.27 by the lowpass FIR filter in figure F.5. The bottom figure is a zoom of the top figure, showing only frequency components from DC to 45 kHz.

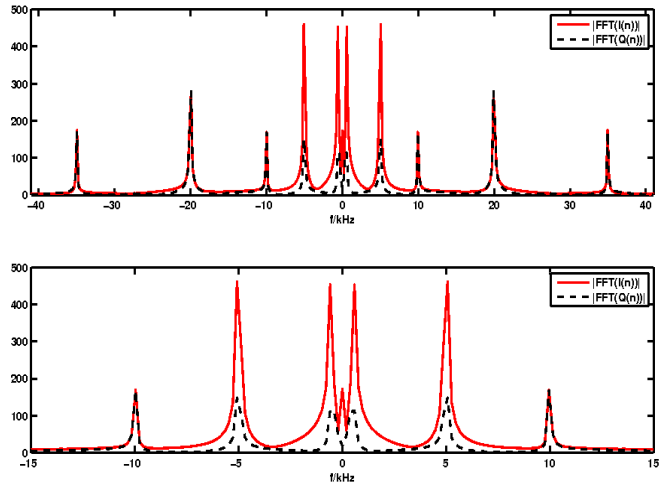

Figure 5.29: After the application of the DC notch filter of figure 4.18, the DC component is attenuated. The bottom figure is a zoom of the top figure, showing only frequency components from -15 kHz to 15 kHz.

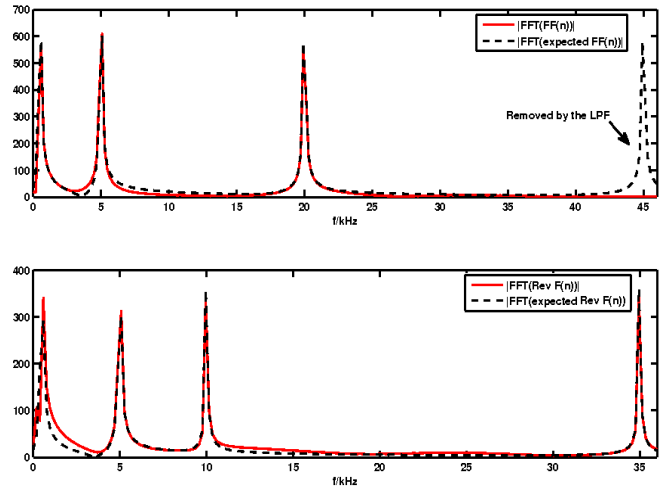

Figure 5.30: Comparison between the obtained and expected magnitude spectra for the forward (top figure) and reverse (bottom figure) flow signals. As desired the 45 kHz component has been removed by the filtering.

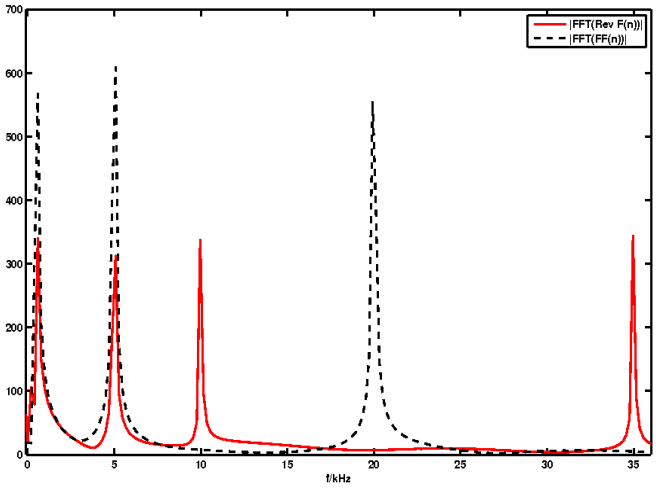

Figure 5.31: Comparison between the obtained forward $FF(n)$ and reverse $Rev\ F(n)$ flow signals magnitude spectra.

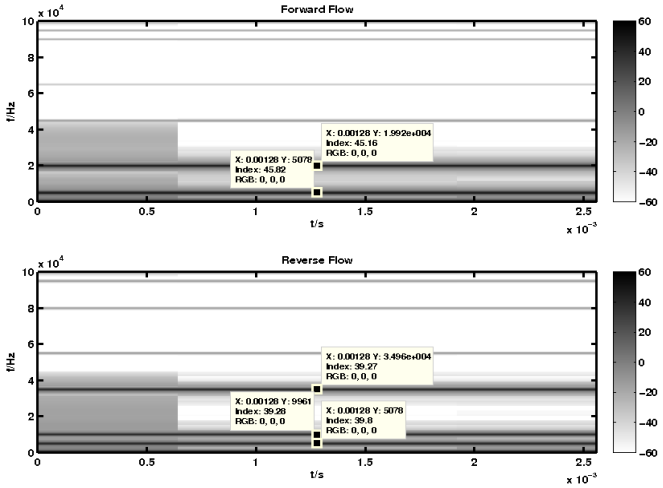

Figure 5.32: Spectrogram of the obtained forward and reverse flow signals

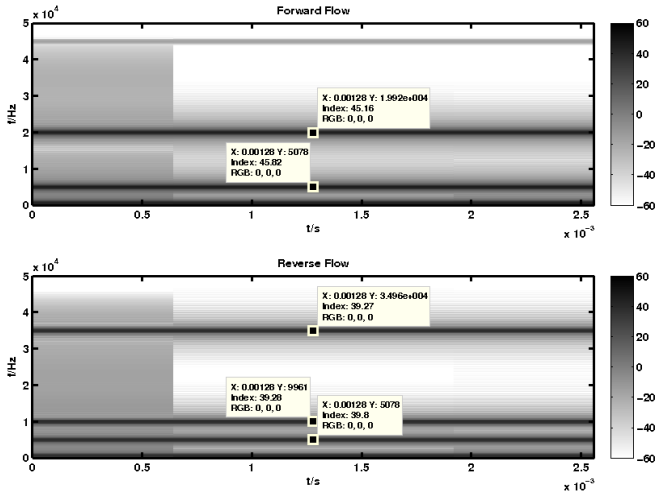

Figure 5.33: Zoom of figure 5.32 on the important frequency range

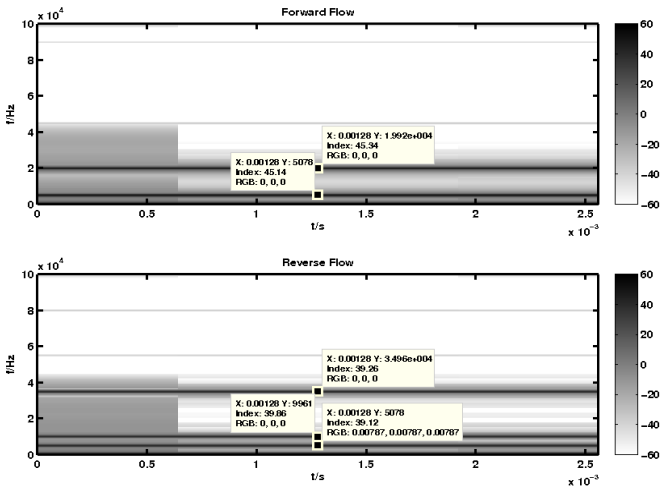

Figure 5.34: Spectrogram of the obtained forward and reverse flow signals, if the lowpass FIR filter used has 81 dB stopband attenuation (figure F.6)

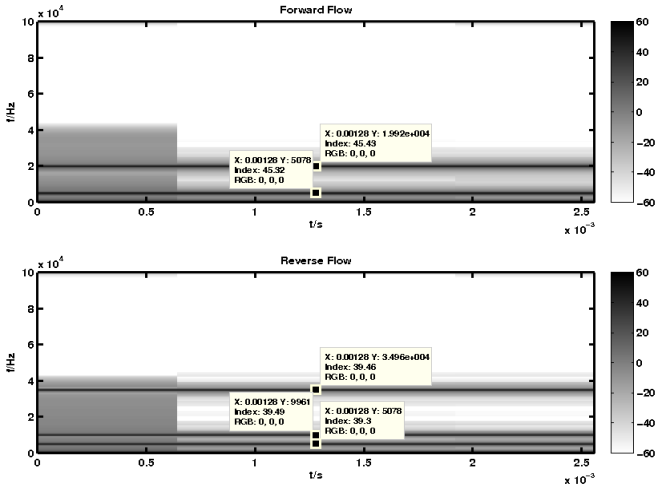

Figure 5.35: Spectrogram of the obtained forward and reverse flow signals, if the lowpass FIR filter used has 120 dB stopband attenuation (figure F.7)

5.1.7 Approach 3: signal with noise

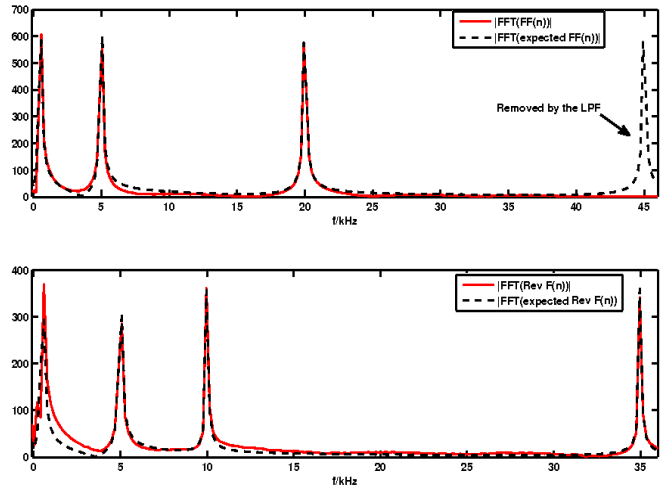

Figure 5.36: Comparison between expected (without noise) and the obtained (with noise) magnitude spectra for the forward (top figure) and reverse (bottom figure) flow signals. (Lowpass FIR filter of figure F.6 was used).

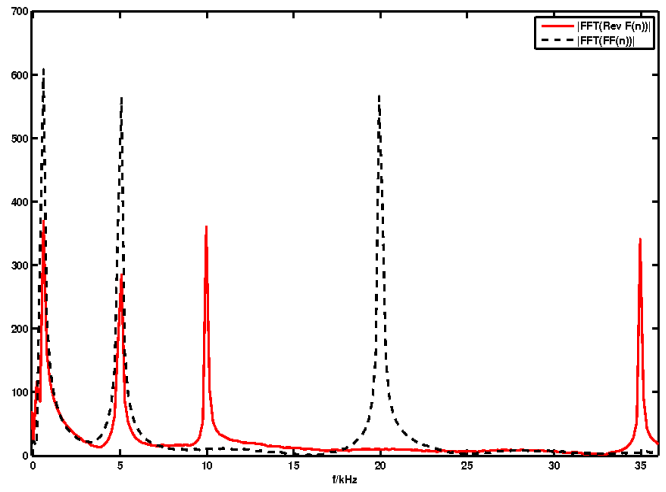

Figure 5.37: Comparison between the obtained forward $FF(n)$ and reverse $Rev\ F(n)$ flow signals magnitude spectra.

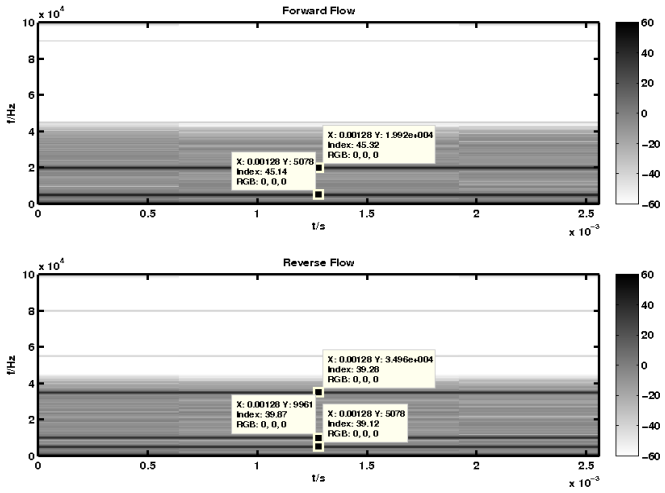

Figure 5.38: Spectrogram of the obtained forward and reverse flow signals

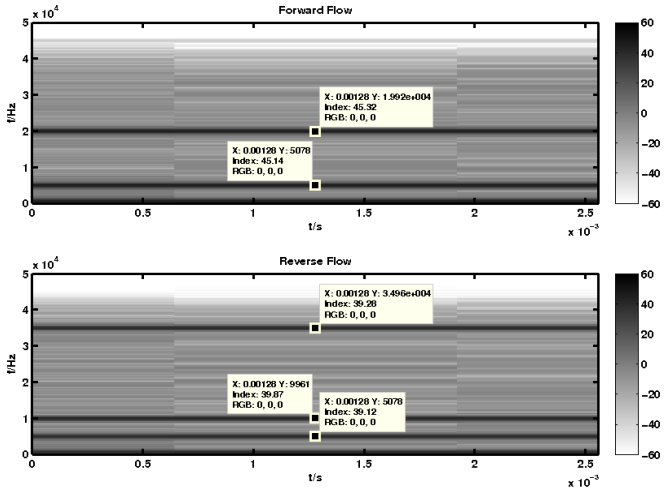

Figure 5.39: Zoom of figure 5.38 on the important frequency range

5.1.8 Approach 4: signal without noise

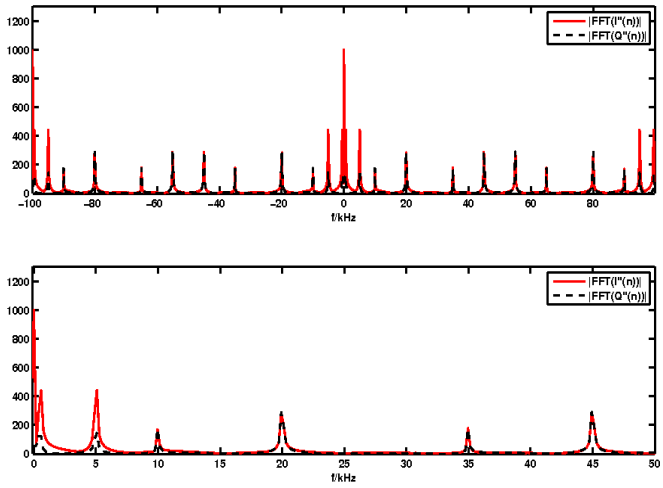

Figure 5.40: Magnitude spectra of the quadrature signals $I"(n)$ and $Q"(n)$. These are obtained by applying the 30th order allpass filters (figures F.39 and F.41, respectively). The bottom figure is a zoom of the top figure, showing only frequency components from DC to 50 kHz.

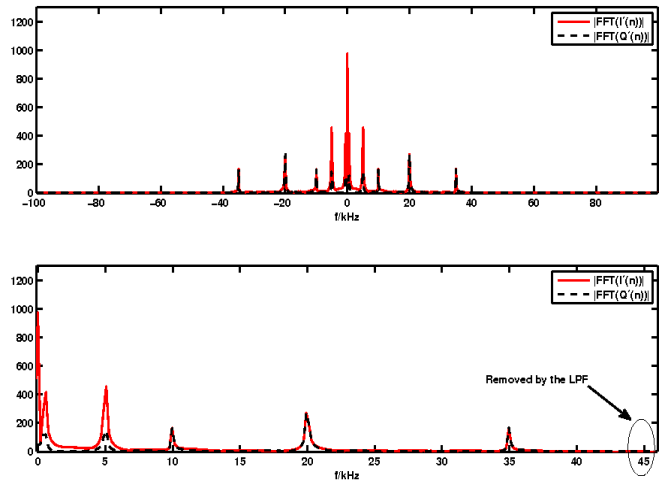

Figure 5.41: Magnitude spectra of the quadrature signals $I'(n)$ and $Q'(n)$, which result on the filtering of the signals whose spectra are presented in figure 5.40 by the lowpass FIR filter in figure F.5. The bottom figure is a zoom of the top figure, showing only frequency components from DC to 45 kHz.

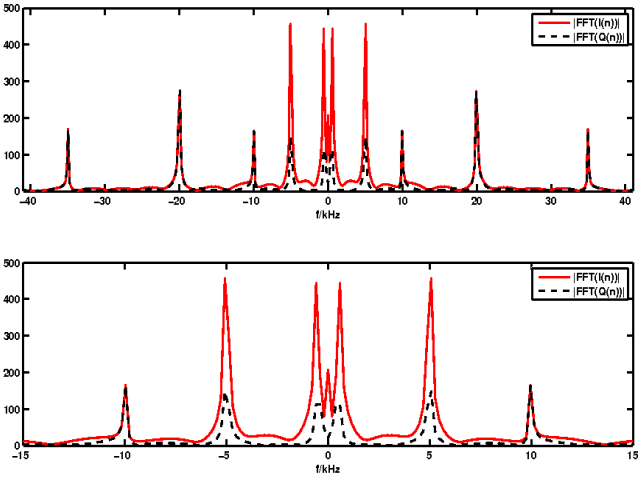

Figure 5.42: After the application of the DC notch filter of figure 4.18, the DC component is attenuated. The bottom figure is a zoom of the top figure, showing only frequency components from -15 kHz to 15 kHz.

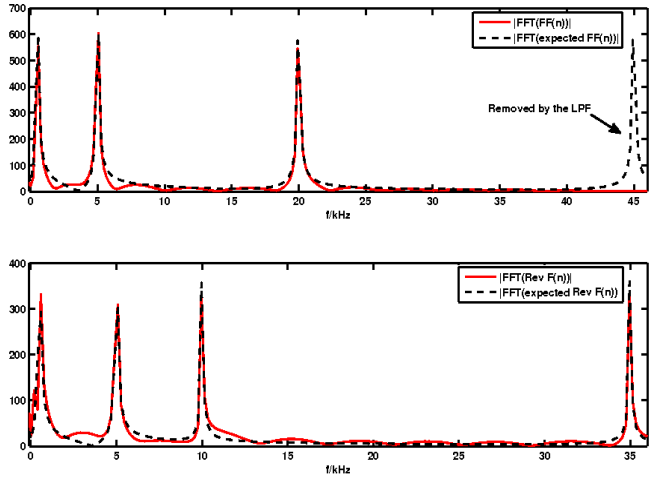

Figure 5.43: Comparison between the obtained and expected magnitude spectra for the forward (top figure) and reverse (bottom figure) flow signals (when used the 30th order allpass filters (figures F.39 and F.41). As desired the 45 kHz component has been removed by the filtering.

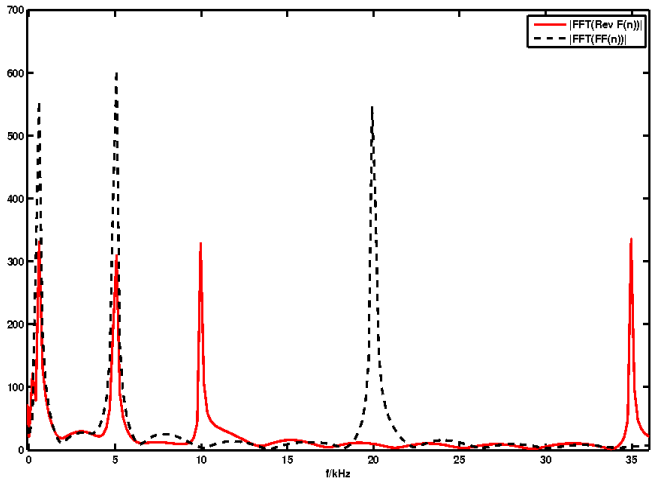

Figure 5.44: Comparison between the obtained forward $FF(n)$ and reverse $Rev\ F(n)$ flow signals magnitude spectra (when used the 30th order allpass filters (figures F.39 and F.41).

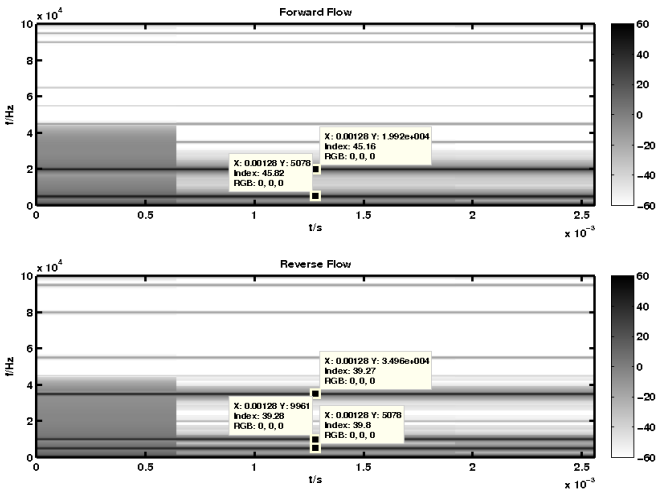

Figure 5.45: Spectrogram of the obtained forward and reverse flow signals (when used the 30th order allpass filters (figures F.39 and F.41)

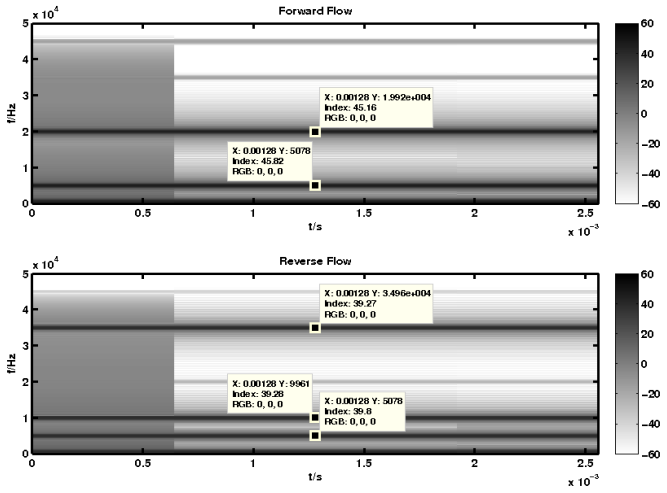

Figure 5.46: Zoom of figure 5.45 on the important frequency range

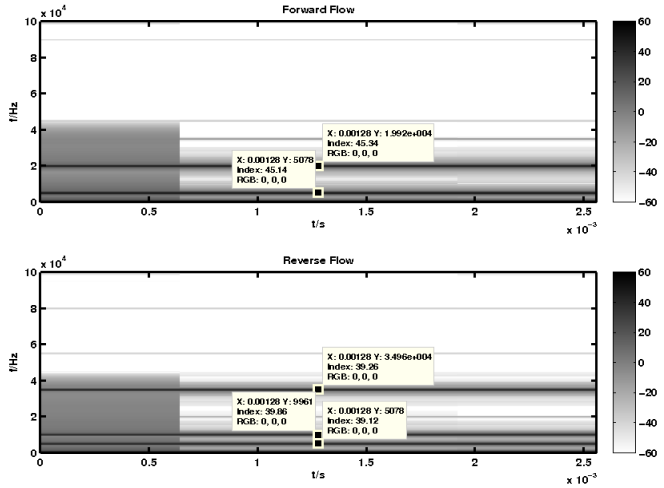

Figure 5.47: Spectrogram of the obtained forward and reverse flow signals, if the lowpass FIR filter used has 81 dB stopband attenuation (figure F.6), when used the 30th order allpass filters (figures F.39 and F.41)

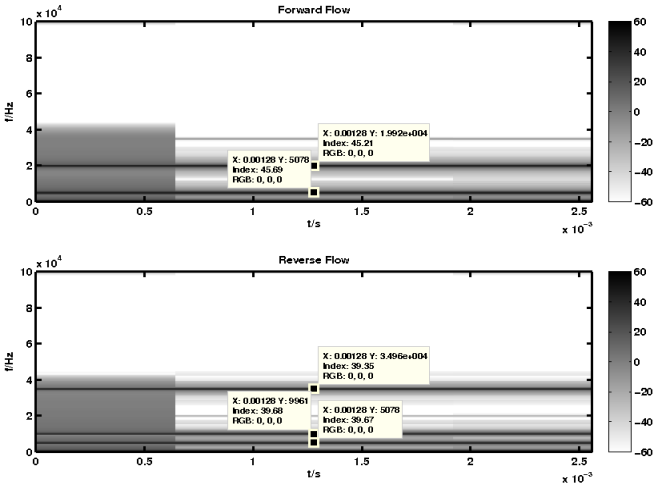

Figure 5.48: Spectrogram of the obtained forward and reverse flow signals, if the lowpass FIR filter used has 120 dB stopband attenuation (figure F.7), when used the 30th order allpass filters (figures F.39 and F.41)

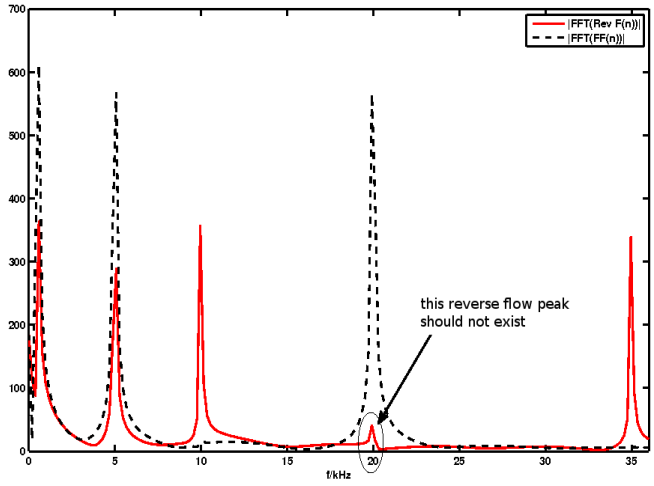

Figure 5.49: Comparison between the obtained forward $FF(n)$ and reverse $Rev\ F(n)$ flow signals magnitude spectra, if the lowpass FIR filter used has 81 dB stopband attenuation (figure F.6) and 5th order allpass IIR filters are used (figures F.31 and F.33)

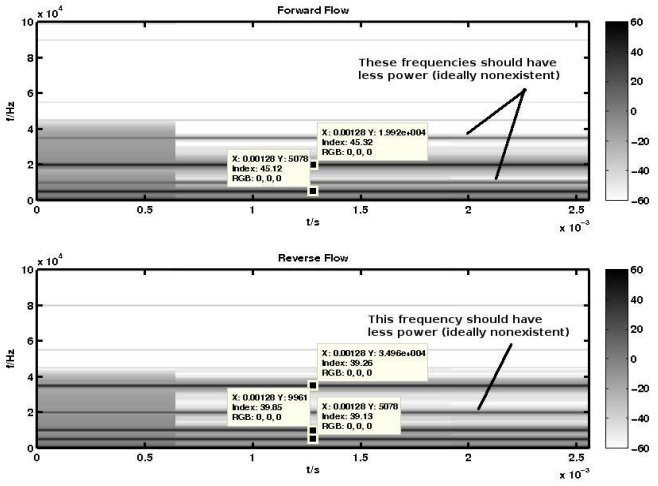

Figure 5.50: Spectrogram of the obtained forward and reverse flow signals, if the lowpass FIR filter used has 81 dB stopband attenuation (figure F.6) and 5th order allpass IIR filters are used (figures F.31 and F.33)

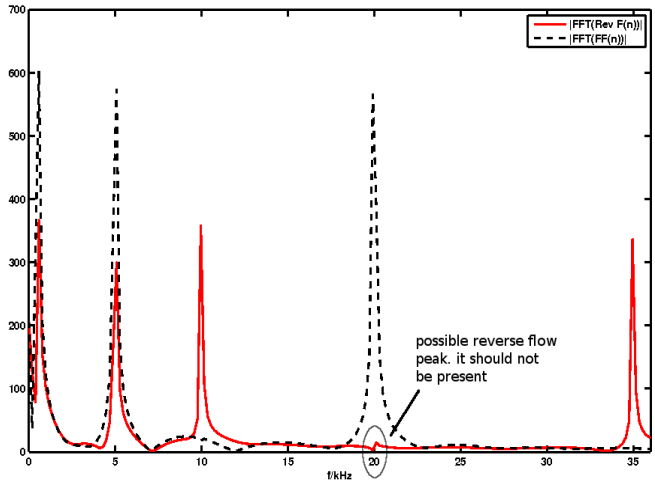

Figure 5.51: Comparison between the obtained forward $FF(n)$ and reverse $Rev\ F(n)$ flow signals magnitude spectra, if the lowpass FIR filter used has 81 dB stopband attenuation (figure F.6) and 15th order allpass IIR filters are used (figures F.35 and F.37)

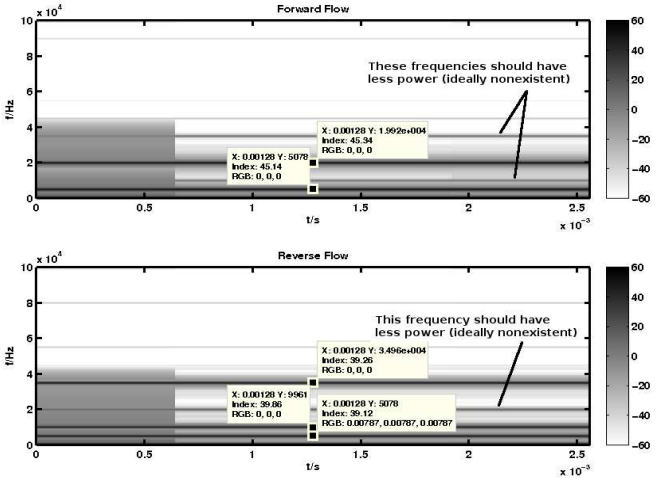

Figure 5.52: Spectrogram of the obtained forward and reverse flow signals, if the lowpass FIR filter used has 81 dB stopband attenuation (figure F.6) and 15th order allpass IIR filters are used (figures F.35 and F.37)

5.1.9 Approach 4: signal with noise

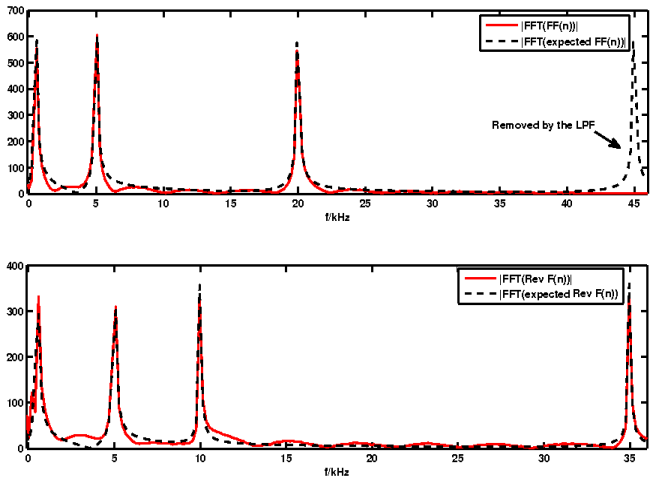

Figure 5.53: Comparison between expected (without noise) and the obtained (with noise) magnitude spectra for the forward (top figure) and reverse (bottom figure) flow signals.(Lowpass FIR filter of figure F.6 was used).

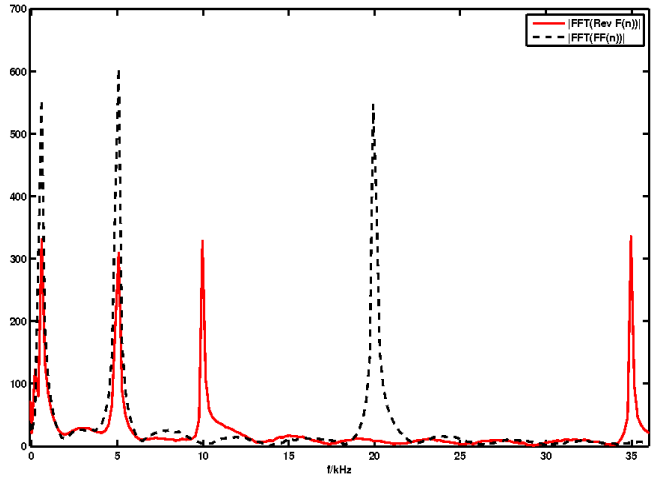

Figure 5.54: Comparison between the obtained forward $FF(n)$ and reverse $Rev\ F(n)$ flow signals magnitude

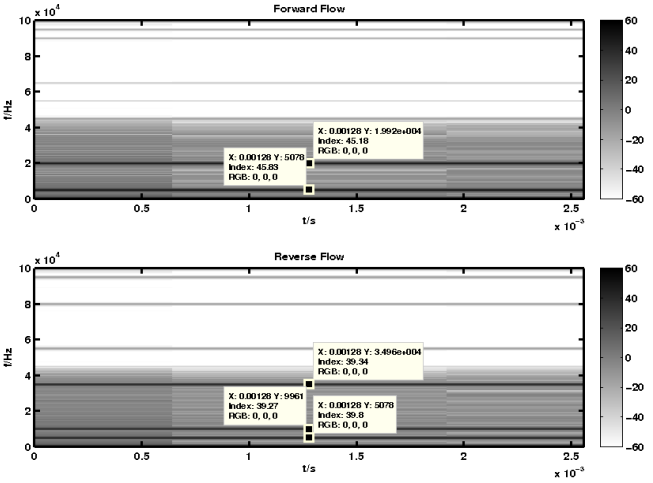

Figure 5.55: Spectrogram of the obtained forward and reverse flow signals

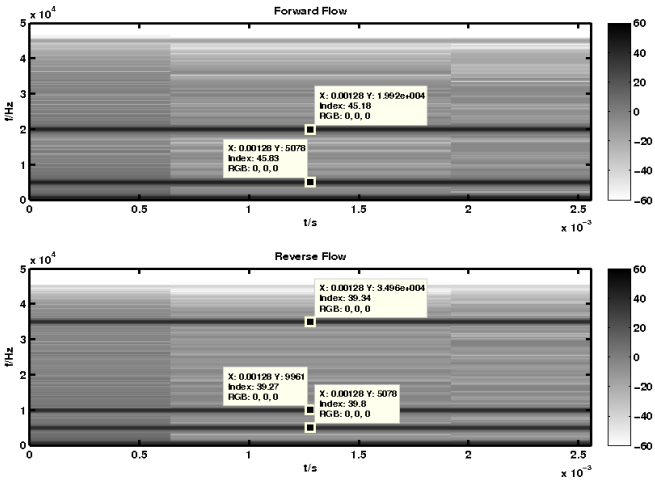

Figure 5.56: Zoom of figure 5.55 on the important frequency range

5.1.10 Approach 5: signal without noise

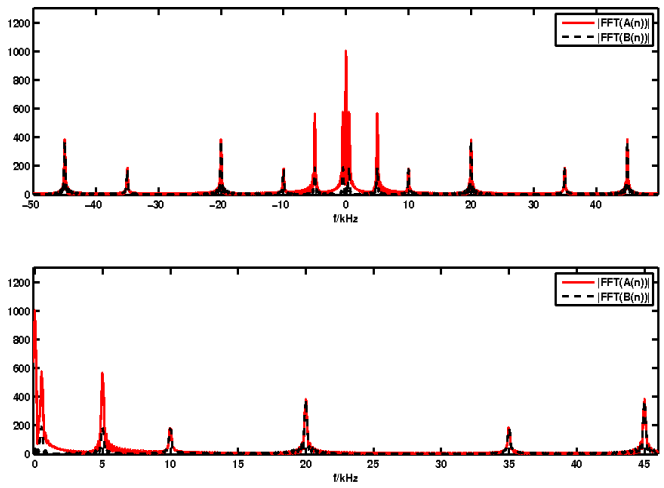

Figure 5.57: Magnitude spectra of the $A(n)$ and $B(n)$ signals. The bottom figure is a zoom of the top figure, showing only frequency components from DC to 45 kHz.

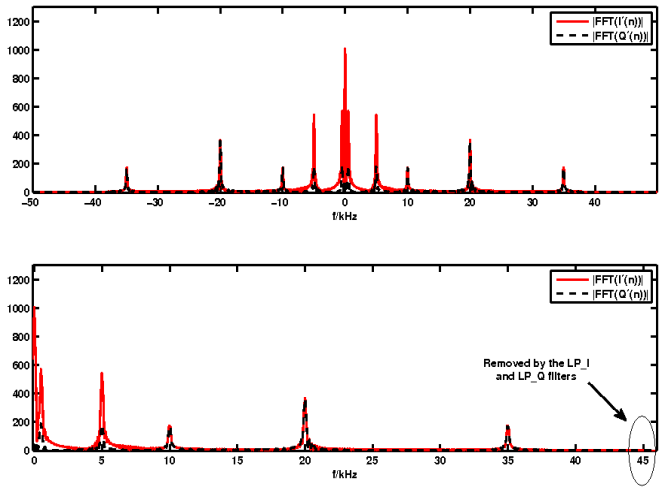

Figure 5.58: Magnitude spectra of the $I'(n)$ and $Q'(n)$ signals, obtained after application of filters in figures F.11 and F.12 respectively. The bottom figure is a zoom of the top figure, showing only frequency components from DC to 45 kHz.

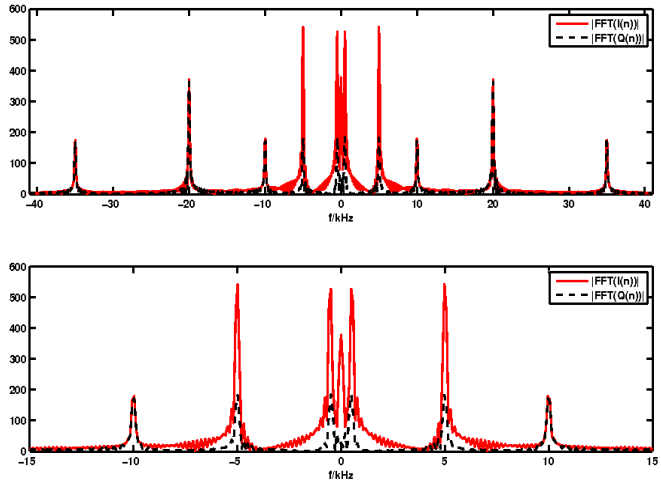

Figure 5.59: After the application of the DC notch filter of figure 4.18, the DC component is attenuated. The bottom figure is a zoom of the top figure, showing only frequency components from -15 kHz to 15 kHz.

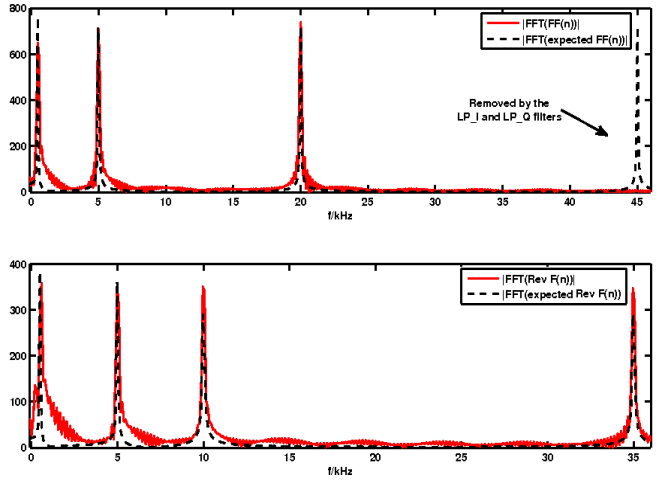

Figure 5.60: Comparison between the obtained and expected magnitude spectra for the forward (top figure) and reverse (bottom figure) flow signals. As desired the 45 kHz component has been removed by the filtering.

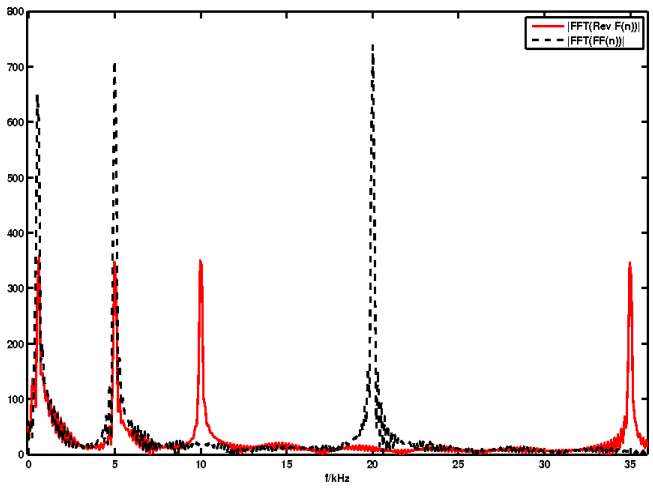

Figure 5.61: Comparison between the obtained forward $FF(n)$ and reverse $Rev\ F(n)$ flow signals magnitude spectra, when filters in figures F.11 and F.12 are used.

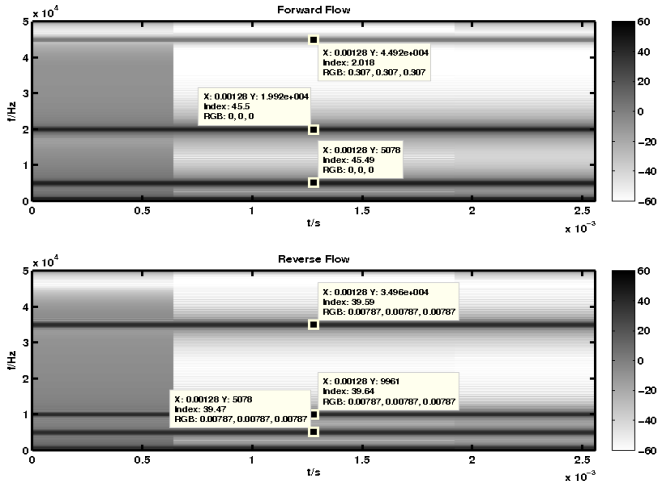

Figure 5.62: Spectrogram of the obtained forward and reverse flow signals , when filters in figures F.11 and F.12 are used

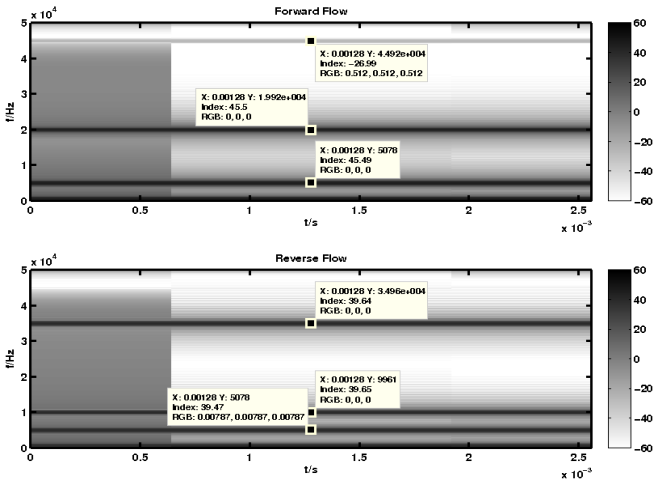

Figure 5.63: Spectrogram of the obtained forward and reverse flow signals, when filters in figures F.14 and F.15 are used

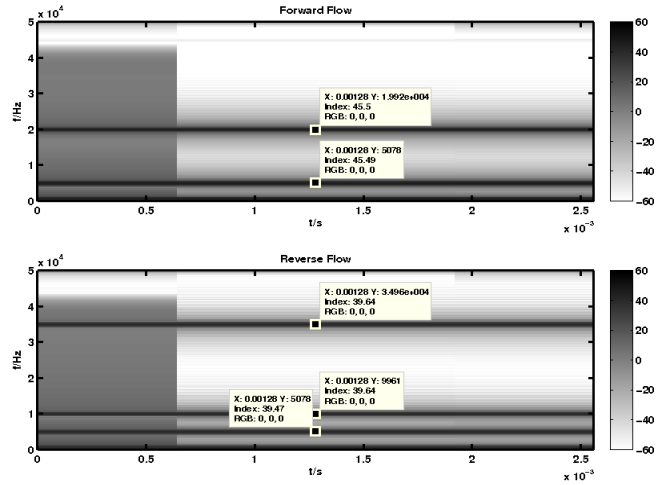

Figure 5.64: Spectrogram of the obtained forward and reverse flow signals, when filters in figures F.17 and F.18 are used

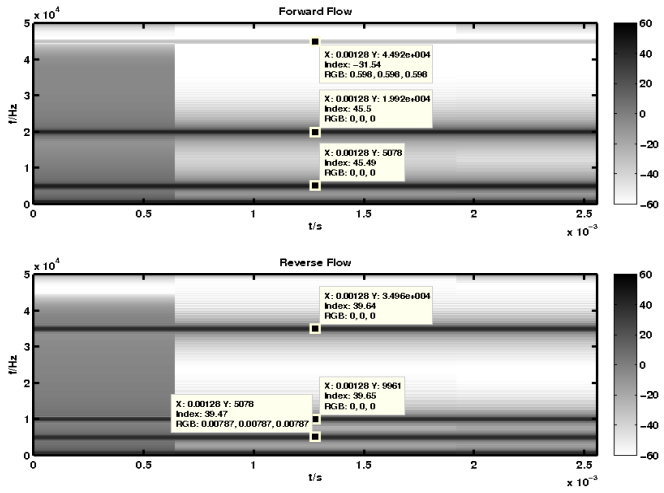

Figure 5.65: Spectrogram of the obtained forward and reverse flow signals, when filters in figures F.20 and F.21 are used

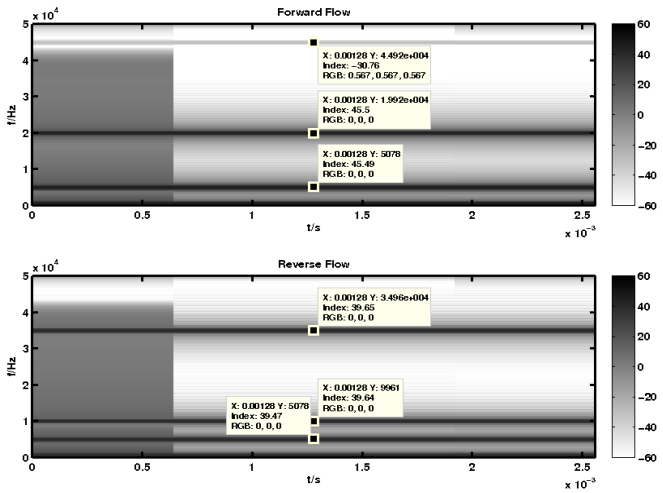

Figure 5.66: Spectrogram of the obtained forward and reverse flow signals, when filters in figures F.23 and F.24 are used

5.1.11 Approach 5: signal with noise

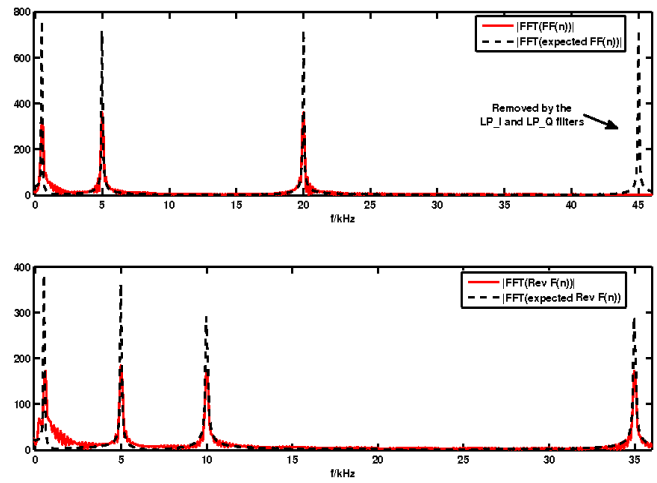

Figure 5.67: Comparison between expected (without noise) and the obtained (with noise) magnitude spectra for the forward (top figure) and reverse (bottom figure) flow signals. (filters in figures F.14 and F.15 are used).

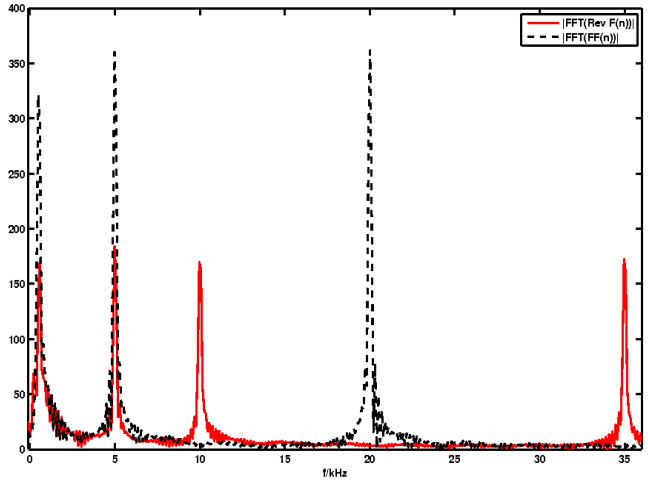

Figure 5.68: Comparison between the obtained forward $FF(n)$ and reverse $Rev\ F(n)$ flow signals magnitude

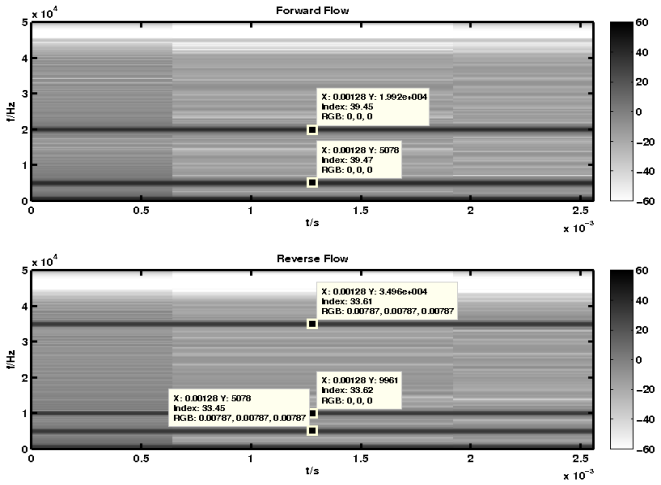

Figure 5.69: Spectrogram of the obtained forward and reverse flow signals

5.1.12 Bandpass Sampling

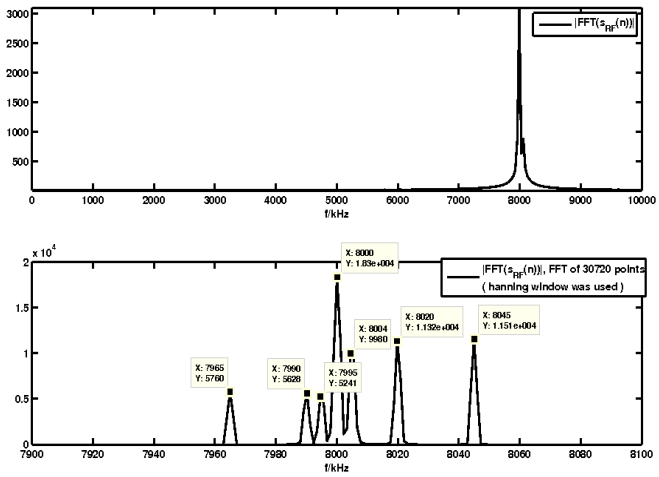

Figure 5.70: RF signal centered at a 8 MHz frequency carrier (see subsection 4.3.1). The bottom figure is a zoom of the top figure, showing only frequency components from 7900 kHz to 8100 kHz.

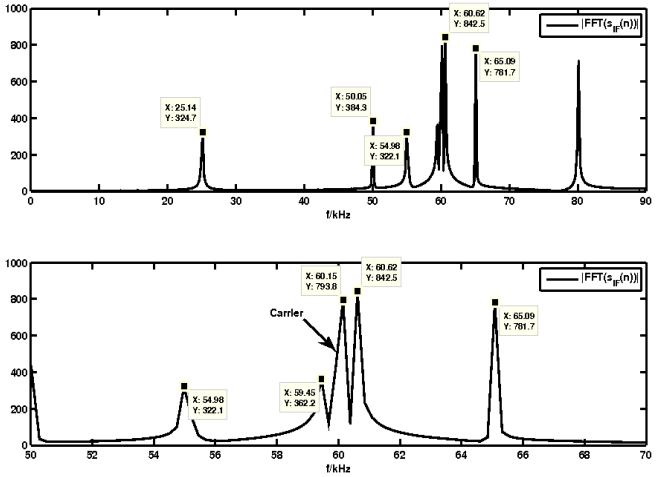

Figure 5.71: Sampled signal using the allowed 240.604 kHz sampling rate. The signal is shifted to the expected frequency of 60.1 kHz (see subsection 4.3.2). The bottom figure is a zoom of the top figure, showing only frequency components from 50 kHz to 70 kHz.

5.1.13 Comments on the Testing Signal Results

In this section a few comments will be made regarding the results presented previously. Focus will be made on the comparison between the obtained and the expected forward and reverse magnitude spectra, and also on the spectrogram results.

First considering the results when noise is not present in the signal, for the studied approaches it can be stated the following:

- in terms of frequency components location, for all the approaches, the obtained forward and reverse blood flow components appear in the same frequency locations than those of the expected forward and reverse blood flow components.

- in general, small differences in some of the magnitudes of the obtained forward and reverse blood flow components occur, in comparison to the expected forward and reverse blood flow components at the same frequencies. Observing figures related to the comparison between the obtained forward and reverse blood flow components (figures 5.5, 5.18, 5.31, 5.44 and 5.61), it can be seen that the magnitude of the reverse blood flow components is about half the magnitude of the forward blood flow components, as defined in the used signal (see section 4.3.1).

- To evaluate the blood flow components separation, it can be seen that with the exception of approach 4, all other approaches present no contamination of forward blood flow components by the reverse blood flow components, and vice-versa. Only spectral leakage occupy the space between the peaks of the spectral blood flow components. In the case of approach 4, observing the spectrogram in figure 5.46, it can be seen that contamination of forward blood flow components by reverse blood flow components are present, and vice-versa. Such contaminations are more visible (present higher power) the lower the order of the allpass filters (see figures 5.50 and 5.52). When the allpass filters used had order 5 and order 15 even in the figures of the obtained forward and reverse blood flow components (see figures 5.49 and 5.51) such contamination is visible (20 kHz forward peak in the reverse blood flow magnitude spectra)

- When noise is added to the testing signal of subsection 4.3.1, the efficiency of all approaches remains the same. Approach 4, maintains its efficiency. However, because of the presence of the noise the contaminations are not visible.

- in terms of the approach 5, better attenuation of the stopband is obtained for a window size of 115 points using the Blackman window - see figures 5.63 (where the Kaiser window was used) and 5.65 (where the Blackman window was used). When the window size is of 167 points better attenuation of the stopband is obtained using the Kaiser window with a parameter of 9.5 - see figures 5.64 (where the Kaiser window was used) and 5.66 (where the Blackman window was used).

- the testing signal employed has a frequency component which would correspond to a forward blood flow component located at 45 kHz. This forward blood flow component was expected to be eliminated by the lowpass filters (equiripple or not) employed. Also, the signal used to test the digital quadrature techniques had a frequency component associated with the reverse blood flow located at 35 kHz. This frequency component was expected to be attenuated by the lowpass filters (equiripple or not) used. From the results presented these expected behaviours occured for all considered lowpass filters (equiripple or not).

- when BPS is employed to acquire the testing signal (figure 5.70), the carrier frequency of the signal is translated to 60.1 kHz (figure 5.71) as expected by theoretical calculations (see section 4.3.2).

5.2 Results of Bandpass Sampling when Experimental Signals are Used

5.2.1 Introduction

Using the so called experimental signals (described in subsection 4.3.1), acquired using an allowed bandpass sampling rate (240.604 kHz) the spectrum of the obtained signal is presented in figure 5.72. Note that the acquired digital signal (in figure 5.72) was amplified by 10 and a Hanning window was primarly applied before the signal was processed by any of the digital quadrature techniques.

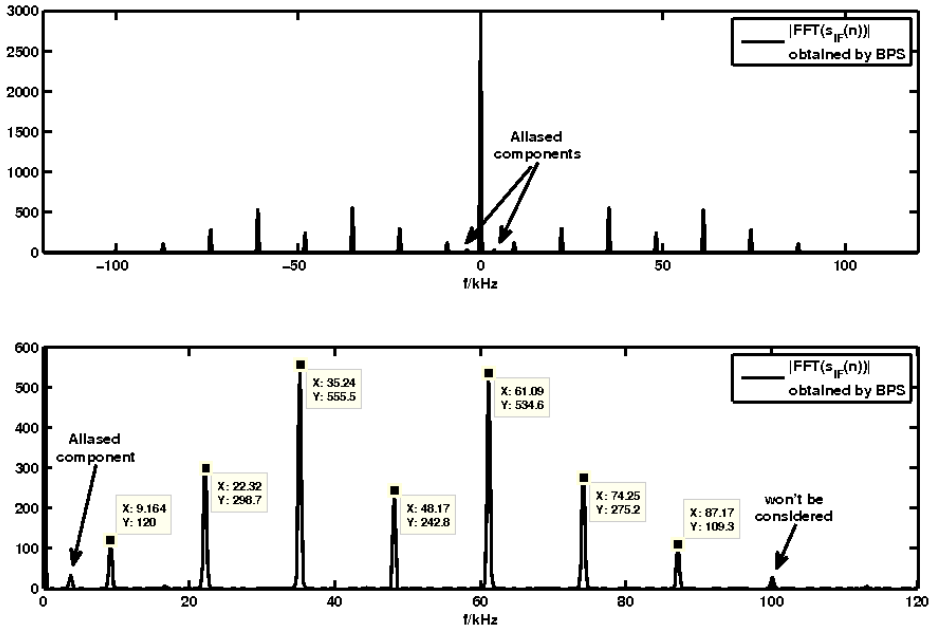

Figure 5.72: Spectrum of the FM signal, created by modulating a 8 MHz carrier with a 13 kHz sine wave, with $\beta = 2$. The FM signal was sampled with a sampling rate of 240.604 kHz. The bottom figure is a zoom of the top figure, showing only frequency components from DC to 120 kHz.

Because approaches 2 to 5 in subsection 3.3.3 assume that the sampling frequency is 4 times the FM signal's carrier frequency (which after BPS is located at 48.17 kHz), the initially acquired FM signal with an allowed sampling rate of 240.604 kHz must be resampled so that the *new* sampling frequency is equal to 192.68 kHz.

If such resampling is not made, given the fact that the signal was sampled with a sampling frequency of 240.604 kHz, $\frac{Fs}{4}$ would be of 60.151 kHz. However the carrier of the signal is located at 48.17 kHz. If we process this sampled signal the carrier will be shifted to -11.98 kHz. Also the carrier in the negative part of the spectrum is shifted from -48.17 kHz to +11.98 kHz. As a consequence inadequate spectrum overlap will occur (see figure 5.73 where only the DC components of figure 5.72 are marked).

So resampling must be made. Care must be taken in choosing the final sampling frequency. The frequency must be four times the carrier frequency. When the quadrature sequences are applied to

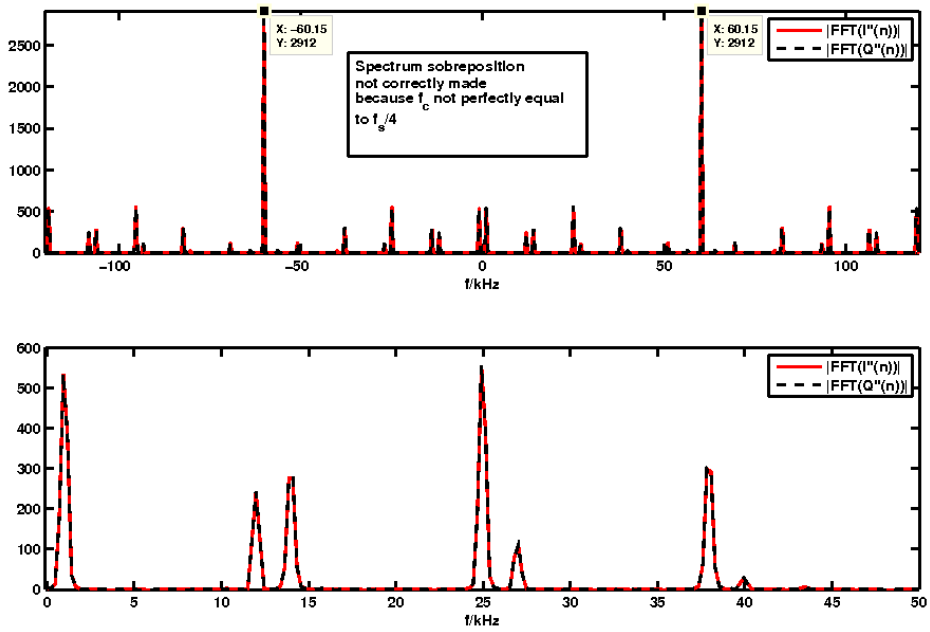

Figure 5.73: Magnitude spectrum of signals $I"(n)$ and $Q"(n)$ in approach 2, when the sampling frequency is not equal to four times the signal's carrier frequency. It can be seen that the alignment of the spectra is not obtained. The bottom figure is a zoom of the top figure, showing only frequency components from DC to 50 kHz.

the signal, the carrier is shifted to DC, as shown in figure 5.74.

Since the carrier is located at 48.17 kHz the new sampling frequency must be $4 \times 48.17\ kHz = 192.68\ kHz$. The initial sampling frequency had the value of 240.604 kHz, therefore the ratio between the two sampling frequencies is $\frac{192.68}{240.604} = 0.80$. Consequently the *Matlab* resampling is made with $resample(signal, 80, 100)$. Also the spectrum frequency scale is adjusted with $freq = (0.80 * Fs). * ((-NFFT/2) : 1 : (NFFT/2) - 1)./NFFT$.

A pertinent question is "Can this resampling be made?". Considering the Nyquist theorem, knowing that we can consider that the signal initially sampled (whose spectrum is presented in figure 5.72) has a bandwidth of approximately 78 kHz, the minimum sampling frequency will be 156 kHz. Since it is used 192.68 kHz, the resample can be made. The result is presented in figure 5.74,

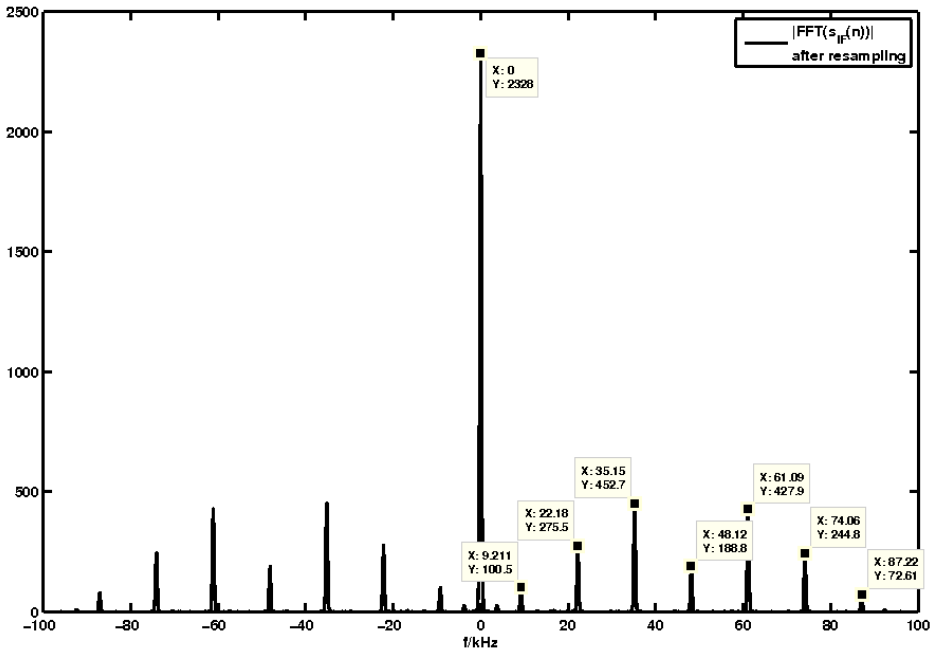

Figure 5.74: Magnitude spectrum of the acquired signal using BPS allowed frequency subjected to resampling so that the *new* sampling frequency is equal to four times the signal's carrier frequency.

For all approaches presented in this section, it was decided to use odd order lowpass FIR filters with stopband attenuation the nearest as possible, but not lower, than 80 dB.

When resampling is not needed (approach 1) the lowpass FIR filter used is the one presented in figure F.2. When resampling is needed (approaches 2 to 4) the lowpass FIR filter employed is the one presented in figure F.8.

In the case of approach 4 two allpass filters with phase difference of $\frac{\pi}{2}$ between them are required. It was decided to use allpass filters of order 30, shown in figures F.39 and F.41.

In the case of approach 5, two special lowpass filters are required. It was decided to use the filters presented in figures F.26 and F.27 obtained from a 91 point Kaiser window with parameter 9.5.

In the following subsections 5.2.2 to 5.2.6 the results obtained with each of the approaches studied on this thesis are presented in terms of graphical results of the magnitude spectra of the $I(n)$ and $Q(n)$ signals, the magnitude spectra of the obtained forward and reverse blood flow components (respectively identified by $FF(n)$ and $Rev\ F(n)$) and the spectrograms of the obtained forward and reverse blood flow components.

5.2.2 Approach 1

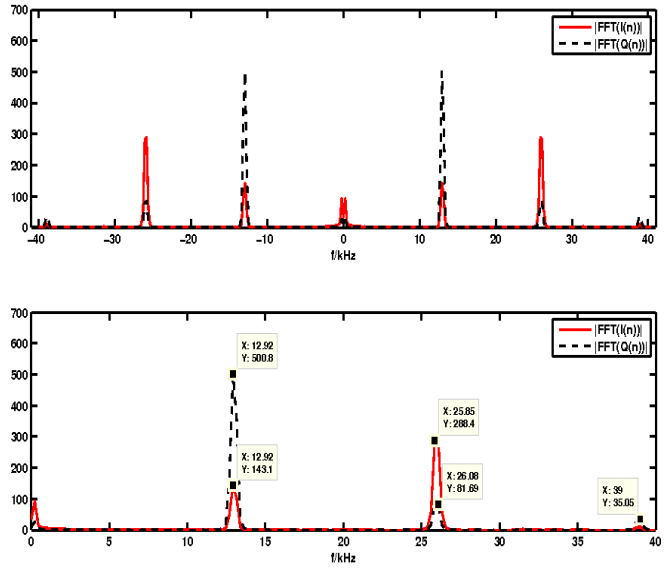

Figure 5.75: Magnitude spectra of the obtained $I(n)$ and $Q(n)$ signals. The bottom figure is a zoom of the top figure, showing only frequency components from DC to 40 kHz.

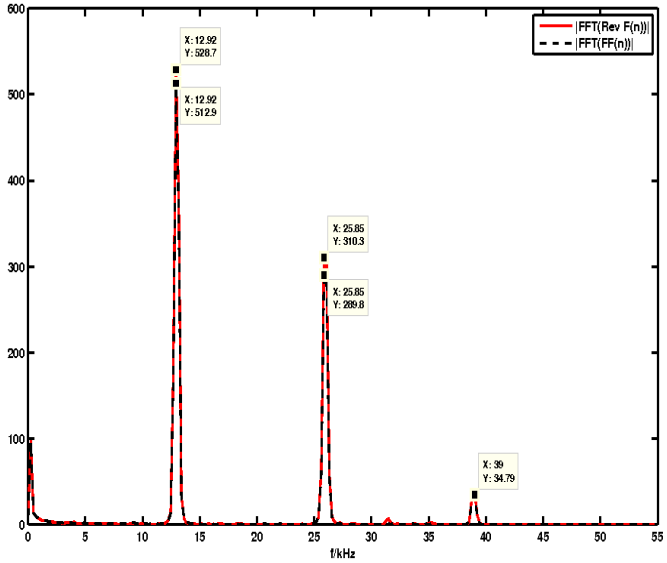

Figure 5.76: Magnitude spectra of the obtained $FF(n)$ and $Rev\ F(n)$ signals.

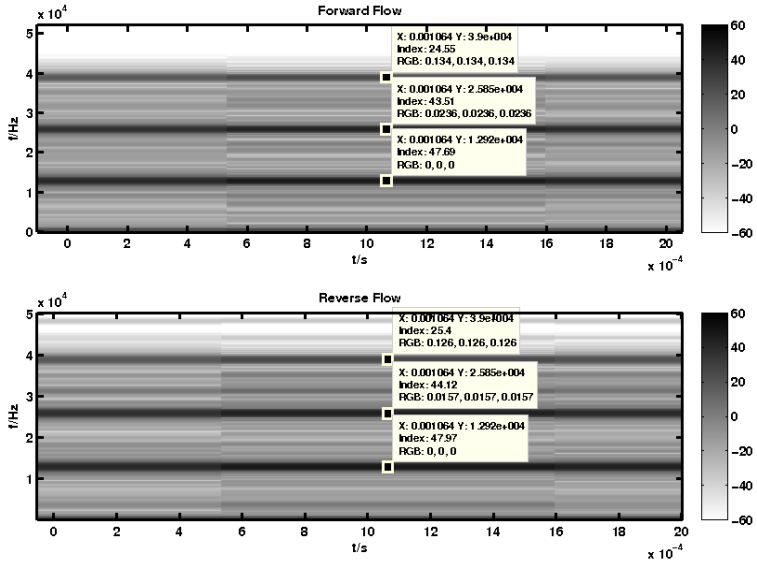

Figure 5.77: Spectrogram of the obtained $FF(n)$ and $Rev\ F(n)$ signals.

5.2.3 Approach 2

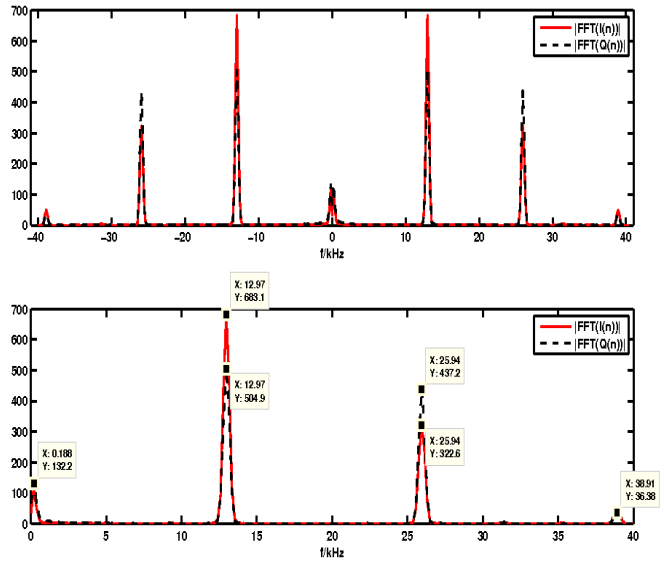

Figure 5.78: Magnitude spectra of the obtained $I(n)$ and $Q(n)$ signals. The bottom figure is a zoom of the top figure, showing only frequency components from DC to 40 kHz.

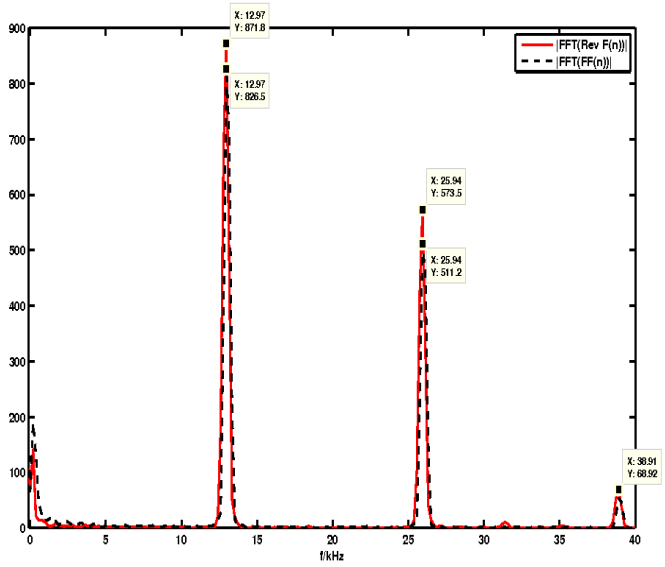

Figure 5.79: Magnitude spectra of the obtained $FF(n)$ and $Rev\ F(n)$ signals.

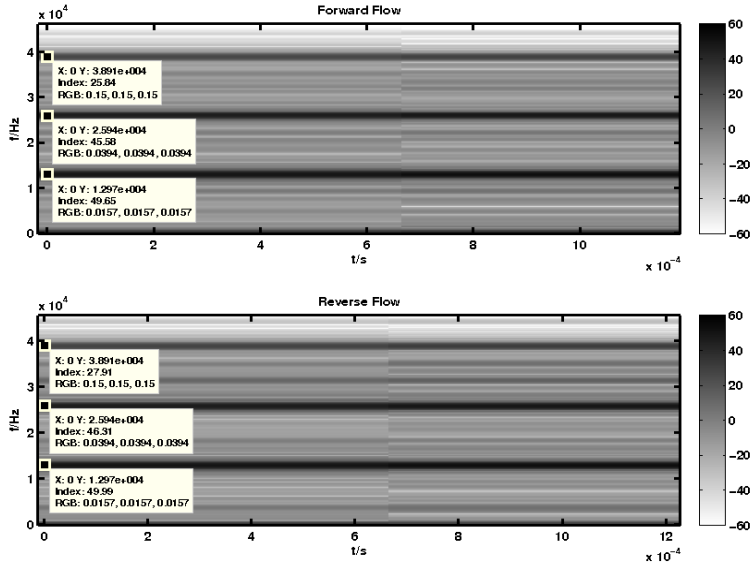

Figure 5.80: Spectrogram of the obtained $FF(n)$ and $Rev\ F(n)$ signals.

5.2.4 Approach 3

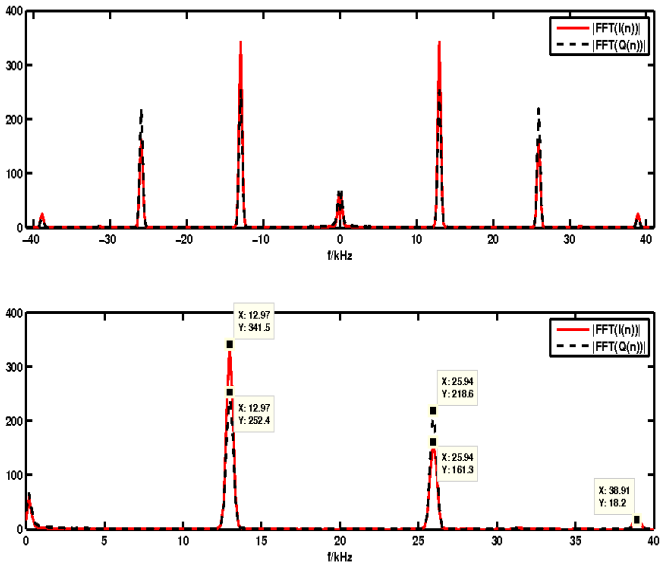

Figure 5.81: Magnitude spectra of the obtained $I(n)$ and $Q(n)$ signals. The bottom figure is a zoom of the top figure, showing only frequency components from DC to 40 kHz.

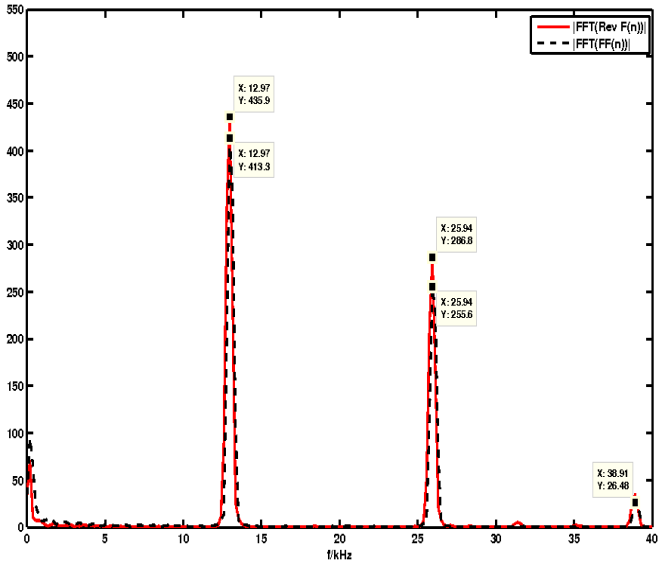

Figure 5.82: Magnitude spectra of the obtained $FF(n)$ and $Rev\ F(n)$ signals.

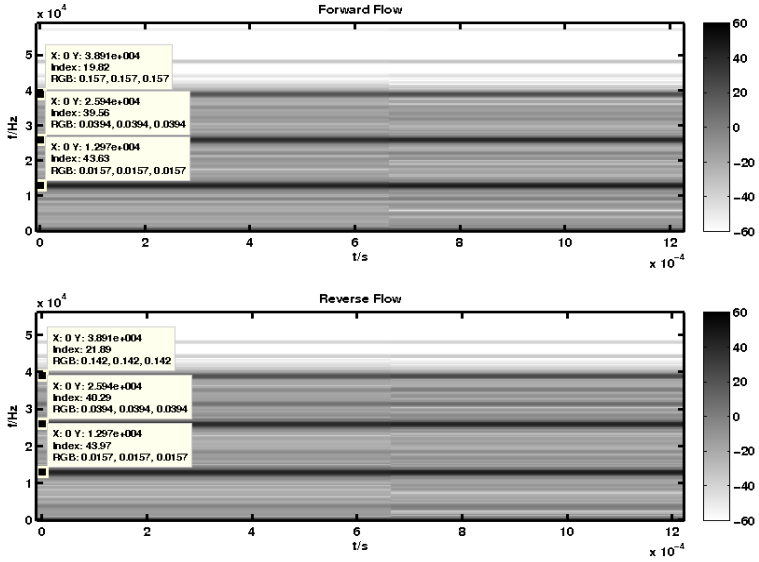

Figure 5.83: Spectrogram of the obtained $FF(n)$ and $Rev\ F(n)$ signals.

5.2.5 Approach 4

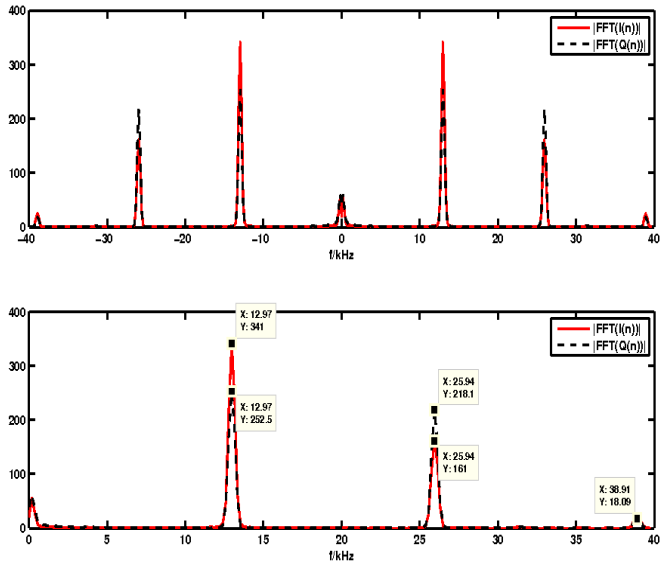

Figure 5.84: Magnitude spectra of the obtained $I(n)$ and $Q(n)$ signals. The bottom figure is a zoom of the top figure, showing only frequency components from DC to 40 kHz.

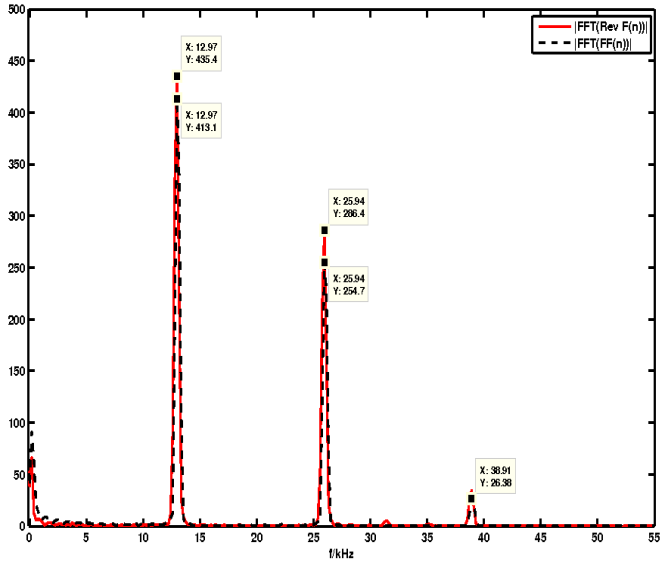

Figure 5.85: Magnitude spectra of the obtained $FF(n)$ and $Rev\ F(n)$ signals.

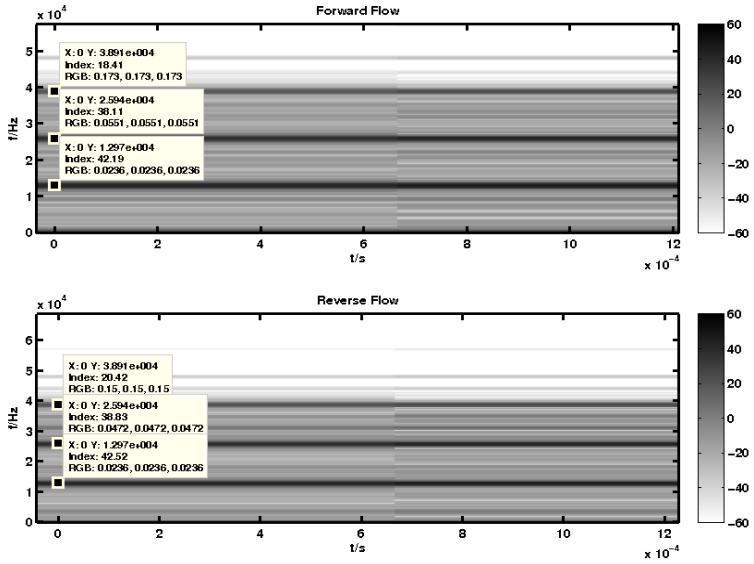

Figure 5.86: Spectrogram of the obtained $FF(n)$ and $Rev\ F(n)$ signals.

5.2.6 Approach 5

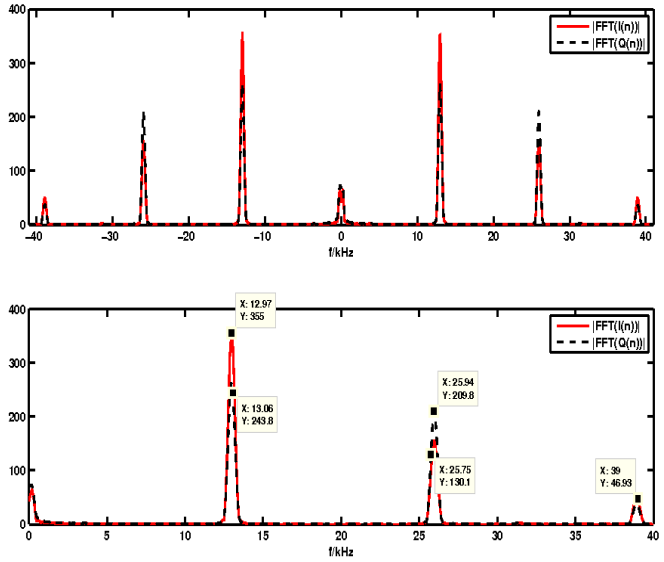

Figure 5.87: Magnitude spectra of the obtained $I(n)$ and $Q(n)$ signals. The bottom figure is a zoom of the top figure, showing only frequency components from DC to 40 kHz.

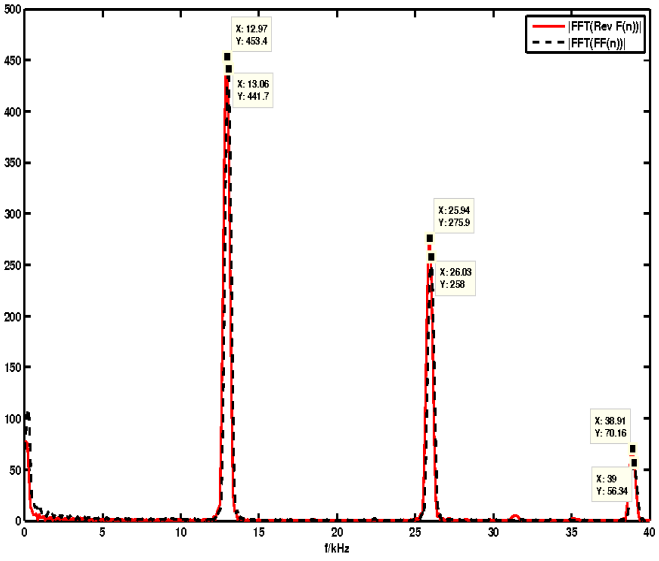

Figure 5.88: Magnitude spectra of the obtained $FF(n)$ and $Rev\ F(n)$ signals.

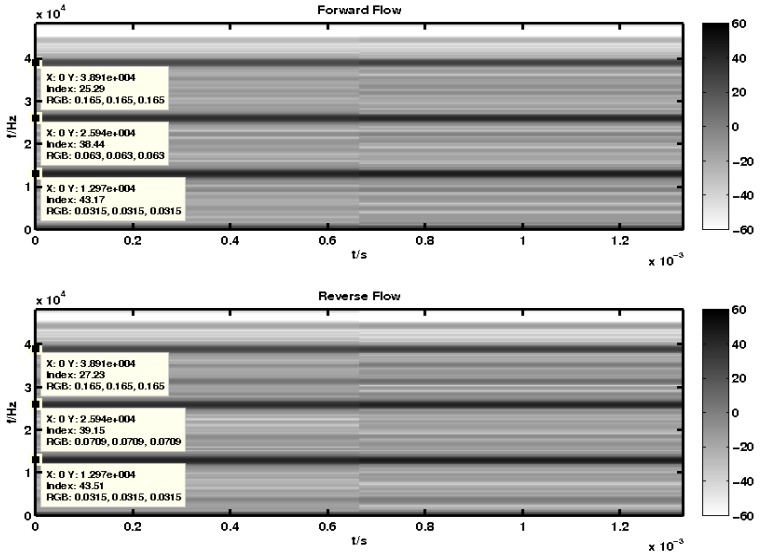

Figure 5.89: Spectrogram of the obtained $FF(n)$ and $Rev\ F(n)$ signals.

5.2.7 Comments on the Experimental Signal Results Obtained by BPS Technique

Considering the results being presented from the beginning of this section (section 5.2), observing the acquired signal spectrum (figure 5.72 before resampling was made - used in approach 1 - and figure 5.74 after resampling - used in approaches 2 to 5), it can be seen that the acquired signal has a magnitude spectrum similar to the expected one, shown in figure 4.15. There are very small differences between the frequency location of the componentes that will originate the forward and reverse blood flow components, before and after resampling.

To be noted that the carrier frequency which should be located at an expected frequency of 60.1 kHz (see section 4.3.2 and figure 5.71) is located at a frequency of 48.1 kHz. To evaluate the reason for this the difference between the expected and the obtained IF frequency, a 8 MHz sine wave was generated by the Agilent 33220A 20 MHz Function/Arbitrary Waveform Generator and was sampled at 240.604 kHz. Again the peak location was 48.1 kHz. Applying equation (3.28) it can be shown that this means that the real sampling frequency was higher, being 240.964 kHz rather than the desired 240.604 kHz. The reason for such difference is not yet understood, since the sampling conditions are set up in the NI DAQ USB 6251 equipment by proper API supplied with the device. However, since in all the experiments performed with a sine wave or RF signal with a 8 MHz carrier were shifted to the 48.1 kHz, it appears that there is a systematic error. If one assumed a correct sampling frequency, and an error in the generated wave's frequency, instead of the 8 MHz such wave would be of 7990 kHz, which seems to be unlikely.

From figures 5.72 and 5.74 it can also be noted that the relative amplitude of the peaks related to reverse blood flow movement are slighty higher than those related to the forward blood flow movement.

Observing figures 5.75, 5.78, 5.81, 5.84 and 5.87 it can be seen that each frequency component is located (with small variations) at its expected frequency (see figure 4.15 which presents the spectral components distribution of the acquired signal). Consequently, the magnitude spectra of the obtained $FF(n)$ and $Rev\ F(n)$ signals (see figures 5.76, 5.79, 5.82, 5.85 and 5.88) show the frequency components at the correct and expected frequency values (with small variations).

Another aspect to be mentioned is that, besides the frequency components of the obtained $FF(n)$ and $Rev\ F(n)$ signals are at the correct and expected frequency values (with small variations), their relative magnitudes are also in accordance to what was expected based on figure 5.74. Observing figure 5.74 it can be seen that the frequency components associated with the reverse blood flow present magnitudes which are slightly higher than the magnitudes of the components related to the forward blood flow.

The spectrograms shown from subsections 5.2.2 to 5.2.6 are important to compare the noise present in the results obtained using BPS (presented in section 5.2) and the results obtained (for the same signal) when applying the heterodyne technique (presented in section 5.3) .

5.3 Results Obtained after Heterodyne Application on Experimental Signals

5.3.1 Introduction

The heterodyne technique was applied to the previously called experimental signal, described in subsection 4.3.1. In this case the RF signal was centered in a carrier with frequency value of 7.9995 MHz, and was mixed with a synthesized square wave with a frequency as close as possible to 8.050 MHz [1].

Since the sampling rates required by approaches 2 to 5 (subsection 3.3.3) are different than the sampling rate required by the approach 1 (subsection 3.3.3) both sampled signal spectra are presented in figures 5.90 and 5.91. In the case of figure 5.90 (signal used in approach 1) the sampling rate employed was of 260 kHz. In the case of figure 5.91 (signal used for approaches 2 to 5) the sampling rate had the value of 208.8 kHz, which was 4 times the carrier frequency (52.2 kHz).

To be noted that figures 5.90 and 5.91 are not related to the same signal conditions, i.e., since the PLL input reference signal can be swapped between acquiring the signal for approach 1 and the signal to be used for approaches 2 to 5, the reference signal was changed. Consequently obtaining an equal PLL input reference signal was impossible. However, the fact that for approaches 2 to 5 the output of the PLL-based frequency synthesizer is a 8.052 MHz square wave, it does not invalidate the application of the digital quadrature approaches 2 to 5, because the sampling rate requirement was that it should be 4 times the carrier frequency, and this is fulfilled.

The digital signals acquired (as previously mentioned) were amplified by 10 and a Hanning window was applied before the signal was processed by any of the digital quadrature techniques.

[1] The expression *as close as possible to* is used because the reference signal used as input in the PLL-based synthesizer was controlled by an analog button. Consequently obtaining exactly the desired 8.050 MHz was not always possible

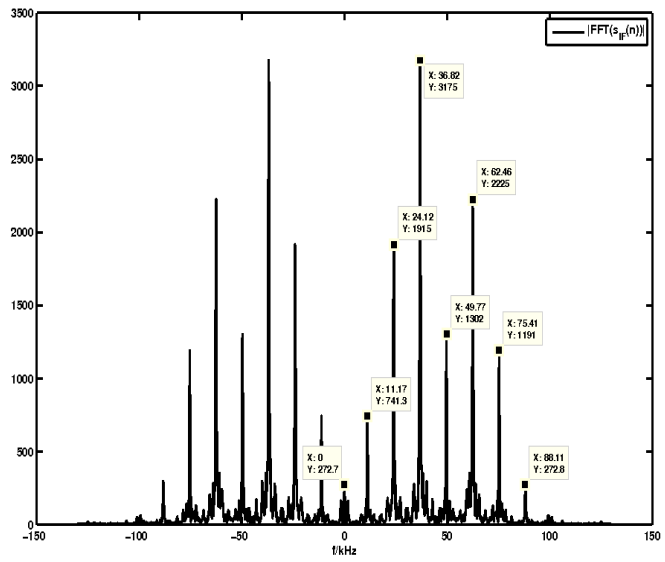

Figure 5.90: Magnitude spectrum of the signal centered at 50 kHz, sampled at a frequency of 260 kHz

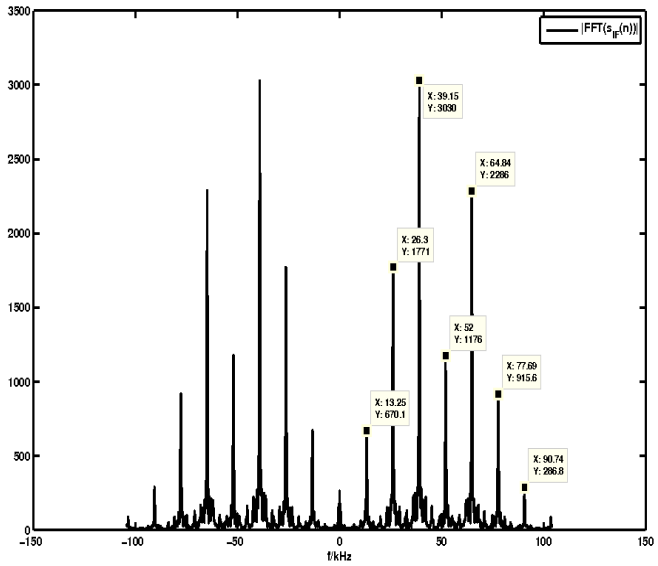

Figure 5.91: Magnitude spectrum of the signal centered at 52.2 kHz, sampled at a frequency of 208.8 kHz

For all approaches presented in this section, it was decided to use odd order lowpass FIR filters with stopband attenuation the nearest as possible, but not lower, than 80 dB.

For approach 1, the lowpass FIR filter used is the one presented in figure F.4. In the case of approaches 2 to 4 the lowpass FIR filter employed is the one presented in figure F.9.

In the case of approach 4 two allpass filters with phase difference of $\frac{\pi}{2}$ between them are required. It was decided to use allpass filters of order 30, shown in figures F.39 and F.41.

In the case of approach 5, two special lowpass filters are needed. Decision was made to use the filters presented in figures F.29 and F.30 obtained from a 91 point Kaiser window with parameter 9.5.

In the following subsections 5.3.2 to 5.3.6 the results obtained with each of the approaches studied on this thesis are presented in terms of graphical results of the magnitude spectra of the $I(n)$ and $Q(n)$ signals, the magnitude spectra of the obtained forward and reverse blood flow components (respectively identified by $FF(n)$ and $Rev\ F(n)$) and the spectrograms of the obtained forward and reverse blood flow components.

5.3.2 Approach 1

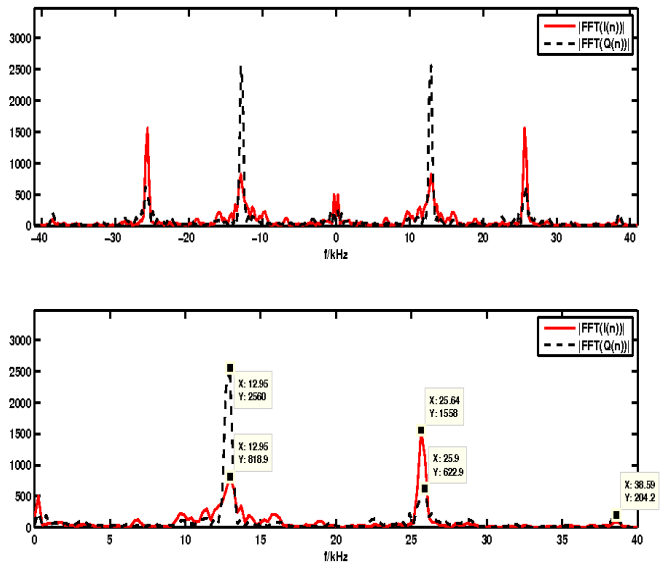

Figure 5.92: Magnitude spectra of the obtained $I(n)$ and $Q(n)$ signals. The bottom figure is a zoom of the top figure, showing only frequency components from DC to 40 kHz.

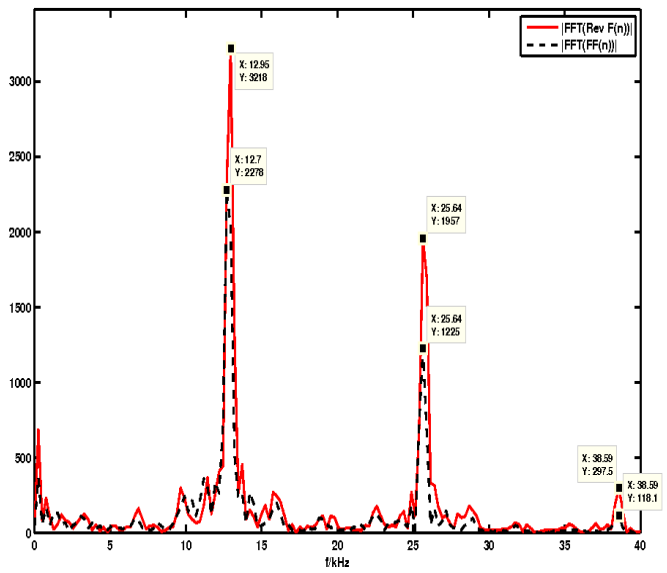

Figure 5.93: Magnitude spectra of the obtained $FF(n)$ and $Rev\ F(n)$ signals.

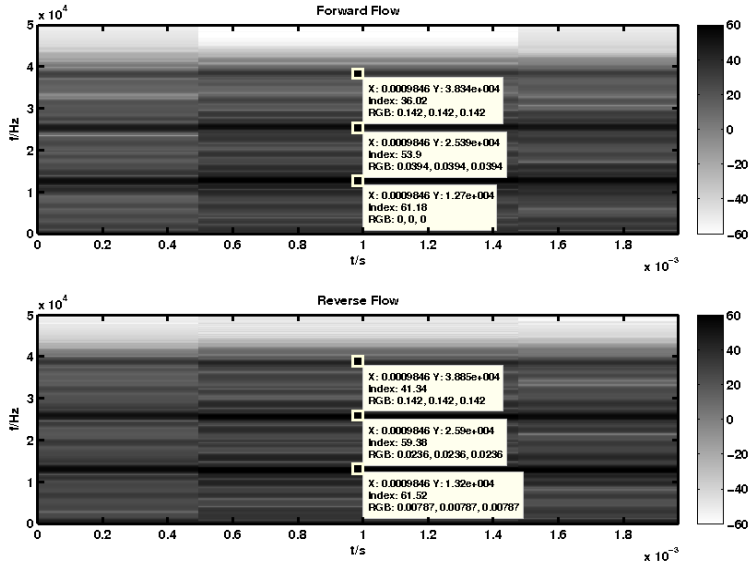

Figure 5.94: Spectrogram of the obtained $FF(n)$ and $Rev\ F(n)$ signals.

5.3.3 Approach 2

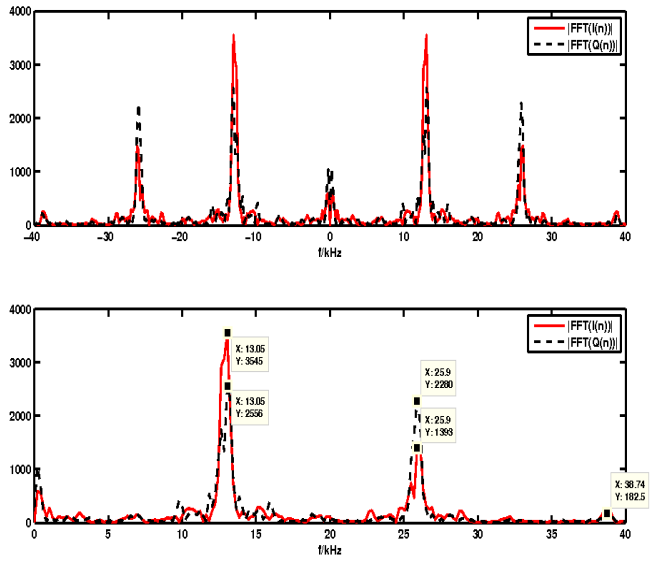

Figure 5.95: Magnitude spectra of the obtained $I(n)$ and $Q(n)$ signals. The bottom figure is a zoom of the top figure, showing only frequency components from DC to 40 kHz.

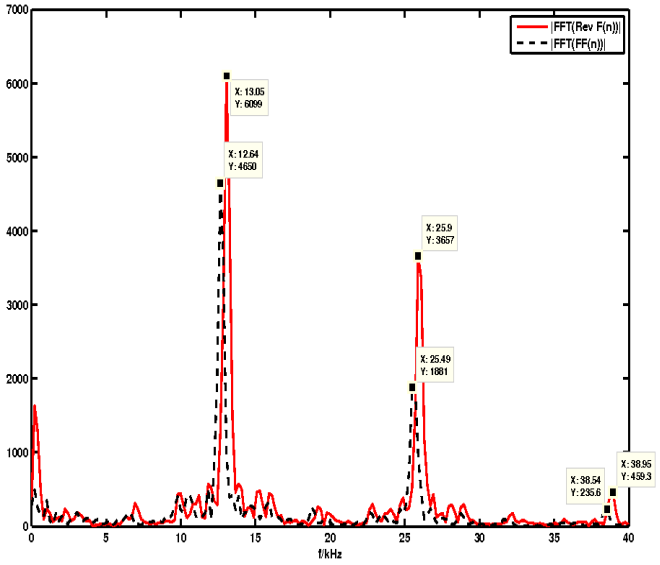

Figure 5.96: Magnitude spectra of the obtained $FF(n)$ and $Rev\ F(n)$ signals.

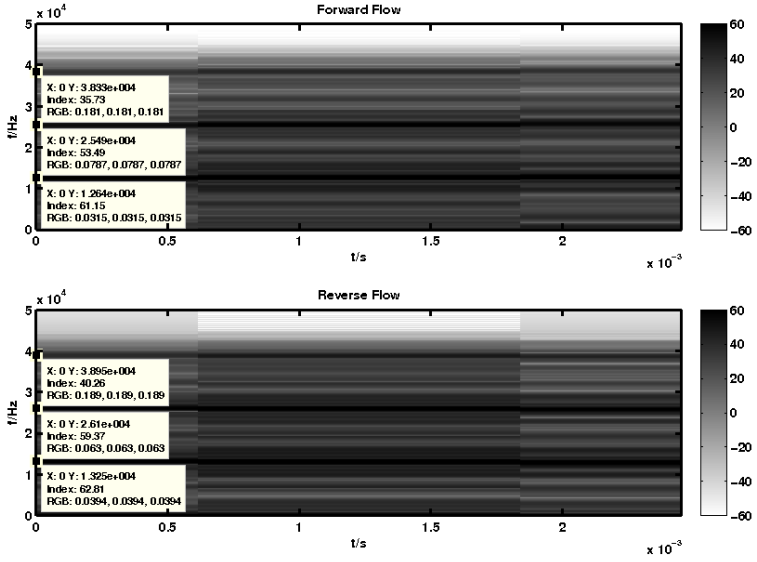

Figure 5.97: Spectrogram of the obtained $FF(n)$ and $Rev\ F(n)$ signals.

5.3.4 Approach 3

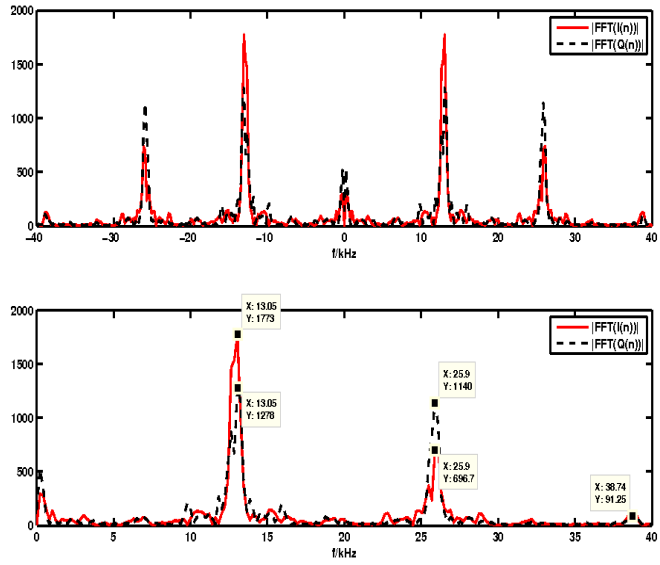

Figure 5.98: Magnitude spectra of the obtained $I(n)$ and $Q(n)$ signals. The bottom figure is a zoom of the top figure, showing only frequency components from DC to 40 kHz.

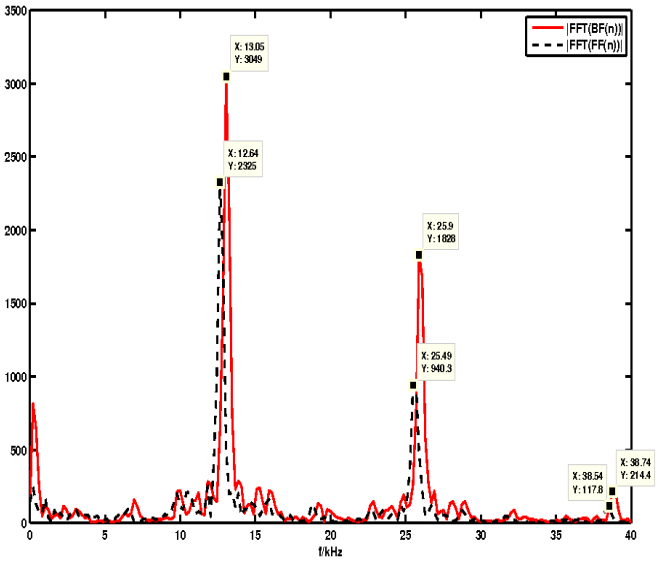

Figure 5.99: Magnitude spectra of the obtained $FF(n)$ and $Rev\ F(n)$ signals.

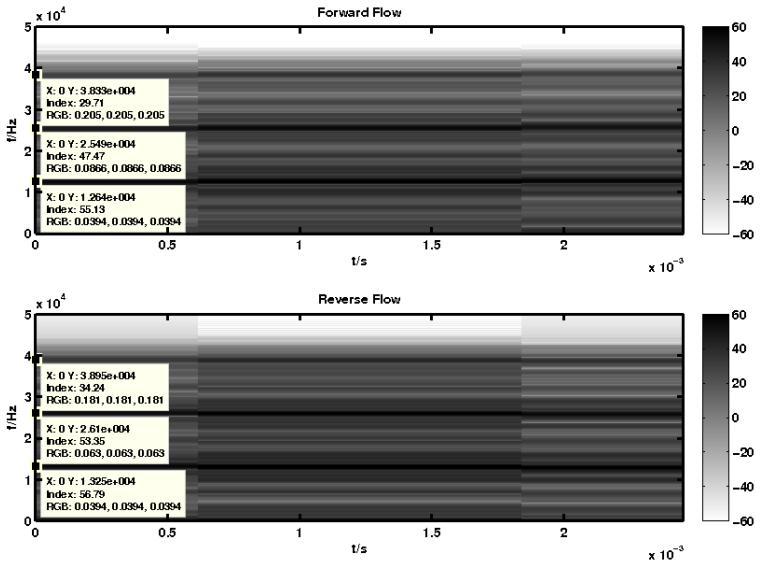

Figure 5.100: Spectrogram of the obtained $FF(n)$ and $Rev\ F(n)$ signals.

5.3.5 Approach 4

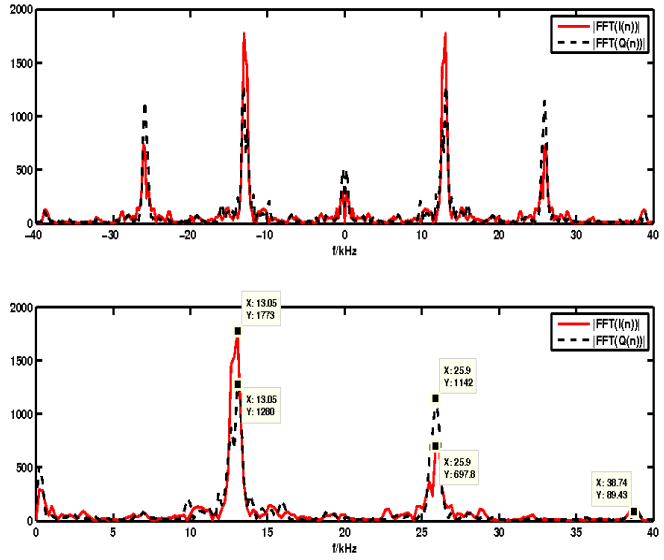

Figure 5.101: Magnitude spectra of the obtained $I(n)$ and $Q(n)$ signals. The bottom figure is a zoom of the top figure, showing only frequency components from DC to 40 kHz.

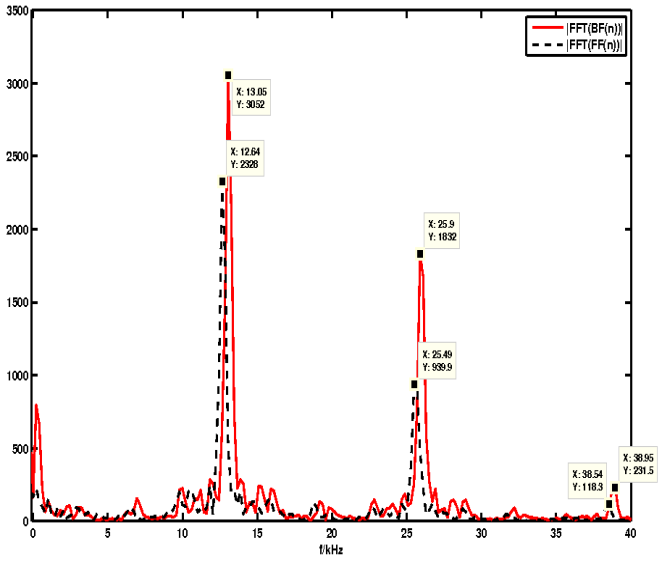

Figure 5.102: Magnitude spectra of the obtained $FF(n)$ and $Rev\ F(n)$ signals.

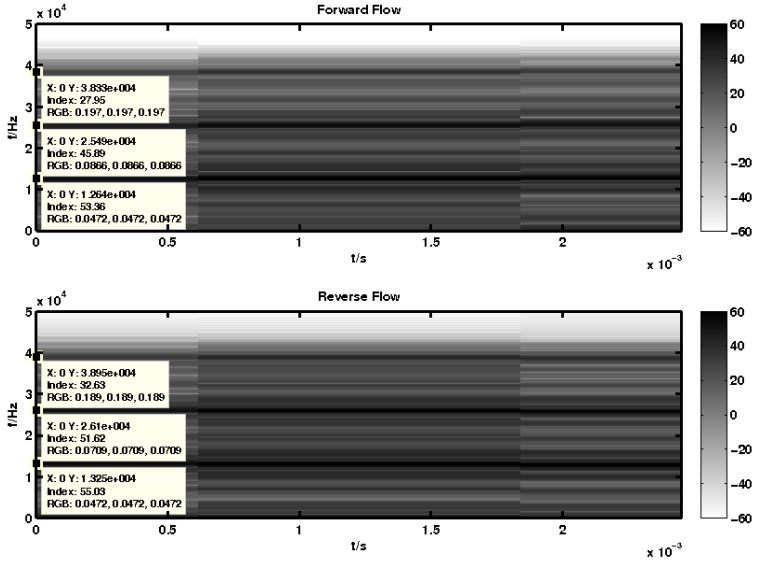

Figure 5.103: Spectrogram of the obtained $FF(n)$ and $Rev\ F(n)$ signals.

5.3.6 Approach 5

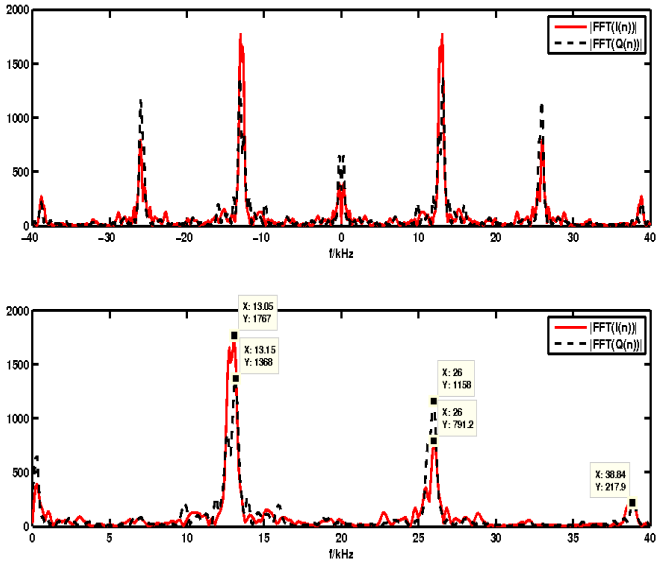

Figure 5.104: Magnitude spectra of the obtained $I(n)$ and $Q(n)$ signals. The bottom figure is a zoom of the top figure, showing only frequency components from DC to 40 kHz.

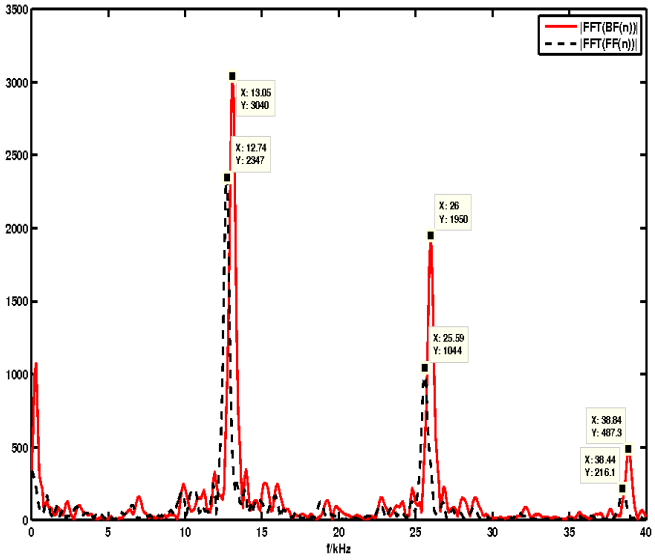

Figure 5.105: Magnitude spectra of the obtained $FF(n)$ and $Rev\ F(n)$ signals.

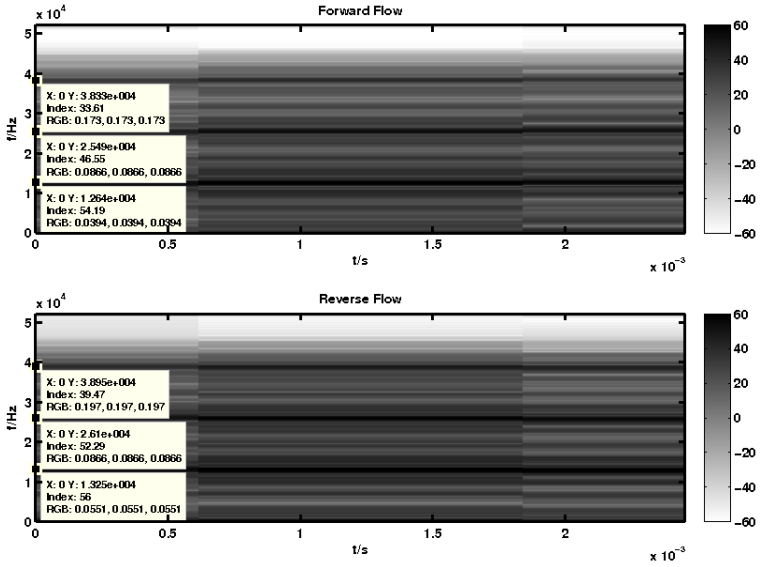

Figure 5.106: Spectrogram of the obtained $FF(n)$ and $Rev\ F(n)$ signals.

5.3.7 Comments on the Experimental Signal Results Obtained After Heterodyne Technique

Observing figures 5.92, 5.95, 5.98, 5.101 and 5.104 it can be seen that each frequency component is located (with small variations) at its expected frequency (see figure 4.15 which presents the spectral components distribution of the acquired signal). Consequently, the magnitude spectra of the obtained $FF(n)$ and $Rev\ F(n)$ signals (see figures 5.93, 5.96, 5.99, 5.102 and 5.105) show the frequency components at the expected frequency values (with small variations). To be notice that the magnitude spectra of the obtained $FF(n)$ and $Rev\ F(n)$ signals, for approaches 2 to 5, there is a difference of about 400 Hz between a given forward component and the reverse component at the same frequency position. Even when the sampling rate in the *Matlab* code was changed, for example to 200 kHz, the difference between forward and reverse blood flow components location was still of about 400 Hz, meaning that the problem is not related to the sampling frequency and the carrier frequency employed. Since the PLL's output frequency variation presents a value of 10 Hz the problem is not related to the developed frequency synthesizer. In fact, it has been discovered that the GW Function Generator Model GFG-8015G used as the reference signal generator for the PLL presented a frequency drift which was not controllable. Consequently we believe that the observed difference of 400 Hz for approaches 2 to 5 must be related to the behaviour of the GW Function Generator Model GFG-8015G employed.

Another aspect to be mentioned is that, the frequency components of the obtained $FF(n)$ and $Rev\ F(n)$ signals have relative magnitudes in accordance to what was expected based on figures 5.90 and 5.91. Observing these figures it can be seen that the frequency components associated with the reverse blood flow present magnitudes which are higher than the magnitudes of the components related to the forward blood flow.

Considering the results presented, observing the spectra of the acquired signals (figure 5.90, used in approach 1, and figure 5.91, used on approaches 2 to 5), it can be seen that the acquired signals have magnitude spectra where the magnitude of the spectral components after the carrier are more attenuated than those before the carrier. The cause of such behaviour is attributed to the lowpass linear phase with equiripple error employed, which has a $-3\ dB$ cutoff frequency of 95 kHz. Nevertheless, the spectra components locations are consistent with the expected ones shown in figure 4.15.

Observing spectrograms shown from subsections 5.2.2 to 5.2.6 with the ones shown from subsections 5.3.2 to 5.3.6 it can be seen that the noise in the results obtained using BPS (presented in section 5.2) is lower than the noise present in the results obtained (for the same signal) when applying the heterodyne technique.

Chapter 6

Discussion of the Results and Concluding Remarks

6.1 Introduction

This chapter will discuss the results obtained by the developed experimental setup (described in Chapter 4), under the circuitry restrictions imposed in section 4.3, when testing and experimental signals (whose differentiation is explained in section 4.3) were applied. The results obtained with the testing signals were presented in section 5.1, and those obtained with the experimental signals (some of them sampled using the principles of BPS (section 5.2) and some of them acquired after downconversion with heterodyning (section 5.3)) were processed by all digital quadrature techniques mentioned on section 3.3.3.

Figure 6.1, summarizes the different digital quadrature techniques studied during this work.

Each one of these approaches was applied to a testing signal originating theoretical results (see section 5.1) that enabled the evaluation of the performance behaviour of each technique. Such behaviour included the efficiency in creating quadrature components which would conduct to a proper forward and reverse blood flow components separation. With such signal, it was also evaluated the effect of changing the lowpass filters' order (and in case of the approach 5, the window used to create the required lowpass filters) as well as the effect in approach 4 of the variation of the order of the allpass filters employed.

After the evaluation of these properties, the signal to be processed by all of the presented approaches was generated by a function generator. This generated signal, the so called experimental signal, needed to be a well known signal, in terms of frequency components localization and their relative amplitudes.

The experimental signal was then sampled and digitized by the available ADC in order to be processed by all of the digital quadrature techniques. Two strategies for sampling this signal were adopted. In one strategy (whose block diagram if presented in figure 4.2) the RF signal is directly sampled with a specific sampling rate determined by the BPS theory. Using this strategy, not only

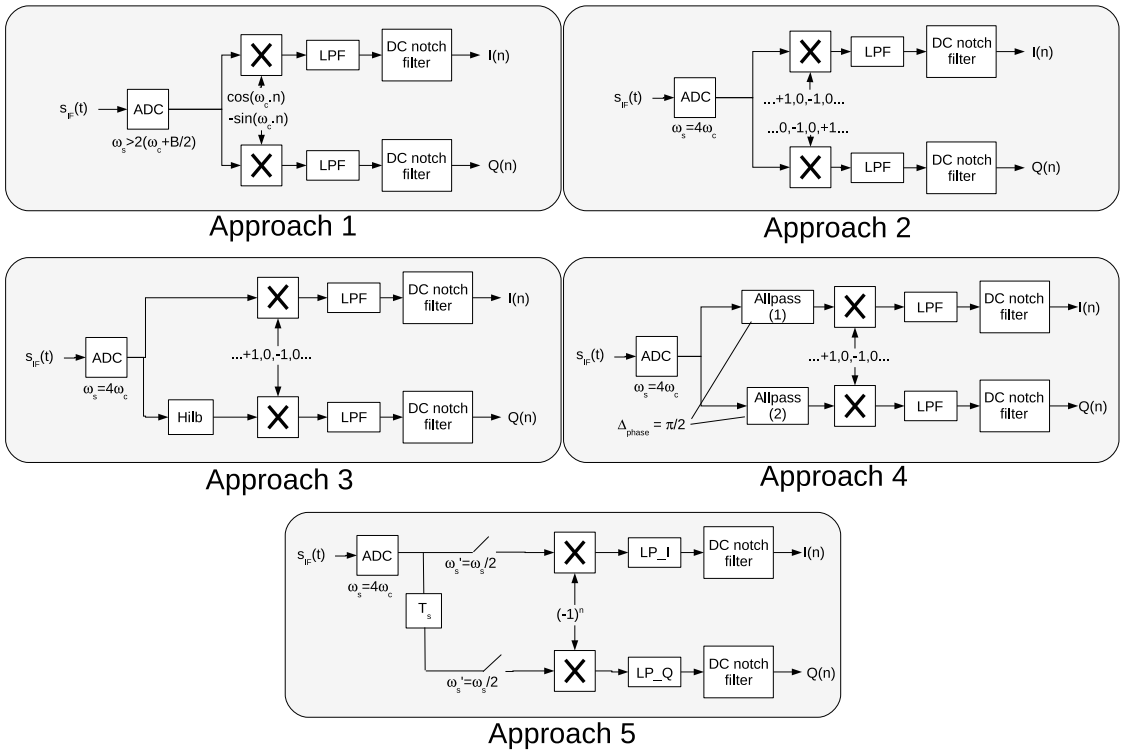

Figure 6.1: Figure presenting the block diagrams of all the five digital quadrature techniques on section 3.3.3

the signal is sampled but also the frequency shift of the RF signal occurs to a desired IF frequency. Another strategy (whose block diagram if presented in figure 4.3) was tested, which sampled the signal resulting from the heterodyning technique that downconverted the RF signal to a desired IF signal. The results from each sampling strategy are presented in sections 5.2 and 5.3 for the BPS technique and for the heterodyning technique, respectively.

In sections 5.1.13, 5.2.7 and 5.3.7 some result aspects were already discussed concerning the behavior of the studied approaches, after processing the testing signal and the experimental signal (sampled using the BPS principles and after the application of the heterodyne technique). In the next sections only summarized comments on such results will be addressed.

6.2 Generic Considerations

In this section some generic considerations will be made regarding the results presented in section 5.1, 5.2 and 5.3. Analysing the results it is easy to understand the choices made when the digital quadrature techniques were applied to the testing signal.

The results of section 5.1 have the advantage (against the results presented in sections 5.2 and 5.3) of enabling the comparison between the obtained forward and reverse blood flow components and the expected components, since the expected amplitude and frequency location of its components were well known. This way, a better understanding of the efficiency of each applied technique can be performed. From this understanding better considerations can be made when the signal to be

processed is not the simulated but the experimental one.

The type of noise added to the testing signal can be questioned regarding the choice of the 30 mV of variance chosen. Based on some preliminary experiments it was observed that depending on the circuits used for implementing the downconversion with heterodyning technique, the maximum noise amplitude could be of 10 mV or even a little more. So decision was made to use a noise with variance of 30 mV in order to consider the worst situation.

As described in section 4.3.1 the testing signal was chosen so that the amplitude of the forward and reverse blood flow components were different. This way, when observing a magnitude spectrum, the identification of the peaks that are related to forward blood flow are better distinguished from the peaks associated to reverse blood flow. Also the frequency components associated with each directional blood flow component were chosen to evaluated different factors, namely the efficiency of the digital quadrature technique being used.

For all digital quadrature techniques that used an equiripple lowpass filter it came with no surprise that the higher the stopband attenuation the better the results, i.e., less visible frequency components outside the passband were obtained. Question was on the value to be used in the stopband. From the results in section 5.1, paying attention to the figures presenting spectrograms, its visible that - for the considered amplitudes of the signals components - a stopband attenuation of 120 dB presents the best results. However, such attenuation value carries the burden of an increase in the filter's order (for the same cutoff frequency and sampling frequency). It was considered that the results with a 80 dB stopband attenuation would be a good equilibrium between the filter order and the attenuation in the stopband. For that matter, the results presented in sections 5.2 and 5.3 were processed with equiripple lowpass filters with stopband attenuation of 80 dB.

Comparisons between the magnitude of the blood flow components obtained will not be made between approaches, since what was important at this stage was the relation between the expected and the obtained blood flow components for each approach.

When observing the results obtained through the processing of the experimental signal, obtained by BPS (section 5.2) and after the application of the heterodyne technique (section 5.3), the first thing that is visible is that the noise intensity is greater when the signal is acquired after heterodyning than when the signal is directly sampled . From section 3.2.5, it is referred that SNR is not preserved when using BPS [50] [58]. However, for the implemented systems which were used in this thesis to acquire signals, the intensity of the noise is smaller using the BPS strategy than using the heterodyning technique with the developed PLL-based frequency synthesizer, mixer and filters.

Based on the comments reported in sections 5.2.7 and 5.3.7, it can be concluded that (with the exception of the slight variation in the frequency components location in the experimental signal acquired after the heterofyne technique, by the reasons explained in section 5.3.7) both strategies behave well for signal acquisition. Both sampling strategies allowed an acquisition of the RF (or a downconversion of it) without loss of information in the desired bandwidth.

A comment must to be made concerning with what happens in the strategies where a signal,

sampled at 4 times its carrier frequency, is multiplied by a given four digit sequence. From the various tests performed, although this mechanism might be useful (specially in approach 2, where such four digit sequences not only translate the signal by $\frac{Fs}{4}$ but also generate the signal's I and Q components) it demands a rigid control over the sampling frequency and the signal's carrier frequency. If one of the parameters is not well controlled, deviations from the expected behaviour will occur. In case of approach 1, where the sampling frequency is always larger than twice the signal's maximum frequency component, the only real concern is the signal's carrier frequency value.

6.3 General Conclusions

As stated in a previous chapter, and according to the general system's constraints, only approach 4 (see section 3.3.3) did not satisfy the main goal of this project, this is, the adequate identification of I and Q signal's components, for proper blood flow forward and reverse components separation.

It can be observed for approach 4 (see figure 5.46), that contamination of forward blood flow components by reverse blood flow components are present, and vice-versa. Such contaminations become more visible (present higher power) as the order of the allpass filters lowers (see figures 5.50 and 5.52). All other approaches allow proper blood flow separation.

For the experimental signals acquired, from the developed hardware, the noise amplitude is lower when the RF signal is directly sampled (BPS strategy) than when the RF signal is sampled after heterodyning (for the hardware used) in order to obtain a downconversion version of such signal.

Comparing expected forward and reverse blood flow spectral content (frequency locations and amplitudes) with obtained results (section 5.1), all approaches (except approach 4 which presents contaminations as previously described) present good results, although at some frequencies slight differences in amplitude are present.

Based on what was previously stated, and given the problems described in the present analog solution (section 3.3.1), approaches 2, 3 and 5 should be considered as digital alternatives to the analog system's demodulator currently used in the SUCoDiC project, and to be tested in real-time implementation (figure 6.2). In the specific case of approach 5, decimation by 2 is inherent to the technique which can make it more suitable for real-time implementation. The other approaches need an additional decimation block, which will be time consuming. Nevertheless all of these techniques may be implemented in real-time.

Regarding the metodology employed to acquired the signal (direct RF BPS or sampling after the RF signal has been downconverted by the heterodyne function), and considering the developed circuitry for this thesis, BPS presents itself as a more flexible, adaptable and with less noise (for the testing environment conditions) than when compared with the application of the heterodyne function.

Real-time implementation of the selected approaches (figure 6.2) will dictate which of the above mentioned demodulator systems will performs best on clinical environment.

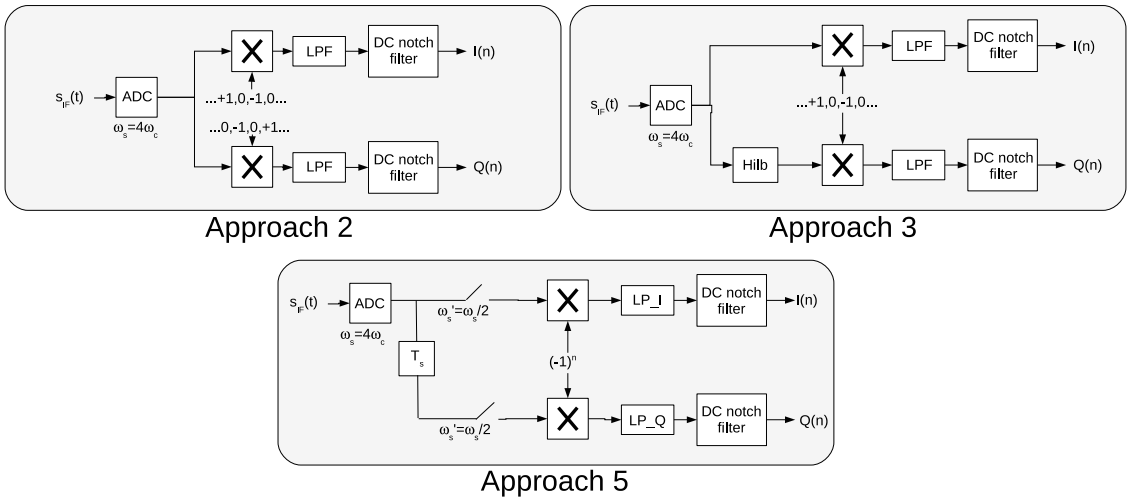

Figure 6.2: Approaches to be considered for real-time implementation, as digital alternatives to the currently used analog system's demodulator in the SUCoDiC project

From the proposed goals (see section 1.2), the last one, involving real-time implementation of the selected approaches was not fulfilled. The reasons for this was in first place related to the time spent in acquiring knowledge related to the various theoretical aspects presented in this thesis. Second, the amount of time spent in developing the required hardware circuits. Third, and last, the expected time duration for the elaboration of a thesis in the course curriculum is of 4 modules of 6 weeks each [113], amount of time already exceeded.

6.4 Future research lines

For future research lines the following sugestions should be taken into account:

- Implementation of the selected digital quadrature techniques for real-time processing.
- Adaptive techniques could be a good solution for noise cancelation and to adjust the lowpass filters bandwidth based on the distribution of the power spectral density.
- In this thesis it was only considered uniform bandpass sampling, however second-order sampling theorem should be considered [50], because with such strategy the allowed minimum sampling rate can be applied independently of the signal's band position.
- Enhanced versions of the used circuits for BPS and heterodyning should be made. In the first case a narrower bandpass filter should be built, and in the last case better frequency synthesizer should be constructed.
- Finally, with the enhanced circuitry, real RF Doppler signal should be processed. Posterior comparison between the results from the studied digital quadrature techniques and the results from the existing system [40] should be performed.

Chapter 7

Appendixes

Appendix A

Acronyms

ADC Analog-to-Digital Converter

API Application Programming Interface

BPF Bandpass Filter

BPS Bandpass Sampling

CW Continuous Wave

FFT Fast Fourier Transform

FIR Finite Impulse Response

FM Frequency Modulated

FT Fourier Transform

GUI Graphical User Interface

HPF Highpass Filter

I inphase

IF Intermediate Frequency

IIR Infinite Impulse Response

LPF Lowpass Filter

NI National Instruments

PCB Printed Card Board

PD Phase Detector

PLL Phase Locked Loop

PW Pulsed Wave

Q quadrature

RF radiofrequency

SNR Signal-to-Noise Ratio

SSB Single Sideband Detection

SUCoDiC Desarrollo de Sistemas Ultrasónicos y Computacionales para Diagnóstico Cardiovascular

TTFM Transit-Time Flow Measurements

VCO Voltage Controlled Oscillator

Appendix B

Relationship between allowed sampling frequencies in [6] and [50]

Lyons [6], presents an expression that relates, as in [50], the allowed sampling frequencies with the maximum and minimum frequency component values preset in the bandpass signal, but with different denominators.

In [50] there is the following expression

$$\frac{2f_U}{n} \leq f_s \leq \frac{2f_L}{n-1} \tag{B.1}$$

where n is an integer given by

$$1 \leq n \leq I_g\left[\frac{f_U}{B}\right] \tag{B.2}$$

with $I_g\left[\frac{f_U}{B}\right]$ representing the largest integer within $\frac{f_U}{B}$.

In [6] a similar relation is presented

$$\frac{2f_U}{m+1} \leq f_s \leq \frac{2f_L}{m} \tag{B.3}$$

where m is an arbitrary positive integer ensuring that $f_s \geq 2B$.

Lets consider the signal used in the book [6], which has a bandwidth of 5 MHz centered in a carrier of 20 MHz, having $f_U = 22.5\ MHz$ and $f_L = 17.5\ MHz$. This signal's spectrum is shown in figure B.1.

Observing the values of m in (B.3) with the values of n in (B.1), both changing from 1 to 4, presented in table B.1 we can conclude three things:

1. Both relations (B.1) and (B.3) present the same results for the allowed sampling frequencies, although with different values for m and n, such that for a given range of sampling frequencies $m = n - 1$.

2. When $n = 1$ the allowed range of sampling frequencies is $[45\ MHz \leq f_s \leq \infty]$, which is the lowpass case for sampling (Shannon's theorem) [50]

3. Lyons states that in equation (B.3) whenever m is an odd integer it will occur spectral inversion (see page 43 of [6]). This means that using the relation (B.1) spectral inversion will occur if n is even.

m	$\frac{2f_U}{m+1} \leq f_s$	$f_s \leq \frac{2f_L}{m}$
1	22.50	35.00
2	15.00	17.50
3	11.25	11.67
4(*)	9.00	8.75

(A)

n	$\frac{2f_U}{n} \leq f_s$	$f_s \leq \frac{2f_L}{n-1}$
1	45.00	∞
2	22.50	35.00
3	15.00	17.50
4	11.25	11.67

(B)

Table B.1: Table comparing the allowed sampling frequencies using (B.3) in (A) and (B.1) in (B). *(*)* with this value of m the obtained sampling frequencies do not fulfil the relation $f_s \geq 2B$

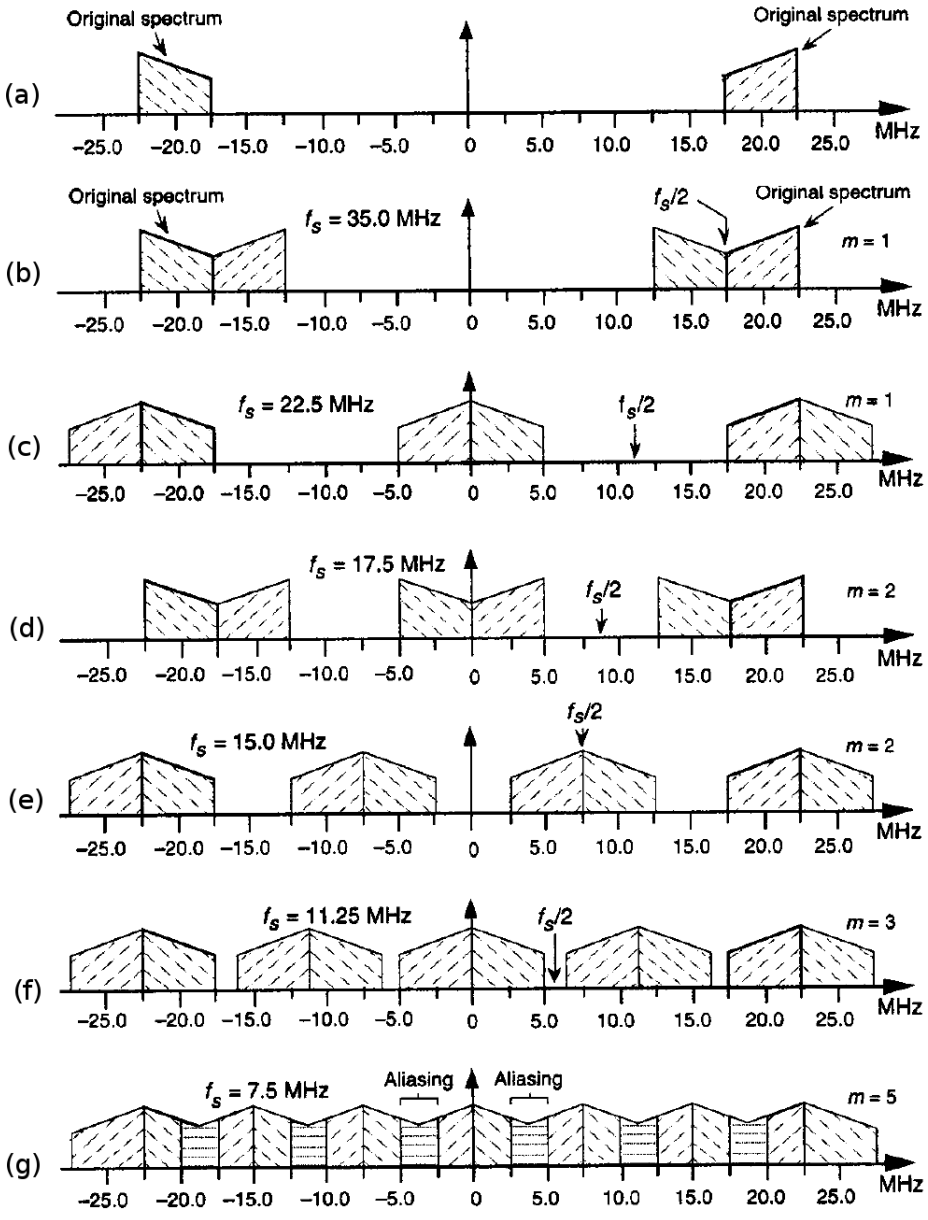

Figure B.1: Spectral replications of the bandpass continuous signal whose spectrum is presented in (a), as the sampling frequency changes: (b) $f_s = 35MHz$; (c) $f_s = 22.5MHz$; (d) $f_s = 17.5MHz$; (e) $f_s = 15MHz$; (f) $f_s = 11.25MHz$;(g) $f_s = 7.5MHz$;(Adapted from figure 2-9 in [6])

Appendix C

PLL-based Frequency Syntesizer Characterization Plots

For each of the values of ξ in table 4.1, the PLL-based frequency synthesizer was characterized by:

- the phase margin and the gain margin, obtained by the Bode plot of the feedforward transfer function (equation (3.9)) [18] [26];
- it's stability, using the root locus [24] [25];
- the error-transfer function [25] (equation (3.8));
- it's step response [24] [25];

The plots for each value of ξ are presented in the next sections.

C.1 Results for ξ=0.65

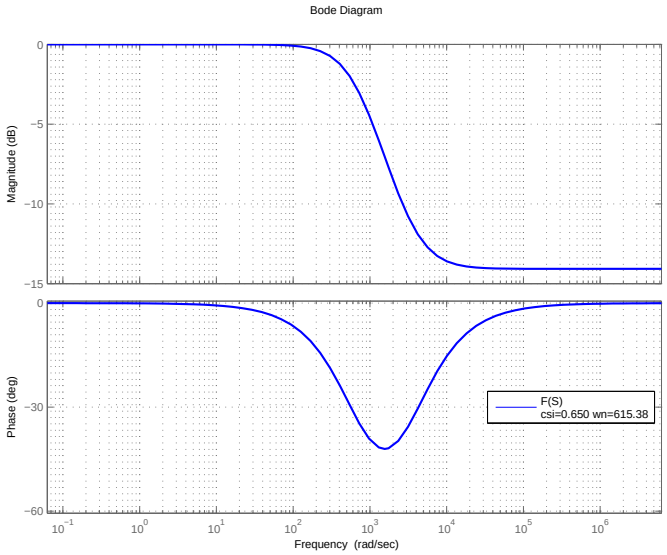

Figure C.1: Bode plot of the loop filter transfer function when ξ=0.65 and $\omega_n = 615.38\ rad/s$

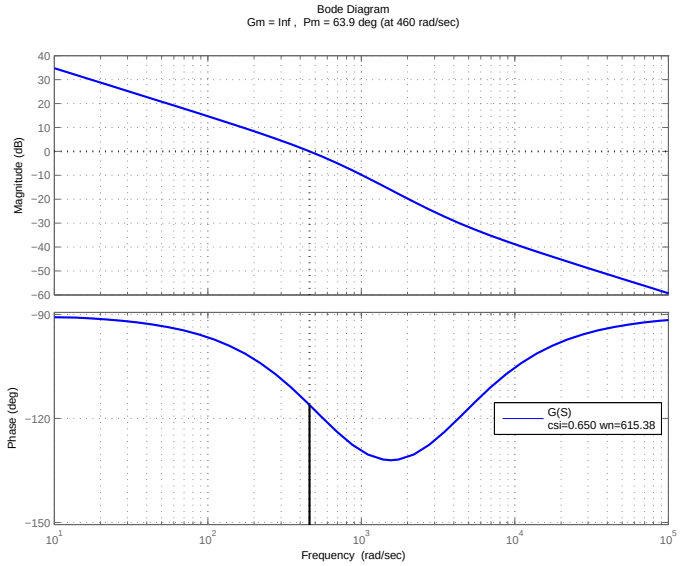

Figure C.2: Bode plot of the feedforward transfer function when ξ=0.65 and $\omega_n = 615.38\ rad/s$

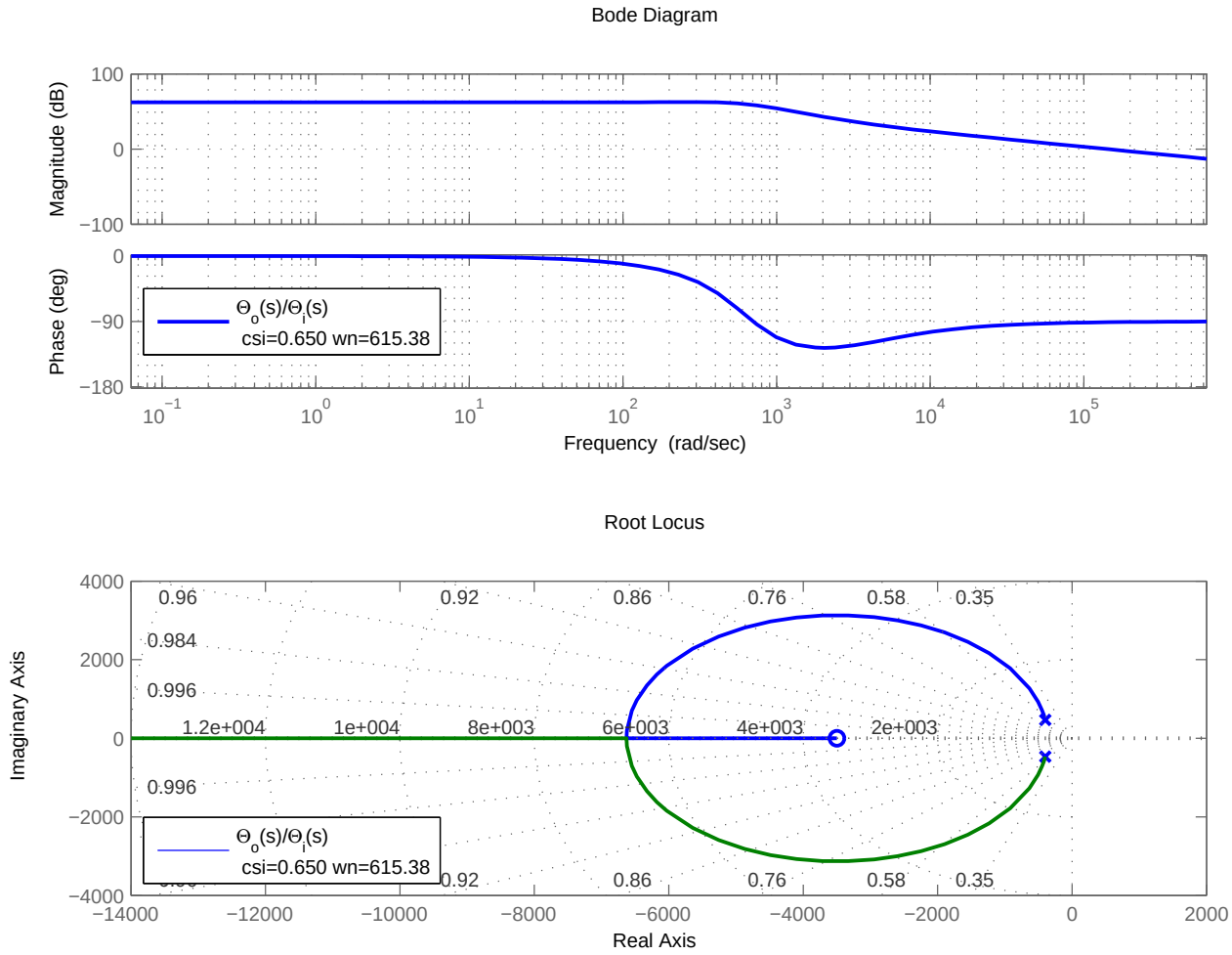

Figure C.3: Bode plot of the closed loop transfer function (equation (3.4)) (top plot) and the root locus (bottom plot) when ξ=0.65 and $\omega_n = 615.38\ rad/s$

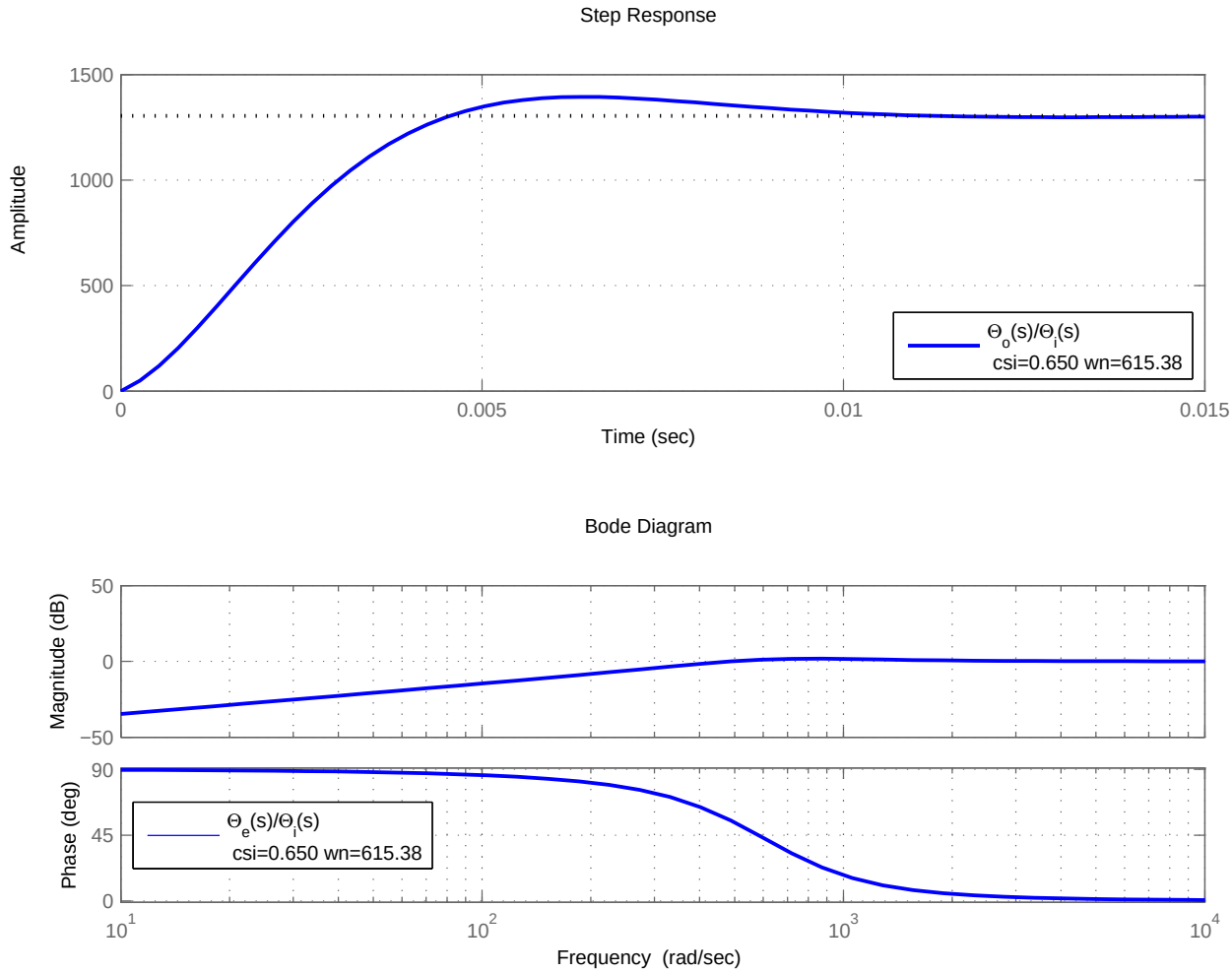

Figure C.4: Step response (top plot) and Bode plot (bottom plot) of the error transfer function (equation (3.8)) when ξ=0.65 and $\omega_n = 615.38\ rad/s$

C.2 Results for ξ=0.707

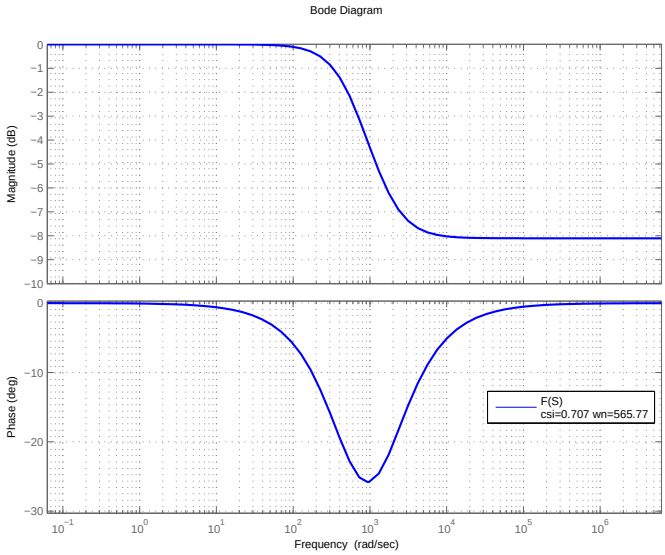

Figure C.5: Bode plot of the loop filter transfer function when ξ=0.707 and $\omega_n = 565.77\ rad/s$

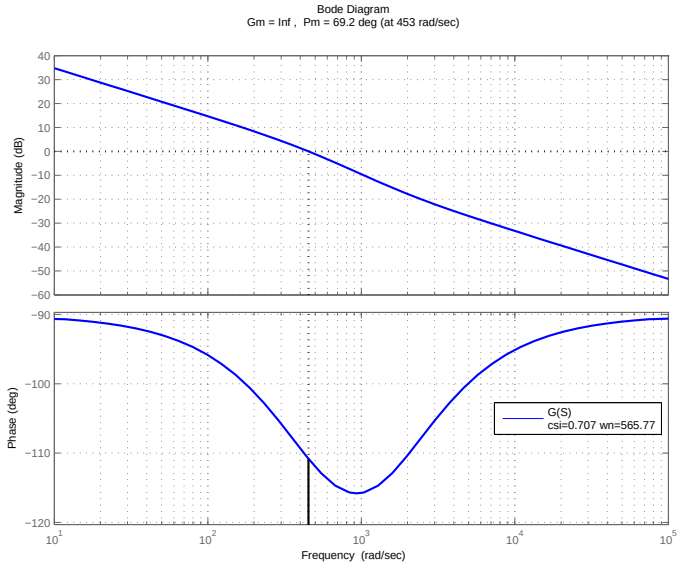

Figure C.6: Bode plot of the feedforward transfer function when ξ=0.707 and $\omega_n = 565.77\ rad/s$

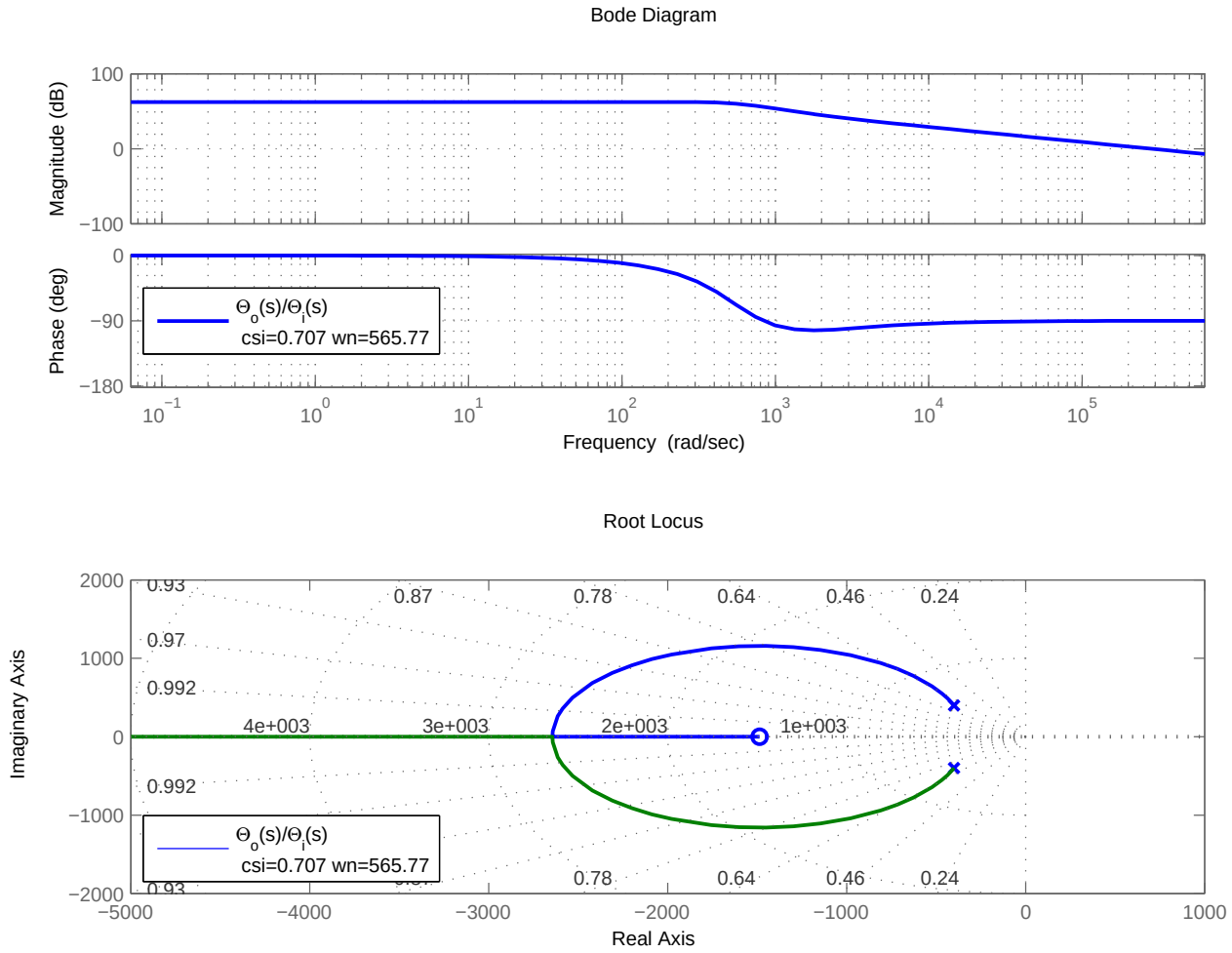

Figure C.7: Bode plot of the closed loop transfer function (equation (3.4)) (top plot) and the root locus (bottom plot) when ξ=0.707 and $\omega_n = 565.77\ rad/s$

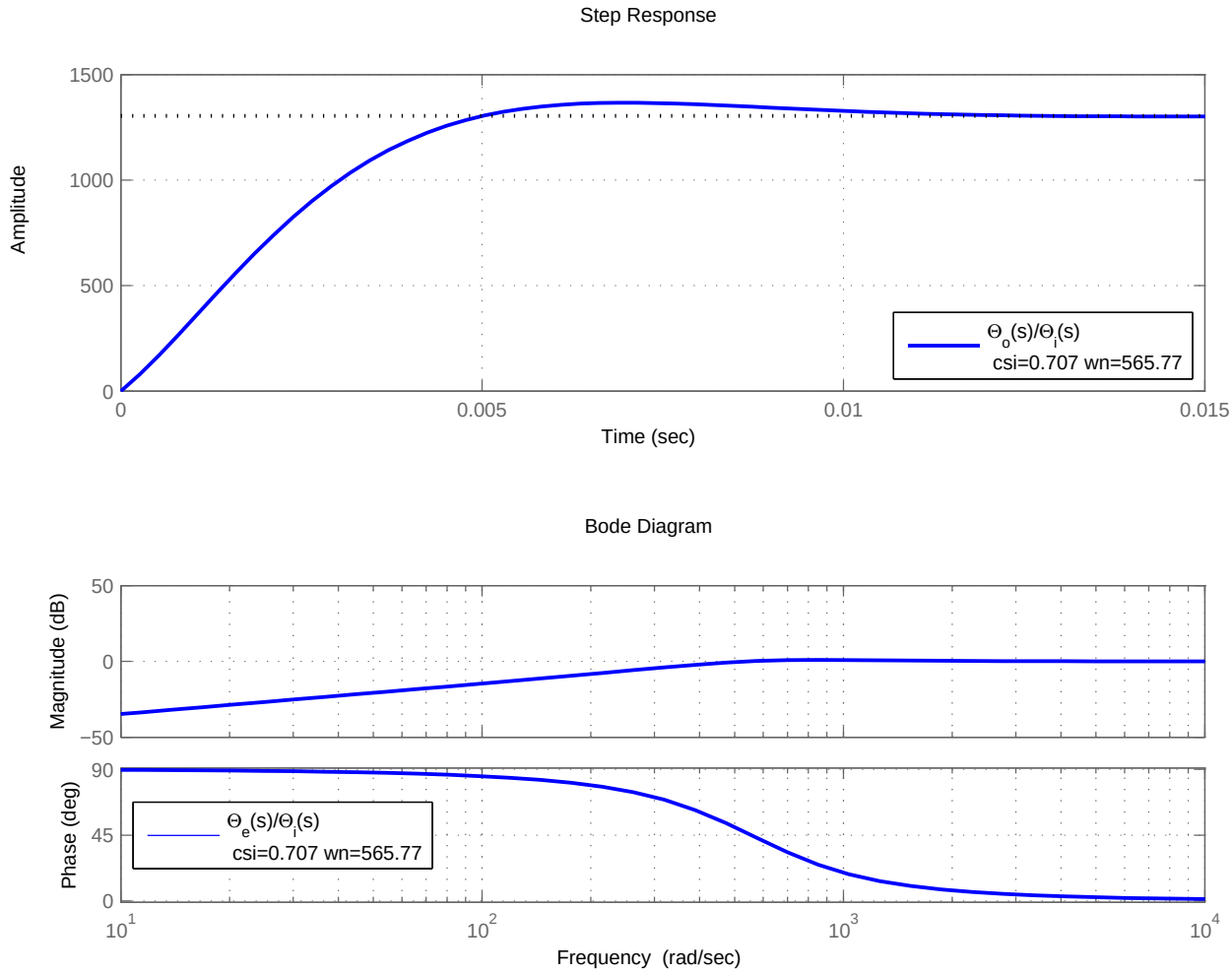

Figure C.8: Step response (top plot) and Bode plot (bottom plot) of the error transfer function (equation (3.8)) when ξ=0.707 and $\omega_n = 565.77\ rad/s$

C.3 Results for ξ=0.80

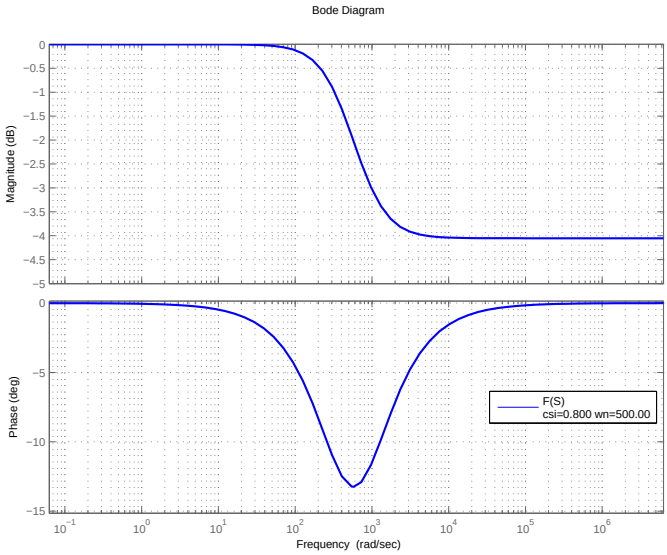

Figure C.9: Bode plot of the loop filter transfer function when ξ=0.80 and $\omega_n = 500.00\ rad/s$

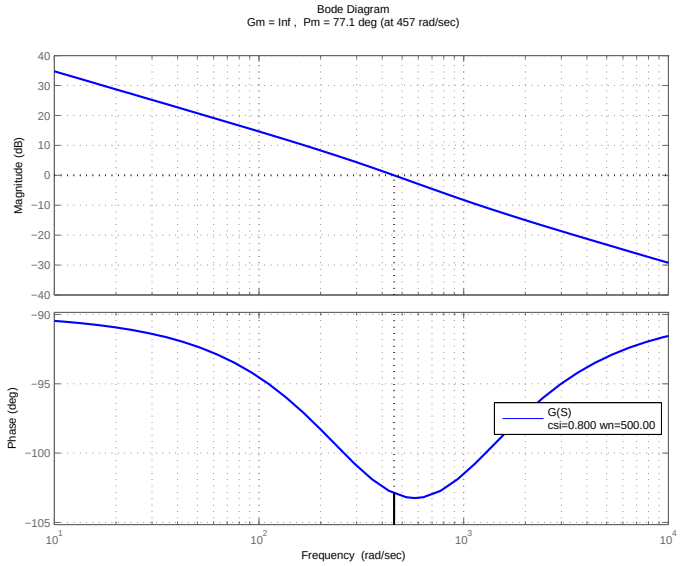

Figure C.10: Bode plot of the feedforward transfer function when ξ=0.80 and $\omega_n = 500.00\ rad/s$

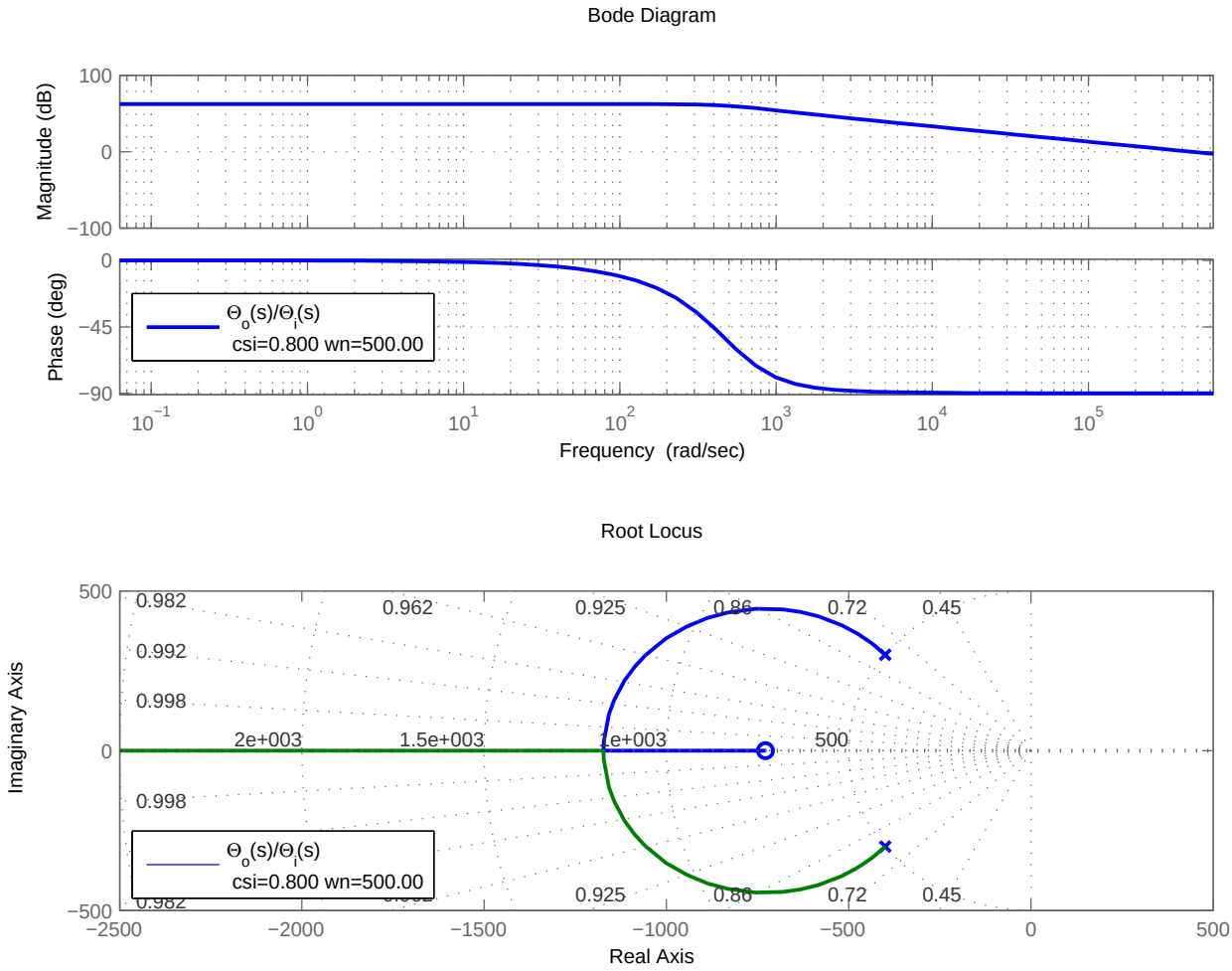

Figure C.11: Bode plot of the closed loop transfer function (equation (3.4)) (top plot) and the root locus (bottom plot) when ξ=0.80 and $\omega_n = 500.00\ rad/s$

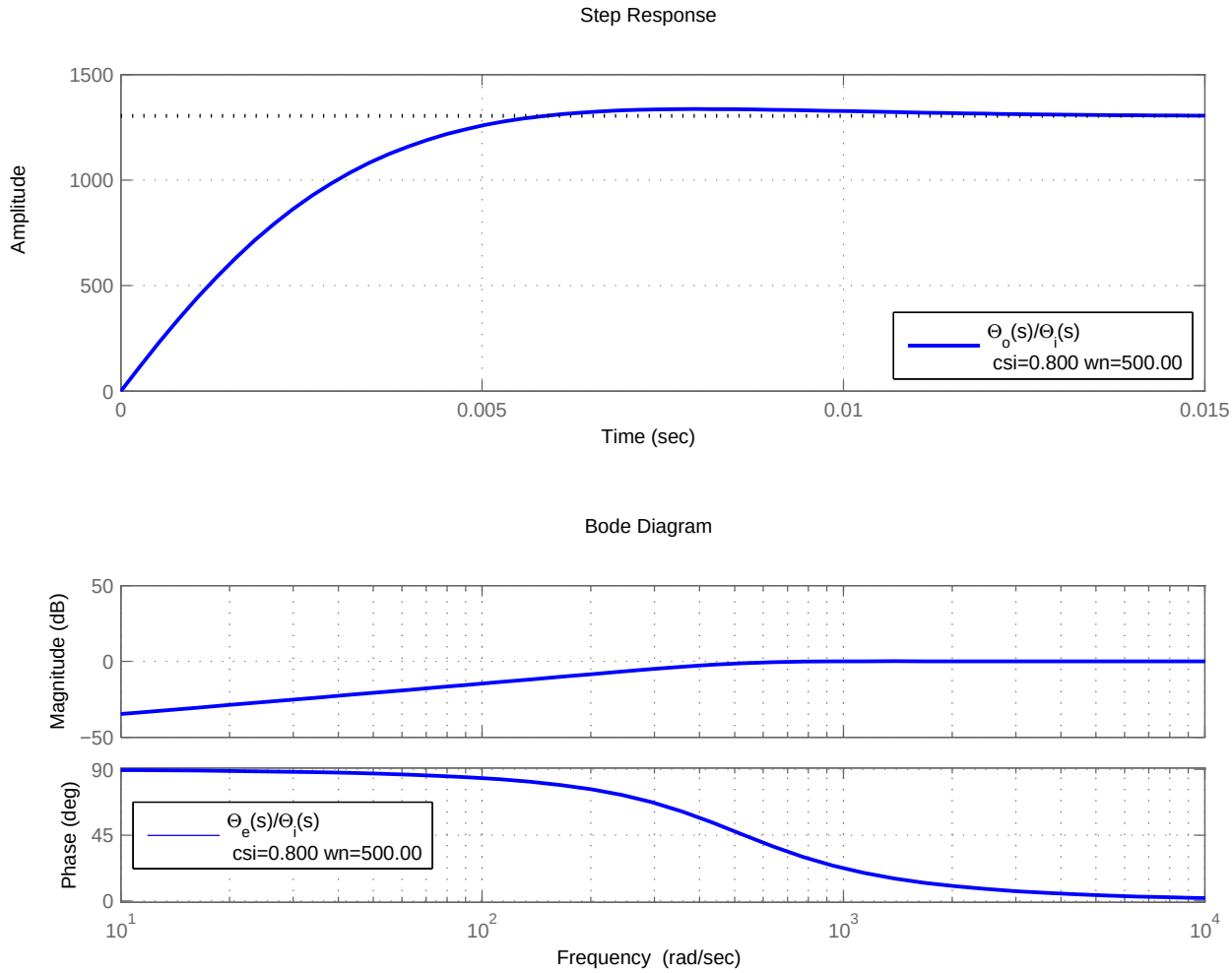

Figure C.12: Step response (top plot) and Bode plot (bottom plot) of the error transfer function (equation (3.8)) when ξ=0.80 and $\omega_n = 500.00\ rad/s$

C.4 Results for ξ=0.90

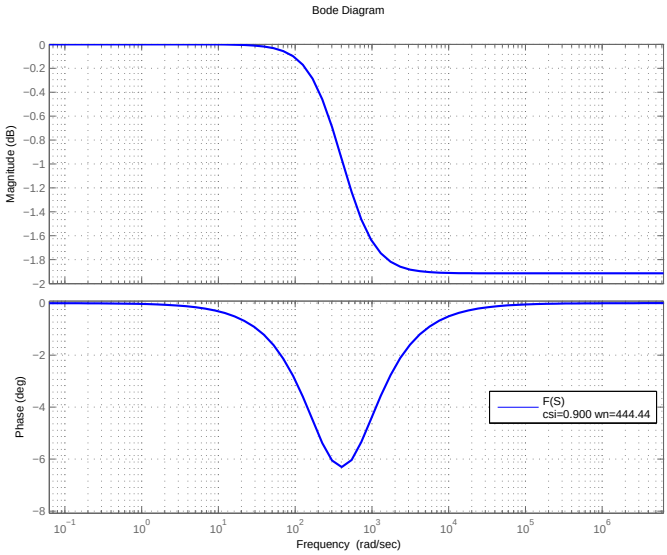

Figure C.13: Bode plot of the loop filter transfer function when ξ=0.90 and $\omega_n = 444.44\ rad/s$

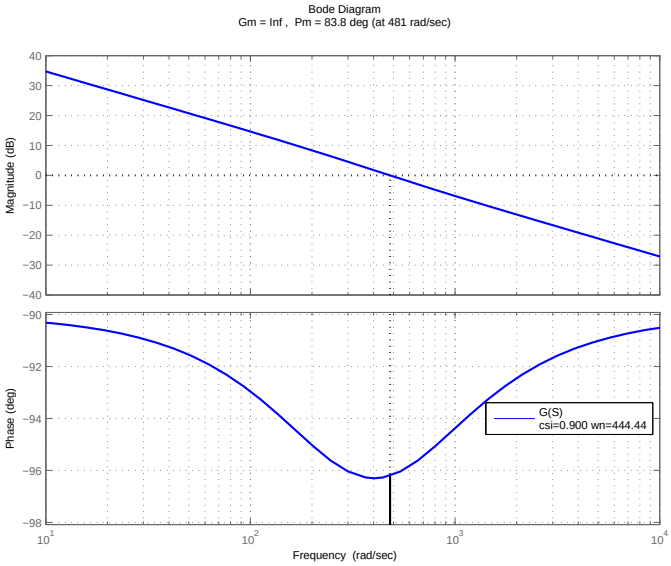

Figure C.14: Bode plot of the feedforward transfer function when ξ=0.90 and $\omega_n = 444.44\ rad/s$

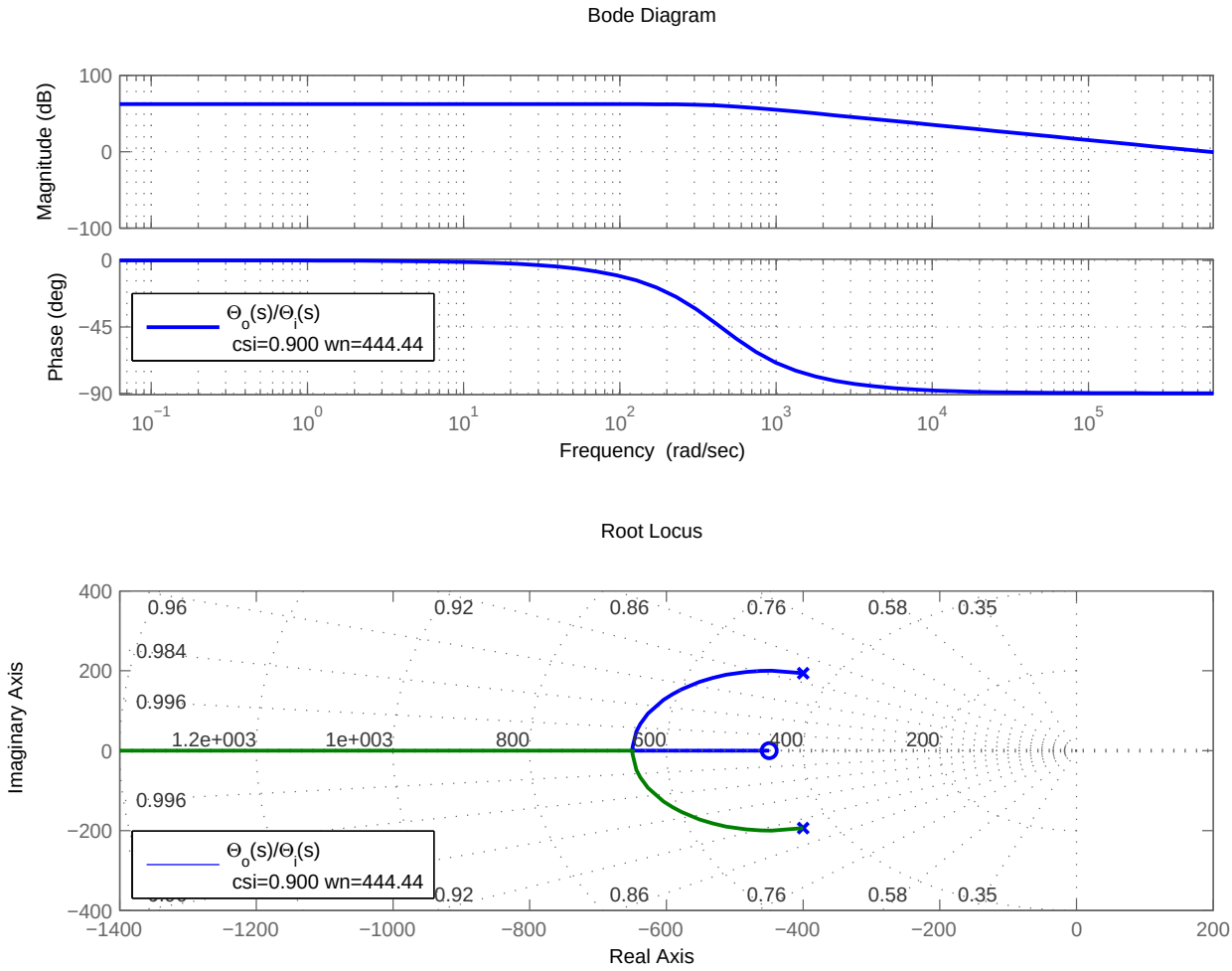

Figure C.15: Bode plot of the closed loop transfer function (equation (3.4)) (top plot) and the root locus (bottom plot) when ξ=0.90 and $\omega_n = 444.44\ rad/s$

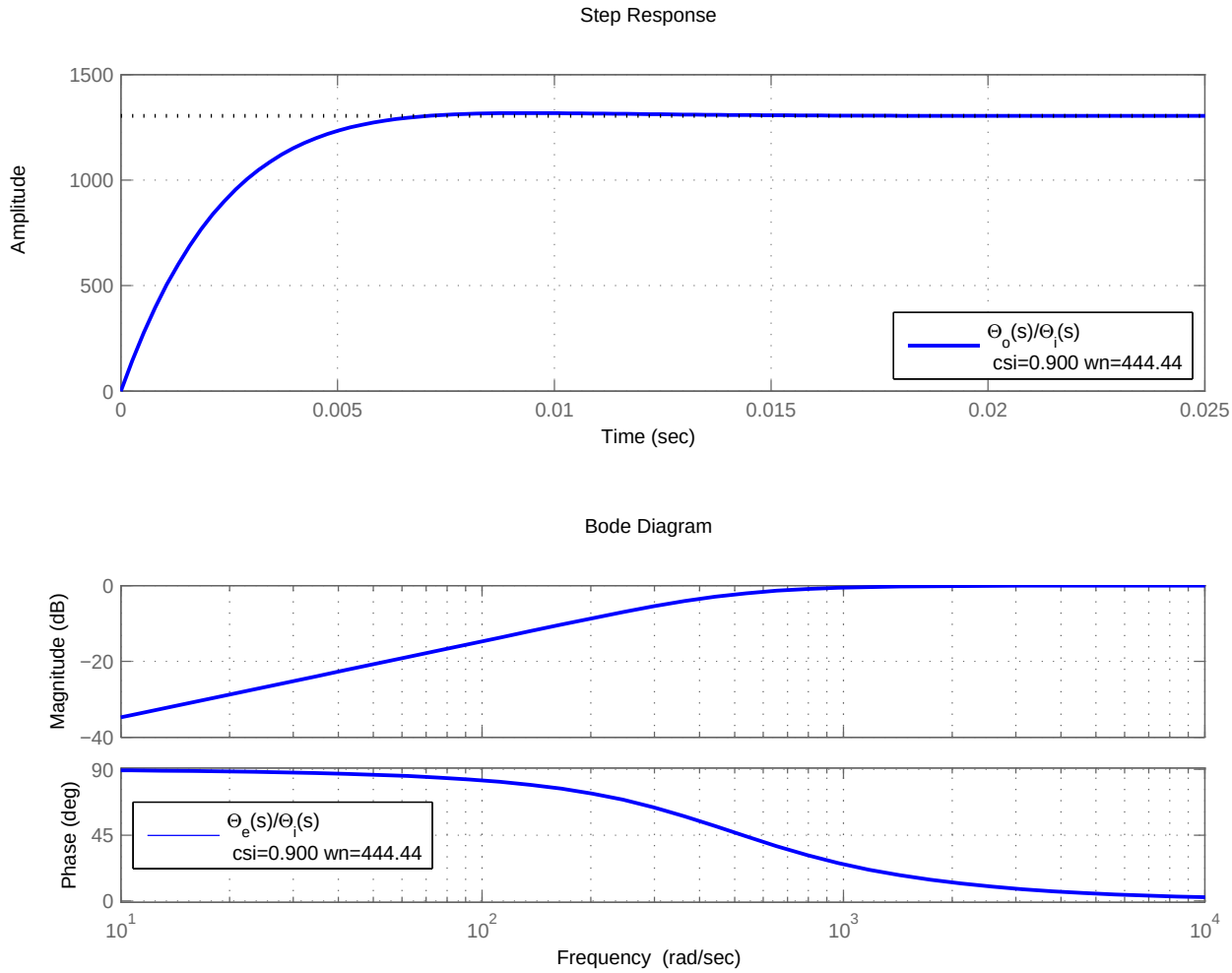

Figure C.16: Step response (top plot) and Bode plot (bottom plot) of the error transfer function (equation (3.8)) when ξ=0.90 and $\omega_n = 444.44\ rad/s$

Appendix D

Predicted Spectra for signals $I''(t)$ and $Q''(t)$

Lets consider a simplified IF signal represented by the expression [28]

$$s_{IF}(t) = A_C \cos(\omega_C \cdot t + \phi_C) + A_F \cos\left[(\omega_C + \omega_F) \cdot t + \phi_F\right] + A_R \cos\left[(\omega_C - \omega_R) \cdot t + \phi_R\right]$$

where $\{C, F, R\}$ represents, respectively, the carrier, forward blood flow and reverse blood flow.

- A_i with $i = \{C, F, R\}$ are the amplitudes of the signal's components;
- ω_i with $i = \{C, F, R\}$ are the frequencies of the signal's components ;
- ϕ_i with $i = \{C, F, R\}$ are the phases of the signal's components;

Making the variable change $\beta = f_C + f_F$ and $\psi = f_C - f_R$, the previous equation can be written as

$$s_{IF}(t) = A_C \cos(2\pi f_C \cdot t + \phi_C) + A_F \cos(2\pi\beta \cdot t + \phi_F) + A_R \cos(2\pi\psi \cdot t + \phi_R)$$

Lets consider the mixing operation presented in the Quadrature Phase Selection block diagram 2.5, on page 12. If we assume that the phases of the cosine and sine waves are not null, but for instances both equal to ϕ, then

$$\begin{aligned} I''(t) &= s_{IF}(t) \cdot \cos(\omega_C \cdot t + \phi) \\ Q''(t) &= s_{IF}(t) \cdot \sin(\omega_C \cdot t + \phi) \end{aligned}$$

Working in the frequency domain, knowing that [11][29][12][13]

- $FT\left[x(t).y(t)\right] = X(f) * Y(f)$
- $\cos(\omega_C \cdot t + \phi) = \frac{1}{2}\left[e^{j(\omega_C \cdot t + \phi)} + e^{-j(\omega_C \cdot t + \phi)}\right]$

- $FT\left[\cos(2\pi f_C \cdot t + \phi)\right] = \frac{1}{2}\left[e^{j\phi}\delta(f - f_C) + e^{-j\phi}\delta(f + f_C)\right]$
- $\sin(2\pi f_C \cdot t + \phi) = \frac{1}{2j}\left[e^{j(\omega_C \cdot t + \phi)} - e^{-j(\omega_C \cdot t + \phi)}\right]$
- $FT\left[\sin(2\pi f_C \cdot t + \phi)\right] = \frac{1}{2j}\left[e^{j\phi}\delta(f - f_C) - e^{-j\phi}\delta(f + f_C)\right]$

then

$$\begin{aligned} S_{IF}(f) &= \frac{A_C}{2}e^{j\phi_C}\delta(f - f_C) + \frac{A_C}{2}e^{-j\phi_C}\delta(f + f_C) \\ &+ \frac{A_F}{2}e^{j\phi_F}\delta(f - \beta) + \frac{A_F}{2}e^{-j\phi_F}\delta(f + \beta) \\ &+ \frac{A_R}{2}e^{j\phi_R}\delta(f - \psi) + \frac{A_R}{2}e^{-j\phi_R}\delta(f + \psi) \end{aligned}$$

For the **Inphase Component** we have:

$$
\begin{aligned}
I''(f) &= S_{IF}(f) * \left\{ \frac{1}{2} \left[e^{j\phi}\delta(f - f_C) + e^{-j\phi}\delta(f + f_C) \right] \right\} \\
&= \frac{1}{2} \left[e^{j\phi} S_{IF}(f - f_C) + e^{-j\phi} S_{IF}(f + f_C) \right] \\
&= \frac{A_C}{4} e^{j\phi} e^{j\phi_C} \delta(f - f_C - f_C) + \frac{A_C}{4} e^{j\phi} e^{-j\phi_C} \delta(f + f_C - f_C) \\
&+ \frac{A_F}{4} e^{j\phi} e^{j\phi_F} \delta(f - \beta - f_C) + \frac{A_F}{4} e^{j\phi} e^{-j\phi_F} \delta(f + \beta - f_C) \\
&+ \frac{A_R}{4} e^{j\phi} e^{j\phi_R} \delta(f - \psi - f_C) + \frac{A_R}{4} e^{j\phi} e^{-j\phi_R} \delta(f + \psi - f_C) \\
&+ \frac{A_C}{4} e^{-j\phi} e^{j\phi_C} \delta(f - f_C + f_C) + \frac{A_C}{4} e^{-j\phi} e^{-j\phi_C} \delta(f + f_C + f_C) \\
&+ \frac{A_F}{4} e^{-j\phi} e^{j\phi_F} \delta(f - \beta + f_C) + \frac{A_F}{4} e^{-j\phi} e^{-j\phi_F} \delta(f + \beta + f_C) \\
&+ \frac{A_R}{4} e^{-j\phi} e^{j\phi_R} \delta(f - \psi + f_C) + \frac{A_R}{4} e^{-j\phi} e^{-j\phi_R} \delta(f + \psi + f_C) \\
\Leftrightarrow I''(f) &= \frac{A_C}{4} e^{j\phi} e^{j\phi_C} \delta(f - 2f_C) + \frac{A_C}{4} e^{j\phi} e^{-j\phi_C} \delta(f) \\
&+ \frac{A_F}{4} e^{j\phi} e^{j\phi_F} \delta[f - (2f_C + f_F)] + \frac{A_F}{4} e^{j\phi} e^{-j\phi_F} \delta(f + f_F) \\
&+ \frac{A_R}{4} e^{j\phi} e^{j\phi_R} \delta[f - (2f_C - f_R)] + \frac{A_R}{4} e^{j\phi} e^{-j\phi_R} \delta(f - f_R) \\
&+ \frac{A_C}{4} e^{-j\phi} e^{j\phi_C} \delta(f) + \frac{A_C}{4} e^{-j\phi} e^{-j\phi_C} \delta(f + 2f_C) \\
&+ \frac{A_F}{4} e^{-j\phi} e^{j\phi_F} \delta(f - f_F) + \frac{A_F}{4} e^{-j\phi} e^{-j\phi_F} \delta[f + (2f_C + f_F)] \\
&+ \frac{A_R}{4} e^{-j\phi} e^{j\phi_R} \delta(f + f_R) + \frac{A_R}{4} e^{-j\phi} e^{-j\phi_R} \delta[f + (2f_C - f_R)]
\end{aligned}
$$

$$
\begin{aligned}
\Leftrightarrow I''(f) &= \frac{A_C}{4}e^{j(\phi-\phi_C)}\delta(f) + \frac{A_C}{4}e^{-j(\phi-\phi_C)}\delta(f) \\
&+ \frac{A_C}{4}e^{j(\phi+\phi_C)}\delta(f-2f_C) + \frac{A_C}{4}e^{-j(\phi+\phi_C)}\delta(f+2f_C) \\
&+ \frac{A_F}{4}e^{j(-\phi+\phi_F)}\delta(f-f_F) + \frac{A_F}{4}e^{-j(-\phi+\phi_F)}\delta(f+f_F) \\
&+ \frac{A_R}{4}e^{j(\phi-\phi_R)}\delta(f-f_R) + \frac{A_R}{4}e^{-j(\phi-\phi_R)}\delta(f+f_R) \\
&+ \frac{A_F}{4}e^{j(\phi+\phi_F)}\delta[f-(2f_C+f_F)] + \frac{A_F}{4}e^{-j(\phi+\phi_F)}\delta[f+(2f_C+f_F)] \\
&+ \frac{A_R}{4}e^{j(\phi+\phi_R)}\delta[f-(2f_C-f_R)] + \frac{A_R}{4}e^{-j(\phi+\phi_R)}\delta[f+(2f_C-f_R)]
\end{aligned}
$$

Passing to the time domain, we get $I''(t)$ equal to

$$
\begin{aligned}
I''(t) &= \frac{A_C}{2}\cos(\phi-\phi_C) \\
&+ \frac{A_F}{2}\cos[2\pi f_F\cdot t + (\phi_F-\phi)] \\
&+ \frac{A_R}{2}\cos[2\pi f_R\cdot t + (\phi-\phi_R)] \\
&+ \frac{A_C}{2}\cos[2\pi(2f_C)\cdot t + (\phi+\phi_C)] \\
&+ \frac{A_F}{2}\cos[2\pi(2f_C+f_F)\cdot t + (\phi+\phi_F)] \\
&+ \frac{A_R}{2}\cos[2\pi(2f_C-f_R)\cdot t + (\phi+\phi_R)]
\end{aligned}
$$

where the term $\frac{A_C}{2}\cos(\phi-\phi_C)$ is the DC term, which is only zero if $\phi-\phi_C = \pm\frac{\pi}{2}$

For the **Quadrature Component** we have:

$$
\begin{aligned}
Q''(f) &= S_{IF}(f) * \left\{ \frac{1}{2j} \left[e^{j\phi}\delta(f - f_C) - e^{-j\phi}\delta(f + f_C) \right] \right\} \\
&= \frac{1}{2j} \left[e^{j\phi} S_{IF}(f - f_C) - e^{-j\phi} S_{IF}(f + f_C) \right] \\
&= \frac{A_C}{4j} e^{j\phi} e^{j\phi_C} \delta(f - f_C - f_C) + \frac{A_C}{4j} e^{j\phi} e^{-j\phi_C} \delta(f + f_C - f_C) \\
&+ \frac{A_F}{4j} e^{j\phi} e^{j\phi_F} \delta(f - \beta - f_C) + \frac{A_F}{4j} e^{j\phi} e^{-j\phi_F} \delta(f + \beta - f_C) \\
&+ \frac{A_R}{4j} e^{j\phi} e^{j\phi_R} \delta(f - \psi - f_C) + \frac{A_R}{4j} e^{j\phi} e^{-j\phi_R} \delta(f + \psi - f_C) \\
&- \frac{A_C}{4j} e^{-j\phi} e^{j\phi_C} \delta(f - f_C + f_C) - \frac{A_C}{4j} e^{-j\phi} e^{-j\phi_C} \delta(f + f_C + f_C) \\
&- \frac{A_F}{4j} e^{-j\phi} e^{j\phi_F} \delta(f - \beta + f_C) - \frac{A_F}{4j} e^{-j\phi} e^{-j\phi_F} \delta(f + \beta + f_C) \\
&- \frac{A_R}{4j} e^{-j\phi} e^{j\phi_R} \delta(f - \psi + f_C) - \frac{A_R}{4j} e^{-j\phi} e^{-j\phi_R} \delta(f + \psi + f_C) \\
\Leftrightarrow Q''(f) &= \frac{A_C}{4j} e^{j\phi} e^{j\phi_C} \delta(f - 2f_C) + \frac{A_C}{4j} e^{j\phi} e^{-j\phi_C} \delta(f) \\
&+ \frac{A_F}{4j} e^{j\phi} e^{j\phi_F} \delta[f - (2f_C + f_F)] + \frac{A_F}{4j} e^{j\phi} e^{-j\phi_F} \delta(f + f_F) \\
&+ \frac{A_R}{4j} e^{j\phi} e^{j\phi_R} \delta[f - (2f_C - f_R)] + \frac{A_R}{4j} e^{j\phi} e^{-j\phi_R} \delta(f - f_R) \\
&- \frac{A_C}{4j} e^{-j\phi} e^{j\phi_C} \delta(f) - \frac{A_C}{4j} e^{-j\phi} e^{-j\phi_C} \delta(f + 2f_C) \\
&- \frac{A_F}{4j} e^{-j\phi} e^{j\phi_F} \delta(f - f_F) - \frac{A_F}{4j} e^{-j\phi} e^{-j\phi_F} \delta[f + (2f_C + f_F)] \\
&- \frac{A_R}{4j} e^{-j\phi} e^{j\phi_R} \delta(f + f_R) - \frac{A_R}{4j} e^{-j\phi} e^{-j\phi_R} \delta[f + (2f_C - f_R)]
\end{aligned}
$$

$$
\begin{aligned}
\Leftrightarrow Q''(f) &= \frac{A_C}{4j}e^{j(\phi-\phi_C)}\delta(f) - \frac{A_C}{4j}e^{-j(\phi-\phi_C)}\delta(f) \\
&+ \frac{A_C}{4j}e^{j(\phi+\phi_C)}\delta(f-2f_C) - \frac{A_C}{4j}e^{-j(\phi+\phi_C)}\delta(f+2f_C) \\
&+ \frac{A_F}{4j}e^{j(-\phi+\phi_F)}\delta(f-f_F) - \frac{A_F}{4j}e^{-j(-\phi+\phi_F)}\delta(f+f_F) \\
&+ \frac{A_R}{4j}e^{j(\phi-\phi_R)}\delta(f-f_R) - \frac{A_R}{4j}e^{-j(\phi-\phi_R)}\delta(f+f_R) \\
&+ \frac{A_F}{4j}e^{j(\phi+\phi_F)}\delta[f-(2f_C+f_F)] - \frac{A_F}{4j}e^{-j(\phi+\phi_F)}\delta[f+(2f_C+f_F)] \\
&+ \frac{A_R}{4j}e^{j(\phi+\phi_R)}\delta[f-(2f_C-f_R)] - \frac{A_R}{4j}e^{-j(\phi+\phi_R)}\delta[f+(2f_C-f_R)]
\end{aligned}
$$

Passing to the time domain, we get $Q''(t)$ equal to

$$
\begin{aligned}
I''(t) &= \frac{A_C}{2}\sin(\phi-\phi_C) \\
&- \frac{A_F}{2}\sin[2\pi f_F\cdot t+(\phi_F-\phi)] \\
&+ \frac{A_R}{2}\sin[2\pi f_R\cdot t+(\phi-\phi_R)] \\
&+ \frac{A_C}{2}\sin[2\pi(2f_C)\cdot t+(\phi+\phi_C)] \\
&+ \frac{A_F}{2}\sin[2\pi(2f_C+f_F)\cdot t+(\phi+\phi_F)] \\
&+ \frac{A_R}{2}\sin[2\pi(2f_C-f_R)\cdot t+(\phi+\phi_R)]
\end{aligned}
$$

where the term $\frac{A_C}{2}\sin(\phi-\phi_C)$ is the DC term, which is only zero if $\phi-\phi_C=0$ or $\phi-\phi_C=\pm\pi$

Appendix E

$I''(n)$ and $Q''(n)$ Magnitude Spectra Behaviour

In this appendix the influence of a signal component amplitude on the $I''(n)$ and $Q''(n)$ magnitude spectra will be studied.

Considering the following signal

$$s_{IF}(n) = A_C \cos(\omega_C \cdot n + \phi_C) + A_F \sum_{i=1}^{3} \cos[(\omega_C + \omega_i) \cdot n] + A_R \sum_{j=1}^{3} \cos[(\omega_C - \omega_j) \cdot n]$$

where $\{C, F, R\}$ represents, respectively, the carrier, forward blood flow and reverse blood flow.

- A_k with $k = \{C, F, R\}$ are the amplitudes of the signal's components;
- ω_i are the frequencies associated with forward blood flow of the signal's components;
- ω_j are the frequencies associated with reverse blood flow of the signal's components;

Considering the approach 1 (see subsection 3.3.3), the behaviour of the magnitude spectra of $I''(n)$ and $Q''(n)$ signals will be studied.

For simplification its assumed that the amplitude A_F does not change. The frequency components associated with the forward blood flow will have the values 5 kHz, 7.5 kHz and 15 kHz. The components associated with the reverse blood flow will have the values 5 kHz, 7.5 kHz and 10 kHz. This means that there are 2 frequency components with equal frequencies (5 kHz, 7.5 kHz) for forward and reverse blood flow.

The following figures for the $I''(n)$ and $Q''(n)$ magnitude spectra were obtained:

From the previous pictures it can be stated the following:

The component located at 10 kHz (associated with reverse blood flow) from figure E.1 to E.7 decreases in magnitude until it vanishes, as a direct consequence of the fact that A_R takes the value zero.

The component located at 15 kHz (associated with forward blood flow) from figure E.1 to E.7 tends to keep with the same magnitude, because A_F has always a constant value in these figures.

Components located at frequencies 5 kHz and 7.5 kHz are influenced by the forward and reverse blood flow amplitudes A_F and A_R, since these components are common between both blood directional components. From figures E.1 to E.7 it can be seen that if $A_F = A_R$ the $I''(n)$ magnitude

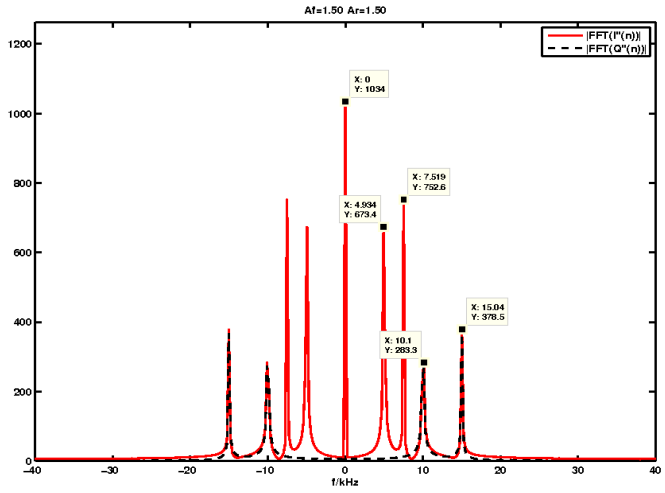

Figure E.1: $I''(n)$ and $Q''(n)$ magnitude spectra, for $A_F = 1.5$ and $A_R = 1.5$

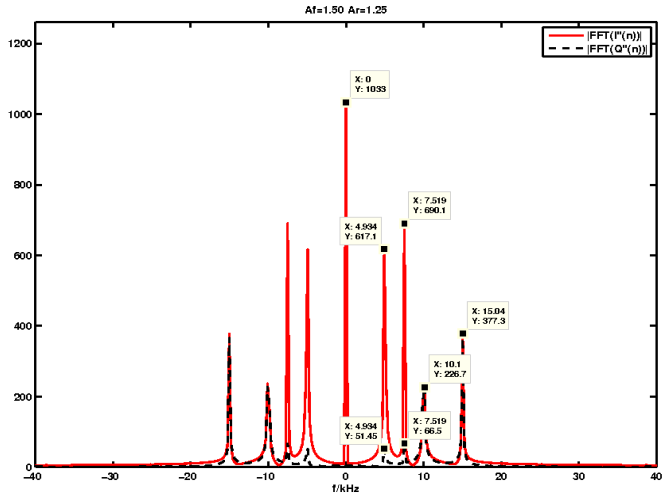

Figure E.2: $I''(n)$ and $Q''(n)$ magnitude spectra, for $A_F = 1.5$ and $A_R = 1.25$

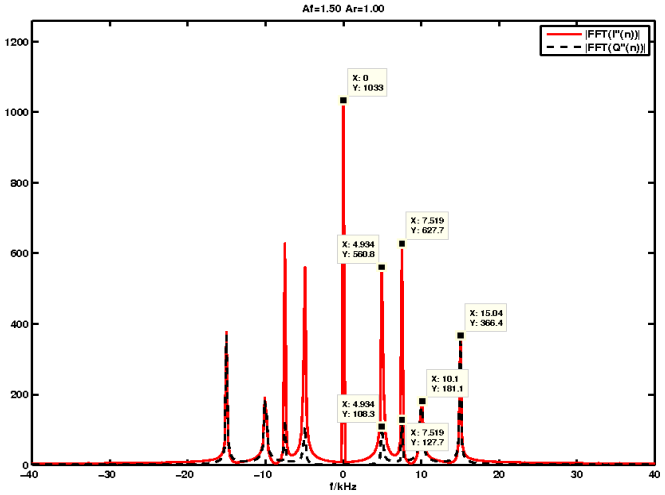

Figure E.3: $I''(n)$ and $Q''(n)$ magnitude spectra, for $A_F = 1.5$ and $A_R = 1.00$

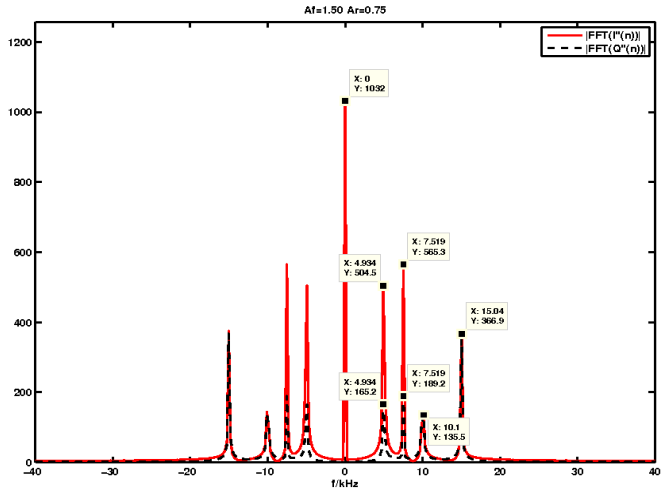

Figure E.4: $I''(n)$ and $Q''(n)$ magnitude spectra, for $A_F = 1.5$ and $A_R = 0.75$

spectra components at these frequencies assume it maximum magnitude, and $Q''(n)$ magnitude spectra components at these frequencies presents magnitude zero. When $A_R = 0$ the magnitudes spectra components at these frequencies of $I''(n)$ and $Q''(n)$ are equal. As A_R decreases the magnitude spectra components of $I''(n)$ tend to decrease and the magnitude spectra components of $Q''(n)$ tend to incresase (at these frequencies).

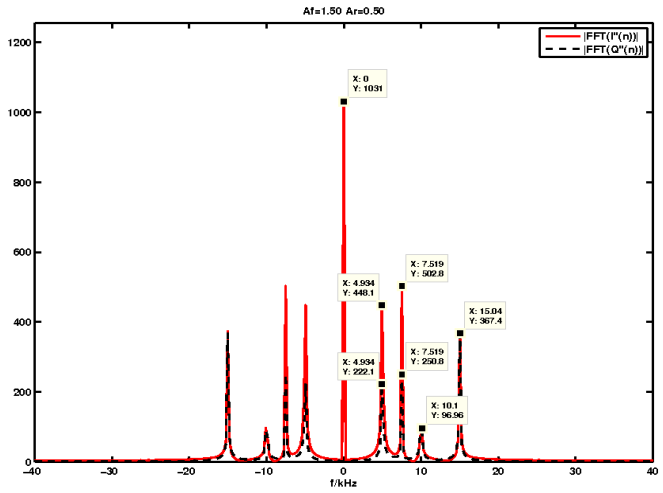

Figure E.5: $I''(n)$ and $Q''(n)$ magnitude spectra, for $A_F = 1.5$ and $A_R = 0.50$

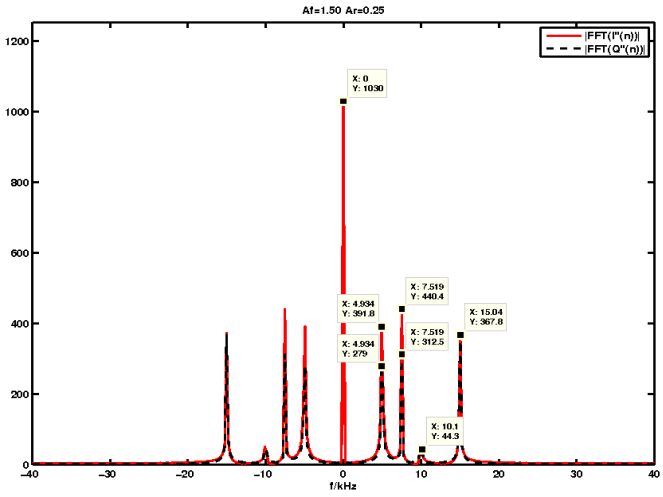

Figure E.6: $I''(n)$ and $Q''(n)$ magnitude spectra, for $A_F = 1.5$ and $A_R = 0.25$

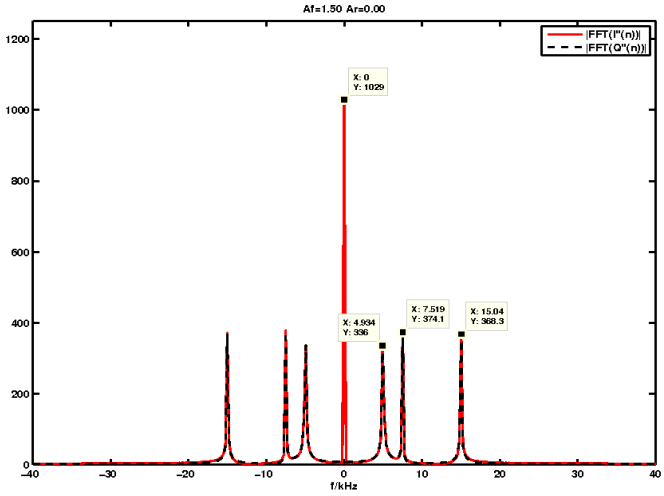

Figure E.7: $I''(n)$ and $Q''(n)$ magnitude spectra, for $A_F = 1.5$ and $A_R = 0.00$

Appendix F

Characteristics of the Filters Employed

F.1 Lowpass Filters Used in Approach 1

F.1.1 For Results Using the Testing Signals

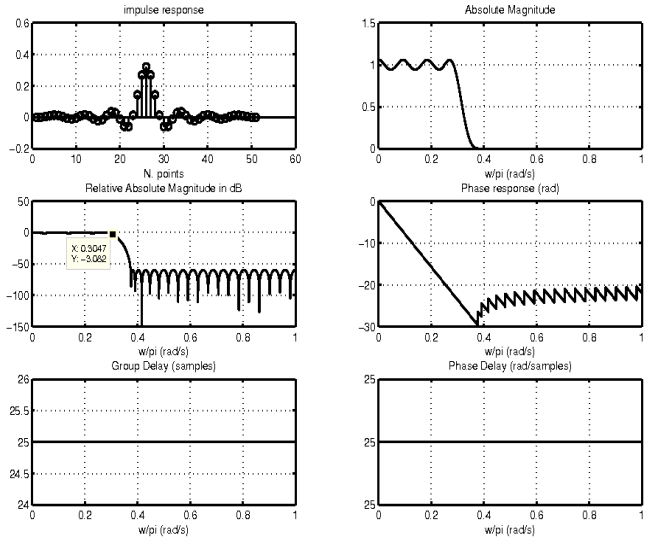

Figure F.1: Lowpass equiripple FIR filter of order 51, with 60 dB stopband attenuation and passband ripple of 1.00562 dB; sampling frequency 240.604 kHz

h(0)=h(50)	-1.0118631e-003	h(13)=h(37)	-1.0130765e-002
h(1)=h(49)	-6.3905670e-005	h(14)=h(36)	-2.3279064e-002
h(2)=h(48)	3.3046894e-003	h(15)=h(35)	-1.5510968e-002
h(3)=h(47)	8.7742998e-003	h(16)=h(34)	1.1362433e-002
h(4)=h(46)	1.2895339e-002	h(17)=h(33)	3.4863437e-002
h(5)=h(45)	1.1330389e-002	h(18)=h(32)	2.8515798e-002
h(6)=h(44)	3.0037574e-003	h(19)=h(31)	-1.2324520e-002
h(7)=h(43)	-7.2622899e-003	h(20)=h(30)	-5.7876536e-002
h(8)=h(42)	-1.1248470e-002	h(21)=h(29)	-5.9677901e-002
h(9)=h(41)	-4.3490424e-003	h(22)=h(28)	1.2920859e-002
h(10)=h(40)	8.7297271e-003	h(23)=h(27)	1.4290200e-001
h(11)=h(39)	1.6023048e-002	h(24)=h(26)	2.6838337e-001
h(12)=h(38)	8.4442733e-003	h(25)=h(25)	3.2020107e-001

Table F.1: Table with the impulse response coefficients of the filter presented in figure F.1

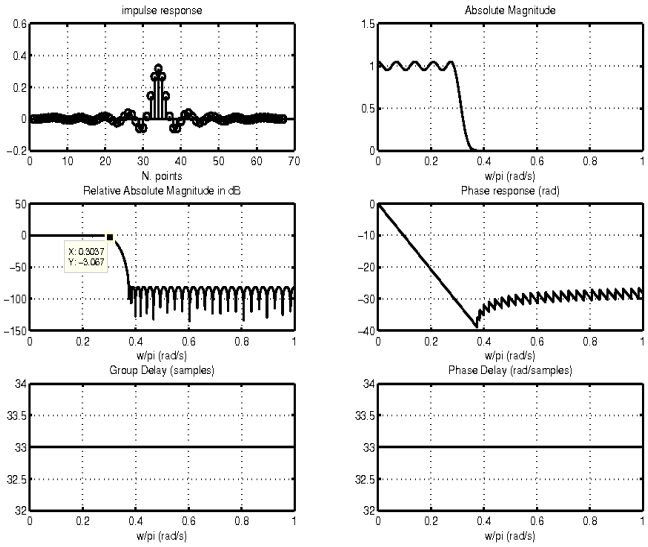

Figure F.2: Lowpass equiripple FIR filter of order 67, with 81 dB stopband attenuation and passband ripple of 0.84211 dB; sampling frequency 240.604 kHz

h(0)=h(66)	-1.2803672e-004	h(17)=h(49)	-2.3355600e-003
h(1)=h(65)	2.1673236e-005	h(18)=h(48)	1.1329673e-002
h(2)=h(64)	1.0017417e-003	h(19)=h(47)	1.6825104e-002
h(3)=h(63)	3.2959764e-003	h(20)=h(46)	6.5684931e-003
h(4)=h(62)	6.4651351e-003	h(21)=h(45)	-1.3015420e-002
h(5)=h(61)	8.7949446e-003	h(22)=h(44)	-2.4394107e-002
h(6)=h(60)	8.0999032e-003	h(23)=h(43)	-1.3668829e-002
h(7)=h(59)	3.5623528e-003	h(24)=h(42)	1.4469234e-002
h(8)=h(58)	-2.8019492e-003	h(25)=h(41)	3.6202729e-002
h(9)=h(57)	-6.7867008e-003	h(26)=h(40)	2.6697934e-002
h(10)=h(56)	-5.0339259e-003	h(27)=h(39)	-1.5586930e-002
h(11)=h(55)	1.6442254e-003	h(28)=h(38)	-5.9377612e-002
h(12)=h(54)	7.8789099e-003	h(29)=h(37)	-5.7886424e-002
h(13)=h(53)	7.6348738e-003	h(30)=h(36)	1.6290431e-002
h(14)=h(52)	-1.9257562e-004	h(31)=h(35)	1.4453907e-001
h(15)=h(51)	-9.5484396e-003	h(32)=h(34)	2.6665807e-001
h(16)=h(50)	-1.1481696e-002	h(33)=h(33)	3.1680277e-001

Table F.2: Table with the impulse response coefficients of the filter presented in figure F.2

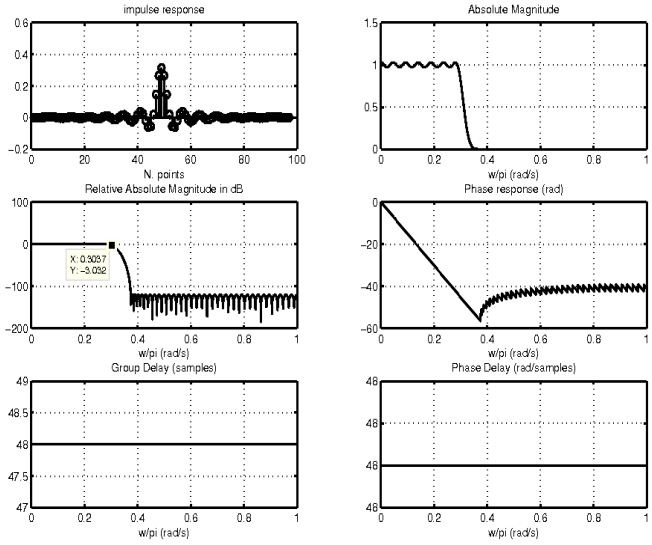

Figure F.3: Lowpass equiripple FIR filter of order 97, with 120 dB stopband attenuation and passband ripple of 0.49852 dB; sampling frequency 240.604 kHz

h(0)=h(96)	1.1069526e-005	h(25)=h(71)	-4.5552404e-003
h(1)=h(95)	8.8621856e-005	h(26)=h(70)	3.3805289e-003
h(2)=h(94)	3.5349632e-004	h(27)=h(69)	9.5947182e-003
h(3)=h(93)	9.6645613e-004	h(28)=h(68)	7.7317107e-003
h(4)=h(92)	2.0024412e-003	h(29)=h(67)	-2.0053367e-003
h(5)=h(91)	3.2709229e-003	h(30)=h(66)	-1.1725049e-002
h(6)=h(90)	4.2270123e-003	h(31)=h(65)	-1.1955274e-002
h(7)=h(89)	4.1530581e-003	h(32)=h(64)	-5.3211903e-004
h(8)=h(88)	2.6330764e-003	h(33)=h(63)	1.3786413e-002
h(9)=h(87)	5.2889780e-005	h(34)=h(62)	1.7564483e-002
h(10)=h(86)	-2.3324503e-003	h(35)=h(61)	4.7813056e-003
h(11)=h(85)	-3.0466384e-003	h(36)=h(60)	-1.5683962e-002
h(12)=h(84)	-1.4855626e-003	h(37)=h(59)	-2.5355118e-002
h(13)=h(83)	1.3557804e-003	h(38)=h(58)	-1.1917690e-002
h(14)=h(82)	3.3092633e-003	h(39)=h(57)	1.7293568e-002
h(15)=h(81)	2.5978677e-003	h(40)=h(56)	3.7351331e-002
h(16)=h(80)	-5.4891776e-004	h(41)=h(55)	2.5002771e-002
h(17)=h(79)	-3.6938640e-003	h(42)=h(54)	-1.8514016e-002
h(18)=h(78)	-3.9537021e-003	h(43)=h(53)	-6.0677248e-002
h(19)=h(77)	-5.6220491e-004	h(44)=h(52)	-5.6255920e-002
h(20)=h(76)	3.9851023e-003	h(45)=h(51)	1.9284692e-002
h(21)=h(75)	5.6136732e-003	h(46)=h(50)	1.4597151e-001
h(22)=h(74)	2.2107319e-003	h(47)=h(49)	2.6511576e-001
h(23)=h(73)	-3.9583973e-003	h(48)=h(48)	3.1378649e-001
h(24)=h(72)	-7.5269101e-003	h(49)=h(47)	2.6511576e-001

Table F.3: Table with the impulse response coefficients of the filter presented in figure F.3

F.1.2 For Results of BPS when Experimental Signals are used

Since the for the theoretical results a sampling frequency of 240.604 kHz was used, which is the same sampling frequency used in practice for acquiring signals using the BPS strategy, the lowpass FIR filter used is the one presented in figure F.2.

F.1.3 For Results after Heterodyne Function Application on Experimental Signals

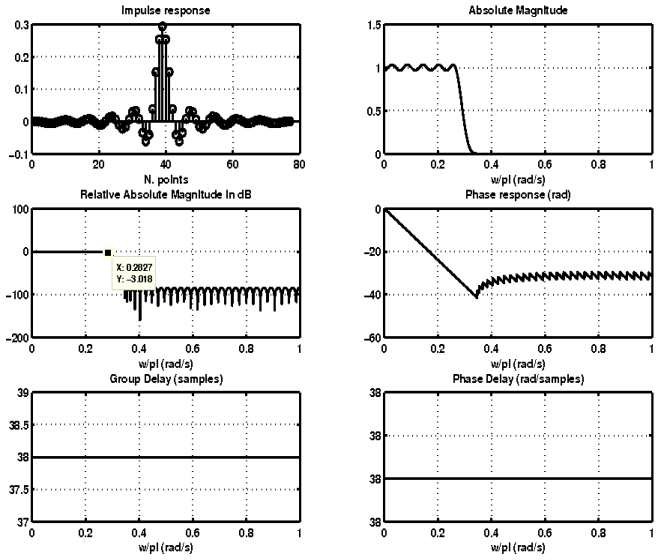

Figure F.4: Lowpass equiripple FIR filter of order 77, with 80 dB stopband attenuation and passband ripple of 0.58237 dB; sampling frequency 260 kHz

h(0)=h(76)	-1.0911069e-004	h(20)=h(56)	-9.2351892e-003
h(1)=h(75)	-6.9443457e-004	h(21)=h(55)	6.6210966e-004
h(2)=h(74)	-1.9152986e-003	h(22)=h(54)	1.2151872e-002
h(3)=h(73)	-3.6900494e-003	h(23)=h(53)	1.5549657e-002
h(4)=h(72)	-5.2823961e-003	h(24)=h(52)	6.0439590e-003
h(5)=h(71)	-5.5906061e-003	h(25)=h(51)	-1.1009919e-002
h(6)=h(70)	-3.8155821e-003	h(26)=h(50)	-2.2394417e-002
h(7)=h(69)	-2.9408337e-004	h(27)=h(49)	-1.6647757e-002
h(8)=h(68)	3.2647629e-003	h(28)=h(48)	5.5706032e-003
h(9)=h(67)	4.6047330e-003	h(29)=h(47)	2.8979826e-002
h(10)=h(66)	2.5220226e-003	h(30)=h(46)	3.2950348e-002
h(11)=h(65)	-1.8753090e-003	h(31)=h(45)	7.6359699e-003
h(12)=h(64)	-5.4534399e-003	h(32)=h(44)	-3.4464745e-002
h(13)=h(63)	-5.1158238e-003	h(33)=h(43)	-6.1572405e-002
h(14)=h(62)	-3.7445572e-004	h(34)=h(42)	-4.0962627e-002
h(15)=h(61)	5.6524753e-003	h(35)=h(41)	3.8101146e-002
h(16)=h(60)	8.0838899e-003	h(36)=h(40)	1.5242285e-001
h(17)=h(59)	4.0651628e-003	h(37)=h(39)	2.5362802e-001
h(18)=h(58)	-4.3206519e-003	h(38)=h(38)	2.9395904e-001
h(19)=h(57)	-1.0757515e-002	h(39)=h(37)	2.5362802e-001

Table F.4: Table with the impulse response coefficients of the filter presented in figure F.4

F.2 Lowpass Filters Used in Approaches 2 to 4

F.2.1 For Results Using the Testing Signals

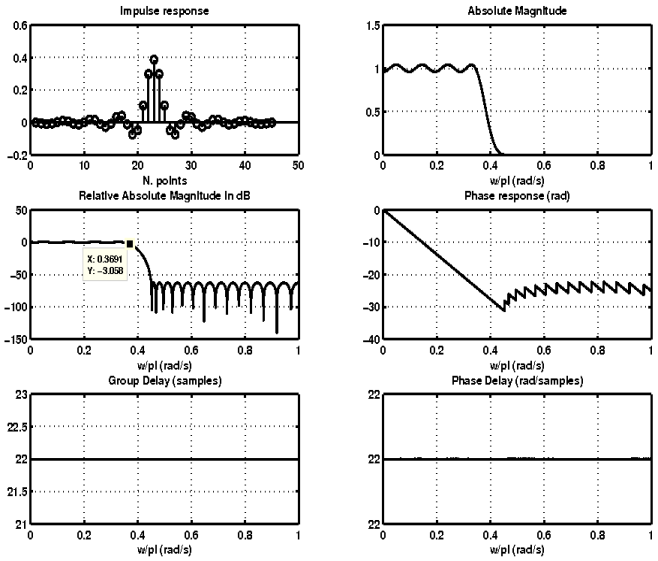

Figure F.5: Lowpass equiripple FIR filter of order 45, with 62 dB stopband attenuation and passband ripple of 0.70745 dB ; sampling frequency 200 kHz

h(0)=h(44)	-2.0463691e-003	h(12)=h(32)	-1.0994514e-002
h(1)=h(43)	-7.0368257e-003	h(13)=h(31)	-2.8753836e-002
h(2)=h(42)	-1.0514670e-002	h(14)=h(30)	-8.9241010e-003
h(3)=h(41)	-7.6558223e-003	h(15)=h(29)	3.2583712e-002
h(4)=h(40)	2.1799119e-003	h(16)=h(28)	4.0538258e-002
h(5)=h(39)	9.4842932e-003	h(17)=h(27)	-1.3181022e-002
h(6)=h(38)	4.9685191e-003	h(18)=h(26)	-7.5780931e-002
h(7)=h(37)	-8.0583279e-003	h(19)=h(25)	-4.9404328e-002
h(8)=h(36)	-1.3042640e-002	h(20)=h(24)	1.0346687e-001
h(9)=h(35)	-1.9806748e-004	h(21)=h(23)	2.9738929e-001
h(10)=h(34)	1.7173940e-002	h(22)=h(22)	3.8603408e-001
h(11)=h(33)	1.4499092e-002	h(23)=h(21)	2.9738929e-001

Table F.5: Table with the impulse response coefficients of the filter presented in figure F.5

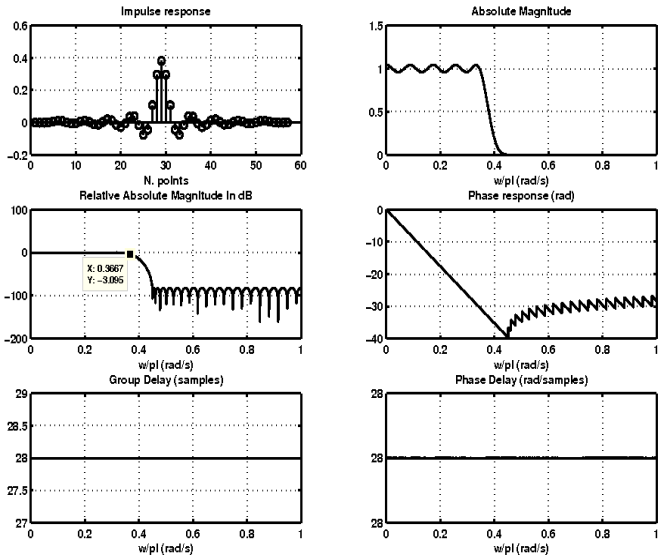

Figure F.6: Lowpass equiripple FIR filter of order 57, with 81 dB stopband attenuation and passband ripple of 0.71508 dB; sampling frequency 200 kHz

h(0)=h(56)	-4.4576843e-004	h(15)=h(41)	2.8535754e-003
h(1)=h(55)	-1.3048109e-003	h(16)=h(40)	1.9420915e-002
h(2)=h(54)	-1.4403287e-003	h(17)=h(39)	1.2781498e-002
h(3)=h(53)	1.0102834e-003	h(18)=h(38)	-1.4606087e-002
h(4)=h(52)	6.1383944e-003	h(19)=h(37)	-2.9365357e-002
h(5)=h(51)	1.0318494e-002	h(20)=h(36)	-5.5016558e-003
h(6)=h(50)	8.5649965e-003	h(21)=h(35)	3.5518897e-002
h(7)=h(49)	5.5862773e-004	h(22)=h(34)	3.8884869e-002
h(8)=h(48)	-6.6049481e-003	h(23)=h(33)	-1.7348092e-002
h(9)=h(47)	-4.7541227e-003	h(24)=h(32)	-7.6823039e-002
h(10)=h(46)	4.9263942e-003	h(25)=h(31)	-4.5798176e-002
h(11)=h(45)	1.0643966e-002	h(26)=h(30)	1.0689705e-001
h(12)=h(44)	3.1018906e-003	h(27)=h(29)	2.9597224e-001
h(13)=h(43)	-1.0809441e-002	h(28)=h(28)	3.8165848e-001
h(14)=h(42)	-1.3102075e-002	h(29)=h(27)	2.9597224e-001

Table F.6: Table with the impulse response coefficients of the filter presented in figure F.6

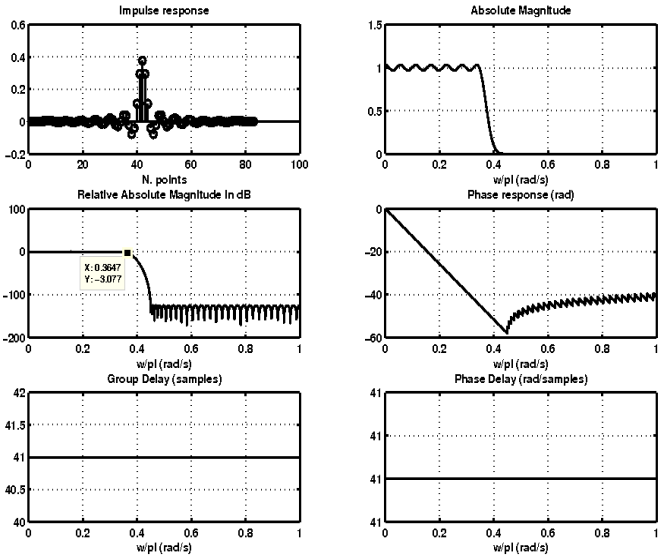

Figure F.7: Lowpass equiripple FIR filter of order 83, with 120 dB stopband attenuation and passband ripple of 0.54902 dB; sampling frequency 200 kHz

h(0)=h(82)	-7.5291246e-006	h(21)=h(61)	-9.1910267e-003
h(1)=h(81)	-1.0190897e-005	h(22)=h(60)	-3.9812451e-003
h(2)=h(80)	1.1231712e-004	h(23)=h(59)	7.8578977e-003
h(3)=h(79)	6.6543308e-004	h(24)=h(58)	1.1724123e-002
h(4)=h(78)	1.9889862e-003	h(25)=h(57)	4.2861268e-004
h(5)=h(77)	3.9693826e-003	h(26)=h(56)	-1.4148119e-002
h(6)=h(76)	5.5871718e-003	h(27)=h(55)	-1.2720715e-002
h(7)=h(75)	5.2643450e-003	h(28)=h(54)	6.6950641e-003
h(8)=h(74)	2.2791349e-003	h(29)=h(53)	2.1723749e-002
h(9)=h(73)	-1.8588126e-003	h(30)=h(52)	1.0287666e-002
h(10)=h(72)	-3.9458328e-003	h(31)=h(51)	-1.8808633e-002
h(11)=h(71)	-1.9462234e-003	h(32)=h(50)	-2.9662333e-002
h(12)=h(70)	2.3373369e-003	h(33)=h(49)	-1.2987598e-003
h(13)=h(69)	4.2688041e-003	h(34)=h(48)	3.8719462e-002
h(14)=h(68)	1.1685231e-003	h(35)=h(47)	3.6716608e-002
h(15)=h(67)	-3.9642224e-003	h(36)=h(46)	-2.2121948e-002
h(16)=h(66)	-4.9354875e-003	h(37)=h(45)	-7.7828522e-002
h(17)=h(65)	3.9620910e-004	h(38)=h(44)	-4.1598828e-002
h(18)=h(64)	6.3567647e-003	h(39)=h(43)	1.1074605e-001
h(19)=h(63)	5.1281712e-003	h(40)=h(42)	2.9431102e-001
h(20)=h(62)	-3.2893867e-003	h(41)=h(41)	3.7667798e-001

Table F.7: Table with the impulse response coefficients of the filter presented in figure F.7

F.2.2 For Results of BPS when Experimental Signals are used

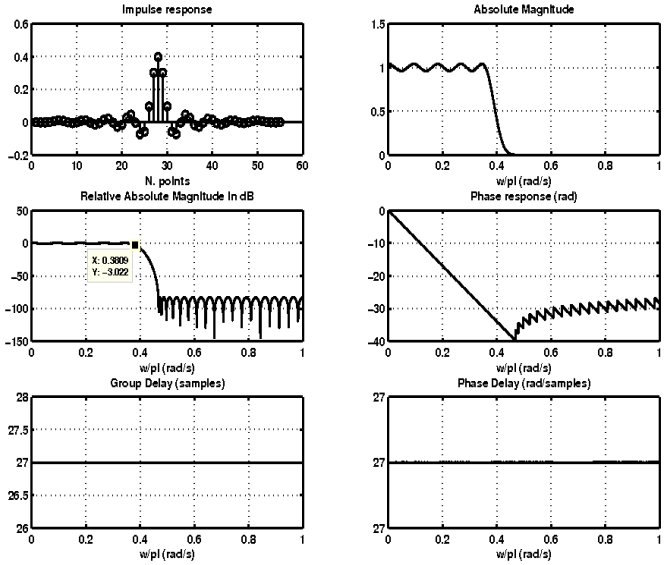

Figure F.8: Lowpass equiripple FIR filter of order 55, with 81 dB stopband attenuation and passband ripple of 0.69153 dB; sampling frequency 192.68 kHz

h(0)=h(54)	-5.2882044e-004	h(14)=h(40)	-7.2513136e-003
h(1)=h(53)	-1.6575600e-003	h(15)=h(39)	1.3867373e-002
h(2)=h(52)	-2.0452327e-003	h(16)=h(38)	2.0014105e-002
h(3)=h(51)	6.1873168e-004	h(17)=h(37)	-3.2190626e-003
h(4)=h(50)	6.4048436e-003	h(18)=h(36)	-2.9084476e-002
h(5)=h(49)	1.0768870e-002	h(19)=h(35)	-1.7630817e-002
h(6)=h(48)	8.0143132e-003	h(20)=h(34)	2.6651314e-002
h(7)=h(47)	-1.0388595e-003	h(21)=h(33)	4.5576056e-002
h(8)=h(46)	-7.0855255e-003	h(22)=h(32)	-3.3240174e-003
h(9)=h(45)	-2.1893401e-003	h(23)=h(31)	-7.4097055e-002
h(10)=h(44)	8.4144633e-003	h(24)=h(30)	-5.8449012e-002
h(11)=h(43)	9.9214165e-003	h(25)=h(29)	9.5431505e-002
h(12)=h(42)	-2.8485784e-003	h(26)=h(28)	3.0103483e-001
h(13)=h(41)	-1.4727046e-002	h(27)=h(27)	3.9665844e-001

Table F.8: Table with the impulse response coefficients of the filter presented in figure F.8

F.2.3 For Results after Heterodyne Function Application on Experimental Signals

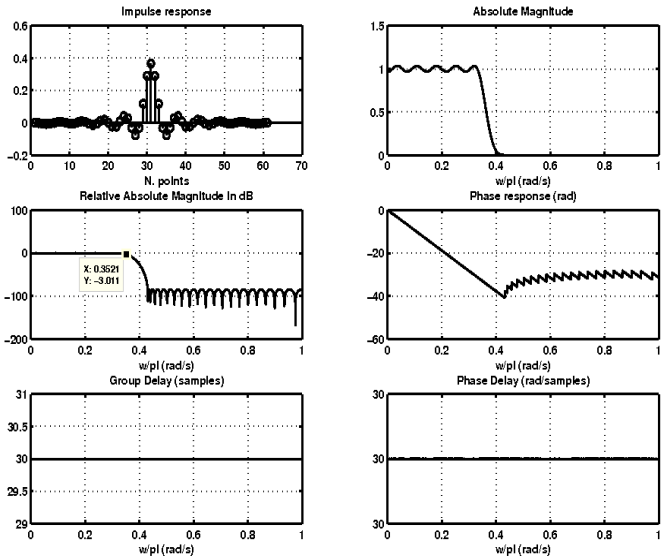

Figure F.9: Lowpass equiripple FIR filter of order 61, with 82 dB stopband attenuation and passband ripple of 0.57907 dB; sampling frequency 208.8 kHz

h(0)=h(60)	-4.8107192e-004	h(16)=h(44)	-5.4416040e-003
h(1)=h(59)	-2.1335003e-003	h(17)=h(43)	1.2860444e-002
h(2)=h(58)	-4.8499081e-003	h(18)=h(42)	1.9123871e-002
h(3)=h(57)	-6.9733044e-003	h(19)=h(41)	1.4615589e-003
h(4)=h(56)	-5.9149386e-003	h(20)=h(40)	-2.3485407e-002
h(5)=h(55)	-1.0446341e-003	h(21)=h(39)	-2.4229230e-002
h(6)=h(54)	4.4176414e-003	h(22)=h(38)	8.1757282e-003
h(7)=h(53)	5.2860762e-003	h(23)=h(37)	4.0906265e-002
h(8)=h(52)	-1.8907386e-005	h(24)=h(36)	2.8654004e-002
h(9)=h(51)	-6.3452746e-003	h(25)=h(35)	-3.1038624e-002
h(10)=h(50)	-6.0125048e-003	h(26)=h(34)	-7.6849187e-002
h(11)=h(49)	2.1987774e-003	h(27)=h(33)	-3.1668690e-002
h(12)=h(48)	9.6951506e-003	h(28)=h(32)	1.1784494e-001
h(13)=h(47)	6.4537148e-003	h(29)=h(31)	2.9003054e-001
h(14)=h(46)	-6.1796963e-003	h(30)=h(30)	3.6607230e-001
h(15)=h(45)	-1.4080394e-002	h(31)=h(29)	2.9003054e-001

Table F.9: Table with the impulse response coefficients of the filter presented in figure F.9

F.3 Lowpass Filters Used in Approach 5

F.3.1 For Results Using the Testing Signals

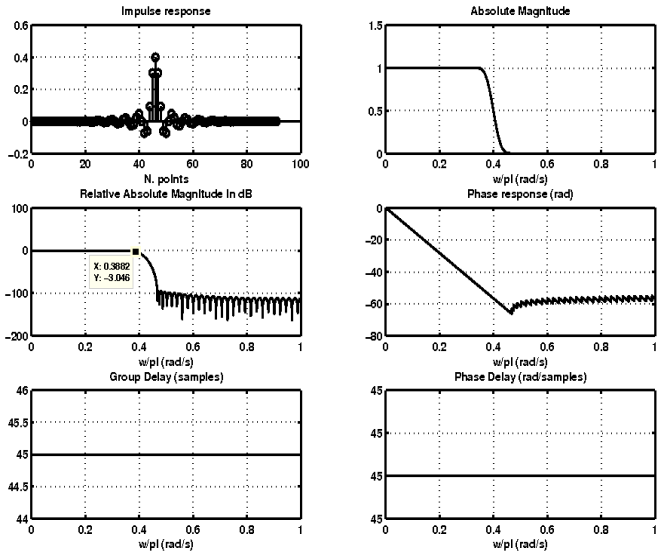

Figure F.10: Lowpass FIR filter of order 91, designed from Kaiser window with parameter equal to 9.5 ; sampling frequency 200 kHz

h(0)=h(90)	-8.8924502e-021	h(23)=h(67)	2.7138271e-003
h(1)=h(89)	-8.8924739e-006	h(24)=h(66)	5.1233194e-003
h(2)=h(88)	-1.0321795e-005	h(25)=h(65)	-6.1332373e-018
h(3)=h(87)	1.7390338e-005	h(26)=h(64)	-6.8944325e-003
h(4)=h(86)	4.4249351e-005	h(27)=h(63)	-4.9190059e-003
h(5)=h(85)	-1.3652591e-019	h(28)=h(62)	5.6639863e-003
h(6)=h(84)	-9.5621435e-005	h(29)=h(61)	1.0530902e-002
h(7)=h(83)	-8.2796055e-005	h(30)=h(60)	-9.3356594e-018
h(8)=h(82)	1.1321512e-004	h(31)=h(59)	-1.3853895e-002
h(9)=h(81)	2.4540949e-004	h(32)=h(58)	-9.8166562e-003
h(10)=h(80)	-5.8233676e-019	h(33)=h(57)	1.1265254e-002
h(11)=h(79)	-4.1871025e-004	h(34)=h(56)	2.0960124e-002
h(12)=h(78)	-3.3089880e-004	h(35)=h(55)	-1.2457343e-017
h(13)=h(77)	4.1801822e-004	h(36)=h(54)	-2.8055805e-002
h(14)=h(76)	8.4516411e-004	h(37)=h(53)	-2.0269845e-002
h(15)=h(75)	-1.6158083e-018	h(38)=h(52)	2.3960098e-002
h(16)=h(74)	-1.2822011e-003	h(39)=h(51)	4.6566563e-002
h(17)=h(73)	-9.6370713e-004	h(40)=h(50)	-1.4749064e-017
h(18)=h(72)	1.1631702e-003	h(41)=h(49)	-7.3038714e-002
h(19)=h(71)	2.2558886e-003	h(42)=h(48)	-6.1131977e-002
h(20)=h(70)	-3.4597181e-018	h(43)=h(47)	9.2722371e-002
h(21)=h(69)	-3.1813511e-003	h(44)=h(46)	3.0206080e-001
h(22)=h(68)	-2.3156226e-003	h(45)=h(45)	4.0000141e-001

Table F.10: Table with the impulse response coefficients of the filter presented in figure F.10

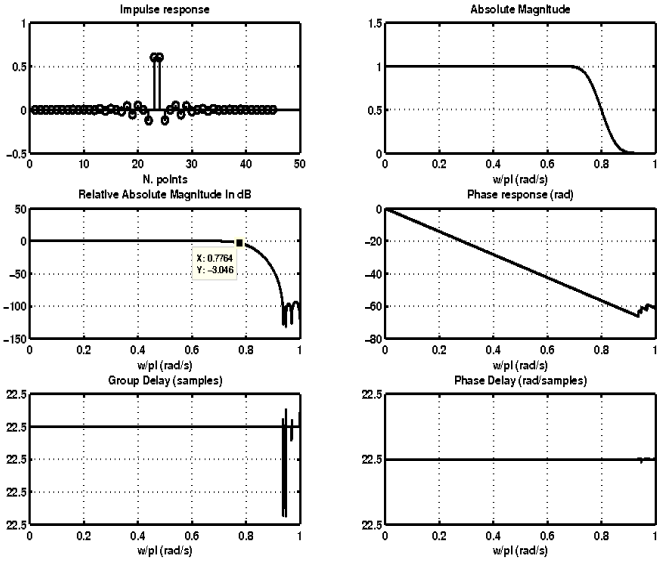

Figure F.11: Lowpass filter (LP_I) of order 46, created from the filter in figure F.10, such that $LP\_I(n) = LP(2n)$, $n = 0, 1, 2, \ldots$

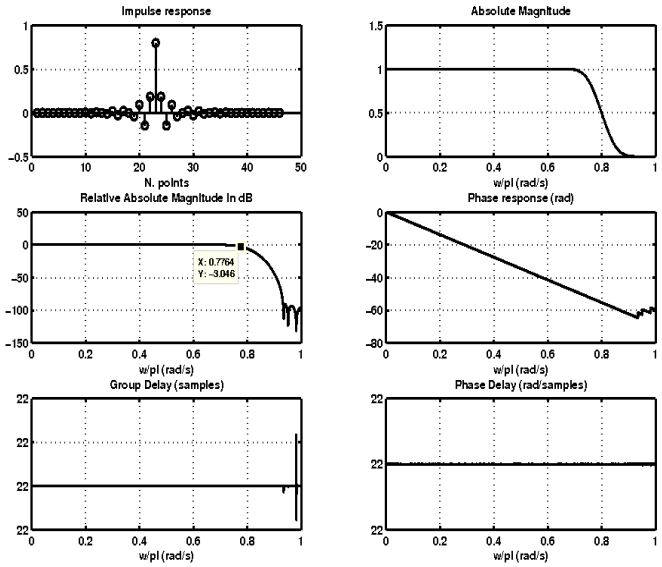

Figure F.12: Lowpass filter (LP_Q) of order 45, created from the filter in figure F.10, such that $LP\_Q(n) = LP(2n+1)$, $n = 0, 1, 2, \ldots$

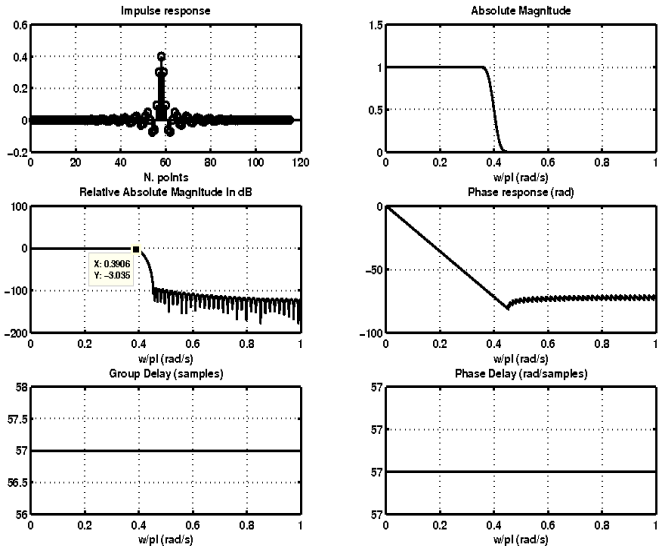

Figure F.13: Lowpass FIR filter of order 115, designed from Kaiser window with parameter equal to 9.5 ; sampling frequency 200 kHz

h(0)=h(114)	1.8719394e-006	h(29)=h(85)	-2.1074508e-003
h(1)=h(113)	6.0202948e-006	h(30)=h(84)	2.3820107e-003
h(2)=h(112)	-1.0595549e-019	h(31)=h(83)	4.3450629e-003
h(3)=h(111)	-1.6137449e-005	h(32)=h(82)	-6.2927434e-018
h(4)=h(110)	-1.4804414e-005	h(33)=h(81)	-5.4846320e-003
h(5)=h(109)	2.1110175e-005	h(34)=h(80)	-3.7970411e-003
h(6)=h(108)	4.7228280e-005	h(35)=h(79)	4.2462891e-003
h(7)=h(107)	-1.6407923e-019	h(36)=h(78)	7.6727664e-003
h(8)=h(106)	-8.4216449e-005	h(37)=h(77)	-8.8168174e-018
h(9)=h(105)	-6.7625930e-005	h(38)=h(76)	-9.5394701e-003
h(10)=h(104)	8.6572194e-005	h(39)=h(75)	-6.5679539e-003
h(11)=h(103)	1.7701103e-004	h(40)=h(74)	7.3159908e-003
h(12)=h(102)	-5.1253846e-019	h(41)=h(73)	1.3189836e-002
h(13)=h(101)	-2.7342615e-004	h(42)=h(72)	-1.1363838e-017
h(14)=h(100)	-2.0702438e-004	h(43)=h(71)	-1.6424968e-002
h(15)=h(99)	2.5149947e-004	h(44)=h(70)	-1.1359580e-002
h(16)=h(98)	4.9056983e-004	h(45)=h(69)	1.2749405e-002
h(17)=h(97)	-1.2098547e-018	h(46)=h(68)	2.3246157e-002
h(18)=h(96)	-6.9836939e-004	h(47)=h(67)	-1.3565201e-017
h(19)=h(95)	-5.1021292e-004	h(48)=h(66)	-3.0052577e-002
h(20)=h(94)	5.9974788e-004	h(49)=h(65)	-2.1397569e-002
h(21)=h(93)	1.1347602e-003	h(50)=h(64)	2.4971168e-002
h(22)=h(92)	-2.3804897e-018	h(51)=h(63)	4.7998603e-002
h(23)=h(91)	-1.5296211e-003	h(52)=h(62)	-1.5061891e-017
h(24)=h(90)	-1.0904222e-003	h(53)=h(61)	-7.4024558e-002
h(25)=h(89)	1.2527387e-003	h(54)=h(60)	-6.1593973e-002
h(26)=h(88)	2.3200277e-003	h(55)=h(59)	9.3032550e-002
h(27)=h(87)	-4.0889278e-018	h(56)=h(58)	3.0231158e-001
h(28)=h(86)	-3.0084405e-003	h(57)=h(57)	3.9999899e-001

Table F.11: Table with the impulse response coefficients of the filter presented in figure F.13

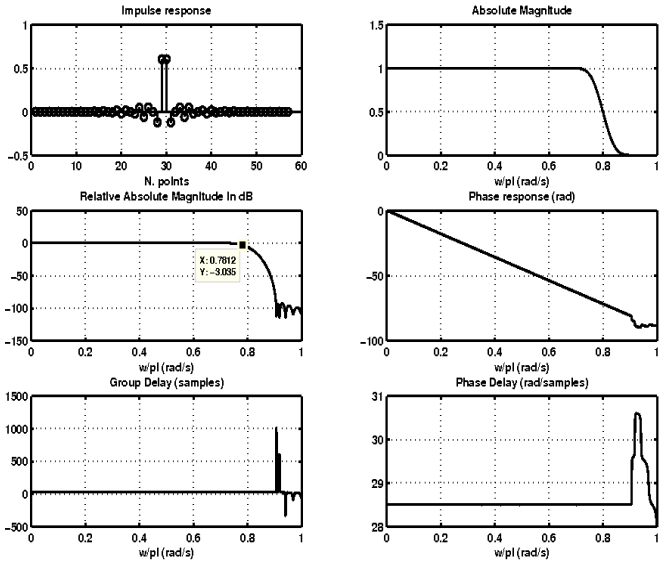

Figure F.14: Lowpass filter (LP_I) of order 58, created from the filter in figure F.13, such that $LP\_I(n) = LP(2n)$, $n = 0, 1, 2, \ldots$

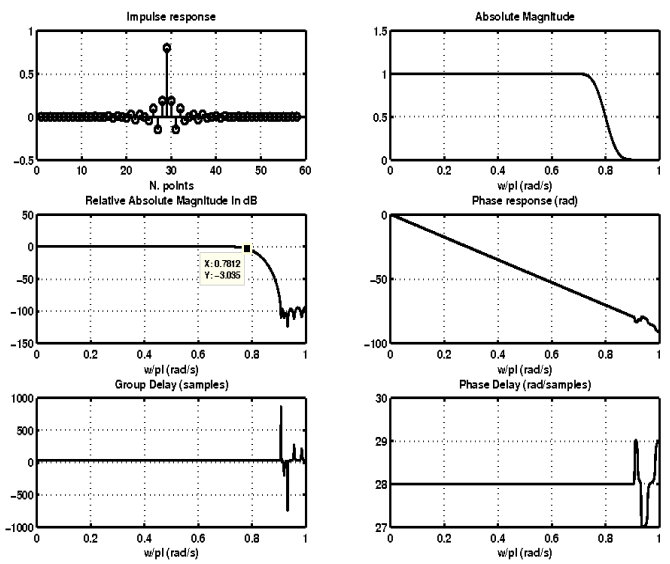

Figure F.15: Lowpass filter (LP_Q) of order 57, created from the filter in figure F.13, such that $LP\_Q(n) = LP(2n+1)$, $n = 0, 1, 2, \ldots$

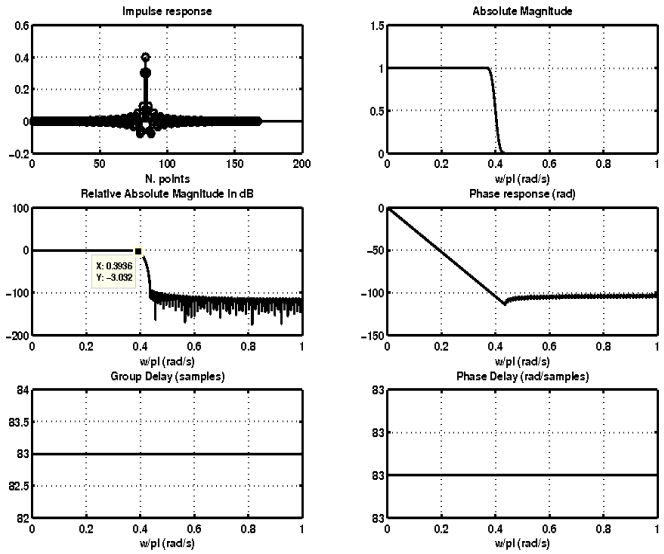

Figure F.16: Lowpass FIR filter of order 167, designed from Kaiser window with parameter equal to 9.5 ; sampling frequency 200 kHz

h(0)=h(166)	-1.2855496e-006	h(42)=h(124)	2.2966982e-003
h(1)=h(165)	2.1053105e-006	h(43)=h(123)	-5.1500008e-018
h(2)=h(164)	5.1145654e-006	h(44)=h(122)	-2.7171366e-003
h(3)=h(163)	-2.9959232e-020	h(45)=h(121)	-1.8231961e-003
h(4)=h(162)	-9.9484261e-006	h(46)=h(120)	1.9772197e-003
h(5)=h(161)	-8.1759453e-006	h(47)=h(119)	3.4658332e-003
h(6)=h(160)	1.0631159e-005	h(48)=h(118)	-6.7620884e-018
h(7)=h(159)	2.1964055e-005	h(49)=h(117)	-4.0559933e-003
h(8)=h(158)	-3.1308260e-019	h(50)=h(116)	-2.7083242e-003
h(9)=h(157)	-3.4294618e-005	h(51)=h(115)	2.9239426e-003
h(10)=h(156)	-2.6021953e-005	h(52)=h(114)	5.1043255e-003
h(11)=h(155)	3.1636080e-005	h(53)=h(113)	-8.5046832e-018
h(12)=h(154)	6.1692489e-005	h(54)=h(112)	-5.9319730e-003
h(13)=h(153)	-2.6599148e-019	h(55)=h(111)	-3.9497943e-003
h(14)=h(152)	-8.7602177e-005	h(56)=h(110)	4.2542214e-003
h(15)=h(151)	-6.3877605e-005	h(57)=h(109)	7.4128682e-003
h(16)=h(150)	7.4923153e-005	h(58)=h(108)	-1.0279146e-017
h(17)=h(149)	1.4142271e-004	h(59)=h(107)	-8.5973853e-003
h(18)=h(148)	6.7684174e-019	h(60)=h(106)	-5.7240919e-003
h(19)=h(147)	-1.8965978e-004	h(61)=h(105)	6.1691052e-003
h(20)=h(146)	-1.3483987e-004	h(62)=h(104)	1.0764550e-002
h(21)=h(145)	1.5448414e-004	h(63)=h(103)	-1.1968521e-017
h(22)=h(144)	2.8528586e-004	h(64)=h(102)	-1.2553558e-002
h(23)=h(143)	-1.0026408e-018	h(65)=h(101)	-8.3944768e-003
h(24)=h(142)	-3.6771211e-004	h(66)=h(100)	9.0979649e-003
h(25)=h(141)	-2.5674846e-004	h(67)=h(99)	1.5987704e-002
h(26)=h(140)	2.8918654e-004	h(68)=h(98)	-1.3449258e-017
h(27)=h(139)	5.2551613e-004	h(69)=h(97)	-1.9012528e-002
h(28)=h(138)	-6.0648903e-018	h(70)=h(96)	-1.2881932e-002
h(29)=h(137)	-6.5753870e-004	h(71)=h(95)	1.4187325e-002
h(30)=h(136)	-4.5285578e-004	h(72)=h(94)	2.5424391e-002
h(31)=h(135)	5.0345414e-004	h(73)=h(93)	-1.4604974e-017
h(32)=h(134)	9.0358361e-004	h(74)=h(92)	-3.1901309e-002
h(33)=h(133)	-2.5756614e-018	h(75)=h(91)	-2.2429115e-002
h(34)=h(132)	-1.1047073e-003	h(76)=h(90)	2.5886234e-002
h(35)=h(131)	-7.5266114e-004	h(77)=h(89)	4.9282860e-002
h(36)=h(130)	8.2817926e-004	h(78)=h(88)	-1.5340291e-017
h(37)=h(129)	1.4718321e-003	h(79)=h(87)	-7.4896521e-002
h(38)=h(128)	-3.7405728e-018	h(80)=h(86)	-6.2000755e-002
h(39)=h(127)	-1.7666658e-003	h(81)=h(85)	9.3305010e-002
h(40)=h(126)	-1.1933933e-003	h(82)=h(84)	3.0253276e-001
h(41)=h(125)	1.3024354e-003	h(83)=h(83)	3.9999925e-001

Table F.12: Table with the impulse response coefficients of the filter presented in figure F.16

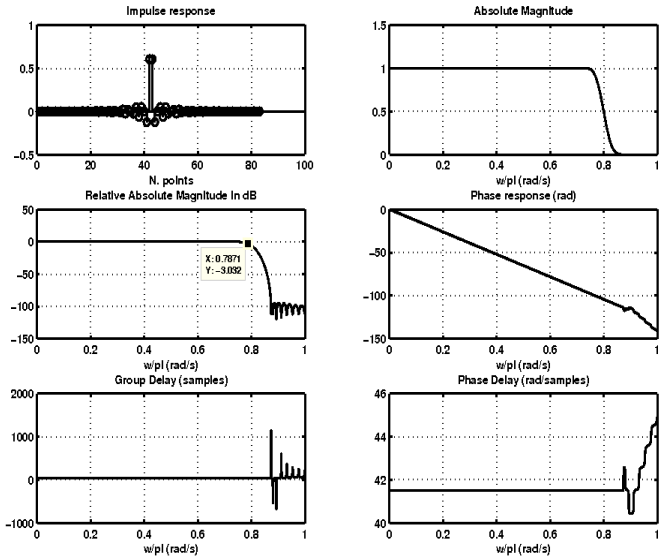

Figure F.17: Lowpass filter (LP_I) of order 84, created from the filter in figure F.16, such that $LP\_I(n) = LP(2n)$, $n = 0, 1, 2, \ldots$

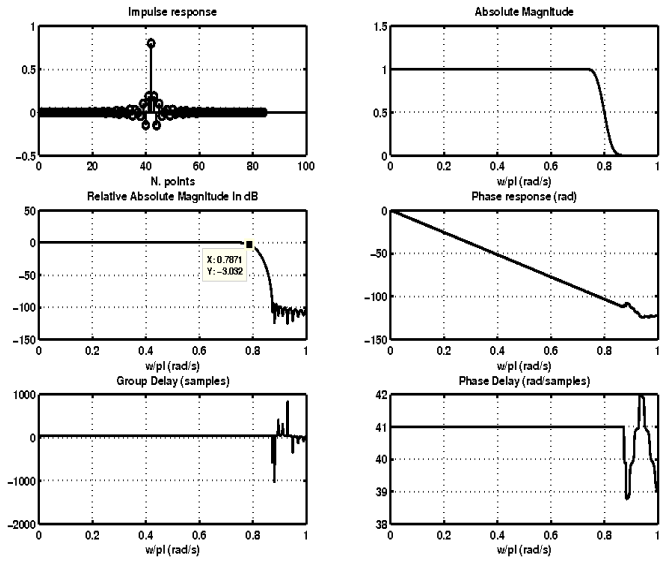

Figure F.18: Lowpass filter (LP_Q) of order 83, created from the filter in figure F.16, such that $LP\_Q(n) = LP(2n+1)$, $n = 0, 1, 2, \ldots$

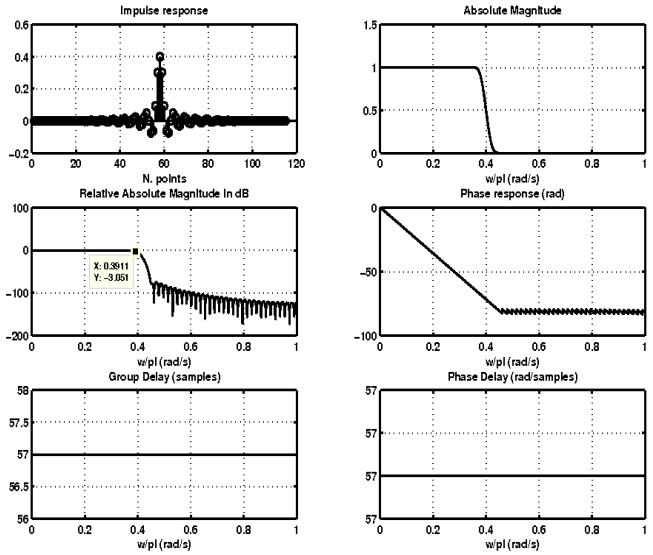

Figure F.19: Lowpass FIR filter of order 115, designed from Blackman window with parameter equal to 9.5 ; sampling frequency 200 kHz

h(0)=h(114)	-4.5552815e-020	h(29)=h(85)	-2.3647798e-003
h(1)=h(113)	1.4795780e-006	h(30)=h(84)	2.6497330e-003
h(2)=h(112)	-6.2294324e-020	h(31)=h(83)	4.7935811e-003
h(3)=h(111)	-1.3929724e-005	h(32)=h(82)	-6.8878643e-018
h(4)=h(110)	-1.5710544e-005	h(33)=h(81)	-5.9585720e-003
h(5)=h(109)	2.5256660e-005	h(34)=h(80)	-4.0959493e-003
h(6)=h(108)	6.0680551e-005	h(35)=h(79)	4.5498075e-003
h(7)=h(107)	-2.1978829e-019	h(36)=h(78)	8.1689214e-003
h(8)=h(106)	-1.1540442e-004	h(37)=h(77)	-9.3304968e-018
h(9)=h(105)	-9.3623119e-005	h(38)=h(76)	-1.0037936e-002
h(10)=h(104)	1.2007318e-004	h(39)=h(75)	-6.8741832e-003
h(11)=h(103)	2.4456813e-004	h(40)=h(74)	7.6186035e-003
h(12)=h(102)	-7.0274200e-019	h(41)=h(73)	1.3670688e-002
h(13)=h(101)	-3.7108664e-004	h(42)=h(72)	-1.1726266e-017
h(14)=h(100)	-2.7765862e-004	h(43)=h(71)	-1.6879343e-002
h(15)=h(99)	3.3300319e-004	h(44)=h(70)	-1.1629477e-002
h(16)=h(98)	6.4091395e-004	h(45)=h(69)	1.3006592e-002
h(17)=h(97)	-1.5592909e-018	h(46)=h(68)	2.3638917e-002
h(18)=h(96)	-8.8793673e-004	h(47)=h(67)	-1.3754067e-017
h(19)=h(95)	-6.4007313e-004	h(48)=h(66)	-3.0390625e-002
h(20)=h(94)	7.4260073e-004	h(49)=h(65)	-2.1587319e-002
h(21)=h(93)	1.3872647e-003	h(50)=h(64)	2.5140389e-002
h(22)=h(92)	-2.8745607e-018	h(51)=h(63)	4.8237215e-002
h(23)=h(91)	-1.8252956e-003	h(52)=h(62)	-1.5113833e-017
h(24)=h(90)	-1.2864389e-003	h(53)=h(61)	-7.4187870e-002
h(25)=h(89)	1.4618526e-003	h(54)=h(60)	-6.1670470e-002
h(26)=h(88)	2.6790927e-003	h(55)=h(59)	9.3084121e-002
h(27)=h(87)	-4.6747209e-018	h(56)=h(58)	3.0235457e-001
h(28)=h(86)	-3.4067128e-003	h(57)=h(57)	4.0000094e-001

Table F.13: Table with the impulse response coefficients of the filter presented in figure F.19

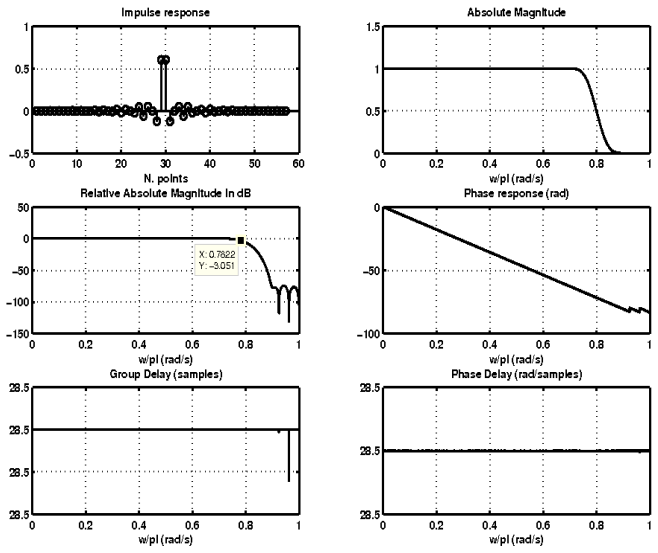

Figure F.20: Lowpass filter (LP_I) of order 58, created from the filter in figure F.19, such that $LP\_I(n) = LP(2n)$, $n = 0, 1, 2, \ldots$

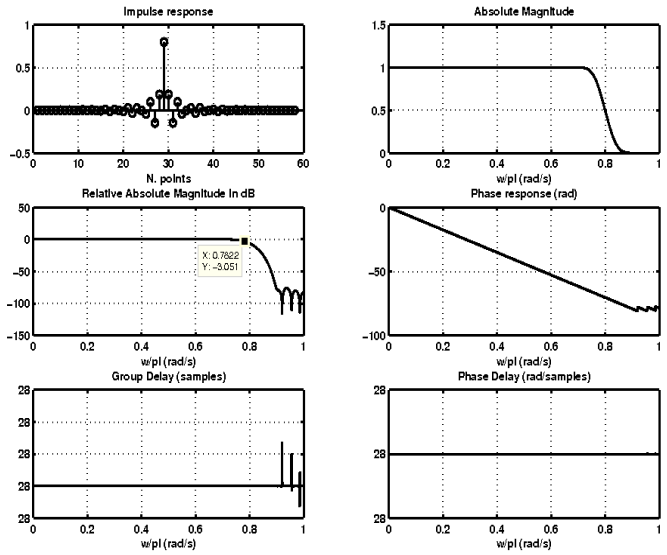

Figure F.21: Lowpass filter (LP_Q) of order 57, created from the filter in figure F.19, such that $LP\_Q(n) = LP(2n+1)$, $n = 0, 1, 2, \ldots$

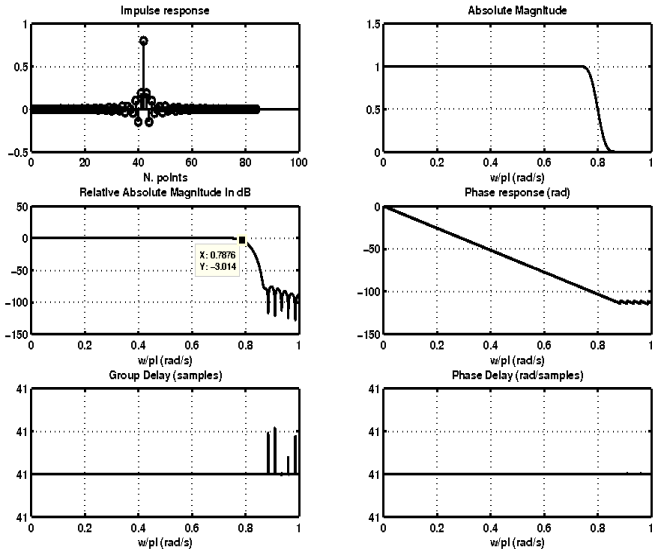

Figure F.22: Lowpass FIR filter of order 167, designed from Blackman window with parameter equal to 9.5 ; sampling frequency 200 kHz

h(0)=h(166)	3.1283210e-020	h(42)=h(124)	2.5807396e-003
h(1)=h(165)	2.9435129e-007	h(43)=h(123)	-5.7519574e-018
h(2)=h(164)	1.9315886e-006	h(44)=h(122)	-3.0169929e-003
h(3)=h(163)	-1.8178675e-020	h(45)=h(121)	-2.0129601e-003
h(4)=h(162)	-7.9707608e-006	h(46)=h(120)	2.1710933e-003
h(5)=h(161)	-7.8314571e-006	h(47)=h(119)	3.7855931e-003
h(6)=h(160)	1.1486841e-005	h(48)=h(118)	-7.3483385e-018
h(7)=h(159)	2.5795831e-005	h(49)=h(117)	-4.3859655e-003
h(8)=h(158)	-3.8980285e-019	h(50)=h(116)	-2.9147704e-003
h(9)=h(157)	-4.4476195e-005	h(51)=h(115)	3.1324402e-003
h(10)=h(156)	-3.4708885e-005	h(52)=h(114)	5.4442196e-003
h(11)=h(155)	4.2994485e-005	h(53)=h(113)	-9.0325518e-018
h(12)=h(154)	8.4828931e-005	h(54)=h(112)	-6.2744688e-003
h(13)=h(153)	-3.6809069e-019	h(55)=h(111)	-4.1614718e-003
h(14)=h(152)	-1.2151237e-004	h(56)=h(110)	4.4653481e-003
h(15)=h(151)	-8.8538012e-005	h(57)=h(109)	7.7526695e-003
h(16)=h(150)	1.0352517e-004	h(58)=h(108)	-1.0713164e-017
h(17)=h(149)	1.9445324e-004	h(59)=h(107)	-8.9307508e-003
h(18)=h(148)	9.2481920e-019	h(60)=h(106)	-5.9272496e-003
h(19)=h(147)	-2.5726179e-004	h(61)=h(105)	6.3687945e-003
h(20)=h(146)	-1.8143576e-004	h(62)=h(104)	1.1081079e-002
h(21)=h(145)	2.0609148e-004	h(63)=h(103)	-1.2286827e-017
h(22)=h(144)	3.7719742e-004	h(64)=h(102)	-1.2854066e-002
h(23)=h(143)	-1.3135460e-018	h(65)=h(101)	-8.5743753e-003
h(24)=h(142)	-4.7727057e-004	h(66)=h(100)	9.2714681e-003
h(25)=h(141)	-3.3014394e-004	h(67)=h(99)	1.6257190e-002
h(26)=h(140)	3.6840294e-004	h(68)=h(98)	-1.3648098e-017
h(27)=h(139)	6.6330603e-004	h(69)=h(97)	-1.9256925e-002
h(28)=h(138)	-7.5855074e-018	h(70)=h(96)	-1.3024463e-002
h(29)=h(137)	-8.1504430e-004	h(71)=h(95)	1.4320866e-002
h(30)=h(136)	-5.5640713e-004	h(72)=h(94)	2.5625190e-002
h(31)=h(135)	6.1326453e-004	h(73)=h(93)	-1.4700181e-017
h(32)=h(134)	1.0914384e-003	h(74)=h(92)	-3.2069566e-002
h(33)=h(133)	-3.0857038e-018	h(75)=h(91)	-2.2522496e-002
h(34)=h(132)	-1.3129293e-003	h(76)=h(90)	2.5968686e-002
h(35)=h(131)	-8.8760091e-004	h(77)=h(89)	4.9398128e-002
h(36)=h(130)	9.6931012e-004	h(78)=h(88)	-1.5365203e-017
h(37)=h(129)	1.7100655e-003	h(79)=h(87)	-7.4974391e-002
h(38)=h(128)	-4.3152299e-018	h(80)=h(86)	-6.2037072e-002
h(39)=h(127)	-2.0240716e-003	h(81)=h(85)	9.3329432e-002
h(40)=h(126)	-1.3581687e-003	h(82)=h(84)	3.0255316e-001
h(41)=h(125)	1.4727074e-003	h(83)=h(83)	4.0000032e-001

Table F.14: Table with the impulse response coefficients of the filter presented in figure F.22

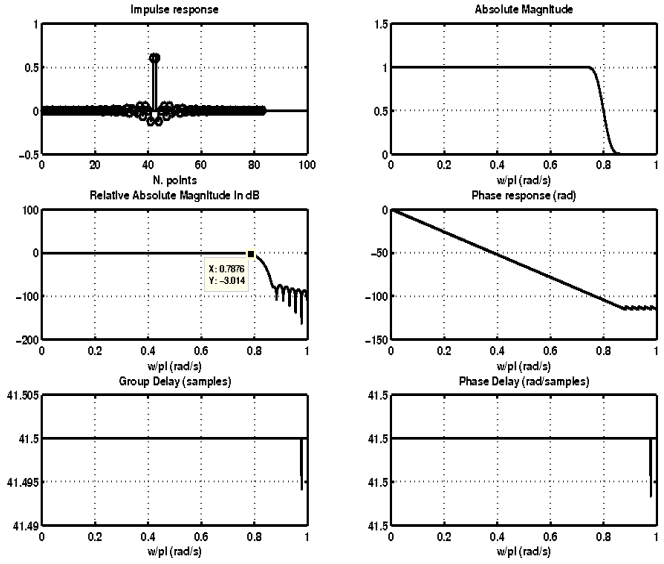

Figure F.23: Lowpass filter (LP_I) of order 84, created from the filter in figure F.22, such that $LP\_I(n) = LP(2n)$, $n = 0, 1, 2, \ldots$

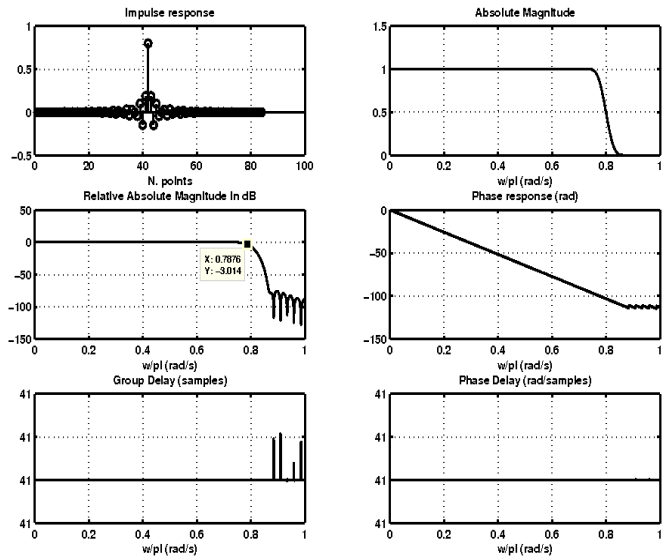

Figure F.24: Lowpass filter (LP_Q) of order 83, created from the filter in figure F.22, such that $LP\_Q(n) = LP(2n+1)$, $n = 0, 1, 2, \ldots$

F.3.2 For Results of BPS when Experimental Signals are used

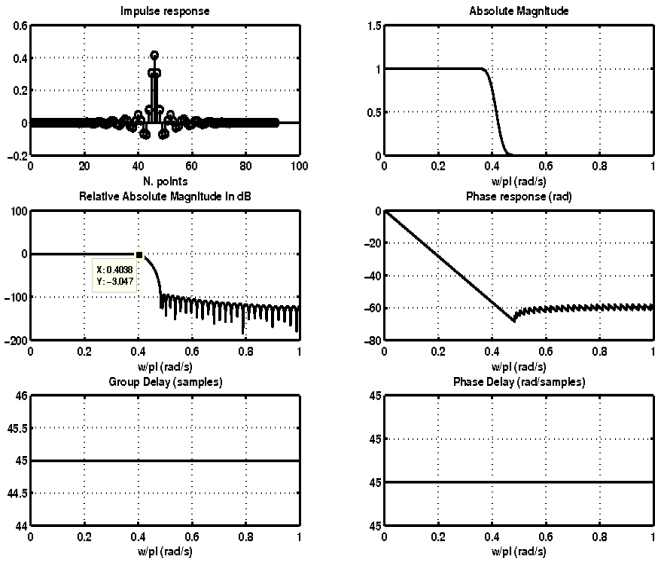

Figure F.25: Lowpass FIR filter of order 91, designed from Kaiser window with parameter equal to 9.5 ; sampling frequency 192.68 kHz

h(0)=h(90)	3.2416046e-006	h(23)=h(67)	-2.0136706e-003
h(1)=h(89)	7.3393060e-006	h(24)=h(66)	4.0627328e-003
h(2)=h(88)	-6.8884351e-006	h(25)=h(65)	5.2042077e-003
h(3)=h(87)	-2.9304743e-005	h(26)=h(64)	-2.3094716e-003
h(4)=h(86)	-5.8962821e-006	h(27)=h(63)	-8.3540384e-003
h(5)=h(85)	6.4386517e-005	h(28)=h(62)	-1.9704308e-003
h(6)=h(84)	6.1424661e-005	h(29)=h(61)	9.8670203e-003
h(7)=h(83)	-8.5074934e-005	h(30)=h(60)	8.5303649e-003
h(8)=h(82)	-1.7862940e-004	h(31)=h(59)	-7.8558355e-003
h(9)=h(81)	3.0454032e-005	h(32)=h(58)	-1.5932628e-002
h(10)=h(80)	3.3599867e-004	h(33)=h(57)	7.5554731e-004
h(11)=h(79)	1.7624625e-004	h(34)=h(56)	2.1479955e-002
h(12)=h(78)	-4.3881372e-004	h(35)=h(55)	1.1984751e-002
h(13)=h(77)	-5.7516875e-004	h(36)=h(54)	-2.1466971e-002
h(14)=h(76)	3.1609725e-004	h(37)=h(53)	-2.9401308e-002
h(15)=h(75)	1.0941629e-003	h(38)=h(52)	1.1453108e-002
h(16)=h(74)	2.2344186e-004	h(39)=h(51)	4.8953235e-002
h(17)=h(73)	-1.4892053e-003	h(40)=h(50)	1.4627664e-002
h(18)=h(72)	-1.2697991e-003	h(41)=h(49)	-6.7007185e-002
h(19)=h(71)	1.3569495e-003	h(42)=h(48)	-7.2812996e-002
h(20)=h(70)	2.6595968e-003	h(43)=h(47)	7.9770115e-002
h(21)=h(69)	-2.6353415e-004	h(44)=h(46)	3.0651015e-001
h(22)=h(68)	-3.8714430e-003	h(45)=h(45)	4.1562020e-001

Table F.15: Table with the impulse response coefficients of the filter presented in figure F.25

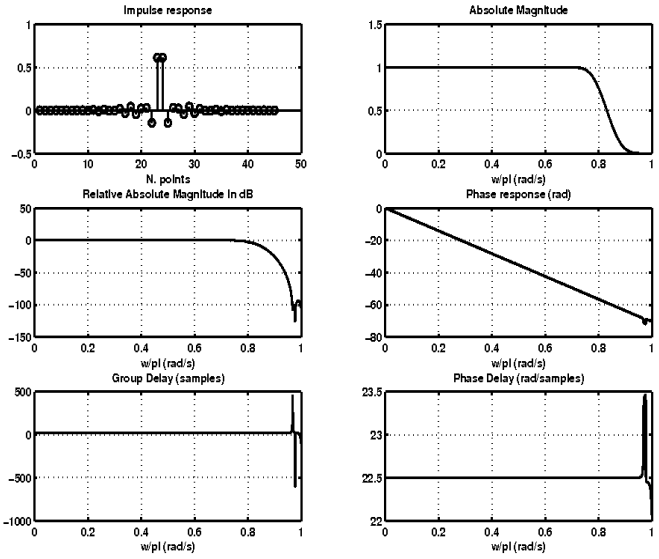

Figure F.26: Lowpass filter (LP_I) of order 46, created from the filter in figure F.25, such that $LP\_I(n) = LP(2n)$, $n = 0, 1, 2, \ldots$

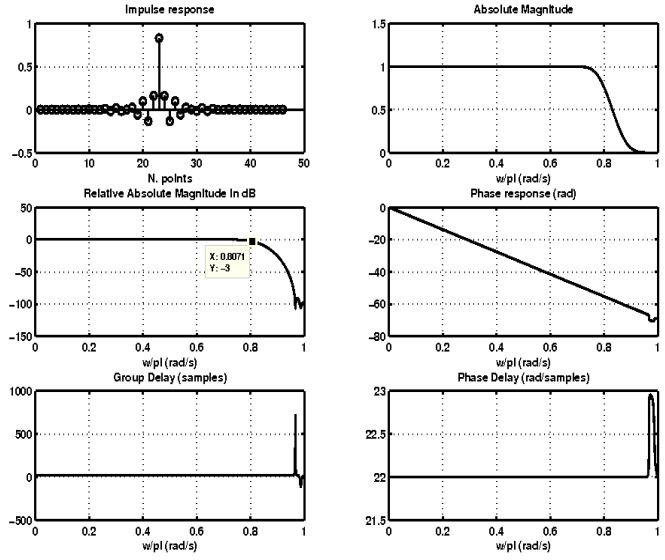

Figure F.27: Lowpass filter (LP_Q) of order 45, created from the filter in figure F.25, such that $LP\_Q(n) = LP(2n+1)$, $n = 0, 1, 2, \ldots$

F.3.3 For Results after Heterodyne Function Application on Experimental Signals

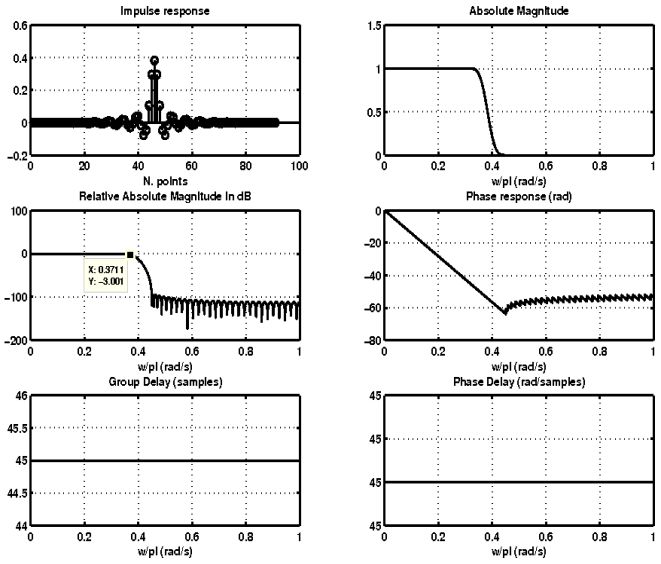

Figure F.28: Lowpass FIR filter of order 91, designed from Kaiser window with parameter equal to 9.5 ; sampling frequency 280.8 kHz

h(0)=h(90)	-2.7741732e-006	h(23)=h(67)	4.5030065e-003
h(1)=h(89)	4.0278317e-006	h(24)=h(66)	7.7539205e-004
h(2)=h(88)	1.7506638e-005	h(25)=h(65)	-5.4587438e-003
h(3)=h(87)	8.4284815e-006	h(26)=h(64)	-5.5811386e-003
h(4)=h(86)	-3.6869042e-005	h(27)=h(63)	2.6721231e-003
h(5)=h(85)	-5.9484813e-005	h(28)=h(62)	9.6275284e-003
h(6)=h(84)	1.8054448e-005	h(29)=h(61)	4.4060856e-003
h(7)=h(83)	1.3841559e-004	h(30)=h(60)	-9.0646314e-003
h(8)=h(82)	1.0128100e-004	h(31)=h(59)	-1.3256987e-002
h(9)=h(81)	-1.5615729e-004	h(32)=h(58)	1.0045207e-003
h(10)=h(80)	-3.2615272e-004	h(33)=h(57)	1.8269726e-002
h(11)=h(79)	-3.7050792e-005	h(34)=h(56)	1.3755662e-002
h(12)=h(78)	5.0657281e-004	h(35)=h(55)	-1.2847460e-002
h(13)=h(77)	5.1924015e-004	h(36)=h(54)	-2.9110793e-002
h(14)=h(76)	-3.3388627e-004	h(37)=h(53)	-7.0073185e-003
h(15)=h(75)	-1.0993191e-003	h(38)=h(52)	3.4280001e-002
h(16)=h(74)	-4.6110338e-004	h(39)=h(51)	3.9507412e-002
h(17)=h(73)	1.2367323e-003	h(40)=h(50)	-1.5760313e-002
h(18)=h(72)	1.7483721e-003	h(41)=h(49)	-7.6395287e-002
h(19)=h(71)	-2.8481856e-004	h(42)=h(48)	-4.7049061e-002
h(20)=h(70)	-2.7394841e-003	h(43)=h(47)	1.0569475e-001
h(21)=h(69)	-1.9268763e-003	h(44)=h(46)	2.9643956e-001
h(22)=h(68)	2.1911567e-003	h(45)=h(45)	3.8314030e-001

Table F.16: Table with the impulse response coefficients of the filter presented in figure F.28

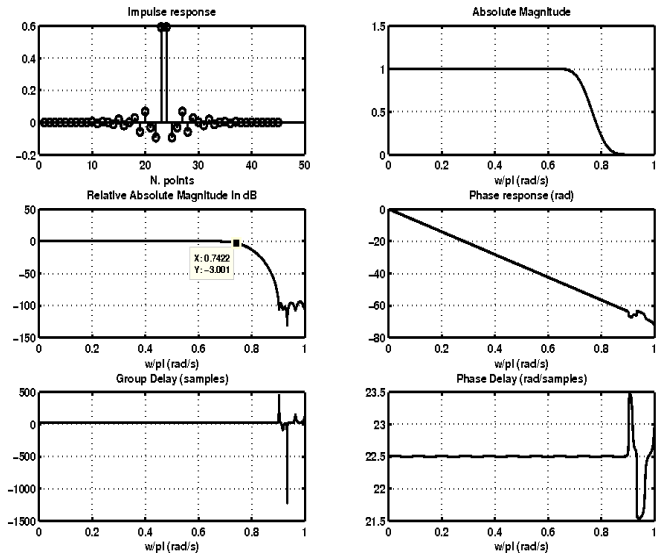

Figure F.29: Lowpass filter (LP_I) of order 46, created from the filter in figure F.28, such that $LP\_I(n) = LP(2n)$, $n = 0, 1, 2, \ldots$

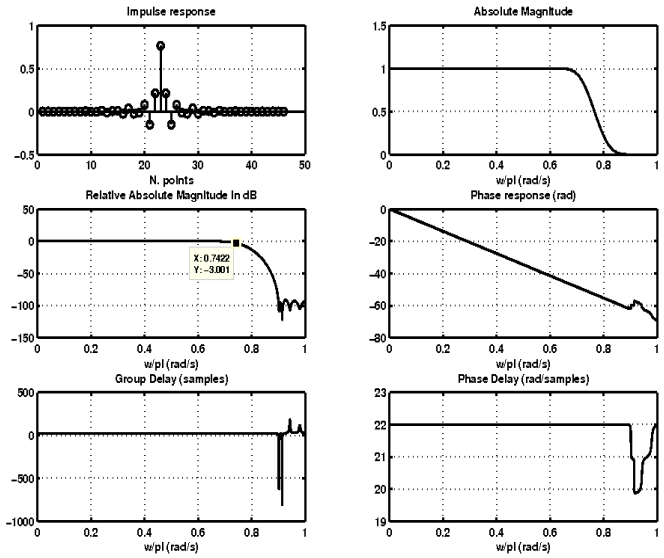

Figure F.30: Lowpass filter (LP_Q) of order 45, created from the filter in figure F.28, such that $LP\_Q(n) = LP(2n+1)$, $n = 0, 1, 2, \ldots$

F.4 Allpass Filters Used in Approach4

For each of these filters, as referred in subsection 3.3.3, an allpass filter [73] presents a frequency response $A(e^{j\omega})$ with unit magnitude in all frequencies, no affecting the signal's amplitude as the signal passes through the filter, only signal's phase is affected.

$$|A(e^{j\omega T})|^2 = 1, \ for\ all\ \omega \tag{F.1}$$

In an IIR allpass filter the frequency response can be written [74] as

$$A(z) \quad = \quad z^{-N}\frac{D(z^{-1})}{D(z)} \tag{F.2}$$

where $D(z) = \sum_{k=0}^{N} a_k \cdot z^{-k}$ with a_k being real coefficients.

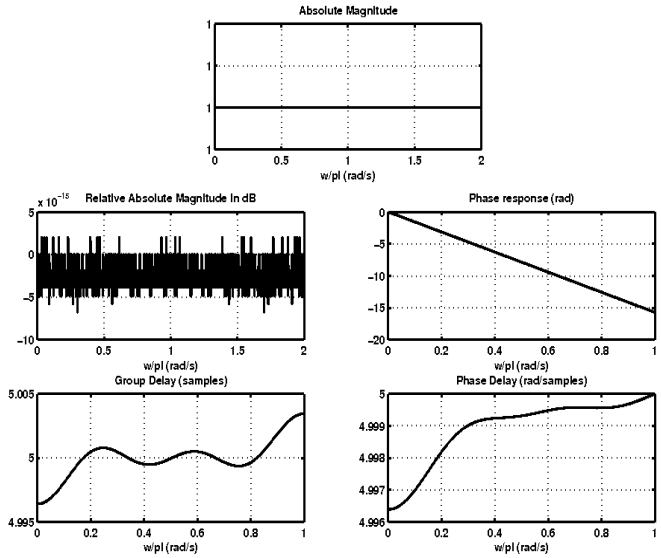

Figure F.31: *Allpass 1* filter with order of 5. The desired phase response ($\theta(\omega) = -N\omega$) is defined for the $\omega = [0.03\pi, 0.94\pi]$

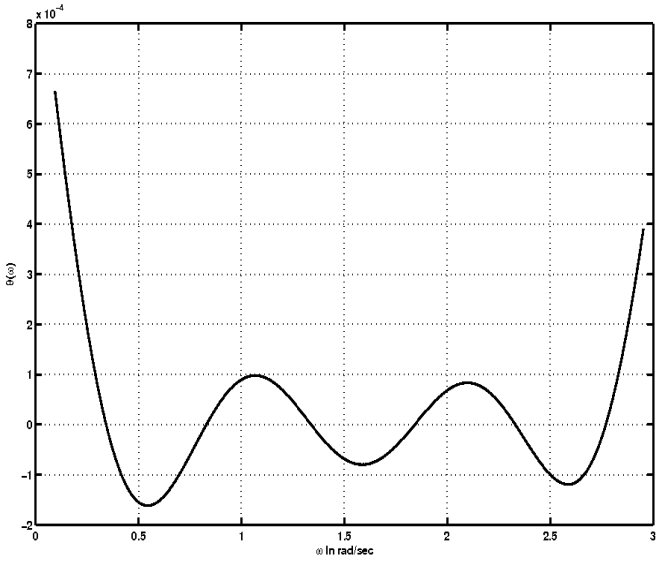

Figure F.32: Phase error for *allpass 1* filter in figure F.31

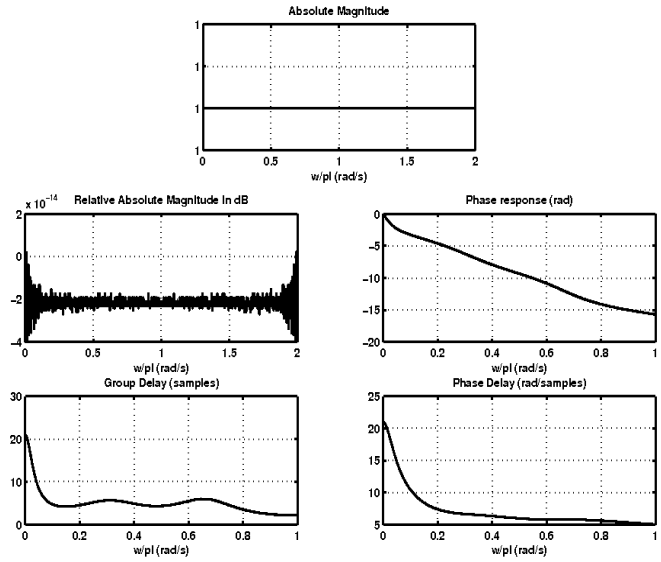

Figure F.33: *Allpass 2* filter with order of 5. The desired phase response ($\theta(\omega) = -N\omega - \frac{\pi}{2}$) is defined for the $\omega = [0.03\pi, 0.94\pi]$

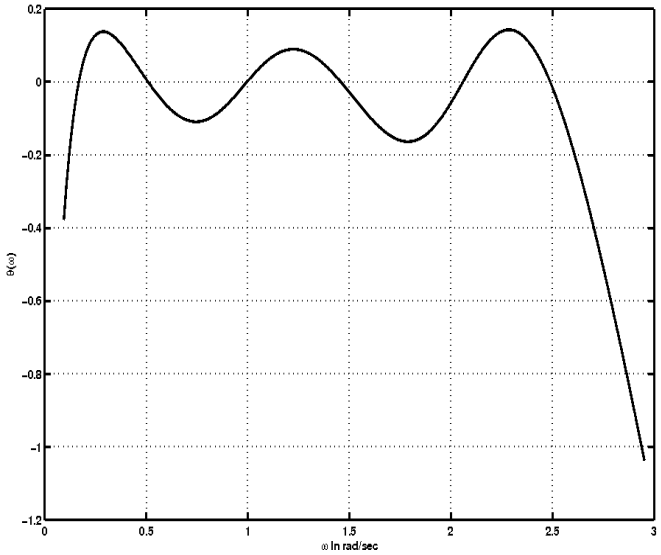

Figure F.34: Phase error for *allpass 2* filter in figure F.33

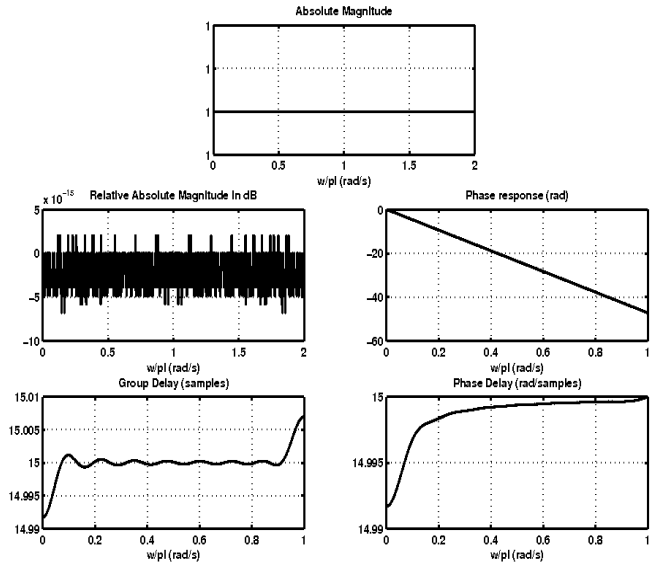

Figure F.35: *Allpass 1* filter with order of 15. The desired phase response ($\theta(\omega) = -N\omega$) is defined for the $\omega = [0.03\pi, 0.94\pi]$

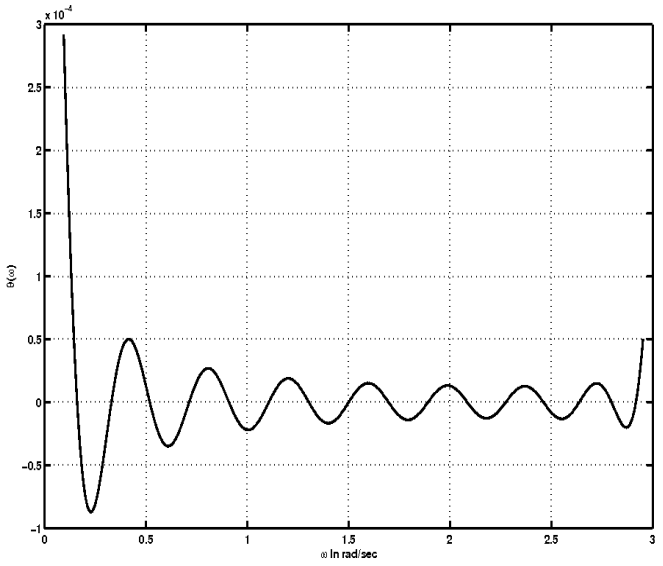

Figure F.36: Phase error for *allpass 1* filter in figure F.35

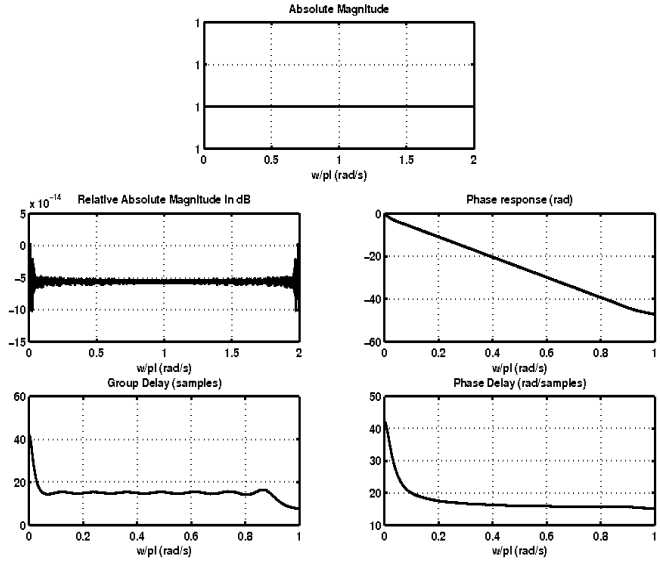

Figure F.37: *Allpass 2* filter with order of 15. The desired phase response ($\theta(\omega) = -N\omega - \frac{\pi}{2}$) is defined for the $\omega = [0.03\pi, 0.94\pi]$

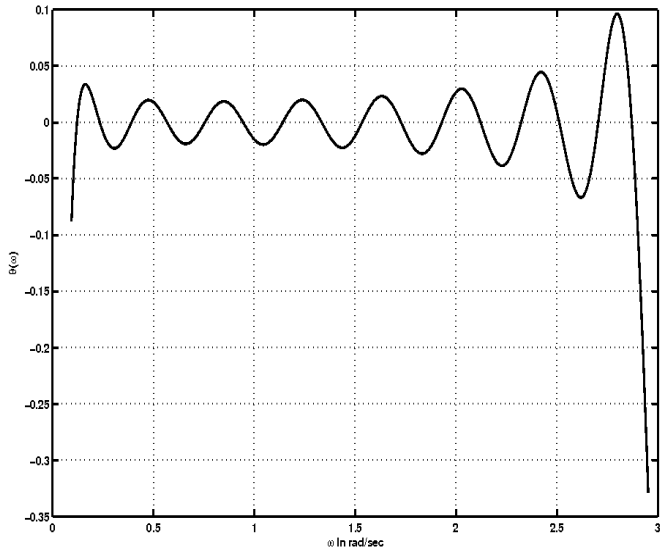

Figure F.38: Phase error for *allpass 2* filter in figure F.37

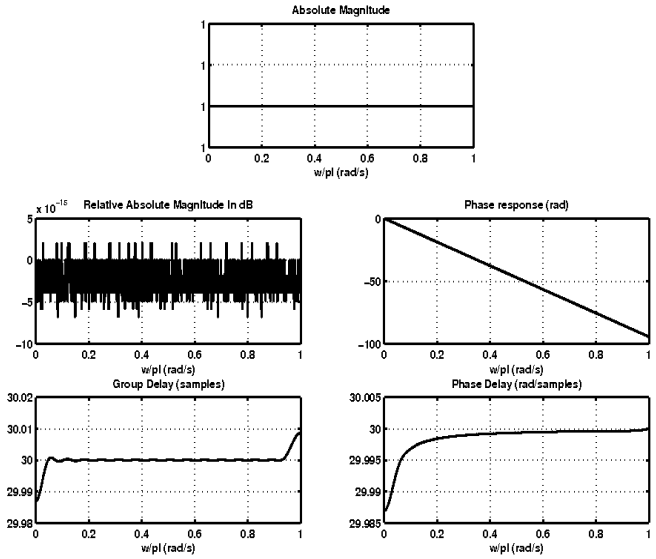

Figure F.39: *Allpass 1* filter with order of 30. The desired phase response ($\theta(\omega) = -N\omega$) is defined for the $\omega = [0.03\pi, 0.94\pi]$

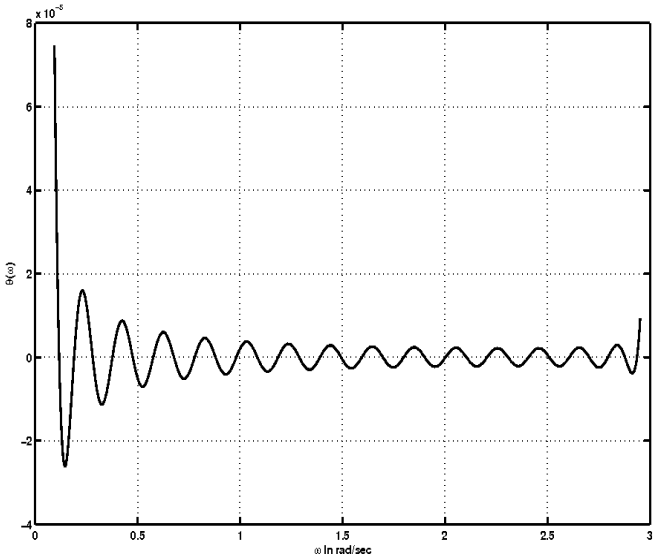

Figure F.40: Phase error for *allpass 1* filter in figure F.39

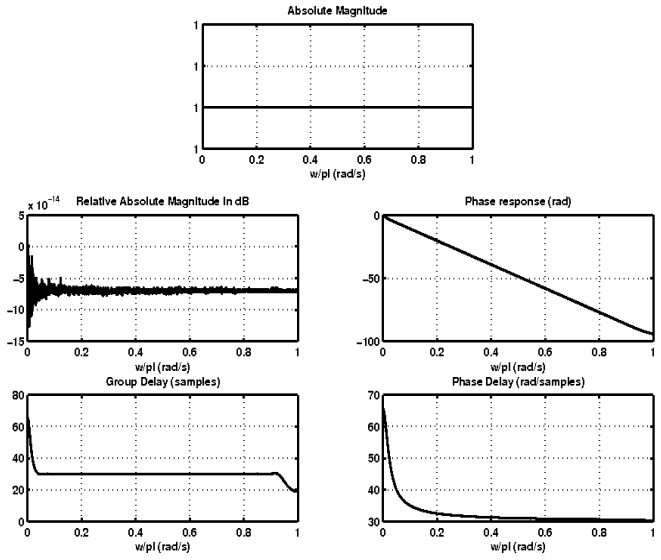

Figure F.41: *Allpass 2* filter with order of 30. The desired phase response ($\theta(\omega) = -N\omega - \frac{\pi}{2}$) is defined for the $\omega = [0.03\pi, 0.94\pi]$

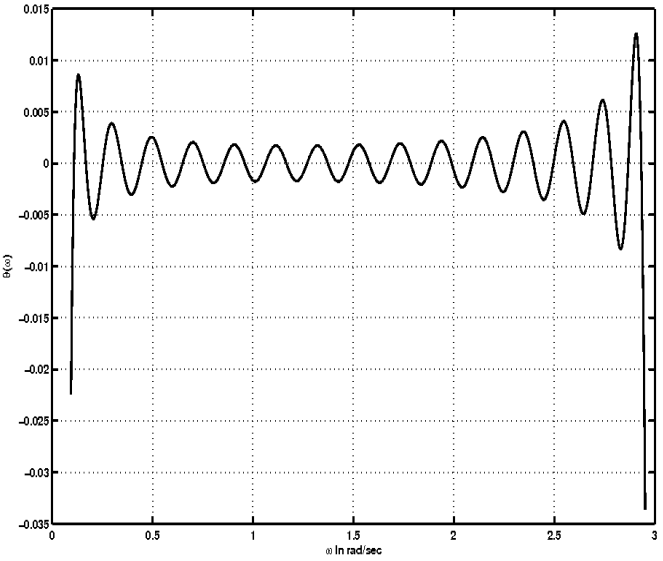

Figure F.42: Phase error for *allpass 2* filter in figure F.41

a_k	*allpass 1*	a_k	*allpass 2*
a(5)	1.0704011e-004	a(5)	-1.3991018e-001
a(4)	8.4013299e-006	a(4)	2.0386281e-001
a(3)	1.9963272e-004	a(3)	-3.7427051e-001
a(2)	4.5072624e-006	a(2)	4.1655784e-001
a(1)	6.3235565e-004	a(1)	-9.6348751e-001
a(0)	1.0000000e+000	a(0)	1.0000000e+000

Table F.17: Coefficients of the transfer function of the allpass filters presented in figures F.31 and F.33

a_k	*allpass 1*	a_k	*allpass 2*
a(15)	1.7272898e-005	a(15)	-2.4742393e-002
a(14)	6.7719776e-006	a(14)	4.1303163e-002
a(13)	2.5470070e-005	a(13)	-6.6057449e-002
a(12)	6.8520689e-006	a(12)	8.0906816e-002
a(11)	3.6655058e-005	a(11)	-1.1144939e-001
a(10)	6.5357249e-006	a(10)	1.2737477e-001
a(9)	5.2396597e-005	a(9)	-1.6613697e-001
a(8)	5.8292836e-006	a(8)	1.8273085e-001
a(7)	7.6036986e-005	a(7)	-2.3393352e-001
a(6)	4.7696503e-006	a(6)	2.5025973e-001
a(5)	1.1631300e-004	a(5)	-3.2467016e-001
a(4)	3.4251691e-006	a(4)	3.3949930e-001
a(3)	2.0545014e-004	a(3)	-4.7503166e-001
a(2)	1.9036828e-006	a(2)	4.8676852e-001
a(1)	6.3434157e-004	a(1)	-9.9462923e-001
a(0)	1.0000000e+000	a(0)	1.0000000e+000

Table F.18: Coefficients of the transfer function of the allpass filters presented in figures F.35 and F.37

a_k	*allpass 1*	a_k	*allpass 2*
a(30)	2.3281609e-006	a(30)	8.7684220e-004
a(29)	2.2642763e-006	a(29)	-3.5443736e-003
a(28)	3.0990560e-006	a(28)	5.0588988e-003
a(27)	3.4268128e-006	a(27)	-8.5419969e-003
a(26)	3.8844039e-006	a(26)	1.0918224e-002
a(25)	4.9994154e-006	a(25)	-1.5884068e-002
a(24)	4.6420237e-006	a(24)	1.9280884e-002
a(23)	7.0973984e-006	a(23)	-2.6084395e-002
a(22)	5.3257608e-006	a(22)	3.0619086e-002
a(21)	9.8616903e-006	a(21)	-3.9588255e-002
a(20)	5.8888769e-006	a(20)	4.5322942e-002
a(19)	1.3469180e-005	a(19)	-5.6790323e-002
a(18)	6.2874378e-006	a(18)	6.3718624e-002
a(17)	1.8152511e-005	a(17)	-7.8051845e-002
a(16)	6.4837339e-006	a(16)	8.6088808e-002
a(15)	2.4238583e-005	a(15)	-1.0374932e-001
a(14)	6.4494714e-006	a(14)	1.1272573e-001
a(13)	3.2226071e-005	a(13)	-1.3438656e-001
a(12)	6.1684713e-006	a(12)	1.4404790e-001
a(11)	4.2951296e-005	a(11)	-1.7083624e-001
a(10)	5.6386659e-006	a(10)	1.8084576e-001
a(9)	5.7979056e-005	a(9)	-2.1488325e-001
a(8)	4.8733030e-006	a(8)	2.2482682e-001
a(7)	8.0666601e-005	a(7)	-2.7061079e-001
a(6)	3.9015659e-006	a(6)	2.7999832e-001
a(5)	1.1978267e-004	a(5)	-3.4880027e-001
a(4)	2.7698970e-006	a(4)	3.5704798e-001
a(3)	2.0759978e-004	a(3)	-4.8740442e-001
a(2)	1.5521260e-006	a(2)	4.9373389e-001
a(1)	6.3507001e-004	a(1)	-9.9742793e-001
a(0)	1.0000000e+000	a(0)	1.0000000e+000

Table F.19: Coefficients of the transfer function of the allpass filters presented in figures F.39 and F.41

Appendix G

PCB and Perfboard Images

G.1 PCB and Perfboard Images

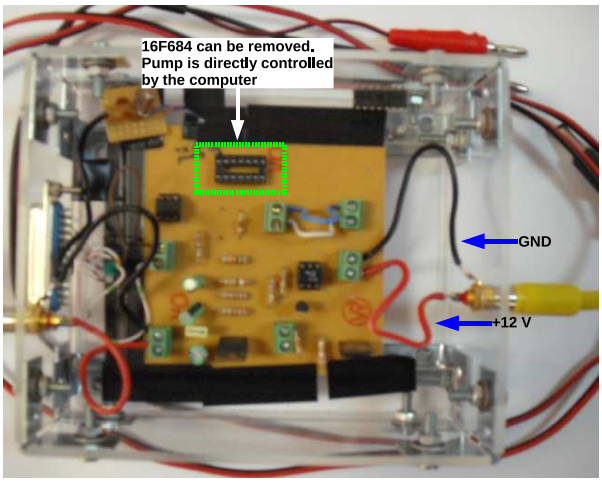

Figure G.1: PCB implementation of the schematics shown in figure 4.4

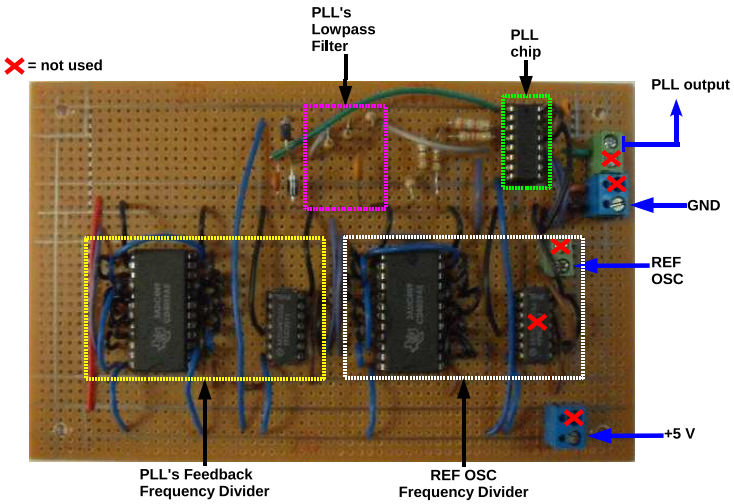

Figure G.2: Perfboard implementation of the schematics shown in figure 4.8. One of the 54HC393J is referred to be *not used* because the expected initial oscillator frequency was in the 8 MHz order, but the available frequency generator (GW function generator Model GFG-8015G) could only produce to a maximum of 2 MHz wave

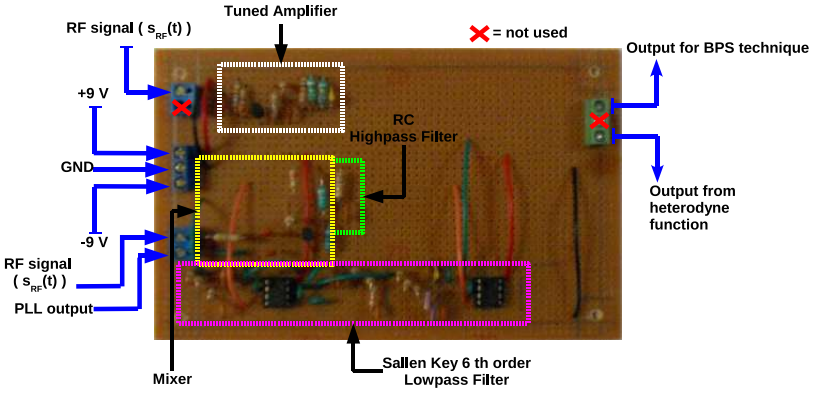

Figure G.3: In this perfboard the circuits in figure 4.7, 4.10 and 4.11 were implemented

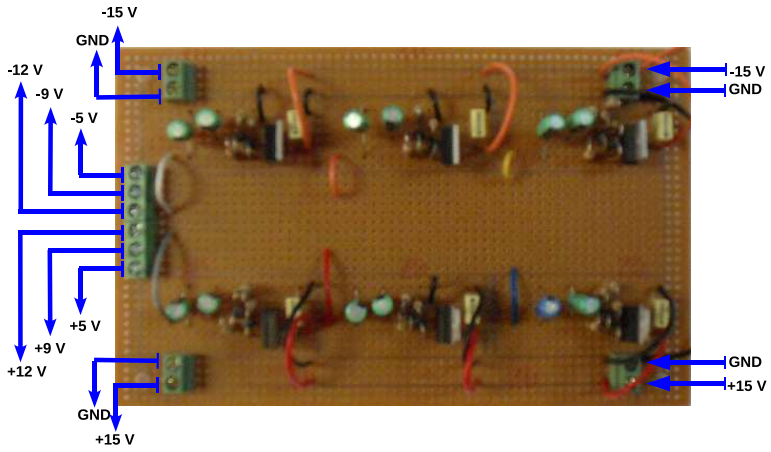

Figure G.4: This perfboard was built to allow a variety of choices of voltages (positive and negative) to be used in all the previous perfboards circuits

Bibliography

[1] Hartshorne, Tim; Thrush, Abigail; *Peripheral Vascular Ultrasound - How, Why and When*; 2nd ed.; Elsevier; 2005; pp 2-3,23-34,49-62,63-73 ;ISBN 0-443-072833

[2] Kerut, Edmund Kenneth; Mcllwain, Elizabeth F.; Plotnick,Gary D.; *Handbook of Echo-Doppler Interpretation*; 2nd ed.; Futura; 2004; pp 1-25 ; ISBN 1-4051-1903-9

[3] Serway, Raymond A.; Jewett, John W.; *Physics for Scientists and Engineers*; 6th ed.; Thomson Brooks/Cole; 2004; pp 513- ISBN 0534408427

[4] Ingle,Vinay K.; Proakis,John G.; *Digital Signal Processing using Matlab V.4*; PWS Publishing Company; 1997; ISBN 0-534-93805-1

[5] Manolakis, Dimitris G.; Proakis, John G.; *Digital Signal Processing: Principles, Algorithms and Applications*; Prentice Hall; 1996; ISBN 0-13-394338-9

[6] Lyons, Richard G.;*Understanding Digital Signal Processing*; 1st ed.; Prentice Hall; 2001; ISBN 0-201-63467-8

[7] Lyons, Richard G.;*Understanding Digital Signal Processing*; 2nd ed.; Prentice Hall; 2004; ISBN 0-13-108989-7

[8] Buck, John R.; Oppenheim, Alan V.; Schafer, Ronald W.; *Discrete-Time Signal Processing*; 2nd ed.; Prentice Hall; 1999; ISBN 0-13-754920-2

[9] Antoniou, Andreas; *Digital Signal Processing - Signals, Systems and Filters*; McGraw Hill; 2006;

[10] Antoniou, Andreas; *Digital filters: analysis, design and applications* ;2nd ed.; McGraw Hill;1993

[11] Oppenheim, Alan V.; Willsky, Alan S.; *et. al*; *Signals and Systems*; 2ns ed.; Prentice Hall;1997; ISBN 7-302-03058-8;

[12] Haykin, Simon; *Communication Systems*; 4th ed.; John Wiley & sons; 2001; ISBN 0-471-17869-1

[13] Carlson, A. Bruce; Crilly, Paul B.; Ruledge, Janet C, *Communication Systems - An Introduction to Signals and Noise in Electrical Communication* ; 4th ed.; McGraw Hill; 2002; ISBN:0070111278

[14] Couch, Leon W. II; *Digital and Analog Communication Systems*;5th ed.;Upper Saddle River, NJ; Prentice Hall; 1996.

[15] Zucker, Ruth; Elementary Transcendental Functions Logarithmic, Exponential, Circular and Hyperbolic Functions In *Handbook of Mathematical Functions with Formulas, Graphs and Mathematical Tables*; 7th ed.; Abramowitz, Milton; Stegun, Irene A.; Eds.;Courier Dover Publications;1972;pp 72-74; ISBN 0-486-61272-4

[16] Best, Roland E.; *Phase-Locked Loops: Design, Simulation and Applications*; 4th ed.; McGraw-Hill; 1999; ISBN 0071349030

[17] Best, Roland E.; *Phase-Locked Loops: Design, Simulation and Applications*; 5th ed.; McGraw-Hill; 2003; ISBN 0071412018

[18] Goldman, Stanley; *Phase-Locked Loop Engineering Handbook for Integrated Circuits*; ARTECH HOUSE; 2007; ISBN-13: 978-1-59693-154-1

[19] Gardner, Floyd M.; *Phaselock Techniques*; 3rd ed.; John Wiley & Sons; 2005; ISBN 0-471-43063-3

[20] Hill, Winfiled; Horowitz, Paul; *The Art of Electronics*, 2nd ed.; Cambridge University Press; 1989; ISBN 0-521-37095-7

[21] Egan, William F.; *Phase-Lock Basics*; 2nd ed.; Wiley-IEEE Press; 2007; ISBN 978-0-470-11800-9

[22] Egan, William F.; *Frequency Synthesis by Phase Lock*; Wiley-Interscience; 1999; ISBN 0471321044

[23] Sedra, Adel S.; Smith, Kenneth C.; *Microelectronic Circuits*; 5 th ed.;Oxford University Press; 2004; ISBN 0-19-514252-7

[24] Ogata, Katsuhiko; *Modern Control Engineering*; 3rd ed.;Prentice Hall; 1997; ISBN 0-13-227307-1

[25] D'Azzo, John J.; Houpis, Constantine H.; Sheldon, Stuart N. *Linear Control System Analysis and Design with Matlab*; 5th ed.; Marcel Dekker Inc.;2003; ISBN 0-8247-4038-6

[26] Levine, William S.;*The Control Handbook, Volume I*; CRC-Press; 1996; ISBN 0849385709

[27] Banerjee, Dean; *PLL Performance, Simulation and Design Handbook*; 4 th Edition; 2006; [Online]. Available:http://www.national.com/analog/timing/pll_designbook

[28] Evans, David H.; McDiken, W. Norman; *et al. Doppler Ultrasound: Physics, Instrumentation and Signal Processing*; John Wiley and Sons;1991 (reprinted); ISBN 0-471-91489-4

[29] Hahn, Stefan L.;*Hilbert Transforms in Signal Processing*; Artech House; 1996; ISBN 0-89006-886-0

[30] Chu, Eleanor; George, Alan; *Inside the FFT Black Box: Serial and Parallel Fast Fourier Transform Algorithms*; CRC Press

[31] Mallik, Ranjan K.; Rangarao, Kaluri Venkata; *Digital Signal Processing A Practitioner's Approach*; John Wiley and Sons; 2005; ISBN 0-470-01769-4

[32] Taylor, Fred J.; Williams, Arthur B.; *Electronic Filter Design Handbook*; 4th ed; McGRAW-HILL; 2006; ISBN 0-07-147171-5

[33] Lam, Harry; *Analog and Digital Filters: esign and Realization*; Prentice Hall Inc; 1979; ISBN 0-13-032755-7

[34] Raff, Hershel; Strang, Kevin T.; Widmaier, Eric P.;*Human Physiology: The Mechanisms of Body Function*; 9th ed; McGraw-Hill ;2003;

[35] White, Frank M.; Fluid Mechanics; 4th ed; McGRAW-HILL;

[36] Calas, H.; Carrillo E.; Jiménez, A.;Moreno E.; Torres D.; Sistema para Medir Flujo Sanguíneo en Vasos Empleando la Técnica "Tiempo de Tránsito Ultrasónico"; *VII Congreso de la Sociedad Cubana de Bioingeniería Habana 2007*;

[37] Fischer, T;Thomas, A.; *et. al*; Real-time elastography - an advanced method of ultrasound: first results in 108 patients with breast lesions; *Ultrasound Obstet Gynecol*; vol 28; pp 335-340; 2006

[38] Hasegawa, Hideyuki; Kanai, Hiroshi; Ultrasonic Vascular Elastography for Tissue Characterization of the Arterial Wall; *5th International Symposium of 2007 Tohoku Univeristy Global COE Program GLobal Nano-Biomedical Engineering Education and Research Network Centre*, pp. 9-12 (March 27-28, 2008, Matsushima)

[39] Davolos,Marian Rosaly; Júnior,Miguel Jafelicci; Martines,Marco Antonio Utrera; O Efeito do Ultra-Som em ReaçõesS Químicas; *Química Nova*; Vol 23; no.2; pp 251-256;2000

[40] Barragán, M.; Fuentes, M.; García, F.;Moreno, E.; Sotomayor,A.; Solano, J.; Sistema Doppler bidireccional para medición de flujo sanguíneo basado en una arquitectura abierta; *Revista Mexicana de Ingeniería Biomédica* ; XXIV ; Num. 2; pp. 135-143; September 2003

[41] Barragán, M.; Fuentes, M.; García, F.; Moreno, E.; Sotomayor, A.; Método Digital para la Detección de la dirección del flujo sanguíneo en Sistemas Doppler ultrsónicos; *Revista Mexicana de Ingeniería Biomédica*; XXIII ; Num. 2; pp. 123-127; September 2002

[42] Acevedo, P.; Fuentes, M.; García, F.; Moreno, E.; Sotomayor, A.; Design and Construction of a Blood Flow Detector Probe for a Continuous Wave Bidireccional Doppler Ultrasound System; *Ingeniería. Investigación y Tecnología*; VII; Num. 2; pp 97-103; 2006

[43] Guler, I.; Guler, N. F.; The electronic detail of a pulsed Doppler blood flow measurement system; *Measurement Science and Technology*; Vol. 1; pp. 1087-1092; 1990

[44] Baker, D.W.; Pulsed Ultrasonic Doppler Blood-Flow Sensing; *IEEE Transactions on Sonics and Ultrasonics*; Vol. 17; Issue 3; pp. 170- 184

[45] Bonnefous, O.; Blood flow and tissue motion with ultrasound for vascular applications; *Comptes Rendus de l'Acadmie des Sciences - Series IV - Physics*; Vol. 2, no. 8; pp 1161-1178; 2001

[46] Bambi, G. Fidanzati, P. Morganti, T. Ricci, S. Tortoli, P.; Real-time digital processing of Doppler ultrasound signals; Vol. 5; pp. v/977- v/980; March 2005

[47] Aydin. N., Evans, D. H.; Implementation of Directional Doppler techniques using a digital signal processor; *Med. Biol. Eng. Comput.*; Vol. 32; pp. S157-S164; July 1994

[48] Aydin. N., Evans, D. H., Fan L.; Quadrature-to-Directional format conversion of Doppler signals using digital methods; Physiol. Meas. ; vol 15; pp. 181-199; 1994

[49] Tortoli, P.;Bessi, L.; Guidi, F.; Bidirectional Doppler signal analysis based on a single RF sampling channel; *IEEE Transactions on Ultrasonics, Ferroelectrics and Frequency Control* ; Vol. 41 ; Issue 1; pp. 1-3; Jan 1994

[50] Vaughn, Rodney G.; Scott, Neil L.; White, D. Rod; The Theory of Banspass Sampling; *IEEE Transactions on Signal Processing* ; Vol. 39 ; Issue 9; pp. 1973-1984; Sep 1991

[51] Qi, Ronggang; Coakley, F.P.; Evans, B.G.; Practical consideration for bandpass sampling; *Electronics Letters* ; Vol. 32 ; Issue 20; pp. 1861-1862; Sep 1996

[52] Coulson, A.J. Vaughan, R.G. Poletti, M.A.; Frequency-shifting using bandpass sampling; *IEEE Transactions on Signal Processing* ; Vol. 42 ; Issue 6; pp. 1556-1559;

[53] Wu, Y.; A proof on the minimum and permissible sampling rates for the first-order sampling of bandpass signal; *Elsevier Digital Signal Processing* ; Vol. 17 ; Issue 4; pp. 848-854 ; July 2007

[54] Diez, R.J.; Corteggiano, F.; Lima, R.A. ; Frequency Mapping in Uniform Bandpass Sampling; *Proceedings of the IEEE Instrumentation and Measurement Technology Conference IMTC 2005*; Vol. 1 ; pp. 672-676; May 2005

[55] Akos, D.M.; Tsui, J.B.Y.; Design and implementation of a direct digitization GPS receiver front end; *IEEE Transactions on Microwave Theory and Techniques* ; Vol. 44 ; Issue 12, Part 2; pp. 2334-2339 ; Dec 1996

[56] Akos, D.M.; Stockmaster, M.; Tsui, J.B.Y.; Caschera, J.; Direct bandpass sampling of multiple distinct RF signals; *IEEE Transactions on Communications* ; Vol. 47 ;, Issue 7; pp. 983-988; Jul 1999

[57] Akos, Dennis M.; A Software Radio Approach to Global Navigation Satellite System Receiver Design; Ph.D. dissertation; College of Engineering and Technology, Ohio University; 1997

[58] Darwazeh, I.; O'Reilly, J.J.; Patel, M.; Bandpass sampling for software radio receivers, and the effect of oversampling on aperture jitter; *IEEE 55th Vehicular Technology Conference, 2002*; Vol. 4; pp. 1901 - 1905; 2002

[59] Sadr,R.; Shahshahani, M.; On Sampling Band-Pass Signals; *TDA Progress Report* 42-96; Oct - Dec 1988

[60] Lee, Jim P.Y.; Effects of Imbalances and DC Offsets on I/Q Demodulation; DREO Report No. 1148, Dec. 1992

[61] Khare, Kedar; George, Nicholas; Direct sampling and demodulation of carrier-frequency signals; *Elsevier Optics Communications* ; *211*; Issues 1-6; pp. 85-94; October 2002

[62] Inan, Umran Savas; Yavuz, Davras; A Novel Approach for Finding the Spectrum of Periodically Modulated FM Carriers; *IEEE Transactions on Communications* ; Vol. 26 ; Issue 8; pp. 1309-1315; Aug 1978

[63] V. Considine; Digital Complex Sampling; *Electronics Letters* ; Vol. 19 ; No. 16

[64] Zhang, G.; Al-Khalili, D.; Inkol, R.; Saper, R.; Novel Approach to the Design of I/Q demodulation filters; *IEE Proceedings; Vis. Image Signal Process.* ; Vol. 141 ; No. 3 ; June 1994;

[65] Inkol, R.J.; Saper, R. H.; Herzig, M.; Design of Digital Filters for Precision Quadrature Demodulation; *IEE Proceedings; Vis. Image Signal Process.* ; Vol. 143 ; No. 2; April 1996

[66] Inkol, R.J.; Novel FIR Designs for Digital Quadrature Demodulation; *Proceedings of the 1999 Canadian Conference on Electrial and Computer Engineering* ;

[67] Inkol, R.J.; Herzig, M.M Saper, R.; High Accuracy Digital Quadrature Demodulation;

[68] Rader, C.M.; A Simple Method for Sampling In-Phase and Quadrature Components; *IEEE Trans. on Aerospace and Electronic Systems* ; *AES-20*; No.6; November 1984 ;

[69] Gold,B.; Oppenheim, A.V; Rader,C. M. Theory and implementation of the discrete Hilbert transform; *Proc. Symp. Computer Processing Communications*; J. Fox, Ed. Brooklyn, NY: Polytechnic Press (Wiley),pp. 235 - 250; 1969

[70] Liu, H.; Ghafoor, A.; Stockmann, P.H.; A new quadrature sampling and processing approach; *IEEE Transactions on Aerospace and Electronic Systems* ; Vol. 25 ; Issue 5; 733-748; Sep 1989

[71] Rice, D.W.; Wu, K.H.; Quadrature Sampling with High Dynamic Range; *IEEE Transactions on Aerospace and Electronic Systems* ; Vol. AES-18 ; Issue 4; 736-739; Nov 1982

[72] Snelgrove, W.M.; Yu, Li; A novel adaptive mismatch cancellation system for quadrature IF radio receivers; Vol. 46, Issue 6; pp. 789-801; Jun 1999

[73] Mitra, S.K.;Regalia, P.A.;Vaidyanathan, P.P.; The digital all-pass filter: a versatile signal processing building block; *Proceedings of the IEEE*; Vol. 76; Issue 1; pp 19-37; Jan. 1988

[74] Kidambi, S.S.; Weighted least-squares design of recursive allpass filters; *IEEE Transactions on Signal Processing*; Vol. 44; Issue 6; pp 1553-1557; Jun 1996

[75] Bascom, Peter A. J.; Cobbold, Richard S. C.; Origin of the Doppler Ultrasound Spectrum from Blood; *IEEE Transactions on Biomedical Engineering*; Vol. 43; No 6; pp. 562-571;1996

[76] Shung, K. Kirk; Wang, Shyh-Hau ;In Vivo Measurements of Ultrasonic Backscattering in Blood; *IEEE Transactions on Ultrasonics, Ferroelectrics, and Frequency Control*; vol. 48; No. 2; pp. 425-431; 2001

[77] Cobbold, Richard S. C.; Mo, Larry Y. L.; A Stochastic Model of the Backscattered Doppler Ultrasound from Blood; *IEEE Transactions on Biomedical Engineering* Vol.BME-33; No. 1; pp 20-27;1986

[78] Shung, K. Kirk;Wang, Shyh-Hau; Backscatter Measurements on Whole Blood Using a real-time Scanner; *IEEE Ultrasonics Symposium*; pp 1109-1112;1996;

[79] Klepper, John R; Moehring, Mark A.; Pulse Doppler Ultrasound Detection, Characterization and Size Estimation of Emboli in Flowing Blood; *IEEE Transactions on Biomedical Engineering*; Vol 41; No. 1; pp 35-44; 1994;

[80] Rao, Y.V.R.; Venkateswaran, N.; Allpass lattice structure based second order digital IIR notch filter for removing DC and very low frequencies; *Conference on Convergent Technologies for Asia-Pacific Region*; Vol. 4: pp 15-17; Oct. 2003

[81] Vlcek, M.; Zahradnik, P.; Fast Analytical Design Algorithms for FIR Notch Filters; *IEEE Transactions on Circuits and Systems I: Regular Papers*; Vol. 51; Issue 3; pp. 608 - 623; March 2004

[82] Vlcek, M.; Zahradnik, P.; Robust Analytical Design of Equiripple Comb FIR Filters; *IEEE International Symposium on Circuits and Systems*, 2008; May 2008 pp 1128 - 1131 ;May 2008;

[83] Cooley, J.W; Helms, H.D.; Jackson, L.B.; Kaiser, J. F.; Rabiner, R. L.; Rader, C. M.; Schafer, R.W.; Steiglitz, K.; Weinstein, C. J.; Terminology in Digital Signal Processing; *IEEE Trans. on Audio and Electroacoustics*; Vol. AU-20; no. 5; pp 322-337; 1972

[84] M INAMI , M., F UKUJU , Y., H IRASAWA , K., Y OKOYAMA , S., M IZUMACHI , M., M ORIKAWA , H., AND AOYAMA , T. DOLPHIN: a practical approach for implementing a fully distributed indoor ultrasonic positioning system; *Proceedings of Ubicomp: Ubiquitous Computing* (Nottingham, UK, Sept. 2004), Springer, pp. 347365.

[85] [online] http://www.ia.csic.es/Proyectos.aspx?Lang=EN&id=37

[86] [online] http://en.wikipedia.org/wiki/3D_ultrasound

[87] *PIC 16F684 datasheet*; [online] ww1.microchip.com/downloads/en/devicedoc/41202D.pdf

[88] [online] http://www.driverlinx.com/DownLoad/DlPortIO.htm

[89] [online] http://www.codeproject.com/KB/system/steppermotorcontrol.aspx?display=PrintAll

[90] [online] www.python.org

[91] [online] http://sine.ni.com/nips/cds/view/p/lang/en/nid/202597

[92] [online] http://sine.ni.com/ds/app/doc/p/id/ds-20/lang/en

[93] MIT OpenCourseWare: *High Speed Communication Circuits*; *Lecture 9: Enhancement Techniques for Broadband Amplifiers, Narrowband Amplifiers*; Spring 2005; [online] http://ocw.mit.edu/OcwWeb/web/courses/courses/index.htm

[94] *Optocouplers: When and How to Use Them*; [online] www.jaycar.com.au/images_uploaded/optocoup.pdf

[95] *PIC 16F684 datasheet*; [online] http://ww1.microchip.com/downloads/en/DeviceDoc/41202E.pdf

[96] Axelson, Jan; *Parallel Port Complete: Programming, Interfacing and Using PC Parallel Printer Port*; Lakeview Research; 2000;

[97] Gadre, Dhananjay; *Programming the Parallel Port: Interfacing the PC for Data Acquisition and Process Control*; R & D Books; 1998;

[98] [online] http://www.logix4u.net/parallelport1.htm

[99] [online] http://engr.nmsu.edu/etti/fall96/computer/printer/printer.html

[100] Philips Semiconductors Application Note *AN177: An Overview of the Phase-Locked Loop*; December 1988

[101] Freescale Semiconductor Application Note *AN535: Phase Locked Loop Design Fundamentals* by Garth Nash; Rev. 1.0, 02/2006

[102] Texas Instruments Application Report *CMOS Phase-Locked-Loop Applications Using the CD54/74HC/HCT4046A and CD54/74HC/HCT7046A* by W. M. Austin; September 2002

[103] Zumbahlen, Hank; Analog Devices Application Note 649 *Using the Analog Devices Active Filter Design Tool*; Rev. 0; 2003;

[104] *Texas Instruments CD54HC4046A, CD74HC4046A, CD54HCT4046A, CD74HCT4046A: High-Speed CMOS Logic Phase-Locked Loop with VCO* data sheet; February 1998 - Revised December 2003

[105] *Philips CD54HC4046A, 74HC/HCT4046A Phase-Locked Loop with VCO* data sheet; 25 November 1995

[106] *Texas Instruments CD4049A Types CMOS Programmable Divide-by-"N" Counter* data sheet; Revised June 2003

[107] *Texas Instruments TLC2933 High-Performance Phase-Locked Loop*; REV. January 2002

[108] *Siemens BC337 BC 338 NPN Silicon AF Transistors* data sheet;

[109] *Motorola MC54/74HC393 Dual 4-Stage Binary Ripple Counter* data sheet

[110] *4N37 Datasheet*; [online] http://www.fairchildsemi.com/ds/4N/4N37.pdf

[111] *LM317T datasheet*; [online] http://physics.gac.edu/ huber/classes/phy270/SpecSheets/LM317.pdf

[112] *LM337T datasheet*; [online] www.datasheetcatalog.org/datasheet2/f/0cp81c95q6hrawsf30y0gq2557w

[113] *Mestrado Integrado em Engenharia Electrónica e Telecomunicações* course curriculum [online] http://deei.fct.ualg.pt/curso/mestrado-integrado-engenharia-electronica-telecomunicacoes